UNIVERSITÉ DE GENÈVE

Section de physique

Département de physique nucléaire et corpusculaire

FACULTÉ DES SCIENCES

Professeur Teresa Montaruli

IceCube searches for neutrinos from dark matter annihilations in the Sun and cosmic accelerators.

THÈSE

présentée à la Faculté des sciences de l'Université de Genève

pour obtenir le grade de Docteur ès sciences, mention physique

par

M. Rameez

de Kozhikode, Kerala (India)

Thèse N° 4923

GENÈVE

2016

UNIVERSITÉ DE GENÈVE

FACULTÉ DES SCIENCES

Doctorat ès sciences
Mention physique

Thèse de *Monsieur Mohamed RAMEEZ*

intitulée :

"IceCube Searches for Neutrinos from Dark Matter Annihilations in the Sun and Cosmic Accelerators"

La Faculté des sciences, sur le préavis de Madame T. MONTARULI, professeure ordinaire et directrice de thèse (Département de physique nucléaire et corpusculaire), Monsieur A. BLONDEL, professeur ordinaire (Département de physique nucléaire et corpusculaire), Monsieur A. W. RIOTTO, professeur ordinaire (Département de physique théorique) et Monsieur C. PEREZ DE LOS HEROS, associate professeur(Department of physics and astronomy, Uppsala University, Sweden), autorise l'impression de la présente thèse, sans exprimer d'opinion sur les propositions qui y sont énoncées.

Genève, le 27 avril 2016

Thèse - 4923 -

Le Décanat

N.B. - La thèse doit porter la déclaration précédente et remplir les conditions énumérées dans les "Informations relatives aux thèses de doctorat à l'Université de Genève".

Declaration of Authorship

I, Mohamed RAMEEZ, declare that this thesis titled, 'IceCube searches for neutrinos from dark matter annihilations in the Sun and cosmic accelerators.' and the work presented in it are my own. I confirm that:

- This work was done wholly or mainly while in candidature for a research degree at this University.

- Where any part of this thesis has previously been submitted for a degree or any other qualification at this University or any other institution, this has been clearly stated.

- Where I have consulted the published work of others, this is always clearly attributed.

- Where I have quoted from the work of others, the source is always given. With the exception of such quotations, this thesis is entirely my own work.

- I have acknowledged all main sources of help.

- Where the thesis is based on work done by myself jointly with others, I have made clear exactly what was done by others and what I have contributed myself.

Signed:

Date:

27 April 2016

Abstract

Doctor of Philosophy

IceCube searches for neutrinos from dark matter annihilations in the Sun and cosmic accelerators.

by Mohamed RAMEEZ

The IceCube neutrino observatory is a cubic kilometre-sized Cherenkov detector embedded deep within the glacial ice at the South Pole. It was completed in 2011 and has been gathering data in its full configuration ever since. A central, more densely instrumented sub-detector array known as DeepCore, lowers the neutrino energy threshold of the detector down to ∼10 GeV. This work summarizes IceCube searches for extraterrestrial point-like sources of neutrinos originating from two different processes, the pair annihilation of gravitationally trapped Dark Matter and interactions of Cosmic Rays at their acceleration sites. Non overlapping samples of events dominated by ν_μ (and $\bar{\nu}_\mu$) charged current interactions from atmospheric neutrinos were isolated from 1019 days of operation of IceCube-DeepCore. Atmospheric muon contamination was lowered in comparison to previous searches using innovative veto techniques. An unbinned maximum likelihood ratio method was used to look for an excess of GeV neutrinos in the direction of the Sun among atmospheric neutrinos and muons. Sensitivity towards signals from WIMP annihilations in the Sun was further boosted by using event energy information for events contained within DeepCore. No statistically significant excess was found. Constraints were placed on the muon flux from the Sun, which can also be interpreted as constraints on the WIMP-Nucleon scattering cross section. For spin-dependent scattering, these constraints are the strongest ever, and are stronger than previous constraints from IceCube by an order of magnitude for high WIMP masses. The interpretations of these constraints on some theoretical scenarios of Dark Matter are explored. The unbinned maximum likelihood ratio method has also been used to carry out stacking searches for astrophysical neutrino emissions from catalogs of Galactic supernova remnants, starburst galaxies, galaxy clusters, active galactic nuclei within the Greisen Zatsepin Kuzmin horizon as well as the arrival directions of ultra-high-energy cosmic rays. A search was also carried out for periodic neutrino emission from known Galactic binary systems. No statistically significant excess was found. Constraints are placed on the fraction of the contribution from each class of sources towards the IceCube astrophysical flux, as well as on theoretical flux predictions for specific catalogs.

Résumé

Doctor of Philosophy

Recherche de neutrinos issus d'annihilations de matière noire dans le Soleil et les accélérateurs cosmiques avec le détecteur IceCube.

by Mohamed Rameez

L'observatoire IceCube est un détecteur Cherenkov d'un volume d'un kilomètre cube situé au plus profond de la glace du pôle Sud. Il est dédié à la détection de neutrinos. Achevé en 2011, il a depuis permis la collecte de nombreuses données dans sa configuration complète. Au centre, le détecteur est plus densément instrumenté (DeepCore) ce qui abaisse le seuil de détection en énergie à ∼10 GeV. Ce manuscrit résume les recherches effectuées à l'aide du détecteur IceCube des sources ponctuelles extraterrestres de neutrinos provenant de deux processus différents 1) annihilation de la matière noire piégée par gravitation et 2) interactions des rayons cosmiques sur leurs sites d'accélération.

Sur 1019 jours de fonctionnement d'IceCube-DeepCore, seuls les échantillons d'événements sans recouvrement dominés pas les ν_μ (et $\bar{\nu}_\mu$) issus des interactions entre courant chargés et neutrinos atmosphériques sont sélectionnés.

La contamination de muons atmosphériques a été abaissée par rapport aux recherches précédentes en utilisant des techniques de veto innovantes. Une méthode de rapport de maximum de vraisemblance non binée a été utilisée pour chercher un excès de neutrinos à l'échelle du GeV dans la direction du Soleil parmi les neutrinos et muons atmosphériques. Pour les événements contenus à l'intérieur de DeepCore, l'information sur l'énergie de l'événement a été utilisée et la sensibilité aux signaux d'annihilations de matière noire a été améliorée. Cette étude révèle qu'un excès statistiquement significatif n'est pas présent. Cela permet néanmoins de fixer des contraintes sur le flux de muons provenant du Soleil, qui peuvent également être interprétées comme des contraintes sur la section efficace WIMP-nucléon. Pour la diffusion dépendant du spin, ces contraintes sont les plus fortes jamais établies, et sont plus fortes d'un ordre de grandeur que les contraintes précédentes d'IceCube pour des masses élevées de WIMP. Les interprétations de ces contraintes sur quelques scénarios théoriques de matière noire sont explorées.

La méthode de rapport de maximum de vraisemblance non binée a également été utilisée pour effectuer des recherches de superpositions pour les émissions de neutrinos astrophysiques à partir des catalogues incluant des restes de supernova Galactique, des galaxies croisées, des regroupements de galaxies,

des noyaux galactiques actifs au sein de l'horizon Greisen Zatsepin Kuzmin, ainsi que les directions d'arrivée des rayons cosmiques d'ultra-haute énergie. Une recherche a également été réalisée sur l'émission périodique de neutrino de systèmes Galactiques binaires ne montrant cependant pas d'excès statistiquement significatif. Les contraintes sont dérivées sur la fraction de la contribution de chaque classe de sources vers le flux astrophysique d'IceCube, ainsi que sur les prévisions de flux théoriques pour les catalogues spécifiques.

List of Papers/Proceedings

The work presented in this thesis has been published in the following papers/proceedings:

E. Morgante *et al.* , Submitted to JHEP
The 750 GeV Diphoton excess, Dark Matter and Constraints from the IceCube experiment

M. G. Aartsen *et al.* [IceCube, Pierre Auger and Telescope Array Collaborations], JCAP 1601 (2016) 01, 037
Search for correlations between the arrival directions of IceCube neutrino events and ultrahigh-energy cosmic rays detected by the Pierre Auger Observatory and the Telescope Array

M. G. Aartsen *et al.* [IceCube Collaboration], Astrophys.J. 807 (2015) 46
Searches for Time Dependent Neutrino Sources with IceCube Data from 2008 to 2012

M. G. Aartsen *et al.* [IceCube Collaboration], Astrophys.J. 796 (2014) 109
Searches for Extended and Point-like Neutrino Sources with Four Years of IceCube Data

M. G. Aartsen *et al.* [IceCube Collaboration], Astrophys.J. 779 (2013) 132
Search for Time-independent Neutrino Emission from Astrophysical Sources with 3 yr of IceCube Data

M. Rameez *et al.* [IceCube Collaboration], PoS ICRC2015 (2015) 1209
Search for dark matter annihilations in the Sun using the completed IceCube neutrino telescope

M. Rameez *et al.* [IceCube Collaboration], Proceedings, 50th Rencontres de Moriond Electroweak interactions and unified theories (2015) 559
WIMP annihilations in the sun: A search based on the first year of data from the completed IceCube neutrino telescope

Acknowledgements

This work would not have been possible without the support of my advisor. I would like to thank Teresa for giving me the opportunity to work on IceCube. She has been incredibly patient, even while pushing me to work harder and giving me the freedom to pursue things I found interesting.

Everything I know about the analysis of IceCube data, I learned from Juanan. His has been the tough task of solving my software problems and bugs, and an immeasurable amount of gratitude is due to him.

I'd like to thank Asen for sharing all the physics knowledge, the programming help, and for being an important part of my PhD experience.

This thesis would be significantly less aesthetically pleasing if not for Matthieu, who has also been a great mentor in the laboratory, and a voice of reason.

My collaborators in IceCube have been extremely helpful. I'd like to thank Jake Feintzeig and Marcel Zoll for all the scripts, Chad, Naoko, Carlos and Carsten for the constructive criticism and direction, Matthias Danninger for helping me catch up and Klaus, Ignacio and Subir for reviewing my analyses and proceedings. I remember enlightening discussions with Chris Weaver, Jakob Van Santen, Mike Richman and Jon Dumm.

I am also grateful to my colleagues in the theory department Toni, Andrey, Thomas, Enrico and Davide. They have helped me further understand what exactly I'm trying to do.

My family has been supportive of my desire to study science, and I'm grateful to them for that.

Gratitude is also due to the Swiss people in general, and the Canton of Geneva in particular for creating an international environment conducive to the pursuit of science.

Contents

List of Figures

List of Tables

Chapter 1

The IceCube neutrino observatory and its detection principles

This chapter explores the neutrino as a particle, the history of its discovery and its properties and interactions. Principles of neutrino detection are discussed with focus on the IceCube neutrino observatory. IceCube instrumentation and data acquisition are discussed, along with the event topologies observed by IceCube. The reconstruction algorithms relevant to the searches in this work are briefly introduced, followed by recent interesting results from IceCube. Finally, atmospheric neutrinos, the principal background in all the searches discussed in this work, are addressed.

1.1   Introduction : The Neutrino

Neutrinos are neutral, weakly interacting particles. They are the lightest known massive particles. Their existence was theorized first in 1930, when Wolfgang Pauli proposed the production of a third, neutral and undetected particle to explain the observed spectrum of the electron in β decay[1]. When a single particle at rest decays into two separate particles, the energies of the decay products are uniquely determined. However, the measured spectrum of the resultant positrons in β decay was found to follow a continuous distribution, hinting at the existence of the neutrino.

Experimental confirmation of the existence of this particle came only much later, in 1956 when Clyde L. Cowan and Frederick Reines demonstrated inverse β decay [2]. Cowan and Reines used a set-up consisting of two large tanks of water acting as a target material, allowing antineutrinos from a nearby nuclear reactor to interact with the protons within the water to produce a neutron and a positron. The resultant positron would quickly annihilate with an electron, producing two γ rays which were detected by sandwiching the water tanks between tanks of liquid scintillator. For added certainty, they also detected the γ ray produced by the absorption of the neutron in a layer of Cadmium Chloride. The detection of all three of these γ rays - the third delayed by 5 μs with respect to the others combined

with the fact that such events were observed only when the reactor was turned on, unequivocally demonstrated the existence of the neutrino.

Later experiments observing the products of muon decay, as well as a long series of reactor neutrino experiments confirmed that the neutrino theorized by Pauli and detected by Cowans and Reines was an electron neutrino, one among a family that also includes neutrinos corresponding to the two other leptons, the muon and the tau neutrinos.

1.2 The Standard Model and Neutrinos

In the standard model of particle physics[3–6], neutrinos are neutral leptons, represented by fermionic fields of 'left' chirality, existing in isospin doublets with the corresponding charged leptons. Thus there are three flavours of neutrinos, one for each flavour of charged lepton. They carry a weak hypercharge (Y_W) of -1 and a weak isospin (T_3) of $+\frac{1}{2}$. Their electrical charge, given by the expression $Q = T_3 + Y_W/2$ is consequently zero and hence they do not take part in Electromagnetic interactions. They carry no colour charge either and are hence uninvolved in strong interactions. They are affected by the weak force and can interact with other particles through processes mediated by the W^+, W^- and Z bosons. Under an accidental global U(1) symmetry of the standard model, each neutrino is assigned a lepton family number similar to the corresponding lepton. The electron neutrino ν_e has an electron number of 1 (-1 for $\bar{\nu}_e$), the muon neutrino ν_μ has a muon number of 1 and so on.

Under the standard model, neutrinos are assumed to be massless and the lepton family numbers are conserved exactly. However a series of experimental observations, beginning with an observation of a deficit in the number of electron neutrinos coming from the Sun with respect to the number predicted by the Standard Solar Model and culminating in a series of dedicated experiments searching for neutrino oscillations have confirmed that neutrinos oscillate from one flavour to another even in vacuum, something which would not be possible if they were massless. As a result, neutrinos are a frontier of 'Physics beyond the Standard Model'.

1.3 Neutrino oscillations and masses

Evidence that neutrinos oscillate come from the following:

1. A deficit in the number of observed electron neutrinos coming from the Sun [7].

2. A deficit in the measured number of muon neutrinos from cosmic ray interactions in the upper atmosphere [8].

3. A deficit in the number of electron neutrinos observed from nuclear reactors [9, 10].

4. An excess in the number of tau neutrinos observed from cosmic ray interactions in the upper atmosphere[11].

5. Observation of the disappearance of muon neutrinos in a muon neutrino beam [12, 13].

6. Observation of the appearance of tau neutrinos in a muon neutrino beam [14].

Here, the term *oscillations* refers to the periodic change in the probability of a neutrino in a flavour eigenstate α to be detected as a flavour eigenstate β ($\alpha \neq \beta$). For this to happen, the neutrino must propagate in a different basis to that which it interacts in, and the general neutrino state must not be simultaneously diagonalizable in the two bases. The widely accepted view today is that neutrinos have mass, there are three different mass eigenstates, and they propagate in the mass basis [15, 16]. This view is also supported by cosmological observations [17].

The relation between the mass and flavour eigenstates for neutrinos can be expressed as:

$$\nu_\alpha = \sum_{k=1,2,3} U^*_{\alpha k} \nu_k \tag{1.1}$$

where $U^*_{\alpha k}$ are elements of the PMNS matrix [15], the index α runs over the flavour eigenstates e, μ and τ, and the index k runs over the mass eigenstates 1,2 and 3. As advocated by the Particle Data Group[18], the PMNS matrix can be parametrized as

$$U = \begin{pmatrix} 1 & 0 & 0 \\ 0 & c_{23} & s_{23} \\ 0 & -s_{23} & c_{23} \end{pmatrix} \begin{pmatrix} c_{13} & 0 & s_{13}e^{-i\delta} \\ 0 & 1 & 0 \\ -s_{13}e^{i\delta} & 0 & c_{13} \end{pmatrix} \begin{pmatrix} c_{12} & s_{12} & 0 \\ -s_{12} & c_{12} & 0 \\ 0 & 0 & 1 \end{pmatrix} \begin{pmatrix} e^{i\rho_1} & 0 & 0 \\ 0 & e^{i\rho_2} & 0 \\ 0 & 0 & 1 \end{pmatrix} \tag{1.2}$$

where s_{ij} and c_{ij} stand for sine and cosine functions of three mixing angles θ_{ij}, the subscripts of which stand for the mass eigenstates they mix. δ, ρ_1 and ρ_2 are complex phases that violate CP symmetry. If the neutrino masses arise from a purely Dirac mechanism [19], ρ_1 and ρ_2 vanish. If there are only three flavour eigenstates of neutrinos, U has to be a unitary matrix.

Following the treatment of Giunti[20] and Bilenky[21] it can be shown that the probability of a neutrino in flavour eigenstate α which was produced at energy E being detected in flavour eigenstate β after distance L can be given by:

$$P_{\nu_\alpha \to \nu_\beta}(L, E) = \sum_{k,j} U^*_{\alpha k} U_{\beta k} U_{\alpha j} U^*_{\beta j} e^{-i\frac{\Delta m^2_{kj}}{2E}L} \tag{1.3}$$

where $\Delta m^2_{kj} = m^2_k - m^2_j$. This equation can be written explicitly in terms of its real and imaginary components separately as:

TABLE 1.1: The current best measured values of the neutrino oscillation parameters as reported by the Particle Data Group[18].

$\sin^2(\theta_{12})$	0.304 ± 0.014
Δm^2_{21}	$(7.53 \pm 0.18) \times 10^{-5} eV^2$
$\sin^2(\theta_{23})$	$0.514^{+0.055}_{-0.056}$ (NH) $0.511^{\pm}0.055$ (IH)
Δm^2_{32}	$(2.44 \pm 0.06) \times 10^{-3} eV^2$ (NH) $(2.49 \pm 0.06) \times 10^{-3} eV^2$ (IH)
$\sin^2(\theta_{13})$	$(2.19 \pm 0.12) \times 10^{-2}$

$$P_{\nu_\alpha \to \nu_\beta}(L, E) = \delta_{\beta\alpha} - 4\sum_{k>j}\mathcal{R}[U^*_{\alpha k}U_{\beta k}U_{\alpha j}U^*_{\beta j}]sin^2(\frac{\Delta m^2_{kj}}{4E}L) \pm 2\sum_{k>j}\mathcal{I}[U^*_{\alpha k}U_{\beta k}U_{\alpha j}U^*_{\beta j}]sin(\frac{\Delta m^2_{kj}}{2E}L)$$

(1.4)

where the sign of the imaginary part is positive for neutrinos and negative for antineutrinos. The multiplication of the mixing masses in equations 1.3 and 1.4 indicate that the Majorana phases ρ_1 and ρ_2 of equation 1.2 have no impact on oscillations.

Table 1.1 summarizes the current state of the art in the measurements of the neutrino oscillation parameters. The absolute values of the masses are not known, only the difference of their squares. Consequently, the hierarchy of the masses is also not known [22].

Matter Oscillations When neutrinos propagate through matter, they are subject to coherent forward scattering on the particles. These include both $W^\pm$ mediated scattering off the electrons in the matter as well as Z^0 mediated scattering off the nucleons. The latter is identical for all neutrino flavours and has no effect on neutrino oscillations. However, the former gives rise to an extra interaction potential energy $V = \sqrt{2}G_F N_e$ (where G_F is the Fermi coupling constant and N_e is the density of electrons) for ν_e, which is of the opposite sign for $\bar{\nu}_e$, and can significantly change the oscillation pattern [23, 24]. In particular at certain resonant values of N_e, given by $\sqrt{2}G_F N_e = \Delta m^2_{1,j}cos(2\theta_{1,j})/2E$, for $j = 2,3$, it can lead to maximal mixing between the mass eigenstates [25]. This is relevant in the scenario of the Sun, in the core of which $N_e \sim 3 \times 10^{31}m^{-3}$, and consequently MeV neutrinos undergo resonant 1-2 mixing, leading to the famous observed solar neutrino deficit[7].

1.4 Neutrino Astronomy and Astrophysical sources of neutrinos

The properties of charge neutrality and small interaction cross section make neutrinos the ideal astronomical messengers at high energies. Cosmic rays in the GeV-PeV energy range are deflected by Galactic and extragalactic magnetic fields and consequently do not point back to their sources.
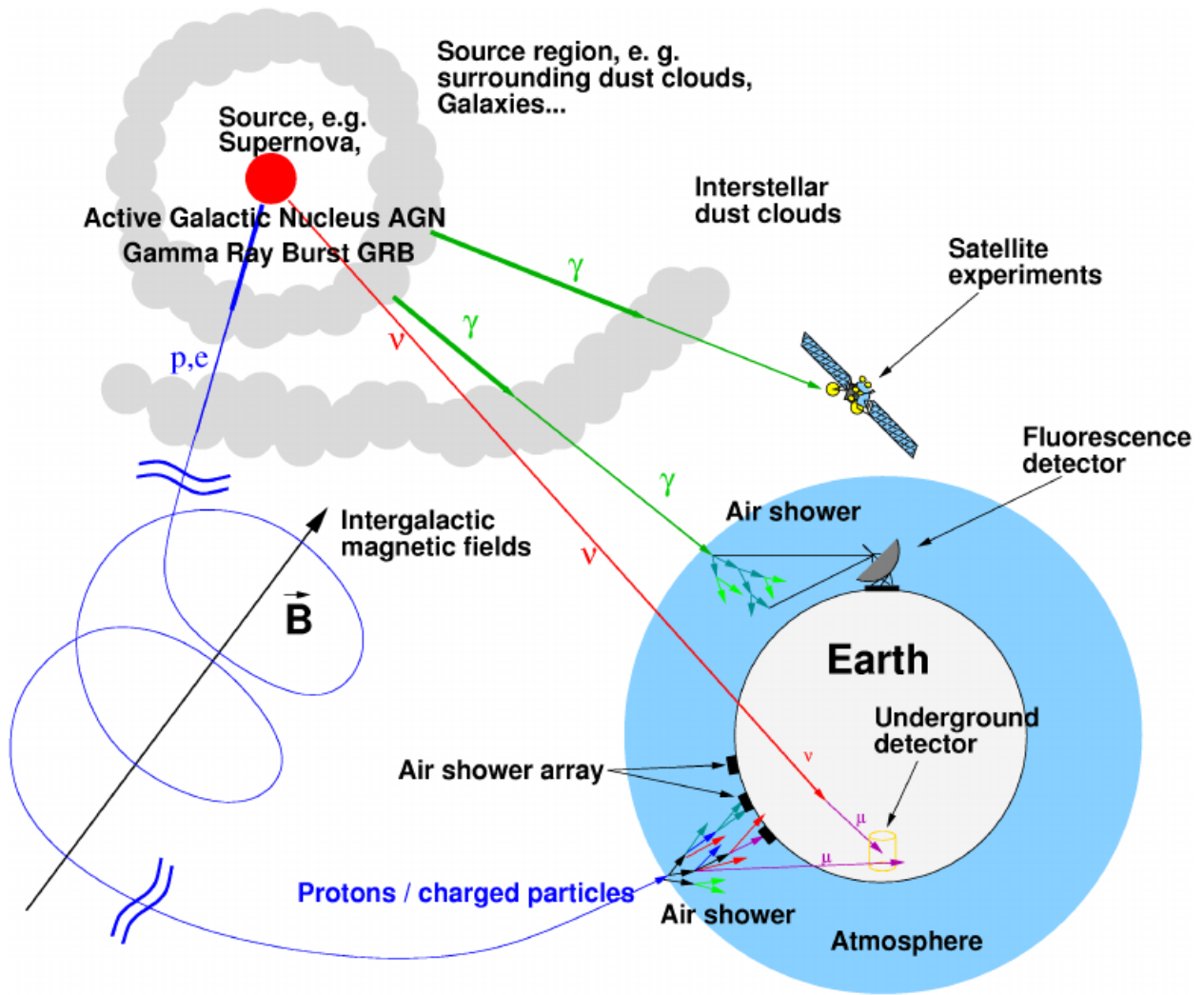
FIGURE 1.1: Schematics of multi-messenger astronomy.

Gamma rays are absorbed in the intervening material or can pair produce with photon backgrounds prevalent in the universe. They are also produced in various scenarios, complicating the interpretation of γ-ray data. Neutrinos however travel undeflected for much larger distances. Figure 1.1 provides an overview of the scenario. Neutrino astronomy is today in its infancy, with only two known astrophysical sources of neutrinos, the supernova SN1987A and the Sun.

Astrophysical neutrinos can arise from two very different scenarios:

Annihilation/decay of massive particles: If a massive particle pair-annihilates or decays into standard model particles, the decay or hadronization of the these SM particles can produce neutrinos as well as other signatures such as γ-rays [26], and antimatter [27]. If these annihilations occur in regions of high baryonic density, such as the Earth or the Sun, neutrinos are the only signatures that can be observed. The Dark Matter problem (see chapter 2) may be explained by the existence of such massive particles.

Cosmic Ray interactions: The protons/nuclei that make up CRs interact with photons and among themselves to produce neutral and charged pions:

$$
\begin{aligned}
p\gamma \to \quad & \Delta^+ \\
& \Delta^+ \to p + \pi^0 \\
& \Delta^+ \to n + \pi^+
\end{aligned}
\tag{1.5}
$$

$$
\begin{aligned}
n\gamma \to \quad & \Delta^0 \\
& \Delta^0 \to p + \pi^- \\
& \Delta^0 \to n + \pi^0
\end{aligned}
\tag{1.6}
$$

$$
\begin{aligned}
pp \to \quad & p + p + \pi^0 \\
& p + n + \pi^+
\end{aligned}
\tag{1.7}
$$

$$
\begin{aligned}
pn \to \quad & p + n + \pi^0 \\
& p + p + \pi^-
\end{aligned}
\tag{1.8}
$$

Subsequently the neutral pions decay into γ rays and the charged pions decay into charged leptons and neutrinos.

$$
\pi^0 \to \quad \gamma\gamma
\tag{1.9}
$$

$$
\begin{aligned}
\pi^+ \to \quad & \mu^+ + \nu_\mu \\
& \mu^+ \to e^+ + \nu_e + \bar{\nu}_\mu
\end{aligned}
\tag{1.10}
$$

$$
\begin{aligned}
\pi^- \to \quad & \mu^- + \bar{\nu}_\mu \\
& \mu^- \to e^- + \bar{\nu}_e + \nu_\mu
\end{aligned}
\tag{1.11}
$$

The interactions of Eqs 1.7 and 1.8 can take place between CRs and the nuclei of the Earth's atmosphere, creating atmospheric neutrinos. IceCube observes a few hundred thousand of these events every year. **Atmospheric neutrinos are the principal background in all searches presented within this work. Consequently, the atmospheric neutrino flux is discussed in more detail in section 1.6.**

These interactions can also take place at the sites of CR acceleration, which are unknown. The mechanisms and potential sites of cosmic ray acceleration are dealt with in detail in Chapter 3.

This work deals with searches for point-like sources of neutrinos arising from the two scenarios presented above. Chapter 5 summarizes a search for neutrinos from Dark Matter annihilations in the
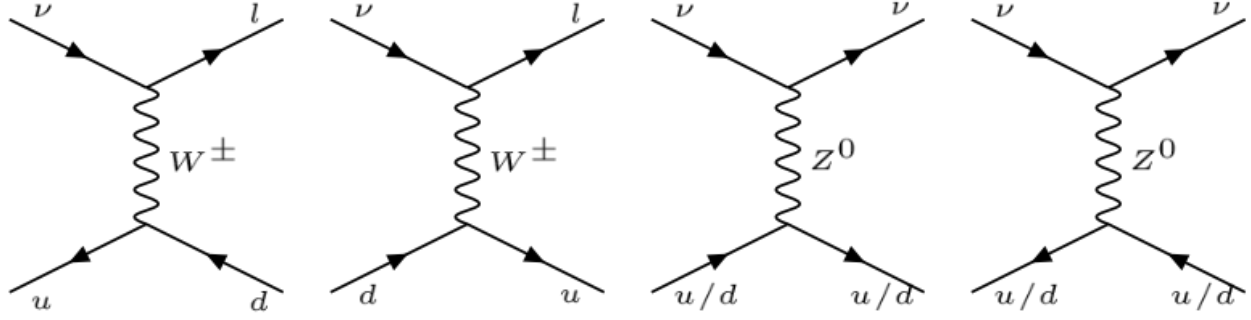
FIGURE 1.2: Feynman Diagrams of the neutrino nucleon Charged Current (CC) and Neutral Current (NC) interactions.

Sun, while searches described in chapters 6 and 7 attempt to identify the sites of CR acceleration by looking for the corresponding neutrino flux. The detection of neutrinos of GeV energies and above from astrophysical sources will serve as a smoking gun signature of either DM annihilation or CR acceleration.

1.5 Neutrino Detection

Neutrinos are detected using their interactions with ordinary matter. They interact with nucleons through both charged current (CC) interactions mediated by $W^{\pm}$ bosons and neutral current (NC) interactions mediated by Z bosons (see Fig. 1.2).

Figure 1.3 shows the integrated CC cross sections as a function of energy[28]. The NC cross sections can be found in [28]. Due to the weak nature of the interactions, the cross sections are 7 to 10 orders of magnitude weaker than those for p-p collisions. The cross section initially increases with the incoming neutrino energy. However, above $10^4 - 10^5$ GeV, the momentum transfer Q^2 is much greater than the mediator masses and since the W/Z boson propagators are inversely proportional to $Q^2 + M_{W/Z}^2$, the cross sections are reduced at higher energies. At higher energies, the sea quark contribution increases and the ν and $\bar{\nu}$ cross sections become similar but at lower energies the valence quark contribution is more significant and due to the helicity suppression of $\bar{\nu}$ scattering with valence quarks, the total cross section is lower for $\bar{\nu}$.

Due to the low neutrino cross section, neutrino detectors require a large target mass to detect a significant number of neutrinos. The resulting interaction products are detected through a variety of methods such as radiochemical detection[29], tracking calorimetry[30], and Cherenkov detection.

1.5.1 The Cherenkov Effect

When an electrically charged particle travels through a dielectric medium with a velocity higher than the phase velocity of light in the medium, it emits Cherenkov radiation[32]. As the charged particle
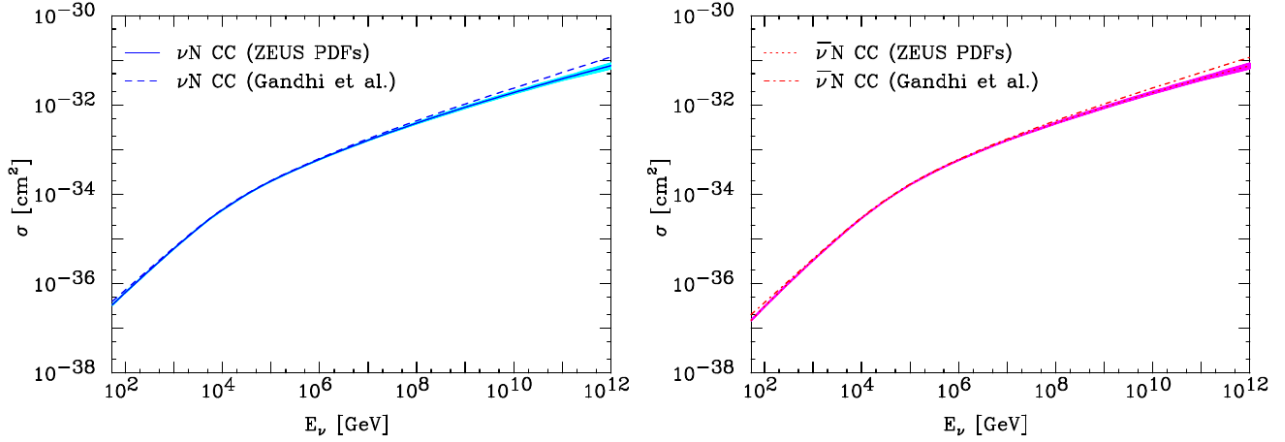
FIGURE 1.3: Total CC cross sections for ν(left) and $\bar{\nu}$(right) for an isoscalar target nucleon from [28]. These calculations have been performed with the latest parton distribution functions available from the ZEUS collaboration, and are compared to a previous calculation by Gandhi et.al.[31]. The shaded region signifies the $\pm 1\sigma$ error from uncertainties in the PDFs. Figure taken from [28].
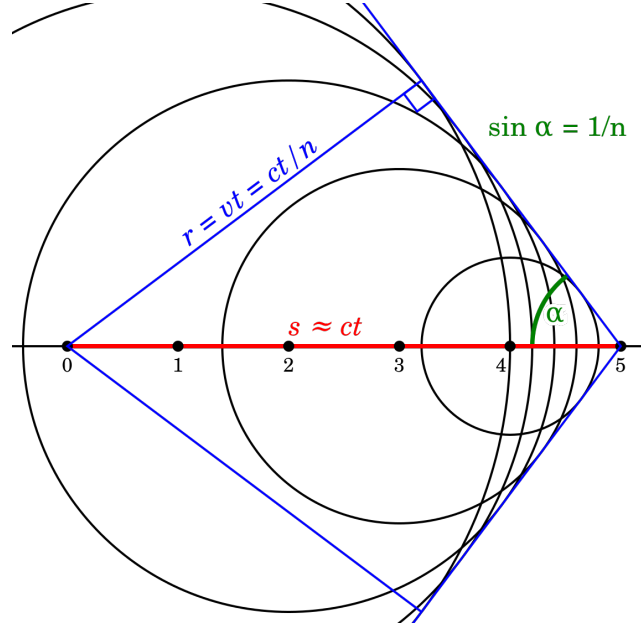
FIGURE 1.4: Cherenkov emission from a relativistic charged particle travelling within a medium faster than the speed of light in that medium. Isotropic emission - indicated by the circles, interfere constructively only within the Cherenkov cone.

itself travels faster than the light can propagate, the wavefront takes a conical form as illustrated in Fig. 1.4. The Cherenkov angle θ_c can be expressed in terms of the velocity of the charged particle as a fraction of the velocity of light β and the refractive index of the medium $n(\lambda)$ as:

$$cos(\theta_c) = \frac{1}{\beta n(\lambda)} \tag{1.12}$$

For a muon of energies in the GeV and above travelling through ice (the scenario relevant to this work), $\beta = v/c \sim 1$ and $n_{ice} = 1.32$, giving $\theta_c \sim 41°$.
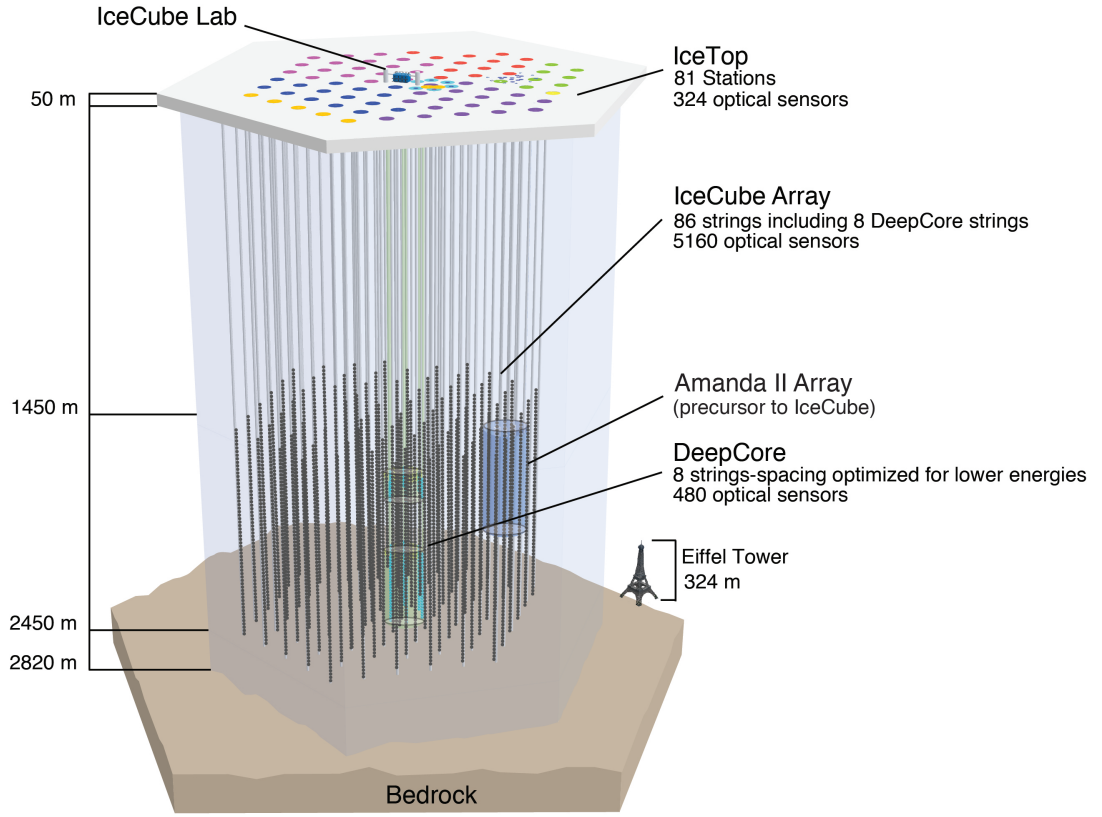
FIGURE 1.5: A perspective view of the IceCube detector

The Frank-Tamm [33] formula lays down the number of Cherenkov photons emitted per unit length and wavelength:

$$\frac{d^2N}{dxd\lambda} = \frac{2\pi\alpha z^2}{\lambda^2} sin^2\left(\theta_c(\lambda)\right) \tag{1.13}$$

where α stands for the fine structure constant. Due to the $1/\lambda^2$ term, shorter wavelengths dominate.

1.5.2 The IceCube Detector

The IceCube Neutrino Observatory consists of 5160 photomultiplier tubes (PMTs) embedded in the ice at the geographic South Pole. It is a cubic-kilometre sized Cherenkov detector optimized to detect neutrinos above TeV energies[34]. The PMTs are instrumented along 86 cables (known as strings) and are housed in pressure resistant spheres with onboard calibration LEDs and digitization hardware, known as Digital Optical Modules (DOMs). The DOMs detect Cherenkov photons from charged leptons traversing the detector. The DOMs are placed at 17 m intervals on each string between 1450 and 2450 m beneath the surface of the ice. The strings are horizontally separated by ∼125 meters. Figure 1.5 illustrates the detector.

Additional strings consisting of high quantum efficiency DOMs are placed at the central-deep region of the detector. They are spaced ∼70 m apart and the DOMs on these strings are vertically spaced at 7 m. These strings constitute the DeepCore sub-array which has a significantly lower energy threshold than the rest of the detector.

1.5.2.1 The South Pole Ice

The deep ice at the South Pole in which IceCube DOMs are embedded is the clearest naturally occurring ice in the world, and allows the DOMs to detect photons originating hundreds of meters away. The two major processes that stand in the way of a Cherenkov photon between production and detection are scattering and absorption. Scattering washes out the arrival time distributions of Cherenkov photons, thus disrupting the accuracy of reconstruction of the directions of particles. Absorption reduces the total number of photons that can be detected and are available for a reconstruction, as well as the accuracy of some energy reconstructions which rely on the total number of detected photons.

The properties of ice with respect to these processes can be quantified by the scattering and absorption lengths respectively. These quantities have been measured by flashing the onboard calibration LEDs on the DOMs and fitting the arrival times of photons at nearby and next to nearby DOMs to a six parameter ice model, described in [35]. At depths up to ∼1300 m, the scattering length has been found to be ≲ 5 m due to high concentrations of air bubbles. At greater depths, the higher pressures compress the air bubbles and eventually cause them to disappear entirely. Consequently, scattering and absorption are dictated by the presence of dust particles within the ice at these depths.

Figure 1.6 shows the inverse of the average absorption and scattering lengths respectively as a function of depth, in the depth range where IceCube is situated. The typical scattering and absorption lengths are ∼25m and ∼70m respectively in the upper half of the detector. A 100m thick layer of ice with significantly worse optical properties can be observed right in the middle of the detector, at a depth of ∼2050m. Referred to as 'the dust layer', this region corresponds to an interglacial period ∼65000 years ago. Below this layer, the optical properties of the ice improve further due to higher pressures. Due to tilts in the ice layers, the optical properties of the ice have been observed to vary also with the x and y coordinates in addition to that of the depth. This is accounted for by using a full three dimensional model of the ice, constructed using various measurements of dust concentrations made during drilling. Preliminary evidence also seems to suggest that scattering and absorption in ice are anisotropic.

1.5.2.2 The DOM

The IceCube Digital Optical Module (DOM) consists of a 0.5 inch thick pressure vessel of glass which houses a Photomultiplier Tube (PMT), electronics to digitize the PMT signal, and calibration LEDs. A diagram of the DOM can be seen in Figure 1.7. It can withstand pressures up to 690 atm. Each
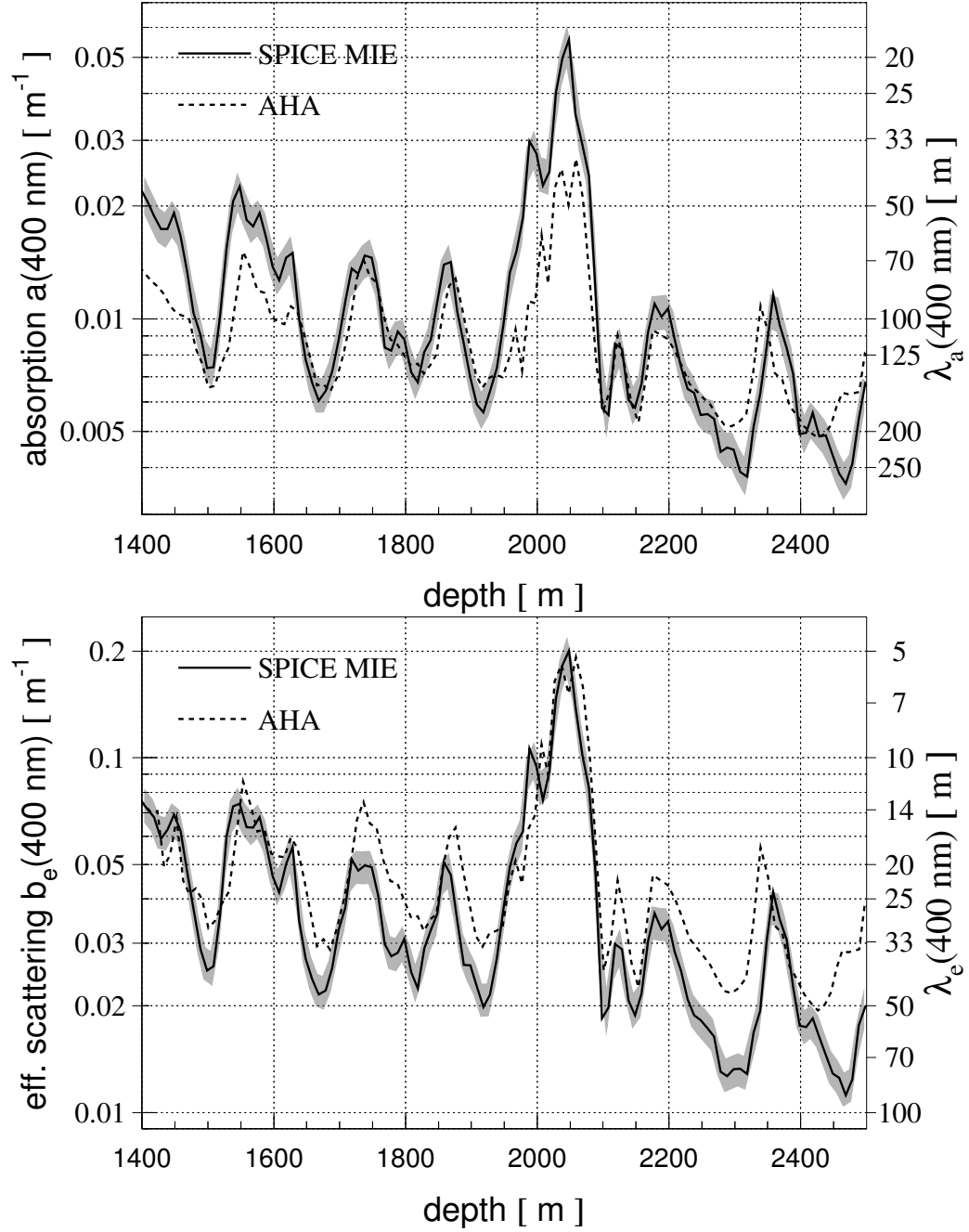
FIGURE 1.6: Scattering(top) and absorption(bottom) coefficients as a function of depth for the up to date SPICE-MIE[35] as well as a previously used model AHA[36]. The peak in both figures at a depth of $\sim 2050m$ corresponds to the dense dust layer that runs through the middle of the detector.
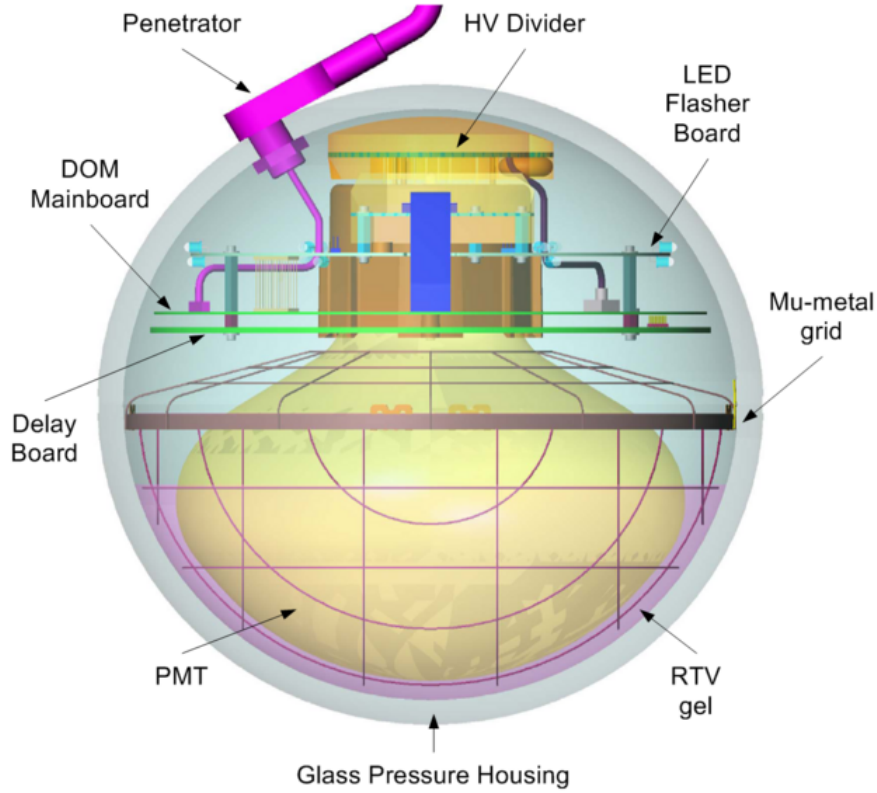
FIGURE 1.7: A schematic diagram of the DOM

DOM communicates to the IceCube Lab on the surface through the IceCube string. The IceCube and DeepCore DOMs use the ten inch R7081-02 PMT with a quantum efficiency of ∼25% at 390nm and the R7081MOD PMT with a 35% higher quantum efficiency respectively. They are manufactured by Hamamatsu Photonics and are sensitive to photons of wavelengths in the 300nm - 650nm range [37, 38]. The PMTs respond to a detected single photon by emitting a 10mV signal for a duration of ∼5ns.

The PMT signals are digitized and read out through both the Analog Transient Waveform Digitizer (ATWD) and the Fast Analog-to-Digital Converter (FADC). The ATWD samples the pulses within a 422ns readout window at 3.3ns intervals and then takes 29 microseconds to digitize it. Since this leads to significant dead-time, each DOM is equipped with two independent ATWDs operating in ping-pong mode. The ATWD is triggered when the PMT pulse rises above the discriminator threshold of 0.25 photoelectrons(PE), and has three channels with different gains, providing a larger dynamic range. The FADC reads out pulses within a $6.4\mu s$ window at a sampling rate of 25ns, however it has no dead-time[39].

The LED flasher boards contain 12 LEDs which can emit pulses that are bright enough to be observed by DOMs on neighbouring strings. They can be flashed individually or together at varying levels of brightness to study ice properties, simulate events and calibrate the detector.

The IceCube DOMs detect photons in the wavelength range of 365 nm (below which the DOM casing is opaque) to 600 nm (above which the ice is opaque). In this range, eq. 1.13 predicts ~ 215 photons emitted per cm for a muon.

1.5.2.3   Construction, Schedule and Seasons

IceCube began construction in the 2004-2005 Austral Summer with the deployment of 1 string. With subsequent seasons, there has been a steady improvement in drilling capabilities and 20 strings were deployed in the 2009-2010 season. Figure 1.5 indicates the strings deployed during different seasons in different colours in the top view. The final 7 strings were deployed in 2010-2011, completing the deployment of the full 86-string detector ten days ahead of schedule. In between, the detector operated in 9-string (2005-2006), 22-string (2006-2007), 40-string (2007-2008), 59-string (2008-2009) and 79-string (2009-2010) incomplete configurations.

Since the completion of construction, IceCube has continued to run with an uptime $\geq 99\%$. 5435 DOMs, corresponding to 99.1% survived deployment, and it is estimated than $\sim 97.2\%$ will continue to be operational after 15 years of data taking.

1.5.2.4   Data Acquisition

Due to the impossibility of continuously acquiring and saving to disk the states of all 5160 PMTs, IceCube relies on a set of logical conditions to trigger data acquisition.

A PMT pulse crossing a 0.25 photo-electron (PE) threshold prompts the DOM to communicate with nearby DOMs on the same string and look for coincident hits. When two neighbouring or next to neighbouring DOMs in the same string are above the threshold within a 1 μs window, the condition is called a Hard Local Coincidence (HLC). If this condition is satisfied, computers on the surface are alerted, which subsequently test for detector wide trigger conditions. Various triggers exist in IceCube, targeted at different types of signal events. Some triggers relevant to this work include:

1. **Simple Majority Trigger-8 (SMT8):** 8 neighbouring or next to neighbouring DOMs in IceCube have hits within a 5 μs window.

2. **DeepCore Simple Majority Trigger-3 (SMT3):** 3 neighbouring or next to neighbouring DOMs within the DeepCore Fiducial Volume (8 DeepCore strings and nearby 7 IceCube strings) have hits within a 2.5 μs window.

3. **Cylinder Trigger :** 4 DOMs within a hexagonal cylindrical volume consisting of 7 strings within the IceCube main array and 5 DOMs in height have hits within a 1μs window.

If one of the many trigger conditions are satisfied, the data acquisition system (DAQ) reads out all hits on all DOMs in the detector for $\pm 10\mu$ in addition to the trigger duration. For all DOMs with HLC hits, digitized waveforms from both ATWD and FADC are recorded, while isolated DOMs transmit their FADC waveforms only, in a condition called soft local coincidence (SLC). An online filtering system reduces the overall rate of all triggered events (~ 2500 Hz) by a factor of ~ 10, by representing the full PMT pulses as a linear combination of PEs with specific charges and arrival times, in a process called feature extraction, based on which basic event information can be calculated and criteria applied to select useful physics events. This information is used to perform preliminary quick reconstructions of particle directions and energies, based on which events with desired properties are selected and transferred to the northern hemisphere via satellite.

Subsequently, more computationally intensive reconstructions are performed on these events, based on which more complex conditions are applied to reject even more background and classify these events based on their topology into many filter streams. Further processing is carried out on these events based on the filter streams they belong to and the resulting data are stored on disk. This is referred to by the collaboration as Level 2.

1.5.2.5 Event Signatures

At this stage, all events fall into one of the two following categories:

Tracks Charged current ν_μ (or $\bar{\nu}_\mu$) interactions with nuclei produce muons, which lose energy in the ice via ionization and stochastic losses from bremsstrahlung, photo-nuclear interactions and e^+e^- pair production. The average energy loss rate is described as:

$$-\frac{dE}{dx} = a + bE \tag{1.14}$$

where $a \approx 0.26$ GeV per meter of water-equivalent (mwe) stands for the average energy independent loss rate due to ionization while $b \approx 3.6^{-4}$/mwe in ice and stands for the average stochastic loss rate which is proportional to the average energy. Consequently, high energy muons travel through many kilometres of ice before dropping beneath the Cherenkov threshold. The light from such a muon forms a series of hits within the detector that can easily be identified as a track. Fig 1.8, left shows the distribution of hits from such an event. Track-like events from ν_μ (or $\bar{\nu}_\mu$) CC interactions are ideal for neutrino astronomy. The direction of the muon can be reconstructed with a very good accuracy ($< 1°$). The kinematic angle between the incoming neutrino and the resultant muon of the CC interaction is inversely dependent on the square root of the energy and is $\sim 0.1°$ for a neutrino of ~ 10 TeV. Consequently the reconstructed muon direction serves as an excellent proxy for the incoming neutrino direction at energies relevant to IceCube. Additionally, the long distances travelled by the muon mean that by observing muons created outside the instrumented detector volume also,
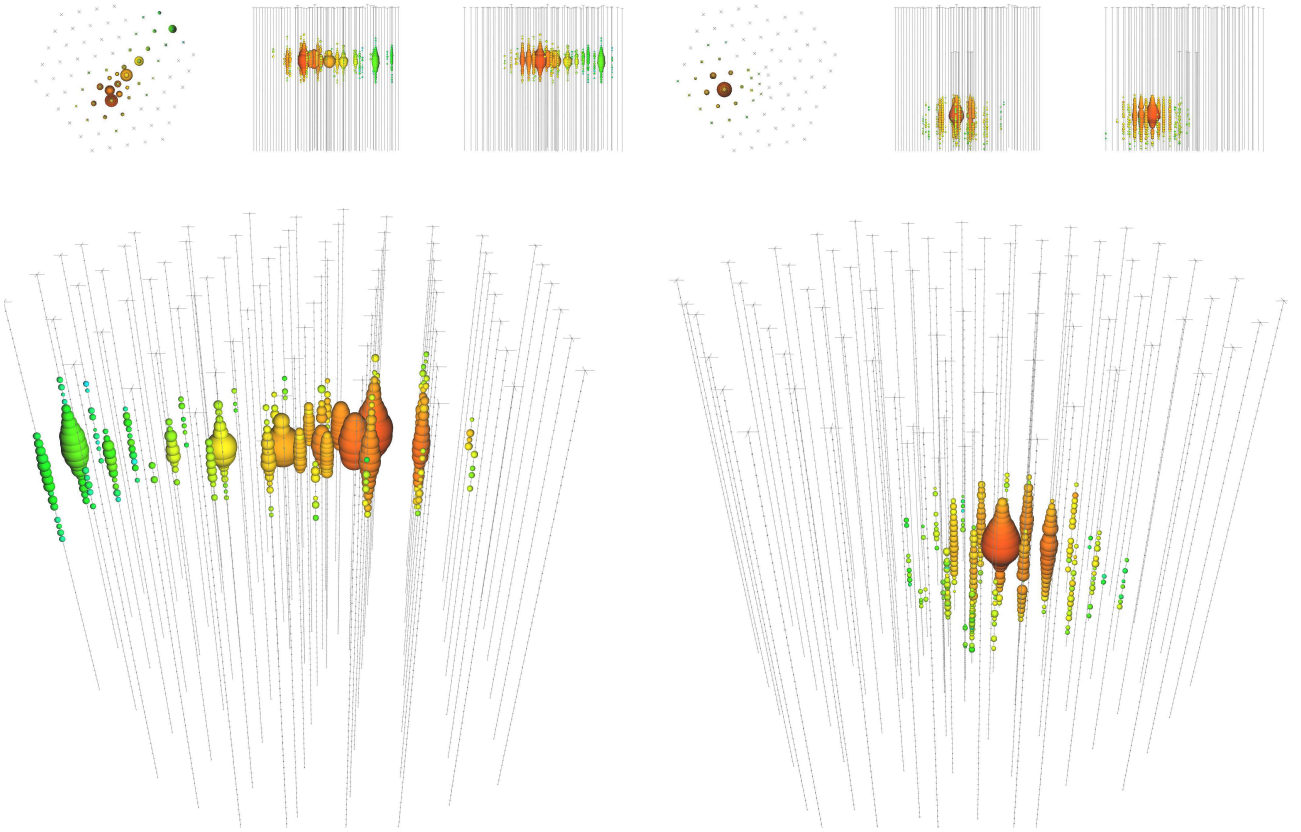
FIGURE 1.8: Left: A track-like event and Right: A cascade-like event.

the effective volume is greatly enhanced. Muons are also produced when CRs interact with the upper atmosphere. These muons that traverse the atmosphere and enter the ice directly, form a significant background in IceCube.

All searches carried out within this work target track like events from ν_μ (or $\bar{\nu}_\mu$) CC interactions.

Cascades Charged current ν_e (or $\bar{\nu}_e$) interactions produce a free electron / positron which quickly loses energy via bremsstrahlung to create a photon, which creates an e^+e^- pair, and the process repeats itself until the created e^+e^- pairs are beneath the Cherenkov threshold or the photon is below the pair production threshold. A part of the neutrino energy is deposited within this electromagnetic cascade of ~ 10m length while the remaining energy goes into the hadronic debris which forms a hadronic cascade.

Charged current ν_τ (or $\bar{\nu}_\tau$) interactions produce τ leptons which have livetimes 7 orders of magnitude smaller than that of muons. They quickly decay with a branching fraction of $\sim$65% into hadronic channels or alternatively into a pair of electrons or muons (with a branching fraction of $\sim$17% each) and a tau neutrino. At energies below ~ 2 PeV, the cascades from the CC interaction and the τ decay are not separated enough to be distinguishable as two different events in IceCube.

Neutral current ν (or $\bar{\nu}$) interactions leave a hadronic cascade within the detector while the outgoing neutrino is not observed.

IceCube is too sparsely instrumented to distinguish the above three processes and consequently they all appear as cascade like events such as in Fig 1.8, right. The direction of the incoming neutrino can be reconstructed with an accuracy of 15°-20° only for cascades depositing more than a 100 TeV within the IceCube array. In the $\sim$100 GeV energy range the incoming neutrino direction for a cascade can be reconstructed with $\sim$20° resolution if the cascade happens to be in DeepCore[40].

Charged Current ν_τ (or $\bar{\nu}_\tau$) at energies of $\sim$ 1PeV and above produce hybrid signatures which have not hitherto been unequivocally identified[41].

1.5.2.6 Reconstructions

The goal of a reconstruction is to infer the energy and direction of the muon track and/or cascade from the observed pattern of hits. Various algorithms exist for these purposes. The ones relevant to this work are:

LineFit The simplest of the various track reconstructions, LineFit performs a least squares fit to the location and time of each hit DOM, penalizing outlying hits using the Huber function [42]. The muon is taken to pass through position $\vec{x}_0$ at time t_0 with velocity $\vec{v}$. Subsequently for each observed hit, the absolute difference

$$\rho_i(t_0, \vec{x}_0, \vec{v}) = |(t_o - t_0)\vec{v} + \vec{x}_0 - \vec{x}_i| \tag{1.15}$$

is constructed using which the Huber penalty function $\phi(\rho)$ defined as

$$\phi(\rho) = \begin{cases} \rho^2 & \text{if } \rho < \mu \\ \mu(2\rho - \mu) & \text{if } \rho \geq \mu \end{cases} \tag{1.16}$$

can be calculated. The optimal value for the parameter μ has been found to be 153 m. Subsequently, the best fit values of $\vec{x}_0$, t_0 and $\vec{v}$ are obtained by minimizing

$$\sum_{i=1}^{N} \phi(\rho_i(t_0, \vec{x}_0, \vec{v})) \tag{1.17}$$

w.r.t these free parameters. This algorithm is extremely fast and despite an oversimplified treatment of the Cherenkov light, produces a median angular resolution of a few degrees for high energy tracks.

Single-PhotoElectron (SPE) Likelihood Reconstruction This reconstruction models the muon as a straight line continuously emitting photons along the Cherenkov cone and travelling at the speed of light. It is performed by numerically maximizing the likelihood

$$\log\mathcal{L} = \sum_i \log p(\vec{x}_i|\vec{a}) \tag{1.18}$$

where $p(\vec{x}|\vec{a})$ is the probability that the track $\vec{A}$ (with track parameters θ, ϕ, x, y, z, denoted by $\vec{a}$) creates the observed hit $\vec{x}_i$. When this reconstruction is performed only the arrival time of the first hit on each DOM is accounted for. The accuracy of this reconstruction depends on the accuracy of $p(\vec{x}_i|\vec{a})$, which can be constructed using an analytical description of photon arrival times, known as the Pandel distribution [43]. Alternatively, this distribution can be constructed by fitting a multi-dimensional spline surface to the arrival time distributions from detailed photon propagation simulations [44]. This latter method has the advantage of incorporating more accurate ice information, such as depth dependent ice properties and ice anisotropy, and is subsequently a better description of the actual photon arrival times. Consequently, it often performs better and is a preferred reconstruction.

Multi-PhotoElectron (MPE) Likelihood Reconstruction   This reconstruction is similar to the SPE Likelihood Reconstruction above but incorporates every hit on each DOM. $p(\vec{x}_i|\vec{a})$ is modified to

$$p(\vec{x}_i|\vec{a}) \rightarrow N_i.p(\vec{x}_i|\vec{a}).\left(\int_{t_i}^{\infty} p(\vec{x}|\vec{a})dt\right)^{N-1} \tag{1.19}$$

where N_i is the total number of observed photoelectrons in the i th DOM. Like in the case of SPE, MPE reconstructions can be done using both the Pandel and the PhotoSpline parametrizations of $p(\vec{x}_i|\vec{a})$.

MuEx Angular Reconstruction   The MuEx angular reconstruction combines the MPE likelihood above with a randomized sampling method. First, a set of N different pulse series are extracted from the full pulse series, randomly using a charge-weighted multinomial distribution that favours high charge pulses over others. Subsequently, the MPE reconstruction is applied on each of these pulse series. Finally, the average of these N MPE reconstructions is used as a seed for one final MPE reconstruction with the entire pulse series. This method has the advantage of avoiding local minima, thus helping in avoiding misreconstructed background. The optimum value of N has been found to be 4.

Paraboloid Angular Uncertainty Estimator   The Unbinned Maximum Likelihood Ratio method of Chapter 4 benefits from having an estimate of the uncertainty on the track reconstruction for each event. This can be obtained for any likelihood based angular reconstruction by calculating the likelihood at points around the minimum and fitting a paraboloid function to the points[45]. A 1σ angular error range can be determined from this function.

MuEx Track Energy Reconstruction   A Poissonian likelihood is used to compare the observed number of photoelectrons k to the expected light yield per unit energy Λ for a particle with energy E and an already reconstructed direction.

$$\log \mathcal{L} = k \log (E\Lambda + \rho) - (E\Lambda + \rho) - \log (k!) \tag{1.20}$$

Photons from noise are accounted for by the parameter ρ. The energy is varied until the expected light yield matches the observed number of photoelectrons.

FiniteReco Vertex Reconstructions   FiniteReco takes an input track reconstruction and makes a first guess about it's starting and stopping vertices, under the assumption that it is a contained track. Subsequently, this track and vertex guesses are used as seeds for a likelihood based reconstruction for a finite track. The likelihood of Equation 1.18 is maximized separately with respect to a starting vertex and a stopping point to obtain the best fit start and stop points. It also returns log likelihood values for the three hypotheses (Infinite, Starting, Stopping). These values serve as classifiers to determine if the event is truly a starting, stopping or infinite track.

Monopod Cascade Energy Reconstruction   Monopod is a simplified implementation of the Millipede linear energy unfolding algorithm [46] that tries to model the stochastic energy losses of very high energy muons as a sum of many cascades.

$$\vec{k} - \vec{\rho} = \Lambda.\vec{E} \tag{1.21}$$

$\vec{k}$ is the observed number of photons on each DOM, $\vec{\rho}$ is the expected number of noise hits on each DOM, $\vec{E}$ is the energy loss on each cascade and the matrix Λ predicts the light yield at every point in the detector for every hypothesis source position. For a single cascade, this system of equations can be reduced to a single equation and its energy can be extracted.

LEERA DeepCore Energy Reconstruction   For ν_μ (or $\bar{\nu}_\mu$) CC interactions in the 10 GeV-100GeV energy range, the range of the resultant muon is smaller than the dimension of the detector. Due to the energy being below the threshold of IceCube, such an event is detected only if it occurs in or near the DeepCore region. For such an event, it is possible to construct an estimator of the full neutrino energy:

$$E_\nu = E_\mu + E_{cascade} \tag{1.22}$$

Here, E_μ can be estimated using Equation 1.14 and the length of the track reconstructed using FiniteReco, while $E_{cascade}$ is estimated using Monopod.

1.5.2.7 Simulation

The detector response to muons and neutrinos is simulated in order to validate our understanding of the detector. This can be used to create samples of simulated signal like events. The first step, known as event generation, simulates fundamental interactions to create observable leptons. The second step, detector simulation, tracks these leptons as they traverse the detector, tracks and propagates the light they radiate through the ice, and simulates the DOM responses to these photons, subsequent to which the different steps of data acquisition explained in section 1.5.2.4 such as local coincidence conditions, trigger conditions, filters and reconstructions are applied, exactly as they are for data.

Event Generation   Various event generators are used within IceCube. The `CORSIKA` package [47] simulates cosmic ray nucleons interacting with the atmosphere above Antarctica using the SIBYLL[48] hadronic interaction model to generate atmospheric muons, the dominant background at trigger level. `CORSIKA` outputs a list of final state particles with relevant properties such as position, direction and energy. Neutrino interactions with the ice molecules in the deep inelastic scattering regime are simulated by `ANIS`[49]. This code also accounts for the propagation of the neutrinos through the Earth. The code again outputs the final state particles and their relevant properties. The neutrino cross sections of [28] and the resultant events can be used to simulate different neutrino fluxes and spectra, using relative weights. At lower energies (< 200 GeV), `GENIE` [50] uses a more accurate model of the cross sections and is preferred. For specific neutrino spectra from Dark Matter annihilations, `WimpSim` [51] is preferred. It accounts for oscillations using a full 3 flavour Monte Carlo approach and can also keep track of secondary neutrinos from interactions inside bodies such as the Sun and the Earth.

Detector Simulation   The particles produced by the above event generators are propagated through the ice using Muon Monte Carlo (MMC) [52]. Keeping track of charged leptons in both the ice and the bedrock, `MMC` keeps track of all energy losses, continuous and stochastic, as well as secondaries, generating photons emitted from each process. These photons are propagated through the ice using `Photonics`[53], `PPC`[54], or `CLSim`[55]. `Photonics` is simply a large lookup table of arrival times and photon yields at each location in the detector, for different starting points of the photon. Its accuracy is limited by the binning of the tables. `PPC` directly propagates the photon, simulating absorption and scattering processes for each photon to determine if it will eventually reach a DOM. This is accurate but computationally expensive. `CLSim` uses a similar approach but uses `GEANT4` [56] at lower energies, and significantly speeds up the computation using the power of Graphic Processing Units (GPUs).
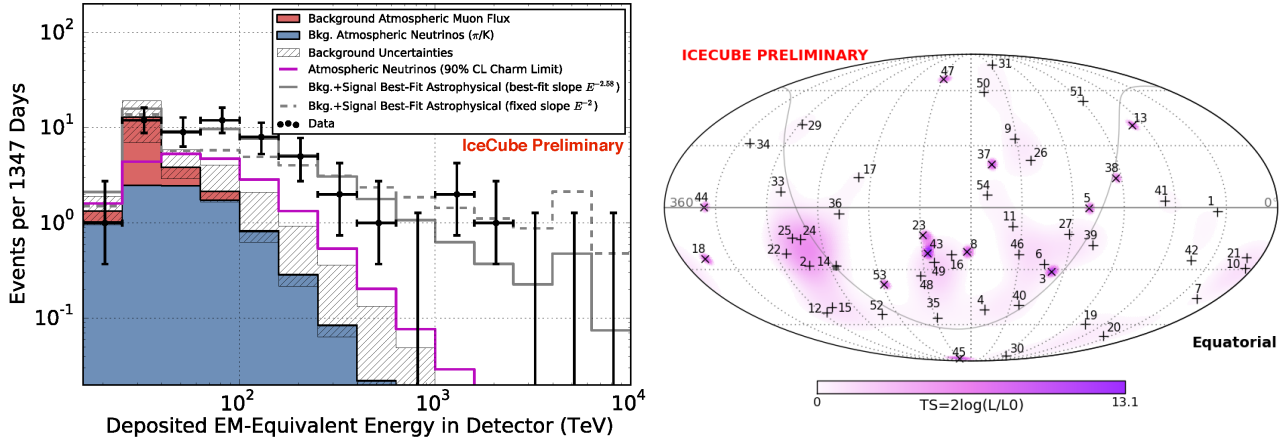
FIGURE 1.9: Left: Distribution of the EM-Equivalent energy deposited within the detector for the 54 events compared against expected atmospheric backgrounds and Right: A significance skymap of the sky testing the hypothesis that events are clustered.

After a photon reaches a DOM, the DOM response is simulated using single PE distributions measured in the lab. Additionally, after-pulses, pre-pulses as well as PMT jitter are added. Both poissonian as well as correlated noise are simulated.

1.5.3 Recent interesting results

In addition to neutrino astronomy, IceCube has a very exciting and diverse science programme, including Dark Matter Searches, neutrino oscillations, exotic signatures, cosmic rays and even glaciology. Some of the recent exciting results are:

Diffuse Astrophysical Neutrino Flux   IceCube recently reported evidence for a diffuse flux of high-energy astrophysical neutrinos, observing a $> 5\sigma$ excess of events between ~ 50 TeV and 2 PeV deposited within the detector. The search, requiring a deposition of at least 6000 photoelectrons within the detector (corresponding to deposited energies of $\sim$TeV) and no hits in the outer layer of the detector (to select only events interacting within the detector volume) found 54 events within a livetime of 1347 days, consistent with an $E^{-2.0}$ neutrino flux at the level of $6.6 \times 10^{-18} GeV^{-1} s^{-1} sr^{-1}$, with a neutrino flavour ratio of 1:1:1[57]. While these neutrinos have established unequivocally that astrophysical neutrinos exist, their sources have not yet been identified. A significant challenge is that only $\sim 20\%$ of these events are track-like. The remaining are cascade-like and have a poor angular resolution of $\sim 15°$. Figure 1.9 shows the distributions of these events in energy and arrival direction.

Evidence of a similar diffuse astrophysical flux has been observed also in other channels such as upward going muons from neutrinos interacting outside the detector and cascades[58]. A global fit of all the different analyses targeting high energy astrophysical neutrinos found that the flux is best described by a power law flux at the level of $7.3^{+0.9}_{-0.9} \times 10^{-18} GeV^{-1} s^{-1} sr^{-1} cm^{-1}$ at 100 TeV with a spectral index of $2.52^{+0.07}_{-0.07}$ [57].
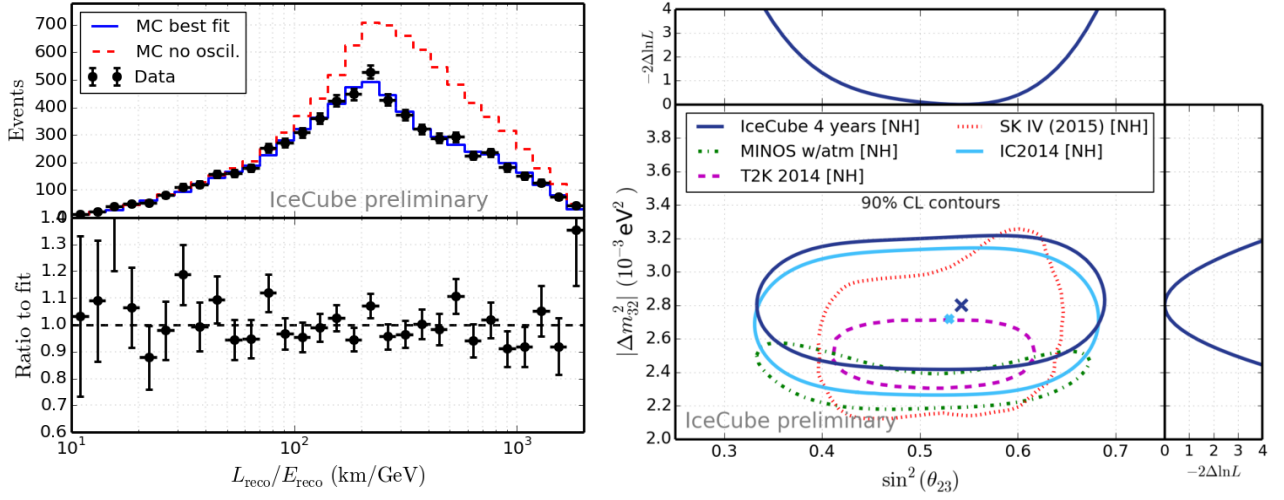
FIGURE 1.10: Left: Distribution of the reconstructed L/E ratio for the data observed in 4 years of operation of IceCube, compared against expectations from Monte Carlo for the case of no oscillations. Right: 90% C.L. contours on Δm_{32} and $\sin^2(\theta_{23})$

.
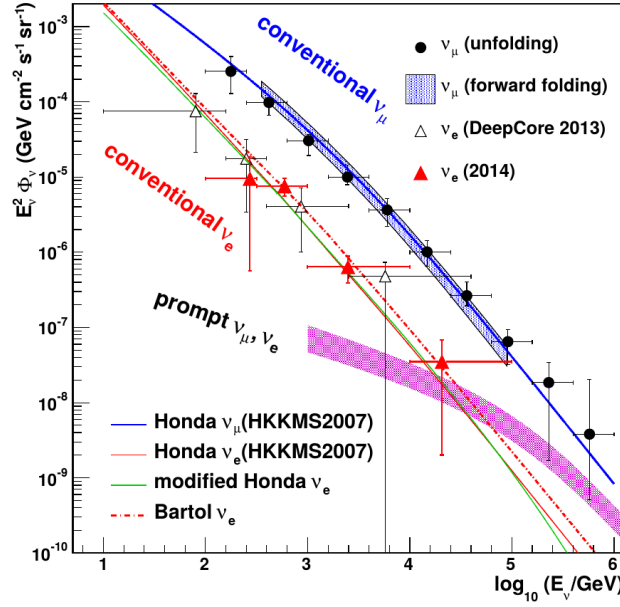
FIGURE 1.11: The measured atmospheric ν_e flux is shown as red filled triangles. ν_μ measurements from throughgoing upward ν_μ analyses are also shown. The unfilled triangles indicate the ν_e measurement from the IceCube-DeepCore dataset. Theoretical predictions are shown in lines, while the magenta band shows the modified prompt neutrino flux prediction by Enberg, Reno and Sarcevic [60].

Measurement of muon neutrino disappearance   In 2014, IceCube reported the observation of a deficit in ν_μ events between 10 and 100 GeV when compared against expectations from the atmospheric flux, a clear evidence of neutrino oscillations[59]. Figure 1.10 summarizes the observed deficit and the resultant 90% C.L. intervals on the parameters Δm_{32} and $\sin^2(\theta_{23})$.

Measurement of atmospheric fluxes   IceCube has measured the atmospheric ν_μ and ν_e fluxes using through-going tracks[61, 62], contained cascades[63] and DeepCore contained events[64]. The
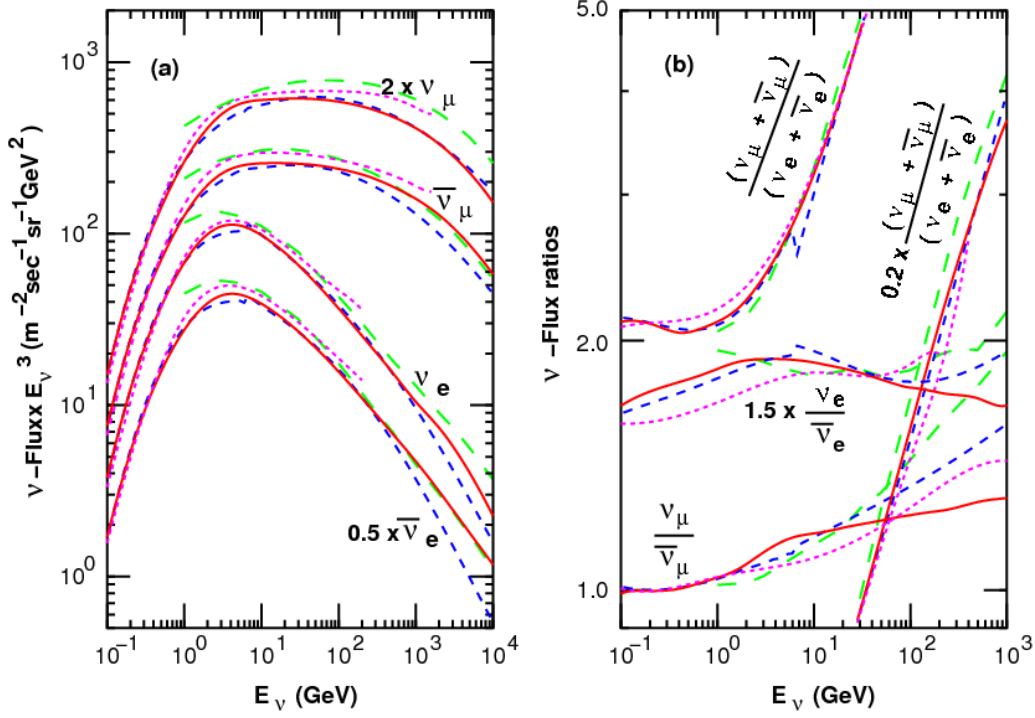
FIGURE 1.12: Left: Comparisons of atmospheric neutrino flux predictions from various Monte Carlo simulations. Right: The ratios of the flux predictions by the different simulations. The solid pink lines correspond to the predictions of [65]. The dotted pink lines, the dashed blue lines and the dashed green lines stand for the predictions from [67], FLUKA[68] and [69] respectively. Image taken from [65]

measurements are in excellent agreement with theoretical predictions based on measured cosmic ray spectra and composition, including the knee[65]. These measurements are illustrated in fig. 1.11.

IceCube has also characterized the atmospheric muon flux [66] at TeV-PeV energies. The multiplicity spectrum of TeV muons in cosmic ray air showers was found to be consistent with results from surface detectors. The single muon energy spectrum, determined up to PeV energies hints at the emergence of a spectral component from prompt decays of short-lived hadrons. The atmospheric neutrino spectrum from such decays will trace the spectrum of the parent nuclei and are referred to as 'prompt neutrinos'. While this component has not been measured so far, it is expected to be observed as more statistics build up in neutrino telescopes.

1.6 The Atmospheric Neutrino Flux

Neutrinos produced in interactions of CRs with the upper atmosphere form the principal background in all searches described within this work. Their spectrum, and zenith dependence are dictated by the spectrum and composition of the primary CR flux. The reference flux of atmospheric neutrinos used throughout this work is the calculation by Honda et. al. [65]. The results of this calculation are compared with alternate models in Figure 1.12.
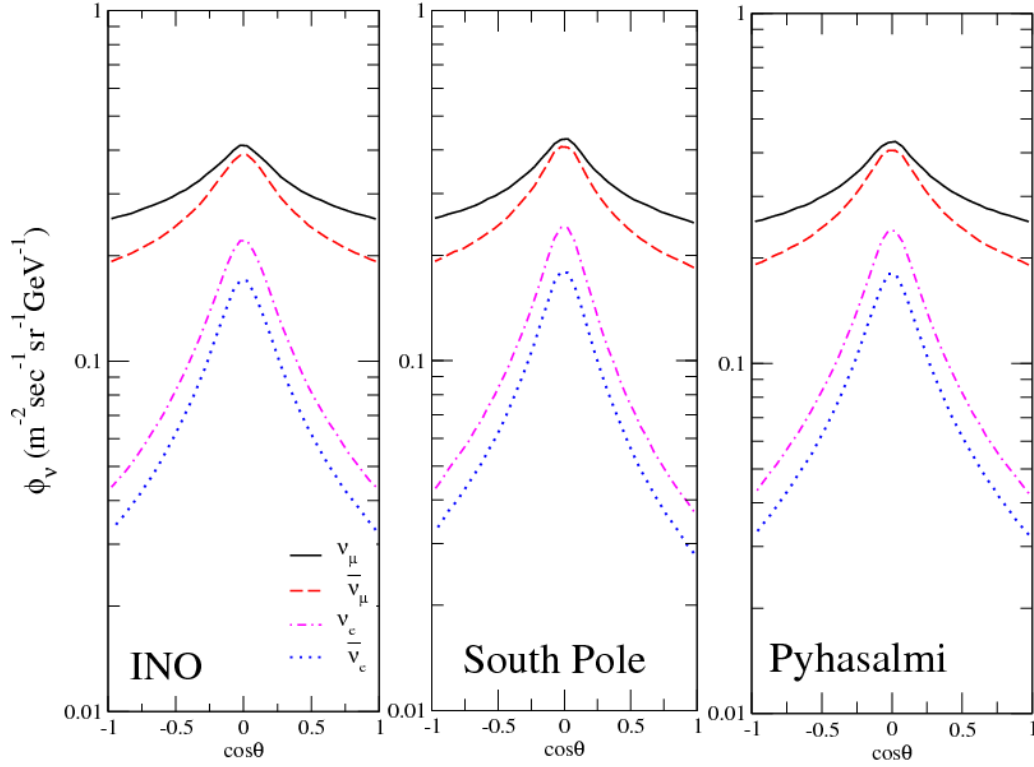
FIGURE 1.13: The zenith angle dependence of the atmospheric neutrino flux at E= 10 GeV, averaged over all azimuthal angles, for three different locations. $\cos\theta = 1$ is for vertically downgoing neutrinos, while $\cos\theta = -1$ is for vertically upward going neutrinos. Image taken from [70]

While there are differences, the different models agree on qualitative aspects of the spectrum. Between 10 GeV and 100 GeV, the ν_μ flux follows a power law shape with a spectral index of $\sim$3, gradually softening at higher energies ($\sim$3.15 at 200 GeV) to become $\sim$3.7 at energies above 10 TeV. This is due to a steep drop in the number of neutrinos produced in muon decay at higher energies, as the decay length of the muon becomes greater than the height of the atmosphere. This happens earlier for vertical directions than the horizontal ones. The ratio of $\nu_\mu : \bar{\nu}_\mu$ is between 1.25 and 1.3 at these energy ranges. As seen in fig. 1.13 the ν_e and ν_μ fluxes are maximum in the horizontal direction, as the distance between the interaction vertex and observer is maximum in this direction, allowing more muons to decay in flight and the contribution from muon decay to increase. Since the ν_e flux comes only from muon decay, the zenith dependence is much stronger for ν_e.

Due to the fact that ν_e are produced only in the decay of muons (Eq. 1.10 and 1.11), the ν_e and $\bar{\nu}_e$ fall much more steeply at energies above 10 GeV.

At energies above 100 TeV, a component of neutrinos from the decay of charmed mesons becomes dominant. Since the livetimes of these particles are very small, the resultant neutrino flux traces the parent CR flux and consequently falls less steeply with energy. Due to the steeper spectrum of ν_e, this transition happens at lower energies for ν_e. This component of the atmospheric neutrino flux, often referred to as the 'prompt' component, has never been measured so far. Predictions from [60] can be seen in figure 1.11. The uncertainties are due to the uncertainties in charm production cross section.

Part I

Part 1 : Point-like sources of Astrophysical Neutrinos

Chapter 2

Dark Matter: Motivation and Constraints

2.1   Introduction

This chapter introduces the evidence that has for long hinted at the existence of Dark Matter(DM). The inferences that can be made about its true nature from each of these evidences are explored. A brief review of the theoretical DM candidates is presented along with constraints from the leading efforts to detect them. The Weakly Interacting Massive Particle (WIMP) paradigm, of particular interest to this work is explored in more detail along with the dynamics of their capture and annihilation in massive bodies such as the Sun, the neutrino flux from which is searched for in the analysis presented in Chapter 5.

2.2   Motivations and Constraints

Starting in the 1930s, evidence began to emerge that the total mass distribution of galaxies and galaxy clusters measured from two independent methods, observations of their luminosity on the one hand and inferences from their gravitational effects on the other, disagreed significantly with each other. In 1933, the Swiss astrophysicist Fritz Zwicky applied the virial theorem to the Coma cluster of galaxies and estimated the total mass of the cluster based on the motions of galaxies near its edge. He made a separate estimate based on the number of galaxies and the total brightness of the cluster and observed that the former estimate was a factor of ∼400 larger than the latter[71]. Labelling this discrepancy the 'Missing mass problem', Zwicky inferred that there must exist some non-visible form of matter that provides enough mass to gravitationally hold the cluster together. While Zwicky's observations have later been shown to be wrong by more than an order of magnitude, more accurate studies of the velocity curves of various galaxies[72] by Rubin et. al. and clusters, as well as studies
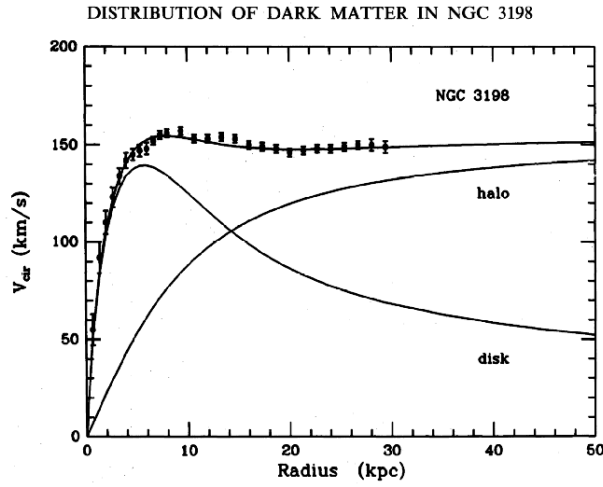
FIGURE 2.1: Observed rotational velocity of NGC 3198 as a function of distance from the centre, compared to predictions from luminous mass distribution, and a DM halo. Image taken from [73].

of the gravitational lensing effect of galaxies on their backgrounds have confirmed that most galaxies must contain ~ 5 times as much dark mass as can be accounted for with the visible stars. It is now well established that most galaxies are dominated by "Dark Matter". Additional observations from cosmology and astrophysics have helped provide more information about Dark Matter and are listed here:

2.2.1 Galactic Rotation Curves

According to Newtonian mechanics and under the assumption that the mass of a galaxy is distributed according to the observed luminosity, the matter in the disk portion of a spiral galaxy should orbit the centre of the galaxy with velocities that follow the line labelled 'disk' in Figure 2.1, i.e. the average orbital velocity of all objects at a specified distance from the majority of the mass distribution should decrease inversely with the square root of the radius of the orbit.

However, actual measurements of various galaxies (such as NGC 3198) show that the velocities do not decrease in the expected inverse square root relationship but are instead flat, as seen in Figure 2.1.

Kepler's third law states that the square of the period of an orbit is proportional to the cube of its radius, or more specifically:

$$T^2 = \frac{r^3 4\pi^2}{GM} \tag{2.1}$$

where G is the universal gravitational constant, T is the period of the orbit at radius r and M is the mass contained within the radius r. Using the fact that $T = 2\pi r/v(r)$ and $M = \int_0^r 4\pi r^2 \rho(r) dr$, it can be shown that the radial density profile $\rho(r)$ is given by:
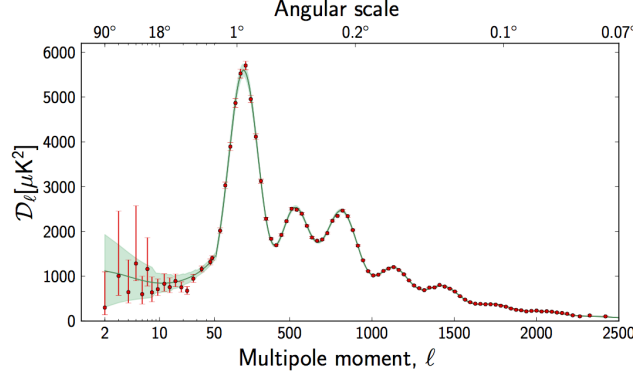
FIGURE 2.2: The angular power spectrum of the cosmic microwave background as reported by the Planck experiment.

$$\rho(r) = \frac{v(r)^2}{4\pi G r^2}\left(1 + 2\frac{d\log v(r)}{d\log r}\right) \tag{2.2}$$

where $v(r)$ is the radial orbital velocity profile[74].

Navarro, Frenk and White (NFW) [74] have observed that a density profile of the form

$$\rho(r) = \frac{\rho_0}{\frac{r}{R_s}\left(1 + \frac{r}{R_s}\right)^2} \tag{2.3}$$

in addition to a density profile that follows the observed luminosity is consistent with many observations, while also agreeing better with some N-body simulations. Here, the central density, ρ_0 and the scale radius R_s are parameters that are different for each galaxy. Since the expression diverges at $r = 0$, alternative profiles such as the Einasto[75] profile have been suggested.

Modern measurements utilizing data from large scale surveys of the sky such as the Sloan Digital Sky Survey (SDSS) [76] have been successful in quantifying the total matter density of the universe (Ω_m), as a fraction of the critical mass energy density to be ≥ 0.1 [77]. Some measurements have also been able to model the local gravitational potential and establish the local density of DM near the Sun (ρ_{DM}) to be $\sim 0.7 \pm 0.2$ GeV/cm^3 [78, 79], while the average density of DM at the distance of the Sun from the Galactic centre seems to be 0.4 ± 0.1 GeV/cm^3 [80].

2.2.2 Cosmic Microwave Background

The Cosmic Microwave Background (CMB) is the thermal radiation left over from the recombination epoch $\sim$378000 years after the Big Bang, when charged electrons and protons recombined to form electrically neutral hydrogen atoms and the universe became transparent to electromagnetic radiation. It follows a black body spectrum to a very high level of precision. It has been observed to be isotropically distributed to one part in 10^5[81], and can be interpreted as the image of a spherical

surface within the universe $\sim$378000 years after the big bang, known as the last scattering surface. The angular scale and intensity of these small fluctuations can be quantified by the angular power spectrum of Figure 2.2. The anisotropy observed in the CMB consists of both primary anisotropies, originating from anisotropies in the matter distribution on the last scattering surface and secondary anisotropies due to effects between the last scattering surface and the observer, such as reionization and structure formation. DM, which does not allow photons to scatter off it but nevertheless contributes to the gravitational potential, influences these anisotropies.

The effect of DM can be observed from two features of the angular power spectrum: the overall amplitude of the peaks and the relative amplitude of the third peak with respect to the second one[82].

Fitting the predictions of the ΛCDM model of big bang cosmology to the CMB angular power spectrum measured by the Planck experiment, it has been shown that the dark matter density of the universe (Ω_{DM}) is 0.268$\pm$0.002. This means that of the total energy content of the universe, $\sim$26.8% consists of Dark Matter. About 4.9% consists of ordinary baryonic matter while $\sim$ 68.3% is made up of Dark Energy. Thus DM makes up 84.5% of the total matter in the universe [82].

2.2.3 Baryon Acoustic Oscillations

While the anisotropy of the last scattering surface as seen in the CMB is less than one part in 10^5, the present universe shows large structure and density variations, with the presence of galaxies which are over $\sim$$10^6$ times the mean density of the universe. It is believed that the density perturbations at the time of recombination propagated through the primordial universe to become the large scale structures such as galaxy clusters that we observe today; analogously to sound waves in matter[83]. Starting from a pre-recombination perturbation that is common to baryons and DM, after recombination the DM perturbation grows in place while the baryonic perturbation is carried forward in an expanding spherical wave by the escaping photons. At recombination, this spherical shell has been theorized to be roughly 150 Mpc in radius[84].

The Sloan Digital Sky Survey, a 2.5 metre wide-angle optical telescope has carried out a 5 year survey to obtain images and spectra of millions of celestial objects and constructed a three dimensional map of the objects in the nearby universe. An analysis of 46,748 luminous red galaxies (LRGs) between redshift 0.16 and 0.47 using a two point correlation function found a clear (3.4 σ) evidence for an acoustic peak at $\sim$ 150 Mpc, in great agreement with predictions from the ΛCDM interpretations of the CMB data [85]. This discovery independently confirms that oscillations occur at $z \gtrsim 1000$ and also survive the intervening time to be detected at low redshift. For the amplitude of the features to be as small as observed, some matter has to exist that carry mass but do not interact with the photon-baryon fluid, namely dark matter.

The combination of CMB and BAO data reveal additional information about dark matter. For the small nonuniformities at recombination as measured by the CMB to grow into the large features found in Large Scale Structure Surveys of the present universe, DM has to consist of particles moving significantly slower than the speed of light, i.e. Cold Dark Matter[86].

2.2.4 Gravitational Lensing

Massive objects such as clusters of galaxies distort the space time around them according to the General Theory of Relativity[87]. This causes light from more distant objects such as a quasar to bend around these massive objects. Observationally, this is seen as 'weak lensing', where images of background objects are distorted in shape near the periphery of a massive foreground object, and also 'strong lensing', where multiple images of the same background object are observed near the core of a massive foreground object due to different possible paths. In general, an analysis the background image provides a third method of gauging the mass of galaxy clusters, independent of the two described in Section 2.2.1. This method has been applied on data gathered by the Hubble telescope to measure the masses of various clusters, and has consistently demonstrated that all clusters contain much more matter than the visible galaxies and gas.

A particularly interesting and historically important example is the Bullet Cluster, which consists of two colliding clusters of galaxies. The distribution of the total mass between the clusters as constructed using strong and weak gravitational lensing is radically different from the distribution constructed using the X-ray emissions as observed by the Chandra X-Ray observatory and provides significant evidence that most of the mass consists of Dark Matter. In this unique scenario of two colliding DM halos, the observed separation between the centre of mass of the total mass and the centre of mass of the visible mass serves as a measure of the self interactions of DM. The mass to light ratios of the subcluster and main cluster have been shown to be consistent, and rules out significant mass loss from DM self interactions. This sets an upper limit on the self interaction cross section by mass σ_{self}/m at $1\ cm^2g^{-1}$[88].

2.3 Candidate Models

While Cosmology and Astrophysics tell us that DM exists, has to be massive, almost non interacting and is unlikely to be relativistic, the particle physics nature of what makes up this mass fraction of the universe is entirely unknown. Viable candidates have often risen out of attempts to solve independent unrelated problems in particle physics. Some of these are:

Axions: Axions were first proposed as a solution to the strong CP problem, wherein Quantum Chromodynamics allows the violation of CP symmetry but this has never been experimentally observed in strong interactions. Experimental probes such as attempts to measure the electric

dipole moment of the neutron have consistently failed to detect any evidence of CP violation. The fact that the effective strong CP violating term $\bar{\Theta} \sim 0$ while it could have any value between 0 and 2π posed a naturalness problem of the standard model. In 1977, Roberto Peccei and Helen Quinn tried to solve this problem elegantly by adding a new global symmetry to the SM that becomes spontaneously broken, effectively promoting $\bar{\Theta} \sim 0$ to a field[89]. The pseudo Nambu-Goldstone boson of this broken symmetry is called the Axion. From theory they would have no electric charge, very small mass in the range of 10^{-6} to 1 eV/c^2, and very low strong and weak interaction cross sections, causing them to interact only minimally with ordinary matter. Remnant axions from the early universe could permeate the cosmos in the form of a very cold Bose-Einstein condensate, providing a Cold Dark Matter candidate. However, experimental searches for axions are currently not sensitive enough to probe the mass regions of relevance to the DM problem[90].

Sterile Neutrinos: Sterile neutrinos are neutrinos that do not interact through any of the fundamental interactions except gravity. The observation of neutrino masses have triggered many efforts to explain them theoretically. Many of these attempts introduce a right handed massive sterile neutrino candidate with a mass anywhere between 1 eV and 10^{15}GeV, giving a majorana mass to the SM neutrinos through the See-Saw mechanism. The sterile neutrino, due to its possible mass range and its lack of interactions is a DM candidate and searches are on for it in terrestrial neutrino experiments and colliders as well as the astrophysical context.

Weakly Interacting Massive Particles (WIMPs) : Being of specific interest to this work, WIMPs are dealt with in more detail in the following section.

2.4 Weakly Interacting Massive Particles

If DM consists of a stable particle χ, in the dense plasma of the early universe, the temperature of which exceeded the mass of χ (hereby denoted as m_χ), this particle would have existed in both thermal and chemical equilibrium with the remaining matter. Thermal equilibrium refers to the fact that the kinetic energy of these particles reflected the temperature of the universe, while chemical equilibrium specifies that the χs were abundant and rapidly pair annihilating into lighter particles and vice versa. As the universe expanded and cooled, its temperature dropped below m_χ and the number density of χs dropped exponentially, as the process $\chi\bar{\chi} \to S\bar{S}$ dominated over the reverse. Soon afterward, the rate of the annihilation reaction $\chi\bar{\chi} \to S\bar{S}$ would have fallen below the expansion rate of the universe and χs would have "frozen out", leaving behind a relic cosmological abundance[91]. This picture can be quantitatively described by the Boltzmann equation:

$$\frac{dn_\chi}{dt} + 3Hn_\chi = -\langle\sigma_a v\rangle \left[(n_\chi)^2 - (n_\chi^{eq})^2\right] \tag{2.4}$$

FIGURE 2.3: The comoving number density of DM as a function of time for different values of $\langle \sigma_a v \rangle$. Figure taken from [91].

where H is the Hubble expansion rate, n_χ is the comoving number density of χ and $\langle \sigma_a v \rangle$ is the velocity averaged pair annihilation cross section of χ. Figure 2.3 illustrates some numerical solutions to Equation 2.4. The relic abundance is determined by $\langle \sigma_a v \rangle$. For a small value of $\langle \sigma_a v \rangle$, the χs would have frozen out earlier, leaving behind a larger relic abundance. For the relic abundance of χ to be the current observed value of DM in the world, the required value of $\langle \sigma_a v \rangle$ is about $\sim 10^{-25} cm^3 s^{-1}$, which is coincidentally also what is expected for a particle in the 1 GeV to 10 TeV range interacting with approximately the strength of Standard Model weak interactions.

Thus a Weakly Interacting Massive Particle (WIMP) is a leading candidate for Cold Dark Matter. This particle would carry no electric or colour charge. It would be massive and stable. In addition to gravity, it interacts only through a force of approximately the same strength as the Weak interaction. While the standard model does not contain any viable candidates for WIMP dark matter, various popular extensions of the standard model do. An illustrative example is the neutralino within the Minimally Supersymmetric Standard Model (MSSM). First formulated to solve other open problems in particle physics such as the hierarchy problem, the MSSM introduces a new multiplicative quantum number, the R-parity, which is given by:

$$R = (-1)^{3B+L+2s} \tag{2.5}$$

where B, L and s are the baryon number, Lepton number and spin of the particle respectively. SM particles carry an R-parity $R = 1$ while their superpartners have $R = -1$. As a result of R parity conservation, supersymmetric particles can decay only into odd numbers of lighter supersymmetric

FIGURE 2.4: Complementarity of the different schemes to detect DM.

particles and SM particles, making the lightest supersymmetric particle stable and a natural WIMP candidate. Other candidates include the bosons that appear in Kaluza Klein theories.

2.5 Dark Matter Detection

Experimental attempts to detect DM fall into three different categories. Direct Detection experiments look for a nuclear recoil signal from WIMPs scattering off the target nuclei within the detector volume. Indirect detection attempts search for the primary or secondary standard model particles such as photons, neutrinos and antimatter from the pair annihilations or decay of dark matter. Searches are also carried out at accelerators for the production of DM in particle collisions. Figure 2.4 provides a schematic illustration of the three approaches. These different approaches are complementary and a credible identification and study of the properties of DM can be made only if it is detected in more than one of these channels.

2.5.1 Direct Detection

Due to the weak interaction scale cross-section for WIMPs, the expected number of dark matter recoils within even the largest of detectors is very low, forcing direct detection experiments to operate at extremely low background, typically deep underground. The differential event rate in the laboratory frame is given by

$$\frac{dN}{dE_T} = \frac{\sigma_n \rho_\chi}{2m_\chi \mu_{n\chi}^2} F^2(E_T) \int_{v_{min}(E_T)}^{\infty} \frac{f(\vec{v} + \vec{v}_E(t))}{v} d^3v \qquad (2.6)$$

FIGURE 2.5: Summary of spin-independent WIMP-nucleon scattering results: The favoured parameter spaces from experiments such as DAMA and Cogent, as well as theoretical considerations are shown. Solid lines are limits while dashed and dotted lines are the sensitivities of future experiments. The orange region at the bottom indicates the neutrino floor, beyond which events from Solar and Atmospheric neutrinos cannot be distinguished from DM signal by a detector with no directional capabilities. Figure taken from [93].

E_T is the recoil energy, σ_n is the WIMP-nucleon scattering cross section, ρ_χ the local dark matter density, $F(E_T)$ the nuclear form factor and $\mu_{n\chi}$ the WIMP-nucleus reduced mass. $\vec{v}_E(t)$ is the relative velocity of Earth within the galactic rest frame and $f(\vec{v})$ is the velocity distribution of the local dark matter, calculated in the galactic rest frame[92].

Detectors with a target volume of liquid noble gas, such as XENON100, LUX and DarkSide look for scintillation radiation from excited target atoms as well as measure the ionization of these atoms in order to distinguish electron recoils from those of WIMPs scattering off nuclei. Cryogenic detectors such as CDMS, CoGeNT, EDELWEISS and CRESST measure the phonons induced within their semiconducting or scintillating crystals by DM recoils. COUPP and PICASSO were bubble chambers based on superheated liquids and searched for the phase transitions triggered by the recoil of atoms from DM scattering. Ideas from the two experiments were merged to create PICO-2L, based on a bubble chamber of superheated C_3F_8.

As the Earth moves around the Sun, the relative velocity of Earth $\vec{v}_E(t)$ is expected to vary annually, causing the event rate to vary annually. The DAMA/LIBRA experiments have observed an annual variation in the scintillation rates in their sodium iodide (NaI) detectors at $\gtrsim 8\sigma$ level of significance, consistent with WIMPs of ~ 60 GeV mass and total cross section of $10^{-41} cm^2$[94]. However, CDMS[95], XENON100[96], COUPP[97] and EDELWEISS[98] have failed to detect such a

signal and have subsequently excluded the parameter space. CoGeNT reports a similar modulation at 2.8σ level of significance. The comparison of results from experiments with different target materials is complicated by the dependence of the WIMP event rate on the $v_{min}(E_T)$, which is given by $v_{min}(E_T) = \sqrt{m_n E_T / 2\mu_{n\chi}^2}$. A comparison of the two claims accounting for these detector effects have concluded that there exists significant tension between them[99]. The DM-ICE [100] detector is an NaI detector similar to DAMA at the South Pole and has already started operations[101]. An evidence of the same modulation signal in the opposite hemisphere of Earth also will strongly support a DM observation.

Figure 2.5 summarizes the upper limits from various direct detection experiments, for spin independent (SI) WIMP-nucleon scattering.

2.5.2 Indirect Detection

Indirect detection experiments look for primary or secondary Standard Model particles created in the pair annihilation or decay of WIMPs, such as photons, neutrinos or antimatter. Since the number of WIMP annihilations or decay is proportional to the square of the DM density or the DM density respectively, the leading targets of these searches are regions where a high density of DM is expected. Since these particles are also produced in the astrophysical context, a low or very well understood astrophysical background is also preferred. Gravitational traps for DM, such as the Earth or the Sun, are particularly good targets for neutrino searches. Other targets include the Galactic centre, the halo, dwarf spheroidal galaxies and nearby galaxy clusters.

The Fermi satellite[102], as well as the H.E.S.S.[103], MAGIC[104], and VERITAS[105] ground-based observatories search for high energy γ signals. In addition to the γ-rays from secondary decays of annihilation products and by internal bremsstrahlung, monochromatic γ-lines from DM annihilations into 2γ and γZ channels are of particular interest because they serve as smoking gun signatures and allow an unambiguous determination of the DM mass. Tight constraints have been placed on the $\langle \sigma_a v \rangle$ based on searches for γ-rays from the Galactic centre, dwarf galaxies and galaxy clusters. Recently, an observation of the diffuse γ-ray emission around the Galactic centre has been found to be consistent with that of annihilations of 25-30 GeV WIMPs distributed according to the NFW profile with a self annihilation cross section equal to the thermal relic expectation[106]. However, alternative explanations include unresolved astrophysical sources such as millisecond pulsars or an injection of cosmic rays. Recent analyses hint that the excess consists of unresolved point sources[107]. A credible detection will require confirmation in other channels and also from other locations, such as dwarf galaxies.

Although far too low in energy to be interpreted within the WIMP paradigm, a 3.5 KeV X-ray line has been observed by different analyses of data from CHANDRA, XMM-Newton and SUZAKU X-ray telescopes, in the direction of different galaxies and galaxy clusters[108]. This could be due to the annihilation of a 3.5 KeV DM particle, or the decay of a 7 KeV DM particle. A hitherto

unidentified molecular line is a possible trivial explanation. If confirmed, due to their low mass, this would constitute 'Warm Dark Matter'.

2.5.3 Accelerator Searches

Experiments at colliders such as the Tevatron and the LHC search for physics beyond the standard model. This quite often includes searches for the production of DM candidate particles within the detectors, as well as the decay of heavier states into DM candidate particles. These searches are often carried out within the framework of a promising theory of physics beyond the standard model, such as the MSSM. A review of all collider searches for Supersymmetry can be found at [109].

While accelerator searches have the advantage of being free of astrophysical backgrounds, a discovery of a candidate DM particle in a collider search will have to be confirmed by its detection in the astrophysical context. The searches are also limited by the maximum centre of mass energy obtainable at the collider.

2.6 WIMP Capture and Annihilation in Massive Bodies

If the DM content of the Galaxy consists of WIMPs, they can scatter off nuclei in the Sun, lose energy to fall below the escape velocity of the Sun, and be gravitationally captured.

The total capture rate of WIMPs in the Sun takes the form:

$$C_C = \frac{\rho_{DM}}{m_\chi} \sum_i \sigma_i \int_0^{R_{Sun}} dr 4\pi r^2 n_i(r) \int_0^\infty dv 4\pi v^2 f_{Sun}(v) \frac{v^2 + v_{esc}^2}{v} p_i(v, v_{esc}) \tag{2.7}$$

where the index i varies over the different nuclei that make up the sun, σ_i is the scattering cross section between the WIMP and nucleus i and $f_{Sun}(v)$ is the velocity distribution of DM particles near the Sun in the rest frame of the Sun and absence of solar gravity[110].

The total number of WIMPs within the Sun, N is governed by

$$\frac{dN}{dt} = C_C - C_A N^2 - C_E N \tag{2.8}$$

where C_C is the WIMP capture rate, C_A is the coefficient of the annihilation rate and C_E is the coefficient of loss due to evaporation, due to the hard elastic scattering of WIMPs with nuclei in the Sun. It has been demonstrated that for WIMP masses above 10 GeV, the evaporation term can be ignored[111].

Ignoring C_E, Equation 2.8 can be solved to give the annihilation rate $\Gamma_A = C_A N^2/2$

$$\Gamma_A = \frac{C_C}{2} tanh^2(t_\odot/\tau) \tag{2.9}$$

where $t_\odot$ is the age of the Sun and $\tau = (C_C C_A)^{-1/2}$ is the time scale required for WIMP capture to reach equilibrium with the annihilation[91].

The absolute capture rate in the Sun depends on the nature and strength of the WIMP-nucleon elastic scattering. Ref. [112] lists 14 linearly independent quantum mechanical operators that can be constructed from Galilean invariant Hermitian operators that act on the two-particle Hilbert space spanned by tensor products of DM and nucleon states, $|\vec{p}, j_\chi\rangle$ and $|\vec{k}, j_N\rangle$, where $\vec{p}$ and $\vec{k}$ are the momenta of the WIMP and the nucleon respectively. The authors have calculated the nuclear response functions for each of these operators for the 16 most abundant elements in the Sun, and the resultant total capture rates. The operators found to contribute towards the largest capture rates have been found to be $\mathbb{1}$, the identity operator and $\hat{S}_\chi.\hat{S}_N$, the product of the spins of the two nucleons. These operators respectively correspond to the standard spin independent and spin dependent WIMP-nucleon scattering scenarios usually considered. Capture rates due to the other 12 operators are suppressed by the low velocities of WIMPs in the Galactic halo. In the non relativistic limit, axial-vector and tensor interactions reduce to the form of the spin-dependent interaction.

Searches such as the one presented in Chapter 5 have uniquely high sensitivity to spin-dependent scattering, as the Sun is predominantly made of hydrogen, a nucleus with spin. In terrestrial DM direct detection experiments such as XENON, signals from spin-dependent scattering are suppressed by the relatively low abundance of isotopes with intrinsic nuclear spin in their target mass.

2.7 Neutrinos from WIMP Annihilations in the Sun

The captured WIMPs pair annihilate into standard model particles. The dominant primary annihilation products cannot be predicted without relying on a specific model. For example, the MSSM neutralino at non relativistic velocities annihilates preferentially into heavy fermion-antifermion pairs such as top, bottom and charm quarks and tau leptons, as well as heavy gauge boson pairs like W^+W^- and Z^0Z^0. Light fermion-antifermion pairs are helicity suppressed. The Kaluza-Klein photon, another attractive WIMP candidate on the other hand is not a Majorana spinor like the neutralino and can dominantly annihilate also into light fermions due to the lack of helicity suppression.

When WIMPs annihilate inside the Sun, neutrinos are the only stable SM particles that can leave the Sun without being completely absorbed. Since long lived primary annihilation products will interact with the dense solar medium and lose most of their energy before decaying, a high energy neutrino flux is expected only from the annihilation of WIMPs into short lived channels. As a result, the

annihilation channels that produce high energy neutrinos are b, c and t quarks, as well as τ-leptons and gauge bosons.

The high energy neutrinos produced at the centre of the Sun interact further with the dense solar medium. Consequently, the Sun is transparent to neutrinos only below ~ 1 TeV. Neutrino fluxes for specific WIMP masses and annihilation channels are discussed in chapter 5.

Chapter 3

Cosmic Rays: Spectra, Composition, Acceleration sites and mechanisms

3.1 Introduction

Cosmic Rays (CRs) are charged particles (mainly protons and heavier nuclei) in outer space. They often extend to energies far higher than those attainable at terrestrial particle accelerators such as the LHC.

This chapter introduces the history of the discovery of CRs. Their spectrum and composition, as understood by the latest measurements are subsequently described, followed by the leading theories about how they are accelerated. Potential acceleration sites, which form the targets of the searches in the following chapters are subsequently described.

3.2 History

The earliest hints about the existence of CRs come from observations by various physicists in the first decade of the 20th century that the rate of ionization of the atmosphere increases with altitude. This was at odds with the expectations from the leading hypothesis that the ionization was due to the radioactive elements in the ground.

In 1912, Victor Hess unequivocally demonstrated that the ionization rate of the atmosphere at 5300 ms was four times that at ground level, using enhanced accuracy Wulf electrometers in a free balloon flight. The Sun was ruled out as the source of these CRs due to the fact that a similar ionization rate was observed even during a complete Solar eclipse[113].

While the initial belief was that these CRs were energetic photons, evidence was soon found that the intensity of these CRs is latitude dependent, implying that the primary particles were charged, not

photons. Subsequently a charge dependent difference was predicted in the intensity of comic rays from the east and the west. When it was confirmed that the intensity is in fact greater from the west, it was concluded that most CR primaries were positive. Since then it has been proven that most CRs are protons and that the secondary radiation in the atmosphere consists of electrons, photons and muons. It has also been established that about 10% of the CRs are helium nuclei, while $\sim 1\%$ are the nuclei of heavier elements such as carbon and iron.

A wide range of modern experiments have measured cosmic rays ranging in energy from a few hundred MeV up to hundreds of EeV. In the 1 GeV to the hundreds of GeV range, the Alpha Magnetic Spectrometer on board the International Space Station provides the most accurate measurements[114]. At higher energies ($\sim$1 TeV and above), the best measurements are provided by satellite born spectrometers such as those on board the 'proton' series of satellites. At PeV energies, due to the low statistics, accurate measurements can be made only by ground-based detectors sampling the shower of charged particles caused by the CRs interacting with the upper atmosphere, such as CASA-MIA. At ~ 10 PeV, the flux reaches the level of 1 particle/m^2/year, requiring large surface detectors with effective areas of many km^2 such as KASCADE GRANDE, Tibet, Akeno etc.

At EeV energies and above, measurements are performed by detectors such as Pierre Auger Observatory and Telescope Array, using detection areas of a few thousand km^2. Such large detection areas are achieved by spacing the ground detectors widely apart, allowing the sampling of only a fraction of the hadronic shower caused by the CR. However, this limits the sensitivity to only the highest energy of CRs. In the future, experiments such as JEM-EUSO will orbit the Earth, measuring fluorescence photons from the showers in the atmosphere to detect CRs.

3.3   Spectrum and Composition

Above a few GeV up to to ~ 1 PeV, the Cosmic Ray spectrum follows a constant E$^{-2.7}$ power law shape. At ~ 3 PeV, the spectrum shows a composition dependent break and becomes gradually softer, with the spectrum of lighter nuclei softening earlier. This is known as the 'knee'. At even higher energies (> 1 EeV), the spectrum hardens again, in a feature often called the 'ankle'. Figure 3.1 summarizes the measured spectrum over 11 orders of magnitudes in energy by various air shower and space based measurements. Beyond 40 EeV, the spectrum shows a sudden break, and is described by a much softer $E^{-4.3}$ power law. This is believed to be due to the GZK process[116], wherein high energy protons interact with CMB photons through the Δ^+ resonance. This process prevents CRs above 10 EeV from propagating more than a few hundred Mpc, the so called GZK horizon.

The knee of the cosmic ray spectrum is believed to be due to a transition from Galactic to extragalactic CRs. At energies around the knee, the gyroradius of protons within the Galactic magnetic field exceeds the radius of the Galaxy, and subsequently higher energy particles escape faster. The shape of the knee is dictated by the fact that heavier nuclei need higher energies to escape. Above the ankle, all

FIGURE 3.1: The measured cosmic-ray spectrum : The observed softening of the spectrum at $\sim$ 3PeV is known as the 'knee' while the hardening of the spectrum at $\sim 10^{10}$ GeV is known as the ankle. Image taken from [115]

CRs are expected to be extragalactic as no known Galactic sources have the required magnetic field strengths to accelerate them. Also, the observed arrival directions of CRs above the knee do not show any significant correlation with the Galaxy, suggesting an extragalactic origin.

Below the knee, CRs are composed mostly of protons. At energies around the knee, the composition may shift to heavier nuclei due to the dependence of the gyroradius on nuclear charge for a given energy. CR composition between the knee and the ankle is not well known due to the experimental difficulties in measuring it.

3.4 Acceleration

The mechanism by which CRs gain such high energies is not very well understood and is an area of contemporary research. The leading theory is that the particles gain energy by interacting with magnetic clouds and shocks in a stochastic manner. The mechanism was originally postulated by Fermi in 1949[117] but its efficiency was found to be insufficient to explain the observed CR spectrum. It is now known as the second order Fermi acceleration. In the late 1970s, a number of publications by researchers working independently of each other proposed a more efficient mechanism known as the Diffusive shock acceleration or the first order Fermi acceleration.

3.4.1 Second order Fermi Acceleration

If a particle with velocity $\vec{v}$ is reflected off a gas cloud with velocity $\vec{u}$, the particle can gain or lose energy depending upon whether $\vec{v}$ and $\vec{u}$ are antiparallel or parallel. The difference in energy is given by[118]:

$$\Delta E_1 = \frac{1}{2}m(v+u)^2 - \frac{1}{2}mv^2 = \frac{1}{2}m(2uv+u^2) \tag{3.1}$$

when they are antiparallel and

$$\Delta E_2 = \frac{1}{2}m(v-u)^2 - \frac{1}{2}mv^2 = \frac{1}{2}m(-2uv+u^2) \tag{3.2}$$

when they are parallel, leading to an average net energy gain of

$$\Delta E = \Delta E_1 + \Delta E_2 = mu^2 \tag{3.3}$$

The relative energy gain on average is then

$$\frac{\Delta E}{E} = 2\frac{u^2}{v^2} \tag{3.4}$$

and this mechanism is called the second order Fermi acceleration due to the quadratic dependence on the cloud velocity. Due to the fact that the cloud velocities observed in nature are rather low compared to the relativistic velocities seen in the particles, the energy gain per collision is very small, requiring extremely long durations of time to achieve the energies observed in the CR spectrum. The problem is exacerbated by the fact that CRs will also lose energy through interactions. Consequently, the second order Fermi mechanism is today believed to be insufficient to explain the observed CR spectrum.

3.4.2 First order Fermi Acceleration

A shock is an abrupt discontinuity between two regions of fluid flow, caused by the gas itself moving faster than the speed of sound in the gas. If a flux of relativistic particles is present both upstream and downstream of the shock, scattering ensures that the velocity distribution of the particles is isotropic in the frame of reference in which the gas is at rest.

Following the treatment in [119] the velocity of the shock is denoted by U. Let the pressure, temperature and density ahead of the shock be $p_1, T_1,$ and ρ_1 while behind the shock they are $p_2, T_2,$ and ρ_2 respectively.

For an ideal gas, by applying conditions of mass, energy and momentum conservation at the shock boundary, it can be shown that $v_1/v_2 = (\gamma + 1)/(\gamma - 1)$, where v_1 and v_2 are the velocities of the gas ahead of and behind the shock respectively in the rest frame of the shock, while γ is the ratio of the specific heats of the gas at constant pressure and constant volume. For an ideal mono-atomic gas (or equivalently a fully ionized plasma), $\gamma = 5/3$ and consequently $v_2 = v_1/4$. Thus a high energy particle ahead of the shock observes the shock advancing through its medium at velocity U but the gas behind travelling at a velocity $V = (3/4)U$, and consequently gains $\Delta E = pV\cos\theta$ of energy for a non relativistic shock. Crucially, a particle that is diffusing from behind the shock to the up stream region encounters gas moving towards the shock front at the same velocity $V = (3/4)U$ and consequently gains an equivalent amount of energy again. Thus unlike the original Fermi acceleration mechanism, in diffusive shock acceleration, there are only head on collisions and the particle always gains in energy.

By integrating over all the relative angles at which the particle encounters the shock, the average gain in energy can be shown to be:

$$\frac{\Delta E}{E} = \frac{4}{3}\frac{V}{c} \tag{3.5}$$

By the arguments of Bell(Ref. [120]), it can be shown that the fraction of particles lost per unit time is U/c.

If we define $\beta = E/E_0$ as the average energy of the particle after one collision and P as the probability that the particle remains in the acceleration region after one collision, then after k collisions, there are $N = N_0 P^k$ particles with energies $E = E_0\beta^k$, and the spectrum can be shown to be:

$$N(E)dE \propto E^{-1+(lnP/ln\beta)}dE \tag{3.6}$$

For $lnP = ln(1 - U/c) \approx -U/c$ and $ln\beta = ln(1 + 4V/3c) \approx 4V/3c = U/c$, it can be shown than $lnP/ln\beta = -1$ and consequently the differential energy spectrum of the high energy particles is an E^{-2} power law spectrum.

3.5   Acceleration Sites

Generally, the maximum energy that can be gained from the Fermi mechanism is determined by the amount of time for which the particles are able to interact with the plasma. This time is limited by both the livetime of the acceleration region (SNR shocks dissipate after a few tens of thousands of years), as well as an increased likelihood of escape from the region at higher energies. As a first approximation, the ability of an astrophysical object to accelerate CRs is determined by its size and

FIGURE 3.2: The size and magnetic field strengths of possible CR accelerators. The three diagonal lines (from top to bottom) correspond to regions below which objects cannot accelerate protons above 10^{21} eV, 10^{20} eV, and Fe nuclei above $10^{2}0$ eV respectively. Objects below these lines can still accelerate CRs, but to energies lower than 10^{20} eV. Figure taken from [121].

the strength of its magnetic field. The maximum energy E_{max} that can be acquired by a particle in a medium with magnetic field B is given by :

$$E_{max} \sim 2\beta c ZeBr_L \tag{3.7}$$

where βc is the velocity of the particle, Z is its charge and r_L corresponds to its maximum Larmor radius, which is of the order of the size of the acceleration region.

The Hillas diagram, figure 3.2 shows a few classes of objects in terms of their typical size and the strengths of their magnetic fields.

A few leading candidates of relevance to this work are discussed here.

3.5.1 Galactic

3.5.1.1 SuperNova Remnants

For an average energy density of $\rho_E = 1eV cm^{-3}$ observed in CRs in the Solar neighbourhood, the total power required to accelerate all the CRs in the disc is given by [122].

$$W_{CR} = \frac{\rho_E \pi R^2 D}{\tau} = 3 \times 10^{41} Jyr^{-1} \qquad (3.8)$$

where $R \sim 15kpc$ and $D = 0.3kpc$ are the radius and width of the Galactic disk respectively while $\tau \sim 3$ million years is the average time a CR spends in the Galaxy before diffusing out or interacting with the interstellar gas.

A Type II supernova typically ejects a shell of material of about 10 solar masses with a velocity of $\sim 10^7 ms^{-1}$. At the observed rate of ~ 3 SuperNovae per galaxy per century, this gives an average power output per galaxy of

$$W_{SN} = 10^{43} Jyr^{-1} \qquad (3.9)$$

from SuperNovae alone. Based on the above considerations Fritz Zwicky remarked that an efficiency of a few percentage is sufficient in the acceleration process to explain the observed CR energy budget.

SuperNovae are extremely high energy explosions observed when massive stars at the end of their life cycle undergo core collapse due to the unavailability of sufficient nuclear fuel to produce the pressure required to support against their own gravity. The fast collapsing core subsequently rebounds from the surface of the inner region, which is at the density of a nucleus and expands outward at velocities higher than the speed of sound. The resultant shock wave is called the shell of the SNR and sweeps up the matter in its path, providing an excellent shock front for diffusive shock acceleration of CRs. The neutron star left behind at the centre often carries a high angular momentum, and forms the central pulsar of the SNR.

As the shell initially expands outwards, the mass of the interstellar medium it encounters is small compared to the mass of the stellar ejecta for the first $\sim 200 - 300$ years. This is known as the free expansion phase. Soon the SNR enters a domain where the mass of the interstellar medium swept up approaches the mass of the stellar ejecta and a significant portion of the energy of the shell has been transferred to the swept up particles. At this stage, the SNR is a few parsecs across. This phase, which goes on for the subsequent ~ 10000 years is known as the Sedov Taylor or the blast wave phase of the SNR, and is believed to be the most efficient in terms of transferring energy from the shell to CRs[123]. Subsequently, the shell decelerates and transfers most of its energy to the surroundings, cools down, becoming visible only in radio and the infrared, and eventually vanishes.

Astronomically, SNRs have been observed within the Galaxy and also in other galaxies at various wavelengths. Their age is estimated from the size of their shell. They are morphologically classified as shell type, composite, or mixed morphology, based on the intensity of the X-ray emissions from the shell and the central pulsar.

In 2013, the Fermi-LAT collaboration reported features consistent with the decay of neutral pions in the MeV spectra of IC443 and W44[124], two Galactic SNRs that are known to interact with giant molecular clouds. This constitutes preliminary experimental evidence for the long held hypothesis that SNRs are indeed the sites of proton acceleration.

The University of Manitoba maintains an exhaustive online catalog of Galactic SNRs, SNRCat [125].

3.5.1.2   Microquasars

Microquasars are Galactic binary systems that emit in X-ray and also radio frequencies. The X-rays are emitted by matter as it is accreted from the donor, usually a regular star to a compact accretor - a white dwarf, neutron star or black hole. Through mechanisms that are not fully understood, the accreting matter can interact with magnetic fields and generate relativistic jets magnetohydrodynamically. Since the microquasar is a binary system revolving around their common centre of mass with a specific period, the jets also often precess with the same period. These relativistic jets are excellent sites for shock acceleration and thus microquasars are believed to be good candidates for CR acceleration [126].

3.5.2   Extragalactic

3.5.2.1   Active Galactic Nuclei

An AGN is a compact region, usually believed to be a black hole, at the centre of a galaxy, which exhibits a higher luminosity than its surroundings in almost the entire electromagnetic spectrum. Cold matter around the black hole falls inward under gravity, heating up in the process and radiatively transferring angular momentum outwards. This phenomena is observed at various wavelengths as a bright disc, known as an accretion disc. Like microquasars, AGNs also often exhibit highly collimated extremely powerful twin jets of relativistic plasma in directions perpendicular to the plane of the accretion disk. These jets often extend thousands of parsecs in length and are excellent sites for the diffusive shock acceleration of CRs. AGNs with their jets pointing towards Earth are observed as Blazars while AGNs with the jets perpendicular to the line of sight are observed as Radio Galaxies. In 2007 the Pierre Auger Observatory reported that the arrival directions of UHECRs correlated with known nearby AGN[127]. However, the statistical significance of this observation reduced with more years of data and it remains inconclusive if AGNs are the sources of UHECRs. Sections 7.4 and 7.5

describe a stacking search for neutrino emission from AGNs within the GZK radius,as well as the arrival directions of the highest energy UHECRs.

3.5.2.2 Gamma Ray Bursts

A Gamma Ray Burst is a highly energetic burst of γ-rays that lasts anywhere between a few milliseconds to several hours. They are believed to be due to a short lived intense jet that forms as a star collapses into a black-hole or neutron star in a supernova like process. BATSE, an experiment onboard the Compton Gamma-Ray Observatory reported the volumetric rate of GRBs in the nearby universe at $300/GPc^3/yr$. The typical 2×10^{51} erg of energy released per cosmological GRB is believed to be sufficient to build up the energy density of extragalactic CRs over Hubble time, and GRB jets are excellent candidate sites for diffusive shock acceleration. However, in 2012, IceCube reported an absence of neutrinos associated with CR acceleration in GRBs, placing an upper limit on the neutrino flux associated with a GRB that is at least a factor of 3.7 below the predictions, implying that GRBs cannot be the only sources of extragalactic CRs[128]. More up to date analyses have concluded that GRBs cannot contribute more than $\sim 1\%$ of the diffuse astrophysical flux observed by IceCube [129].

3.5.2.3 Galaxy Clusters

Galaxy clusters are large clusters of 100s to 1000s of galaxies bound together by gravity. With masses ranging from, 10^{14} to 10^{15} solar masses, they are some of the largest gravitationally bound structures in the universe and according to standard scenarios of cosmological evolution are believed to virialize last. They continue to grow through mergers and accretion of dark matter and baryonic scales, generating powerful shocks on Mpc scales which serve as excellent sites for diffusive shock acceleration[130]. Even though they have relatively weak magnetic fields, the immensity of the shock fronts place them in a favourable position in the Hillas plot. They are thus believed to be candidate sites for the acceleration of UHECRs. Section 7.2 describes a stacking search for neutrino emission from galaxy clusters in the nearby universe.

3.5.2.4 Starburst Galaxies

Starburst galaxies are galaxies that exhibit star formation rates far in excess of the long term average star formation rate observed in other galaxies and have been demonstrated to have dense interstellar media. This leads to higher rates of supernovae, as well as the resultant heating of ambient dust [131]. Consequently, a significant correlation has been observed between the radio emission, believed to be due to the synchrotron losses of the CR electrons and the emission in the far infrared (FIR), believed to be from the hot ambient dust. The elevated number of SNRs are believed to make them excellent candidate sources of hadronic CRs and consequently also of neutrinos. Ref. [132] predicts the cumulative background of high energy neutrinos from starburst galaxies to be at the level of

$2 \times 10^{-8\pm0.5} \mathrm{GeVcm}^{-2}\mathrm{s}^{-1}\mathrm{sr} - 1$ with a spectral index softer than -2, making them excellent candidates to be the sources of the IceCube astrophysical neutrino flux. A stacking search for neutrino emission from 127 starburst galaxies in the nearby universe is described in 7.3.

3.6 Neutrinos from CR Acceleration sites

At all sites of CR acceleration, neutrinos are expected to be produced through pp and $p\gamma$ interactions detailed in section 1.4. As can be seen in equations 1.5 to 1.11, roughly twice as many ν_μ and $\bar{\nu}_\mu$ are expected to be produced, compared to ν_e and $\bar{\nu}_e$, making the $\nu_e(+\bar{\nu}_e) : \nu_\mu(+\bar{\nu}_\mu)) : \nu_\tau(+\bar{\nu}_\tau)$ flavour ratio at source 1:2:0. Due to the near maximal nature of 2-3 mixing and the extremely long baselines over cosmic distances, astrophysical fluxes at Earth are expected to be of 1:1:1 ratio. However, significant contributions from neutron beam sources (1:0:0), or muon-damped sources (0:1:0) can significantly modify the flavour ratio of the flux expected at Earth. A detailed discussion of the flavour physics of astrophysical neutrinos can be found in refs [133] and [134].

The diffuse astrophysical flux observed by IceCube (section 1.5.3) is consistent with a 1:1:1 flavour ratio.

The spectrum of the neutrinos is expected to follow the spectrum of the parent protons in the acceleration site. Consequently, E^{-2} power law spectra are expected. Fluxes from Galactic sources are expected to have a break before ∼PeV energies, as there are no known Galactic sources than can accelerate protons to these high energies. The searches of chapters 6 and 7 look for unbroken power law spectra, with the spectral index as a free parameter of the search. Where specific flux predictions are available based on theoretical considerations or γ-ray observations, sensitivities and discovery potentials are expressed in relation to these predictions.

Part II

Part 2 : Searches for the sources of Astrophysical Neutrinos

Chapter 4

The Unbinned Maximum Likelihood Ratio method to find Point Sources of Neutrinos

4.1 Introduction

This chapter reviews the methods used to quantify statistically significant clustering of events of a specific spectra within samples of IceCube events. The basic unbinned maximum likelihood based method is revisited and generalized to scenarios involving non stationary sources and event samples with very poor angular resolution. This method is later used in chapter 5 to look for signals from DM annihilating within the Sun. Subsequently, the modifications to the method to look for spatially extended sources are discussed, followed by the stacking method, used in chapters 6 and 7 to look for astrophysical neutrinos from multiple sources simultaneously. The method used to look for periodic signals, used in 6 is also discussed. Finally, methods for setting frequentist confidence intervals on the signal are discussed. The classical approach of Neyman[135] and the unified approach of Feldman and Cousins[136] used within this work for the Point Source and DM searches respectively, are compared and contrasted.

4.2 The Point Source Method

A point source of astrophysical neutrinos can be identified in a sample by looking for a statistically significant cluster of high energy events using the unbinned maximum likelihood ratio method [137].

For a given direction in the sky $\vec{r}_j$, the data can be described by two hypotheses:

H_0 - **The data consists of events from atmospheric muons and/or neutrinos only**: Under this hypothesis, all events are expected to be distributed uniformly within each declination band. The distribution of the values of the energy estimator E of these events can be indicated by $P(\delta_i, E|\phi_{atm})$ which also accounts for the declination dependence of the energy response of the detector. The background probability distribution can then be expressed as:

$$\mathcal{B}(\vec{r}_i, E_i) = B(\delta_i) \times P(\delta_i, E_i|\phi_{atm}) \tag{4.1}$$

and can be constructed in its entirety using real experimental data that has been randomized in right ascension (r.a.).

H_s - **The data is described by atmospheric muon and/or neutrino events as well as astrophysical neutrino events produced by a source of power law spectral index γ and a specific strength** : While the atmospheric neutrino and muon events are expected to follow the same distribution as in the case of H_0 - spatially and in energy, the additional events from an astrophysical source are expected to be clustered around the direction of the source according to the Gaussian distribution:

$$S_i^j = \frac{1}{2\pi(\sigma_i^2)} e^{-\frac{\theta_{|\vec{r}_i-\vec{r}_j|}^2}{2\sigma_i^2}} \tag{4.2}$$

where σ_i is the angular resolution of event i and $\theta_{|\vec{r}_i-\vec{r}_j|}$ is the angle between the direction $\vec{r}_i$ of event i and the direction $\vec{r}_j$ of source j. The distribution of the values of the energy estimator E of these astrophysical events can be indicated by $\mathcal{E}(\delta_i, E_i|\gamma)$ and can be constructed from Monte Carlo simulations of the signal. Thus the signal probability distribution for a source of power law spectrum of index γ is:

$$\mathcal{S}(\vec{r}_i, \vec{r}_j, E_i, \gamma) = S_i^j \times \mathcal{E}(\delta_i, E_i|\gamma) \tag{4.3}$$

For a sample of N events consisting of n_s signal events from a source j at $\vec{r}_j$ and $N - n_s$ background events, the likelihood can then be written as:

$$\mathcal{L}(\vec{r}_j, n_s, \gamma) = \prod_N (\frac{n_s}{N}\mathcal{S}_i + (1 - \frac{n_s}{N})B_i) \tag{4.4}$$

The log of the ratio of the likelihoods of obtaining the observed data under each of these hypothesis serves as the test statistic:

$$TS = -2 \times \log[\frac{P(\text{Data}/H_0)}{P(\text{Data}/H_S)}] \tag{4.5}$$

The number of signal events n_s and the source spectral index γ are unknown. However, the best estimate of these two parameters for given data can be obtained by maximizing the likelihood $\mathcal{L}$. Computationally, this can be performed by minimizing the quantity $-log(\mathcal{L})$ using the MIGRAD minimizer available in MINUIT [138] with respect to the unknown quantities n_s and γ. The test statistic then is:

$$TS = 2 \times log[\frac{\mathcal{L}(\vec{r}_s, \hat{n}_s, \hat{\gamma})}{\mathcal{L}(\vec{r}_s, n_s = 0)}] \qquad (4.6)$$

where $\hat{n}_s$ and $\hat{\gamma}$ are the best fit values of n_s and γ respectively.

The significance of an observation can be estimated by repeating the process on datasets randomized in r.a. and computing the fraction of randomized samples that produce a value of the TS bigger than that observed in actual data.

4.3   Generalization to all Angular Resolutions and Spectra

The spatial signal p.d.f. of equation. 4.2 is the expression for a radially symmetric Gaussian on a planar surface and its normalization is such that:

$$\int_0^\infty \frac{1}{2\pi(\sigma_i^2)} e^{-\frac{\theta^2_{|\vec{r}_i - \vec{r}_j|}}{2\sigma_i^2}} d\theta = 1 \qquad (4.7)$$

However, $\theta_{|\vec{r}_i - \vec{r}_j|}$ cannot be larger than π (corresponding to diametrically opposite directions). Thus the true normalization of 4.2 is smaller than 1. Nevertheless, for small values of σ_i, (the angular resolutions of the events in IceCube point source searches are typically $< 1°$) the difference is very small and this extremely small difference in normalization makes no difference to the sensitivity.

But when looking for clustering in samples of IceCube events near the lower energy threshold of IceCube-DeepCore such as the samples in the Solar WIMP analysis of chapter 5, the angular uncertainties of the events can be as bad as $60°$ (see Fig 5.26). Consequently, a spatial p.d.f. of the form:

$$\mathcal{K}_i^j = \frac{\kappa_i e^{\kappa_i cos(\theta_{|\vec{r}_i - \vec{r}_j(t_i)|})}}{2\pi(e^{\kappa_i} - e^{-\kappa_i})} \qquad (4.8)$$

is preferred. This is the Fisher Bingham distribution [139], the generalization of a Gaussian distribution to directional statistics. The concentration factor κ_i is obtained from the angular uncertainty of the event σ_i, by solving the expression $1 - \kappa\sigma^2 = e^{-2\kappa}$ numerically. At small angles, this reduces to

$\kappa = \sigma^{-2}$. The position of the source $\vec{r}_j$ is allowed to vary with time in equation 4.8 to keep track of sources which are not stationary in equatorial coordinates, such as the Sun.

In general, the spectrum need not be a power law in energy and the energy p.d.f. $\mathcal{E}(E_i|\gamma)$ of equation 4.3 can be replaced with any energy p.d.f. derived from Monte Carlo reweighted to a theoretical flux.

4.4 Extended Sources

A search for spatially extended sources can be carried out by modifying the signal p.d.f. to incorporate the shape of the source. If the shape can be approximated with a circular Gaussian profile, this can be achieved by replacing σ_i of Eq 4.2 with $\sigma_i^{effective} = \sqrt{(\sigma_i^2 + \sigma_j^2)}$ where σ_j is the width of the source j. In practice due to the limited angular resolution of IceCube, the circular Gaussian profile serves as a good approximation for all extended sources.

For a truly extended source, a search employing the true extension of the source in likelihood has been shown to perform better than a search looking for a point source [140].

4.5 Time Dependence or Periodicity

A source with a time varying signal offers the opportunity to use event arrival times to better distinguish signal from background. In case of a search for a periodic signal from a source with a known period T, the event times t_i are converted to event phases ϕ_i using the relation:

$$\phi_i = \frac{\mathcal{F}_{mod}(t_i - T_0, T)}{T} \tag{4.9}$$

where $\mathcal{F}_{mod}(a, b)$ is function which returns the floating point remainder of a/b and T_0 is an arbitrary reference in time that sets the overall phase of the signal. As illustrated in Fig 4.1, signal events from different cycles get nearby values of ϕ_i and events from many weak periodic flares add up to produce one strong flare in phase space.

Subsequently the source signal is described by including a time/phase p.d.f. $\mathcal{T}_i^j/\phi_i^j$ along with the spatial and energy p.d.f.s of equation 4.3. This is used in case of the periodic search of chapter 6, where the signal p.d.f. $\mathcal{S}(\vec{r}_i, \vec{r}_j, E_i, \gamma)$ in equation (4.3) is multiplied with a phase dependence $\mathcal{P}_i^{\text{signal}}$ of the form::

$$\mathcal{P}_i^{\text{signal}}(\Phi_j, \sigma_{\Phi,j}) = \frac{1}{\sqrt{2\pi}\sigma_{\Phi_j}} exp\left(-\frac{(\phi_i - \Phi_j)^2}{2\sigma_{\Phi,j}^2}\right), \tag{4.10}$$

FIGURE 4.1: The function $\mathcal{F}_{mod}$ in equation 4.9 has the property that $\mathcal{F}_{mod}(t_i - T_0, T) = \mathcal{F}_{mod}(t_i + T - T_0, T)$. Consequently, various weak flares from different cycles of the source (left) add up to produce one stronger flare in phase space (right).

Here, Φ_j is the phase at which the flare of the source j peaks, while $\sigma_{\Phi,j}$ is the width of the flare in the phase space. Since both parameters are unknown, they can be made free to float in the likelihood maximization.

A background phase p.d.f. uniform in phase space has to be added to the background p.d.f. 4.1. When a likelihood of the form Eq. 4.4 is constructed using these p.d.f.s (with Φ_j and $\sigma_{\Phi,j}$ as additional free parameters) and maximized as explained in section 4.2, the minimizer was found to favour extremely short flares, due to effective trials factor from the fact that during a given period, more independent shorter flares are possible compared to longer ones. As a result, a test statistic of the form:

$$TS = -2 \log \left[\frac{1}{\sqrt{2\pi}\hat{\sigma}_\Phi} \times \frac{\mathcal{L}(n_{\mathrm{s}} = 0)}{\mathcal{L}(\hat{n}_{\mathrm{s}}, \hat{\gamma}_{\mathrm{s}}, \hat{\sigma}_\Phi, \hat{\Phi})} \right], \tag{4.11}$$

is employed where $1/\sqrt{2\pi}\hat{\sigma}_\Phi$ is a marginalization term which penalizes extremely short flares.

4.6   Stacking of Multiple Sources

A class of sources of similar spectral behavior that are individually too weak to be detected by the above method can still be detected by the stacking technique. The signal p.d.f. of Eq. 4.3 is modified by breaking it into a sum over all the stacked sources.

$$\mathcal{S}_i^{tot} = \frac{\sum\limits_{j=1}^{N_s} W_j R_{\mathrm{IC}}(\delta_j, \gamma) \mathcal{S}_i^j}{\sum\limits_{j=1}^{N_s} W_j R_{\mathrm{IC}}(\delta_j, \gamma)}, \tag{4.12}$$

where

$$\mathcal{S}_i^j = \frac{1}{2\pi(\sigma_i^2 + \sigma_j^2)} e^{-\frac{|\vec{r}_i - \vec{r}_j|^2}{2(\sigma_i^2 + \sigma_j^2)}} \mathcal{E}_i(E_i, \delta_i, \gamma) \qquad (4.13)$$

is the single source p.d.f. of event i with respect to the source j and $R_{\mathrm{IC}}(\delta_j, \gamma)$ is the detector acceptance at the declination of source j for a flux of spectral index γ. N_s is the number of sources stacked in the analysis. A prior knowledge of the expected relative flux contribution from these sources can be utilized to weight the contribution of each source in the total p.d.f. (the term W_j) to make the search optimal for that signal hypothesis. The sources are assumed to have the same spectral behaviour and consequently the stacking method is best applied to sources of the same type.

4.7 Combining Data Samples

Independent non overlapping samples of events can be combined statistically using the combined likelihood:

$$\mathcal{L}(n_s) = {}^1\mathcal{L}({}^1n_s) \times {}^2\mathcal{L}({}^2n_s) \times {}^3\mathcal{L}({}^3n_s)... \qquad (4.14)$$

where $n_s = {}^1n_s + {}^2n_s + {}^3n_s...$ and ${}^i\mathcal{L}({}^in_s)$ is the likelihood function for the independent sample i as defined in equation 4.4. The parameters ${}^in_s$ are not independent, but are related to each other by the signal hypothesis. For a steady source, this relationship is of the form:

$$^in_s = n_s \frac{{}^iT_{live}{}^iV_{eff}}{\sum_j {}^jT_{live}{}^jV_{eff}} \qquad (4.15)$$

where ${}^iT_{live}$ and ${}^iV_{eff}$ is the livetime and effective volume of sample i. In this way, samples of different properties and even experiments can be combined into one single hypothesis test.

4.8 Confidence Intervals

In addition to quantifying the statistical significance of the observation, it is desirable to provide 90% confidence intervals on the true signal content $\mathcal{N}_s$. The objective is to find an interval $[n_{s1}, n_{s2}]$ such that

$$P(\mathcal{N}_s \in [n_{s1}, n_{s2}]) = 90\% \qquad (4.16)$$

If the choice is not to be influenced by the data $\hat{n}$, two kinds of 90% confidence intervals can be defined. The upper limit, defined by

$$P(\mathcal{N}_s > n_{s2}) = 10\%$$ (4.17)

and the central interval, defined by

$$P(\mathcal{N}_s > n_{s2}) = P(\mathcal{N}_s < n_{s1}) = 5\%$$ (4.18)

4.8.1 The classical method of Neyman

Following the classical method of Neyman[135], it is not prescribed whether to present upper limits or central intervals. The intuitive thing to do is to present upper limits in the absence of a statistically significant signal, or present a central interval if the observed signal is found to reject the null hypothesis at a threshold significance (say $>5\sigma$).

Upper Limit : For each value of $\mathcal{N}_s$, 3000 scrambled trials are performed with $\mathcal{N}_s$ additional events injected into the sample. The value of $\mathcal{N}_s$ for which the 90% of the time the TS is greater than the observed $\widehat{TS}$ is the 90% C.L upper limit.

Sensitivity : The sensitivity is similar to the upper limit, but is defined with respect to the median of the TS values observed in scrambled trials with no signal injected, TS^{med}, instead of the observed $\widehat{TS}$. In other words, it is the median upper limit.

Within this work, the searches for point sources of neutrinos presented in chapters 6 and 7 employ upper limits as defined by the classical method of Neyman.

4.8.2 The unified method of Feldman & Cousins

The method of choosing between upper and central limits described in the above section leads to undercoverage for certain values of the actual measurement, as noted by Feldman and Cousins [136]. The ordering principle proposed by them for summing up the regions of the parameter space automatically produces a central limit for significant signals and an upper limit for observations consistent with the background. It also ensures the correct coverage for all observations. The ordering is based on the rank $\mathcal{R}$, given by

$$\mathcal{R}(\mathcal{N}) = \frac{\mathcal{L}(\mathcal{N}_s, ...)}{\mathcal{L}(\hat{n}_s)}$$ (4.19)

Since $\hat{n}_s$ is the value of n_s for which $\mathcal{L}$ is maximum, $\mathcal{R}$ is always smaller than one. In practice we prefer to work with $ln(\mathcal{R}(\mathcal{N}))$, an always negative quantity. The critical value $ln(\mathcal{R}^{90\%C.L.}(\mathcal{N}))$ for

each value of $\mathcal{N}$ is calculated by performing 1000 scrambled trials with $\mathcal{N}$ signal events injected. The median of the 10% quantiles of $\mathcal{R}(\mathcal{N})$ for each value of $\mathcal{N}$ forms the critical region.

Limits : The values of $\mathcal{N}$ for which the $\mathcal{R}_{true}(\mathcal{N})$ is above the critical region forms the 90% confidence region on $\mathcal{N}$. If $\mathcal{N} = 0$ is included in this region, the limit can be considered an upper limit.

Sensitivity : 10000 scrambled trials are performed with no signal injected. The median value of the 10% quantile of $\mathcal{R}(\mathcal{N})$ is the sensitivity.

Within this work, the search for neutrinos from DM annihilations in the sun presented in chapter 5 uses the unified method of Feldman and Cousins to set confidence regions.

Chapter 5

Search for Dark Matter Annihilations in the Sun using data from 3 years of operation of the completed IceCube-DeepCore detector

5.1 Introduction

This chapter describes the search that was performed for neutrinos from DM annihilations in the Sun with 3 years of IceCube data. The signal simulation is described, followed by the different steps of background rejection cuts that go into obtaining the analysis level samples. Subsequently, the analysis method is dealt with, followed by the results obtained on unblinding.

5.2 Signal Simulation

5.2.1 Neutrino Fluxes

The predictions for neutrino fluxes at Earth from WIMP annihilations in the Sun are obtained using the `WimpSim` code[51]. This code uses Pythia 6.4 to simulate the hadronization and decay of annihilation products and collect the neutrinos and antineutrinos produced. For channels such as $b\bar{b}$ which hadronize to produce B mesons and subsequently interact before they decay, these interactions are simulated in an approximate fashion by performing the Pythia simulations as if in free space and then rescaling the energy of the resulting neutrinos to account for the energy loss of the B mesons due to their interactions.

The resultant neutrinos as they propagate towards the Earth can oscillate as well as interact with the different nuclei inside the Sun. The CC and NC interaction cross sections are calculated using the expressions in ref. [141] using the CTEQ-6 DIS Parton Distribution Functions. The WimpEvent Monte Carlo code, a module of `WimpSim` simulates all neutrino nucleon interactions within the Sun and returns the energy and angles of the final state lepton as well as the hadronic shower. The resultant predictions have been shown to be more accurate than that of Pythia, particularly at low momentum transfer Q^2.

Neutrino oscillations, both within the Sun and as they propagate in vacuum towards the Earth are simulated using a full 3 flavour Monte Carlo approach. At these energies in the Sun, neutrino propagation is not adiabatic[51], and the mass eigenstates are not decoherent[25]. Consequently, oscillation probabilities are treated on an event by event basis rather than as energy spectra for different mass eigenstates. The densities of different nuclei within the Sun for all calculations are obtained from the Standard Solar Model. Figure 5.1 illustrates the differential neutrino fluxes at Earth expected for a few select annihilation scenarios.

Subsequently, neutrino interactions within the glacial ice at the South Pole are simulated by WimpEvent. Thus each WimpSim output is an event corresponding to an annihilation process that results in a neutrino. It contains the directional and energy information of the final lepton, the hadronic shower, as well as the incoming neutrino. The interaction vertices of these events are randomly placed inside a cylindrical Volume V_i, the size of which is dependent on the muon range.

Due to the wide variety of WIMP models predicting a very diverse scenario of standard model branching ratios in pair annihilation, this work considers scenarios that envelop the extremes. WIMPs annihilating 100% into $b\bar{b}$s, a scenario in which the neutrino emission peaks at energies much below the WIMP mass is considered in addition to 100% annihilation into W^+W^- and $\tau^+\tau^-$, channels in which the neutrino emission is peaked at energies close to the WIMP mass. The neutrino channels are even harder than $\tau^+\tau^-$, and the gg channel is softer than $b\bar{b}$. However, direct annihilation to either of these channels is suppressed in most real theories of DM.

5.2.2 Detector Simulation

The charged particles produced by `WimpSim` are propagated through ice, accounting for stochastic and continuous energy losses using the Muon Monte Carlo (MMC) code. The photons emitted from these particles are propagated within the ice using clsim, an OpenCL-based photon tracking simulation using a ray tracing algorithm that models the scattering and absorption of light in the deep glacial ice. Clsim overcomes the limitations of earlier photon tracking algorithms such as photonics and PPC, such as binning artefacts and large memory requirements.

Subsequently, the icetray simulation framework constructs IceCube hits from photons that were propagated by clsim, accounting for the quantum efficiency of the PMT as well as the effective DOM
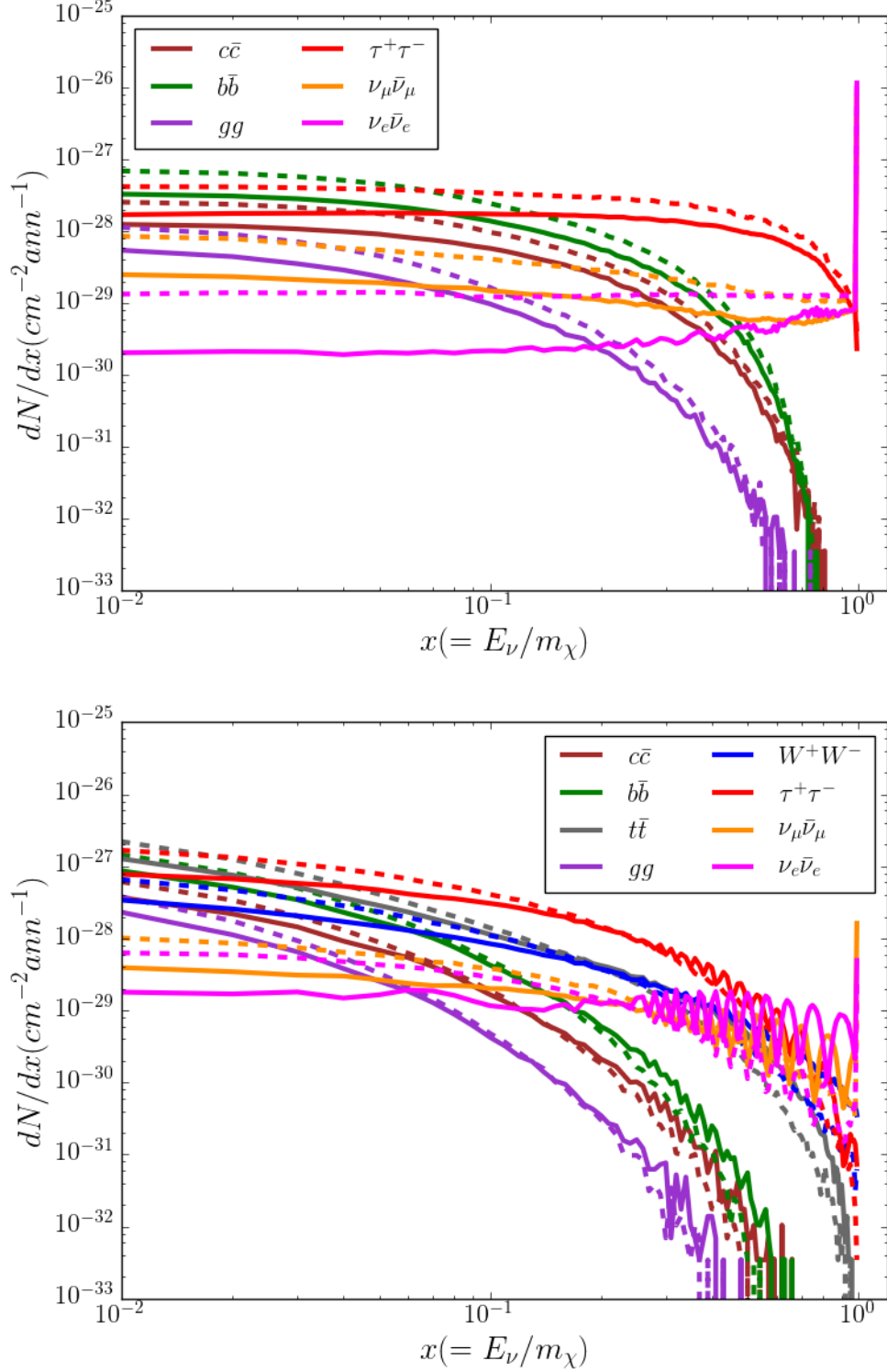
FIGURE 5.1: ν_μ (solid lines) and $\bar{\nu}_\mu$ (dashed lines) fluxes at Earth as a function of the ratio of the neutrino energy and WIMP mass, for selected channels at Earth. The sharp peaks at $E_\nu/m_\chi = 1$ for the $\nu_\mu\bar{\nu}_\mu$ and $\nu_e\bar{\nu}_e$ channels correspond to the primary neutrinos from the annihilation that escape the Sun without interacting, while the neutrinos at lower energies come from the interactions of some of these primary neutrinos for these channels. The top and bottom plots correspond to WIMPs of mass 50 GeV and 1 TeV respectively. $\nu_\mu\bar{\nu}_\mu$ and $\nu_e\bar{\nu}_e$ channels produce a comparable number of ν_μ and $\bar{\nu}_\mu$ due to the maximal 1-2 mixing from MSW resonance in the Sun.

area. Additionally, pulses associated with dark noise, correlated noise, pre pulses and afterpulses are also created according to probabilities based on empirical studies of these processes. Responses of the PMT and the digitization hardware on board the DOM are simulated, following which IceCube trigger logic is applied and the event is treated just as if it were an event from experimental data.

5.3 Analysis Strategy

Dark Matter annihilations at the centre of the Sun can cause the Sun to appear as a point source of neutrinos. The analysis strategy consequently is to look for an excess of neutrinos in the direction of the Sun. Since the expected energy range of the signal is $\lesssim 1\text{TeV}$, this would be a very low energy point source analysis by the standards of IceCube.

The first challenge is then to reduce the background of all events detected by IceCube to a sample/samples of events in the energy range of the signal, indistinguishable from the signal in all except the direction. This is achieved by the event selection process. From the point of view of the topology of events from the Sun observed at IceCube, the data taking period of IceCube can be divided into two, the Austral Summer (AS) when the Sun is above the horizon and a source of downgoing signal neutrinos, and the Austral Winter (AW) when the Sun is below the horizon and a source of upgoing signal neutrinos.

Muons created in cosmic ray interactions in the Earth's atmosphere form the dominant background during the AS, and they are indistinguishable from muons created in ν_μ CC interactions of signal neutrinos taking place in the ice above the detector. A sample of pure ν_μ induced muon events can be obtained by using the outer layers of the detector as a veto to restrict the selection to only events from interactions taking place within a specific detector volume. While this sacrifices the detector effective volume in most of the IceCube energy range, for signals that are below the IceCube threshold ($\sim 100\text{GeV}$) but above the DeepCore threshold ($\sim 10\text{GeV}$), the effective volume comes only from the DeepCore sub array and can be preserved. In addition to lower background, a sample of events contained within the detector offers the advantage of better energy resolutions.

During the AW, even though muons from the other side of the Earth do not make it through, downgoing muons that are misreconstructed as upgoing form a significant background. They can be rejected only by imposing stricter quality controls on event reconstruction variables and discarding events that are very high in energy. Using these methods, samples of ν_μ induced muon events can be obtained in the ~ 10 to 100 GeV (DeepCore domain) as well as above 100 GeV up to a few TeV (IceCube domain).

Subsequently, the unbinned maximum likelihood ratio method is applied to construct confidence intervals on the number of signal events in the direction of the Sun within the samples.
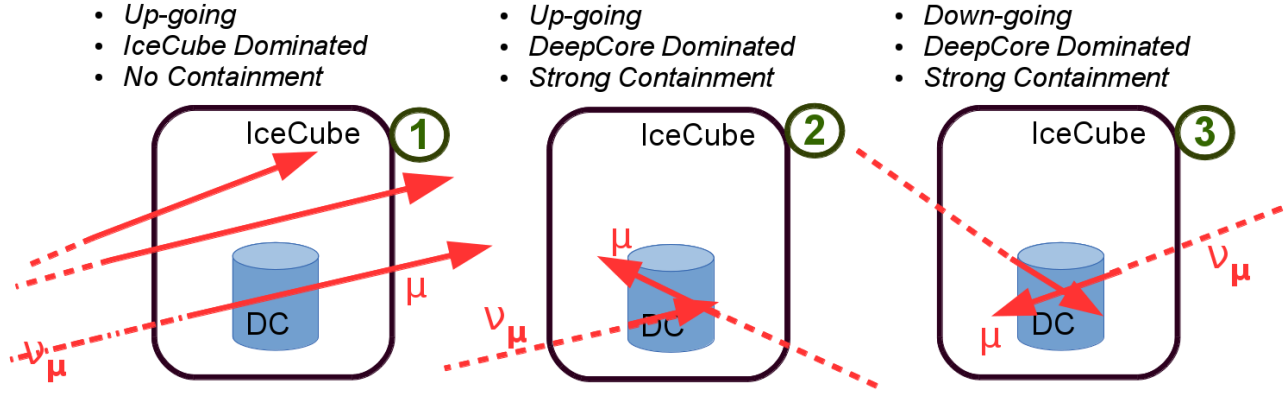
FIGURE 5.2: The three event selection strategies for the solar WIMP analysis. Most of the sensitivity for neutrino signals below 100 GeV comes from the DeepCore (DC) dominated low energy samples(2 and 3). During the austral summer (when the Sun is a source of downgoing neutrinos), the very large muon background forces us to use the outer detector as a Veto (see Fig. 5.20) and consequently there is only a DeepCore dominated-low energy sample (3). This approach is similar to that of earlier IceCube analyses such as [142].

To prevent experimental bias from affecting the result, the actual directions of the events are not examined until the last step. While the event selection steps involve criteria on the zenith, no azimuth dependent cuts are applied. Consequently, this analysis is a blind one [143].

5.4 Event Selection

Event selection begins at the IceCube collaboration wide Level 2, which admits more than 500 Hz of data. Since the rate of directionally well reconstructed atmospheric neutrinos is $\sim$ 3 mHz, the objective of the event selection process is to reduce the data rate by $\sim$ 6 orders of magnitude. Figure 5.3 provides a summary of the different levels of event selection and the rates at various levels.

Due to the very different natures of the dominant backgrounds during AW and AS, starting at Level 2, data acquired during these two periods are treated differently. AS is defined as the period during which the declination of the Sun is $\leq$ 90° in equatorial coordinates and includes the IceCube runs between MJD 55827.39 and 56006.22 (0921 Hrs, 23rd September 2011 to 0517 Hrs, 20th March 2012) during the IceCube 2011 season, MJD 56192.63 and 56371.46 (1507 Hrs, 22nd September 2012 to 1102 Hrs, 20th March 2013) during the IceCube 2012 season and MJD 56557.87 to 56736.71 (2053 Hrs, 22nd September 2013 to 1702 Hrs, 20th March 2014) during the IceCube 2013 season respectively. The remaining runs in these seasons are included in the AW selection. Table 5.1 summarizes the key dates of the various data taking seasons and livetimes.

Data from IceCube runs with run numbers ending in '0' are taken to be the 'Burn Sample'. Variable occupancy distributions at different stages of the event selection are constructed using these data and different background rejection methods are optimized based on these distributions.
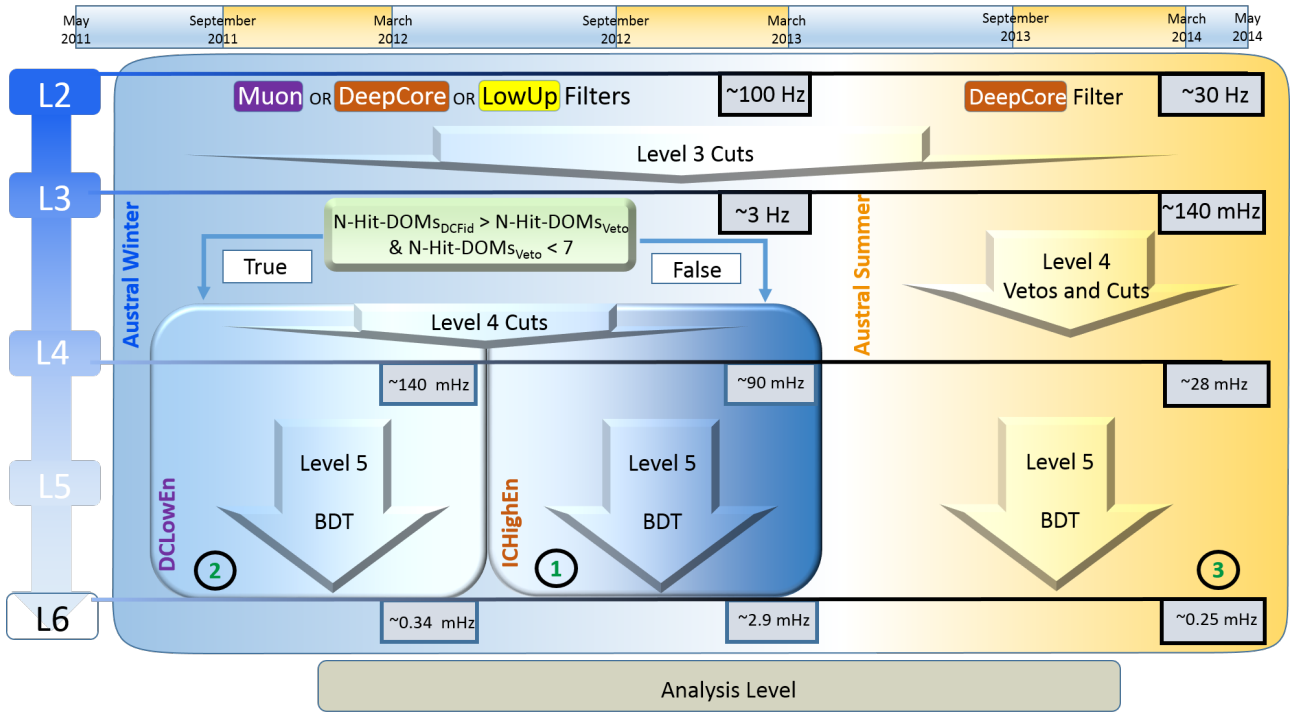
FIGURE 5.3: A diagram summarizing the different levels of the event selection process: Data during austral summer and winter are treated differently. Initial cuts focus on rejecting muons. At Level 3, more time consuming reconstruction algorithms are used to recover more event information.

TABLE 5.1: Summary of the various data taking periods and livetimes

Period	Starting Date(s) [MJD]	Stopping Date(s) [MJD]	livetime(days)
IC86-1 Austral Winter	13/5/2011[55694.42] 20/3/2012[56006.22]	23/9/2011[55827.39] 15/5/2012[56062.42]	177.32
Ic86-1 Austral Summer	23/9/2011[55827.39]	20/3/2012[56006.22]	163.54
IC86-2 Austral Winter	15/5/2012[56062.42] 20/3/2013[56371.46]	22/9/2012[56192.63] 2/5/2013[56414.41]	162.25
IC86-2 Austral Summer	22/9/2012[56192.63]	20/3/2013[56371.46]	162.73
IC86-3 Austral Winter	2/5/2013[56414.41] 20/03/2014[56736.71]	22/9/2013[56557.87] 17/5/2015[56794.01]	188.71
IC86-3 Austral Summer	22/9/2013[56557.87]	20/03/2014[56736.71]	164.50
Total			1019.05

TABLE 5.2: Real data rates as well as signal selection efficiencies (as a fraction of all events at L2) for different signals of interest, for various filter selection criteria for the Austral Winter

Filter Selection	Data Rate(Hz)	$\chi\chi(50GeV) \to b\bar{b}$	$\chi\chi(100GeV) \to W^+W^-$	$\chi\chi(250GeV) \to W^+W^-$	$\chi\chi(500GeV) \to W^+W^-$	$\chi\chi(1TeV) \to W^+W^-$
LowUp Filter	35.4	65.1%	71.21%	77.4%	82.8%	84.2%
Muon Filter	47.6	10.9%	12.6%	18.2%	21.9%	24.3%
DeepCore Filter	28.8	57.6%	53.1%	38.9%	26.4%	17.9%
Lowup, Muon or DeepCore Filters	108.1	89.5%	91.2%	88.4%	89.7%	93.9%

5.4.1 Austral Winter

Table 5.2 summarizes the data and simulation rates of various signals of interest at IceCube Level 2, during the AW period. Keeping only events that have passed one among the LowUp filter, the Muon Filter or DeepCore filter reduces the event rate to ∼100 Hz, while preserving more than 90% of all simulated signal events in the entire range of interest. Consequently it becomes computationally affordable to carry out the following processing:

5.4.1.1 Level 2 additional processing

HiveSplitting: This algorithm splits events triggered with a coincident muon into separate events, allowing future event selection steps to distinguish between the two.

SPE Pandel Fit, 4 iterations: More iterations of the SPE Pandel reconstruction using both HLC and SLC pulses improve the angular resolution of the events, allowing future event selection steps to cut harder in direction to reject background.

FiniteReco: This reconstruction identifies the interaction vertex of events starting within the detector. Since the range of muons below 100 GeV is of the order of the size of the detector, the reconstruction serves as a valuable tool in future steps of background rejection.

This stage, consisting of all events at the collaboration wide Level 2 with the above additional processing, is referred to as Level 2w.

5.4.1.2 Level 3 Cuts

The objective of Level 3 cuts is to reduce the ∼ 100 Hz of data at Level 2w further to ∼ 3 Hz, so that more computationally intensive algorithms can then be applied. Since the selection criteria and hence the preferred event topologies of the three filter streams are different, the cuts were optimized separately on each stream. Table 5.3 summarizes the IceCube event variables used within the event selection and their definitions.

Since some events are classified into more than one streams, the following more stringent criteria were used.

DeepCore Filter and NOT(Muon Filter or LowUp Filter)   Events that have passed the DeepCore Filter but not the Muon or LowUp filters are low energy events often contained within the DeepCore fiducial volume. Since the interaction vertex is within DeepCore, a significant portion of the total photons detected is often from the hadronic cascade of the interaction and consequently, the angular resolution and reconstruction quality are not particularly good with a simple track hypothesis.

TABLE 5.3: IceCube event variables and definitions. Alternate names for the variables that have been sometimes used in figure labels are given in bold inside square brackets.

N-Hit-$DOMs$	The total number of DOMs with registered hits within the trigger window for an event.[**N_Hit_Doms, NChan**]
N-Hit-$strings$	The total number of strings with registered hits within the trigger window for an event.
Z-$travel$	The average distance of hits from the first quartile of hits $(\sum_i^{N-\mathrm{Hit}-\mathrm{DOMs}}(z_i - \langle z_{1^{st}qartile}\rangle)/N-\mathrm{Hit}-\mathrm{DOMs})$.[**Z_Travel**]
σ_{COG_Z}	The spread of the hit DOMs in the z direction.[**COG_Z_Sigma**]
$\theta_{COG-z_{vertex}}$	The zenith angle of the vector between the Centre of Gravity (COG) and the FiniteReco vertex.[**Cog_z_vertex**]
LLh_{Reco}	The log of the maximum likelihood found by the reconstruction '*Reco*'.
$Reco_{RLogL}$	The reduced log-likelihood. $LLh_{Reco}/(N-\mathrm{Hit}-\mathrm{DOMs}-5)$
$time$-$extension$	The time separation between the first and the last hit within the readout window of an event.[**Time_Ext**]
Z-$extension$	The distance along the z direction between the highest and lowest hits of an event.[**Z_ext**]
$Z_{FiniteReco}$	The z coordinate of the vertex of an event as reconstructed by FiniteReco.[**FiniteRecoFit_Masked_z**]
X-Y-$Radius_{FiniteReco}$	The distance of the vertex of an event as reconstructed by FiniteReco from the centre of IceCube's local coordinate system in the plane.[**FiniteRecoFit_Masked_XY_Radius**]
$LineFit$-$Velocity$	The velocity of the particle as reconstructed by the LineFit algorithm.
$L-Dir_{C\mathrm{orA,B,DorE}}$	Largest distance projected along the direction of the reconstructed track between direct hits of class C(or A, B, D, or E).[**LDir_C**]
N_{Dir}-E **(or** B, C, D, E**)**-$DOMs$	The total number of DOMs with registered hits within the trigger window, within the time residual class A(or B, C, or D).
N_{Dir}-A **(or** B, C, D, E**)**-$pulses$	The total number of hits within the trigger window, within the time residual class A(or B, C, D).
$\sigma_{paraboloid}$	The 1 σ error on the direction of the track as determined by the paraboloid algorithm [45] described in section 1.5.2.6.
$\Psi_{Reco1-Reco2}$	The angle between the directions of the track as determined by the reconstructions *Reco*1 and *Reco*2.
$COG_{X(\mathrm{or Y,Z})}$	X (or Y, Z) coordinate of the centre of gravity of the event.[**COG_X**]
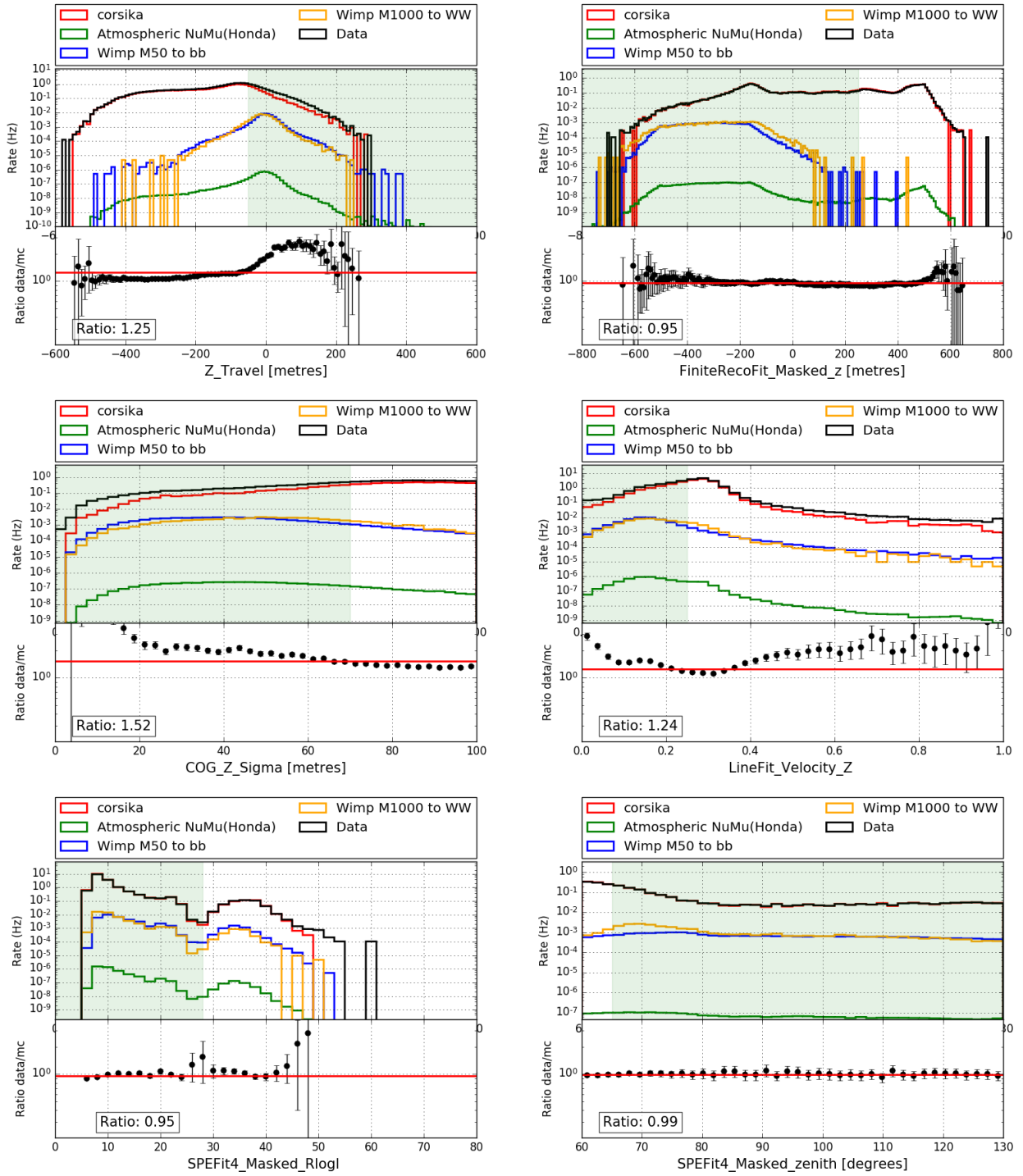
FIGURE 5.4: Distributions of the variables used in level 3 cuts for the 'DeepCore Filter and NOT(Muon Filter or LowUp Filter)' stream before the level 3 cuts. CORSIKA is the atmospheric muon simulation and it closely follows the distribution of data, which is dominated by atmospheric muons at this level. The signal simulations have been scaled arbitrarily for visibility. NuGen, the neutrino simulation, reweighted to follow the atmospheric neutrino spectrum as predicted by Honda et.al. [65] is much lower in rate. The ratio corresponds to the total ratio between data and Monte Carlo within the displayed range of a variable. The discrepancy between data and Monte Carlo at low values of 'COG_Z_Sigma' is due to the lack of noise simulation described in sec. 5.4.2.4. The regions selected by the cuts have been marked in light green shading.
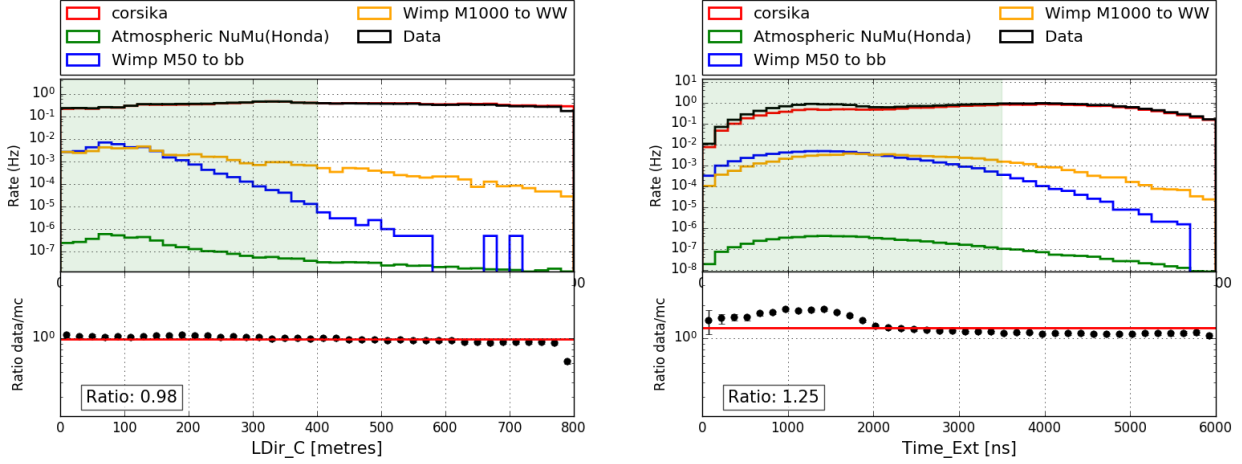
FIGURE 5.5: The rest of the variables used in level 3 cuts for the 'DeepCore Filter and NOT(Muon Filter or LowUp Filter)' stream. The discrepancy between data and Monte Carlo in the variable 'Time_Ext' is due to the lack of correlated noise simulation described in sec. 5.4.2.4.

Consequently, Level 3 cuts on these reconstructed variables cannot be too strict in this stream. Cuts on variables quantifying the statistical distribution of detected photons in space and time are preferred. The following cuts are applied:

1. $Z\text{-}travel \geq -50m$

2. $SPE4_{DC}\text{-}RlogL \leq 28$

3. $65° \leq \theta_{SPE4_{DC}} \leq 165°$

4. $Z_{FiniteReco} < 250m$

5. $\sigma_{COG_Z} < 70m$

6. $L\text{-}Dir_C < 400m$

7. $time\text{-}extension < 3500ns$

8. $LineFit\text{-}Velocity < 0.25$

Figure 5.4 summarizes the distribution of observed data as well as signal and background simulations for the above variables.

LowUp Filter and NOT(Muon Filter)   The LowUp filter favours well reconstructed tracks starting at the bottom of the detector and often extending out of the DeepCore fiducial region. Consequently, the track quality and zenith cuts are more stringent. The following cuts are applied:

1. $Z\text{-}travel \geq -10m$
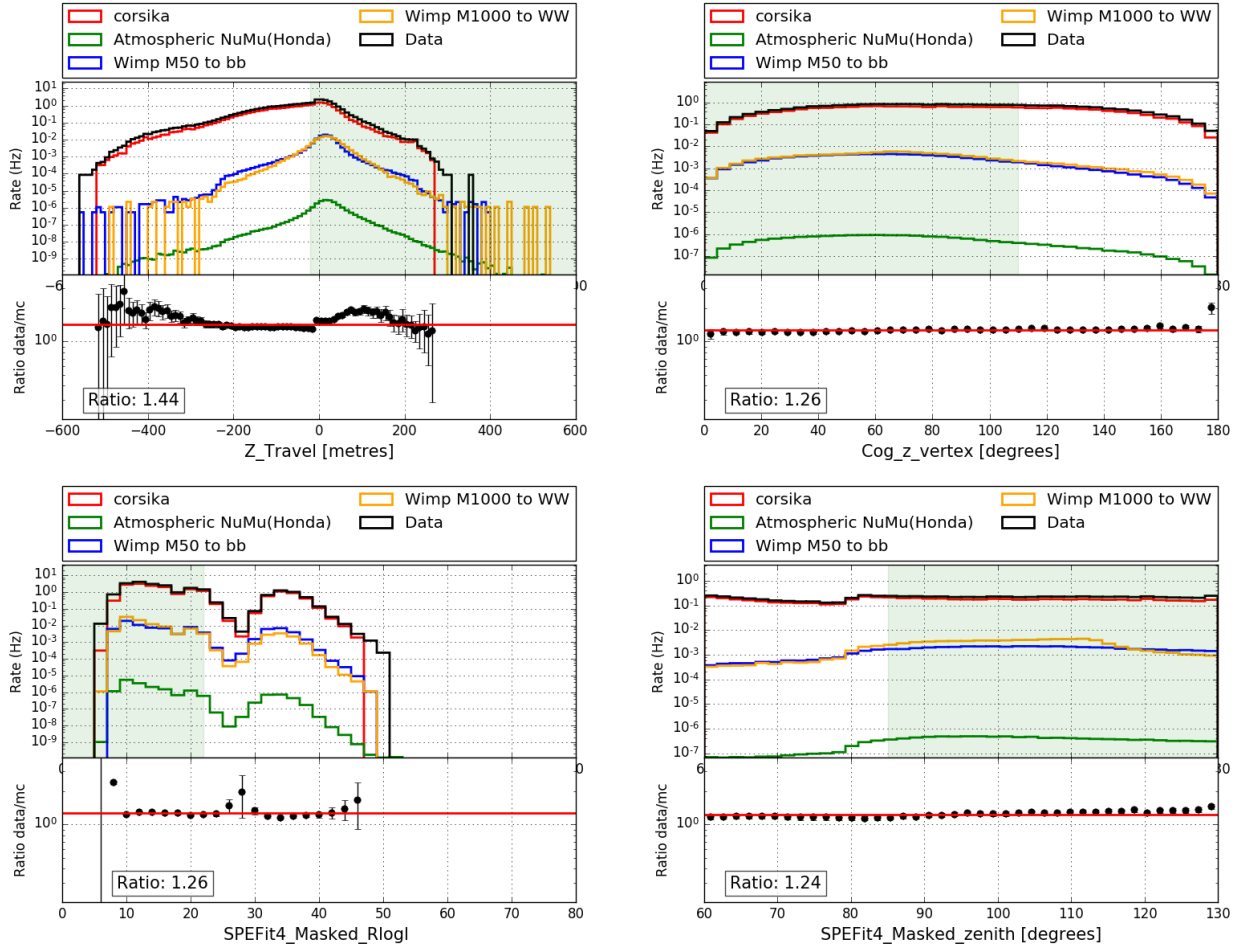
FIGURE 5.6: Similar to Figure 5.4 but for the LowUp Filter and NOT Muon Filter stream.

2. $SPE4\text{-}RlogL \leq 22$

3. $85° \leq \theta_{SPE4} \leq 140°$

4. $\theta_{COG-z_{vertex}} < 110°$

5. $\sigma_{COG_Z} < 110m$

Muon Filter   The Muon filter stream contributes the best reconstructed long tracks in the highest energy range of Solar WIMP signals. The events are mostly through-going muons with hits not confined to any portion of the detector. Reconstruction quality and zenith cuts are consequently more stringent.

1. $Z\text{-}travel \geq -20m$

2. $SPE4\text{-}RlogL \leq 22$

3. $85° \leq \theta_{SPE4} \leq 125°$
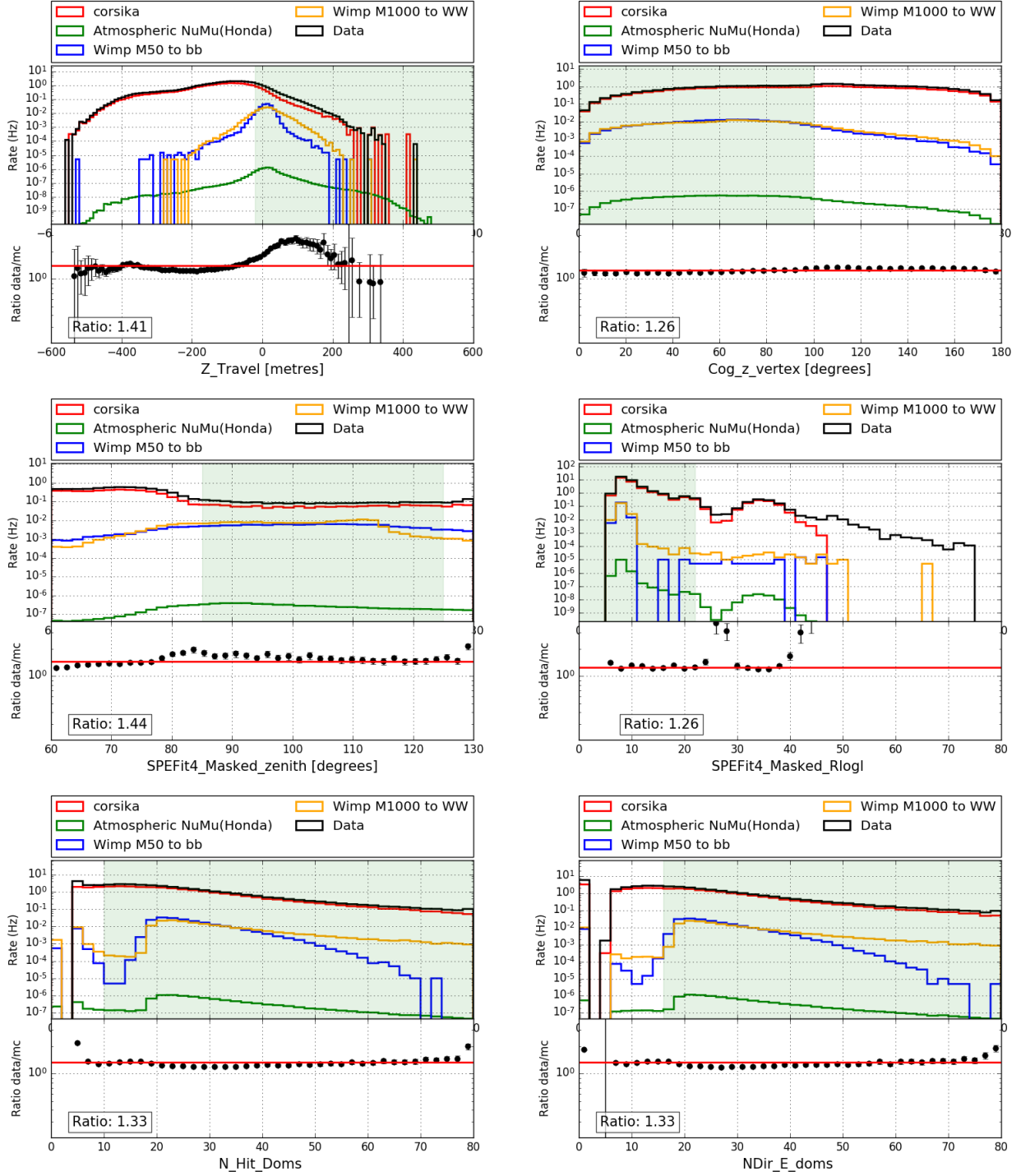
FIGURE 5.7: Similar to Figure 5.4 but for the Muon Filter stream.

4. $\theta_{COG-z_{vertex}} < 100°$

5. $\sigma_{COG_Z} < 110m$

6. $N\text{-}Hit\text{-}DOMs > 10$

7. $N_{Dir}\text{-}E\text{-}DOMs > 16$

The Level 3 Cuts reduce the data rate to ~ 2.8 Hz.

5.4.1.3 Level 3 Processing

Paraboloid Fit on SPE4 : At this stage a Paraboloid fit is performed on the SPE4 track reconstruction to estimate the error on this reconstruction.

4 Iteration Bayesian Fit : This fit uses a Bayesian prior of a down going muon track hypothesis to carry out a likelihood fit on the track reconstruction.

5.4.1.4 Level 4 Split

At this stage, the AW stream of data are split into two non overlapping selections. The requirement for this is dictated by the very different properties of IceCube and DeepCore. Fig 5.8 illustrates the DeepCore fiducial volume based on which an event is classified into one of the two streams. The two streams are:

Winter Low Energy ('DCLowEn') : Events that satisfy the criteria that the number of DOMs inside the fiducial volume with hits is more than those outside and that the total number of DOMs hit outside the fiducial volume is not more than six are classified into this stream. Formally, the cut is $(N\text{-}Hit\text{-}DOMs_{DCFid} > N\text{-}Hit\text{-}DOMs_{Veto})$ AND $(N\text{-}Hit\text{-}DOMs_{Veto} < 7)$

Winter High Energy ('ICHighEn') : Events that do not make it to the DCLowEn stream are classified into this stream.

5.4.1.5 Level 4 Cuts

DCLowEn

1. $\sigma_{paraboloid} < 40°$

2. No Hits within top 10 DOM layers

3. $LLh_{Bayesian}/LLh_{SPE4} < 1.0$
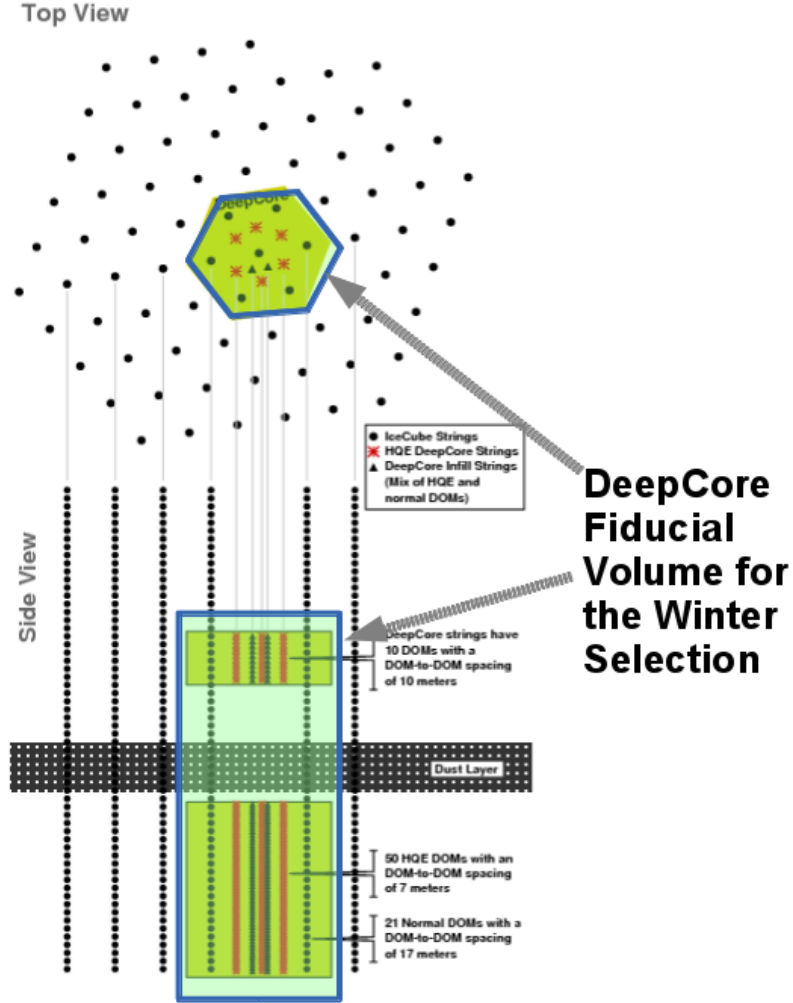
FIGURE 5.8: The austral winter DeepCore fiducial volume: The 8 DeepCore Strings, the 6 Surrounding IceCube strings and one central IceCube string are included.

ICHighEn

1. $\sigma_{paraboloid} < 20°$

2. $SPE4\text{-}RlogL \leq 18$

3. $\Psi_{SPE4-LineFit} < 45°$

4. $N\text{-}Hit\text{-}Strings \geq 3$

5. $InnerStringCriterion$

5.4.1.6 Level 5: Boosted Decision Trees

At this stage, when the DCLowen and ICHighEn streams are at ~ 90mHz and ~ 140mHz respectively, separate instances of a multivariate classification algorithm known as a Boosted Decision Tree(BDT)[144] are employed to quantify how signal-like the event is. A BDT assigns a score in the range of -1.0 to +1.0 to each event based on values of a given set of variables. The BDT is constructed (or 'trained') based on sets of events which consist of signal and background separately. For this purpose the `WimpSim` signal simulation is used as the signal training sample while the Burn Sample of data, which are still background dominated, are taken to be the background training sample.

The best variables upon which the BDT is to be trained are the ones offering maximum signal-background discrimination power. However, variables which are vulnerable to poorly simulated phenomena, which consequently show a high level of Data-Monte Carlo discrepancy are not desired as these variables will cause the BDT to favour unphysical events. It is also preferable that the variables not show a significant amount of correlation among themselves, as this makes the multivariate classification problem more complex. However, if the level of correlation between two variables is considerably different for signal and background, it can contribute towards the separation power.

DCLowEn   For the Winter Low Energy selection, the following variables were chosen:

1. σ_{COG_Z}

2. $\theta_{COG-z_{vertex}}$

3. $Z_{FiniteReco}$

4. $L\text{-}Dir_C$

5. $N_{Dir-B}\text{-}pulses$

6. $N_{Dir-E}\text{-}DOMs$

7. $SPE4\text{-}RlogL$

8. θ_{SPE4}

9. $time\text{-}extension$

10. $N_{Dir-A+B+C}\text{-}strings$

11. $Z\text{-}travel$

For the signal sample, a sum of $\chi\chi(50GeV) \to \tau^+\tau^-$, $\chi\chi(100GeV) \to W^+W^-$ and $\chi\chi(100GeV) \to b\bar{b}$ `WimpSim` signal events were selected. For the background, Burn Sample of data with a livetime of $\sim$12.2 days were chosen. Both samples are randomly split in a 2:1 ratio into training and testing samples respectively.
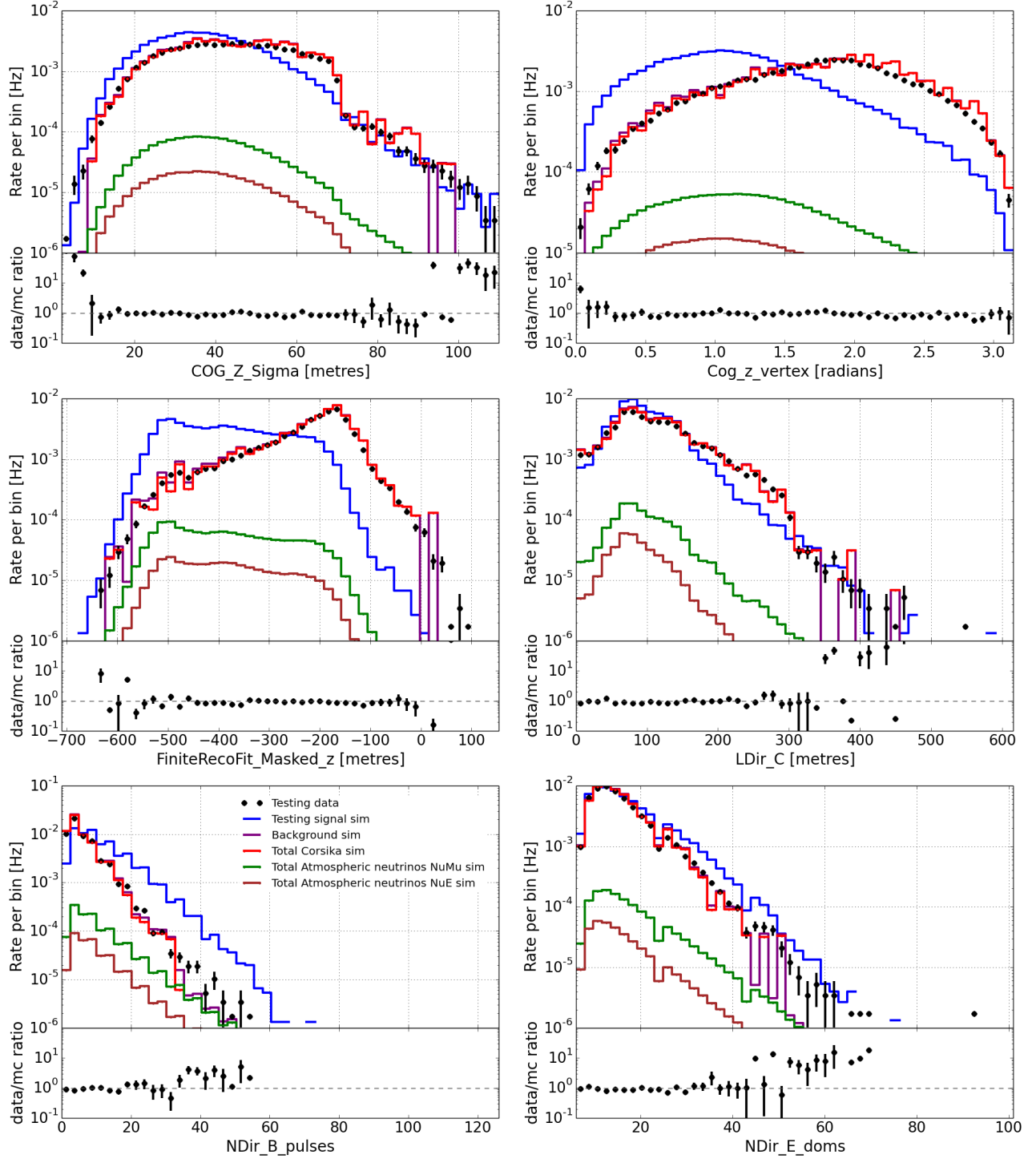
FIGURE 5.9: DCLowEn Stream BDT Variable Distributions 1. The discrepancy between data and CORSIKA at high values of 'Cog_z_vertex' can be attributed to the deficiencies in shower simulation described in sec. 5.4.2.4.
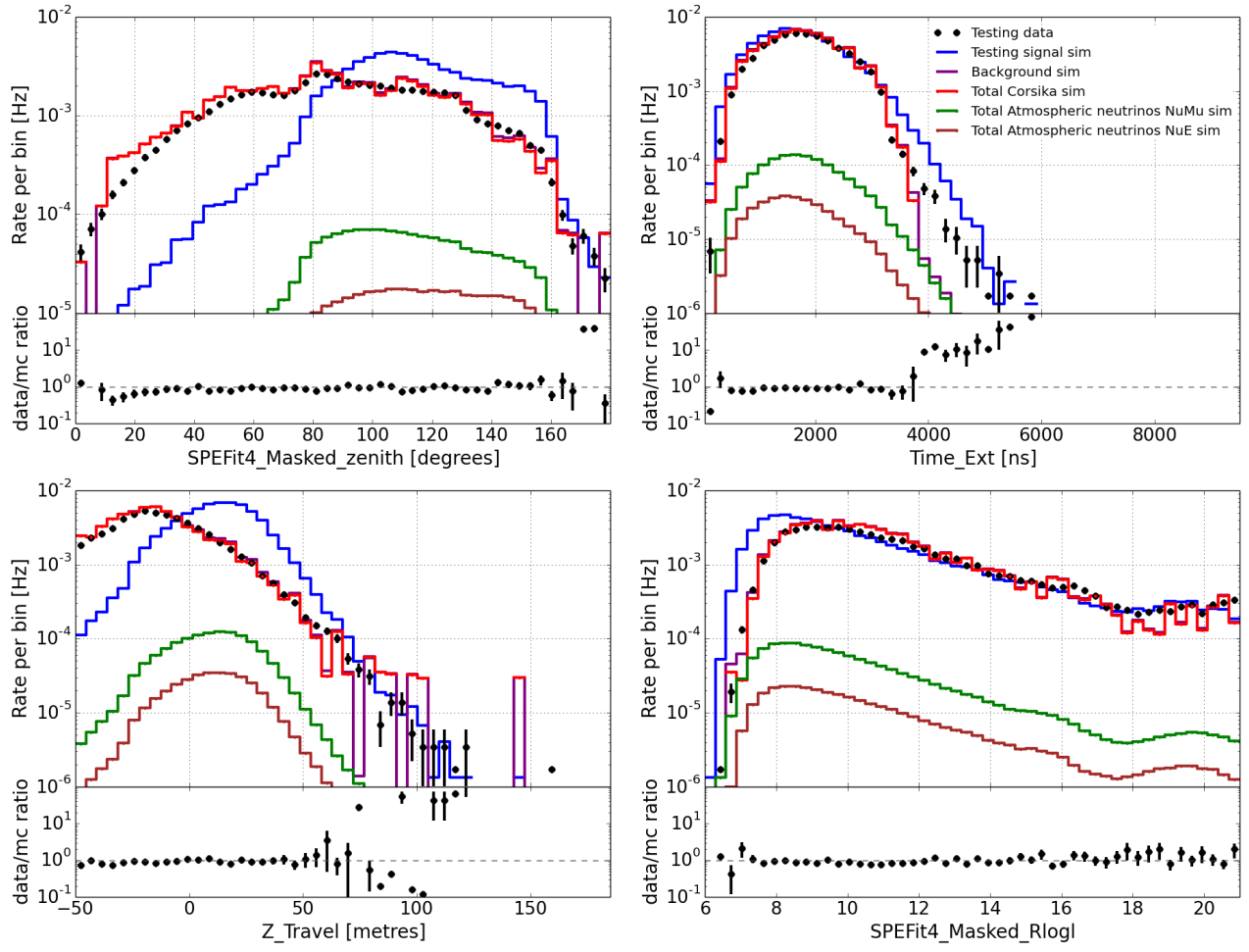
FIGURE 5.10: DCLowEn Stream BDT Variable Distributions 2.
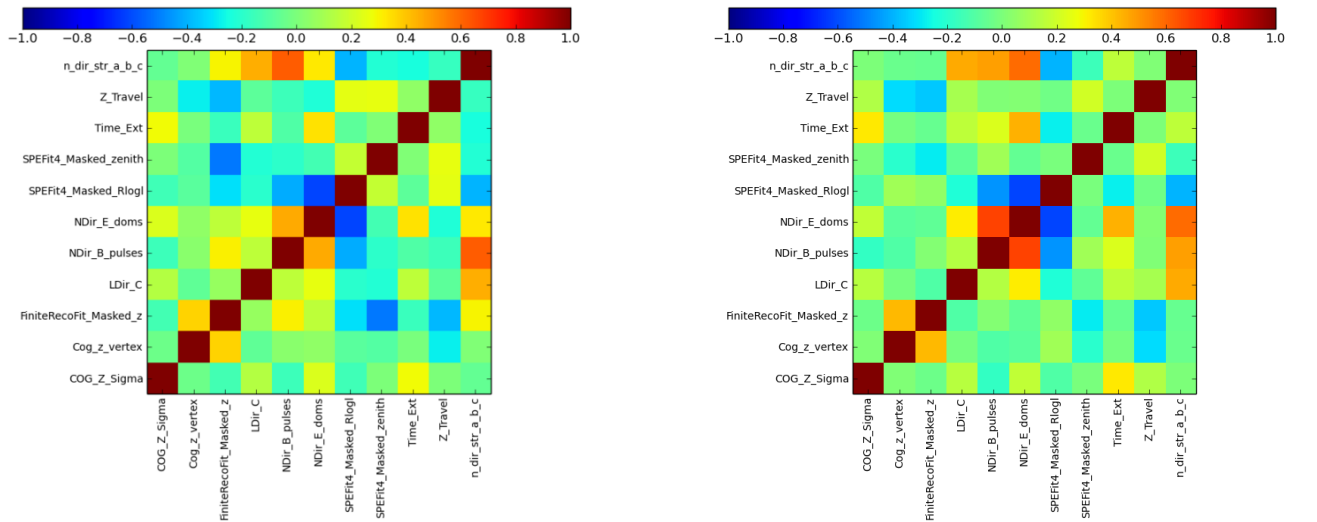
FIGURE 5.11: DCLowEn stream BDT variable correlation matrices: Variables that are highly correlated with each other for signal and background do not offer much separation power and are not desired
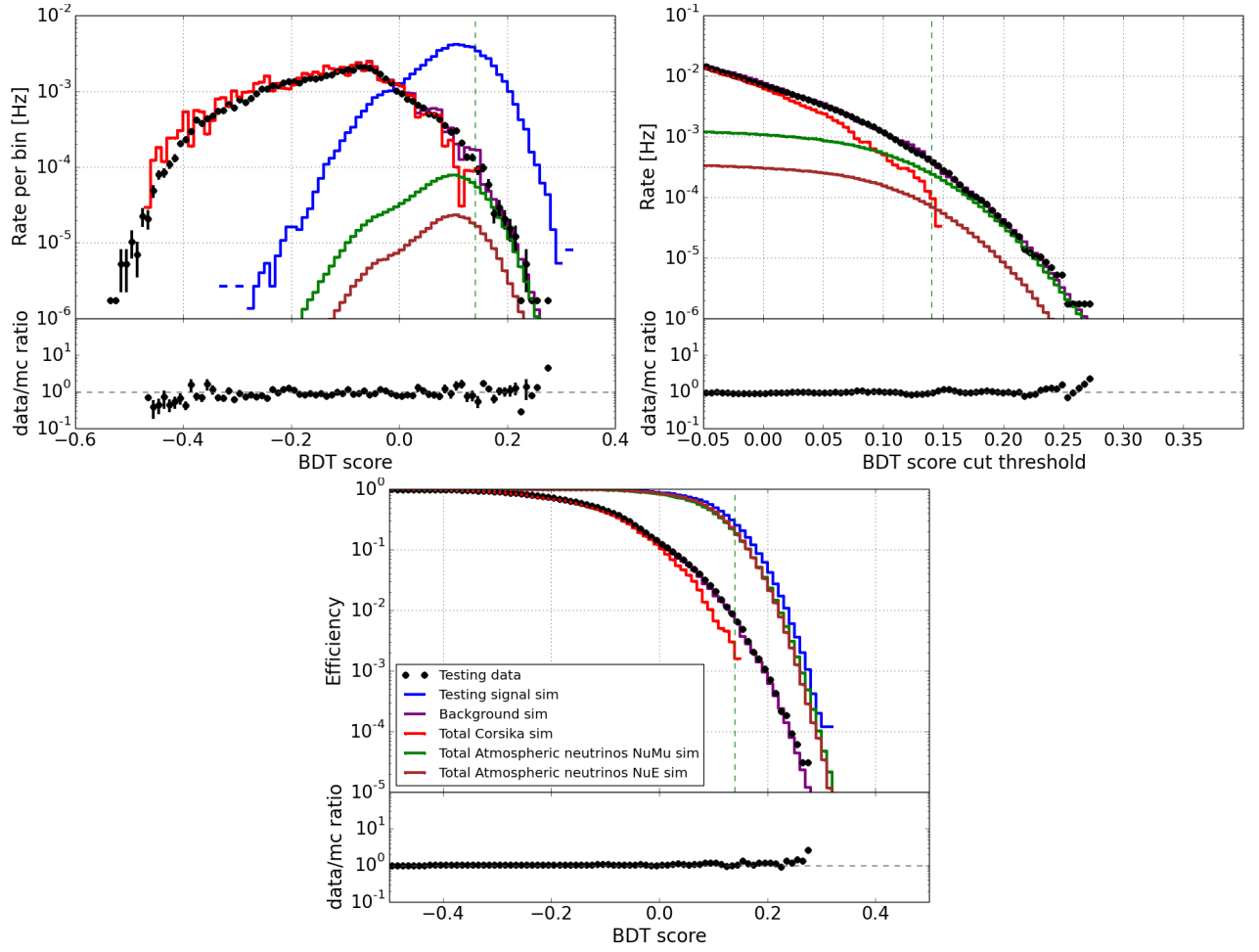
FIGURE 5.12: Top Left : Distribution of the BDT score for the Data Burn Sample, as well as the signal and background Monte Carlos. Top Right: The rate of events that pass the cut for various BDT cut thresholds. Bottom: Efficiency as a function of BDT cut thresholds.

ICHighEn

1. $LLh_{Bayesian}/LLh_{SPE4}$

2. Cog_X

3. Cog_Y

4. Cog_Z

5. σ_{COG_Z}

6. $\theta_{COG-z_{vertex}}$

7. $LLh_{FiniteReco}/N\text{-}Hit\text{-}DOMs$

8. $L\text{-}Dir_C$

9. $N_{Dir-B}\text{-}pulses$

10. N_{Dir-E}-*DOMs*

11. $N_{Dir-A+B+C}$-*strings*

12. $\Psi_{SPE4-LineFit}$

13. *SPE4-RlogL*

14. θ_{SPE4}

15. *time-extension*

16. *Z-travel*

`WimpSim` $\chi\chi(1000GeV) \to W^+W^-$ Monte Carlo events are used as the signal sample while 12.2 days of data Burn Sample are used as the background. As before, the samples are split in a 2:1 ratio into training and testing samples.

Figures 5.9 to 5.17 summarize the distributions of these variables after Level 4 Cuts, their correlations for signal and background, and the distribution of the BDT scores for the training and testing samples separately as well as the Monte Carlo events for the two streams.

5.4.1.7 Analysis Level Processing

At the final analysis level, further reconstructions are applied that were not computationally affordable earlier. For the two streams these are:

DCLowEn

1. SplineMPE

2. PandelMPE

3. SplineSPE, 4 iterations.

4. LEERA

ICHighEn

1. SplineMPE

2. PandelMPE

3. SplineSPE, 4 iterations.
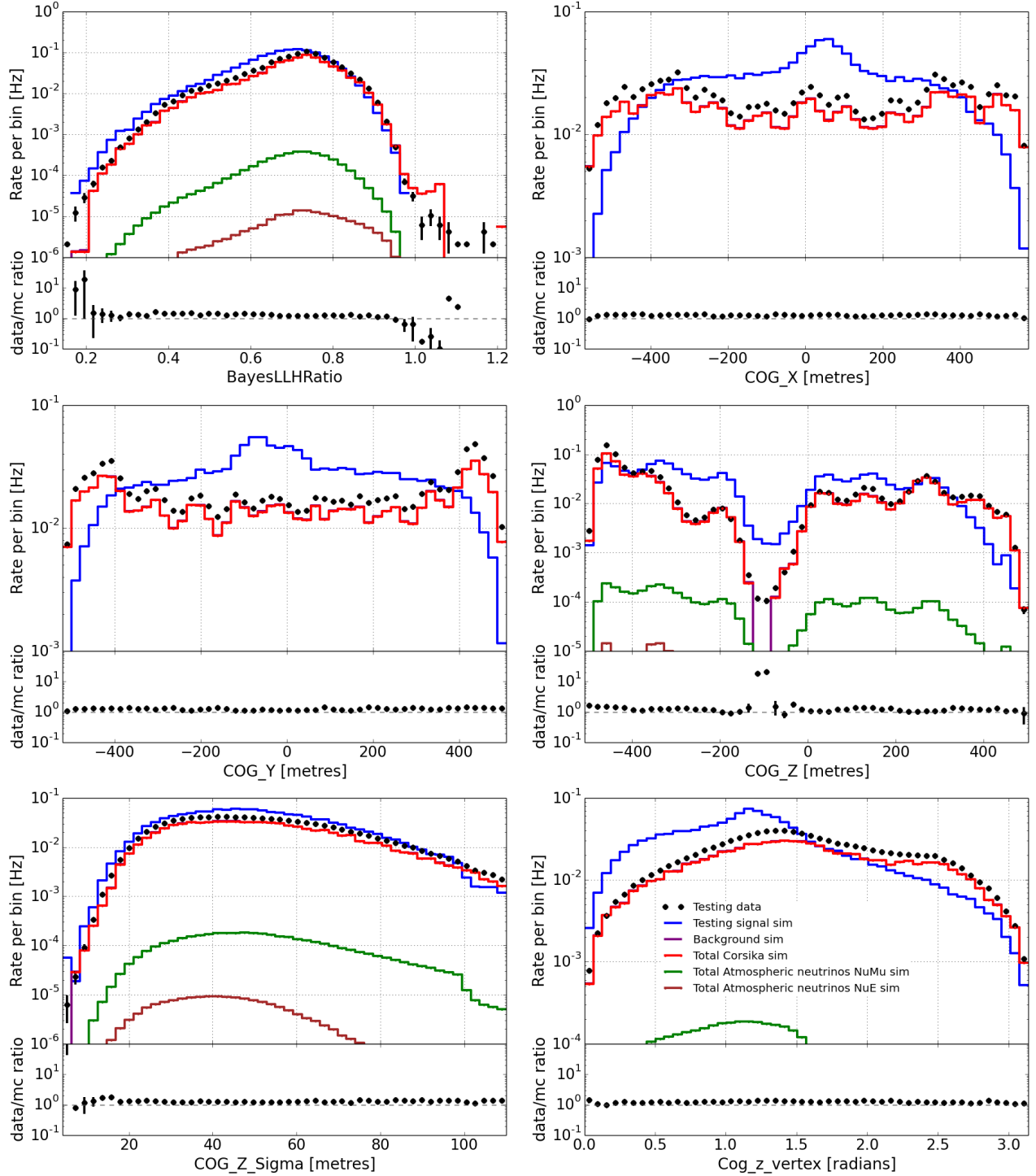
FIGURE 5.13: Distributions of the variables used by the BDT for the ICHighEn stream.
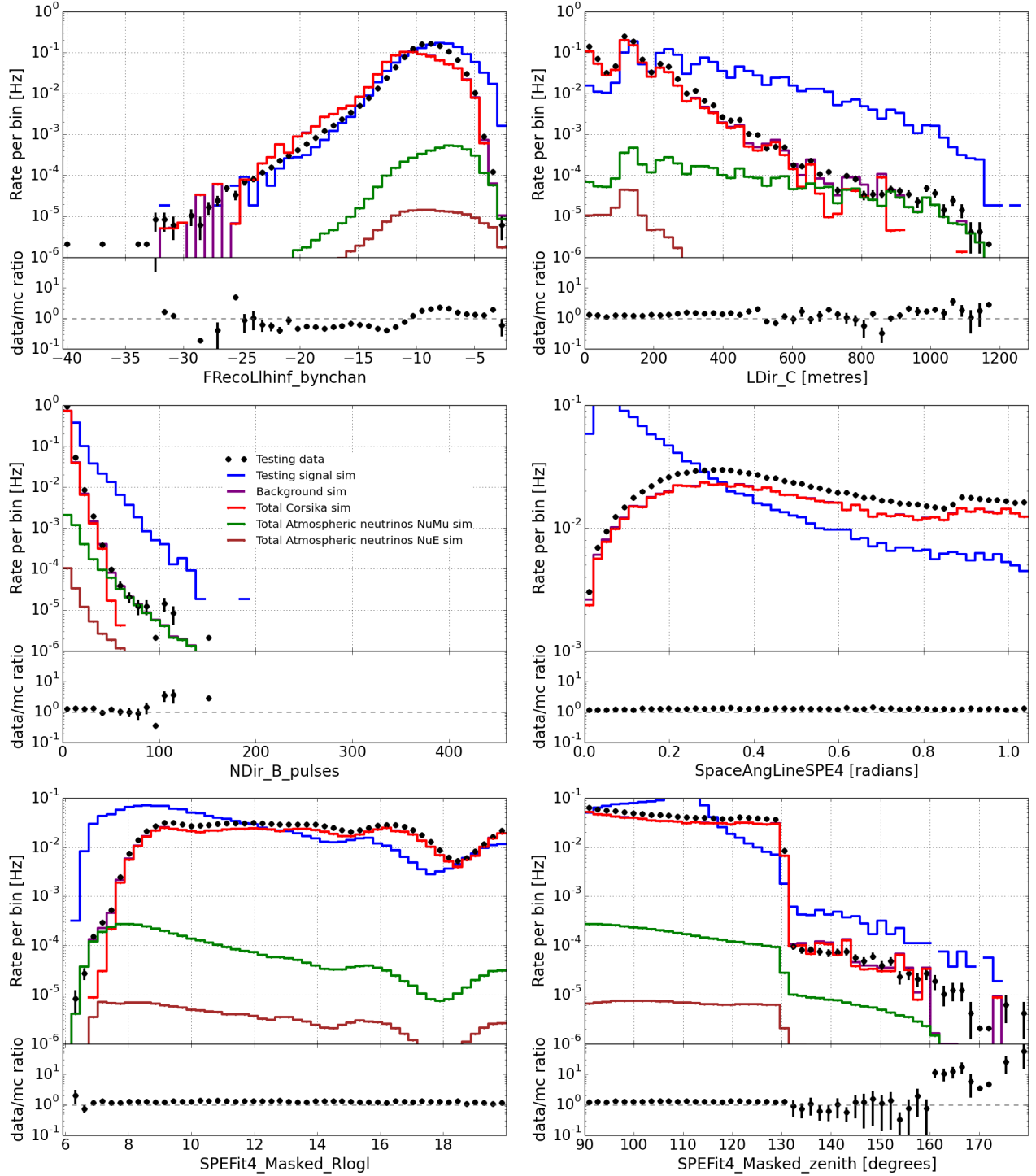
FIGURE 5.14: ICHighEn Stream BDT Variable Distributions 2.
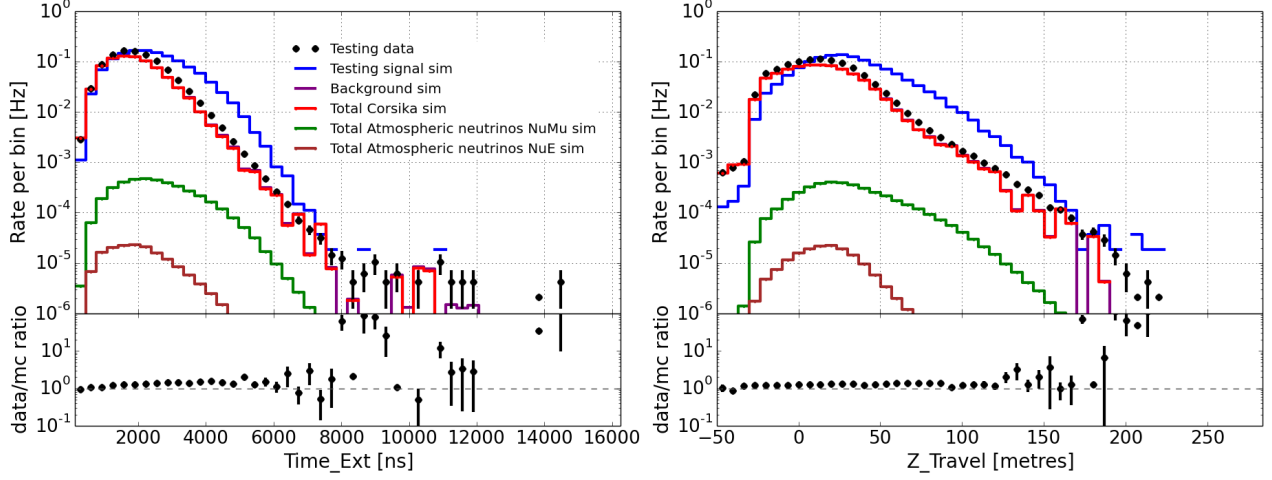
FIGURE 5.15: ICHighEn Stream BDT Variable Distributions 3.
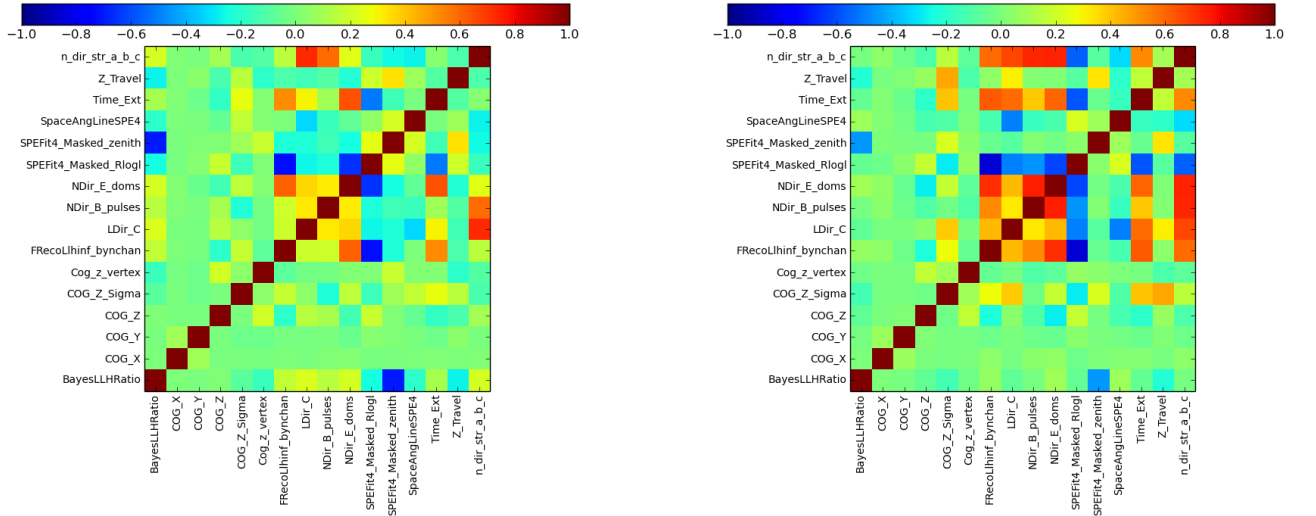
FIGURE 5.16: ICHighEn stream BDT variable correlation matrices.
Data Burn Sample (left) and Signal simulation (Right), for the ICHighEn stream.

5.4.2 Austral Summer

Only events passing the DeepCore filter stream are kept in the AS, following which the additional Level 2 processing of Section 5.4.1.1 is carried out. This corresponds to about ~30 Hz of data.

5.4.2.1 Level 3 Cuts

The objective of the AS Level 3 cuts is to reject atmospheric muon background and reduce the total data rate to ~ 1 Hz or lower by selecting only events starting within the detector. Thus the following cuts are applied.

1. $N\text{-}Hit\text{-}DOMs_{DCFid} > N\text{-}Hit\text{-}DOMs_{IC}$
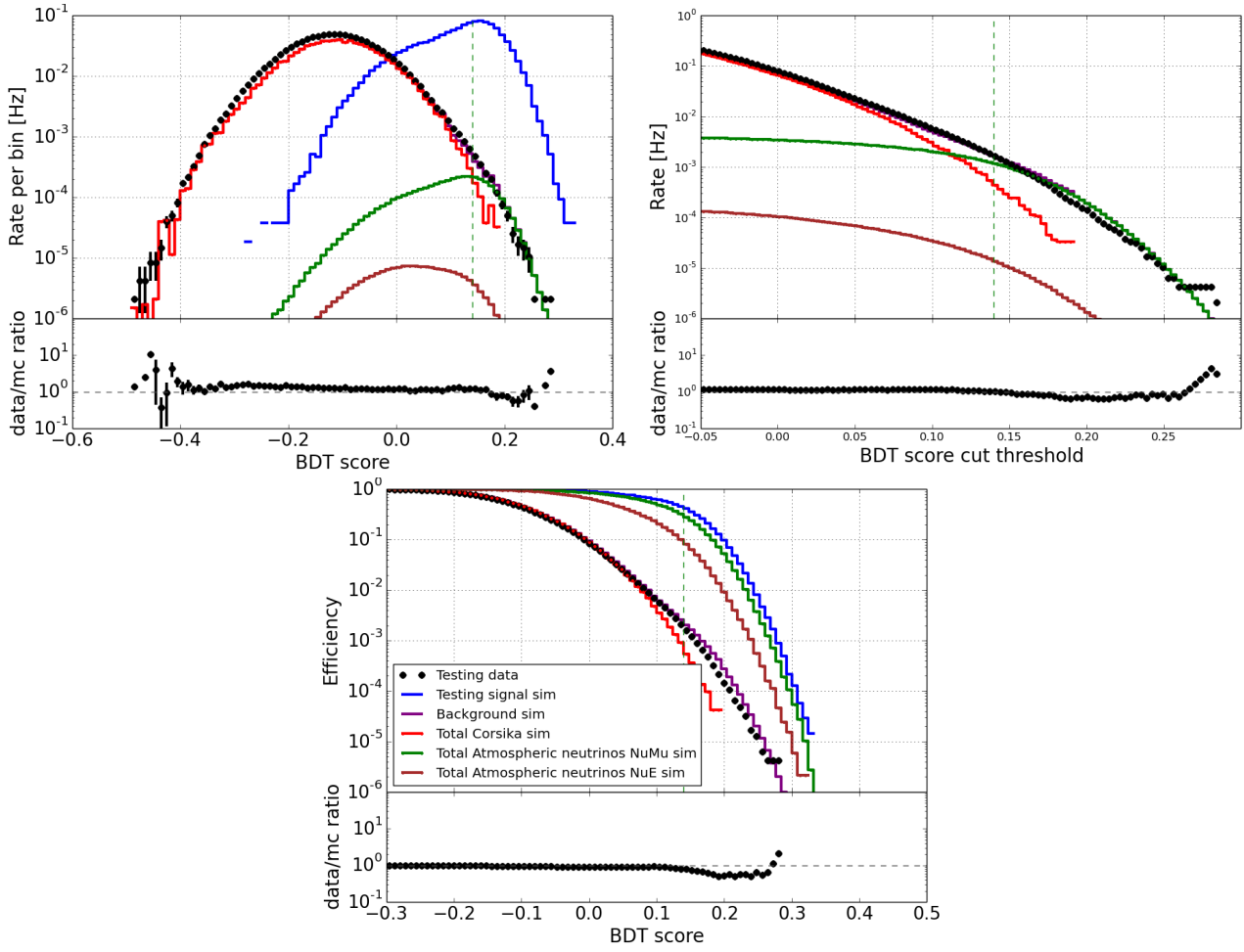
FIGURE 5.17: BDT score distributions for the ICHighEn stream. Top Left : Distribution of the BDT score for the Data Burn Sample, as well as the signal and background Monte Carlos. Top Right: The rate of events that pass the cut for various BDT cut thresholds. Bottom : The efficiencies as a function of BDT cut thresholds.

2. $N\text{-}Hit\text{-}DOMs > 6$

3. $N\text{-}Hit\text{-}Strings > 1$

4. $Z_{FiniteReco} < -225m$

5. $X\text{-}Y\text{-}Radius_{FiniteReco} < 400$

6. $Z\text{-}extension < 420m$

7. $Z\text{-}travel > -75m$

8. $\sigma_{COG_Z} < 100m$

9. $50° \leq \theta_{SPE4} \leq 80°$

10. Event should have at least one hit in an inner string as defined by the LowUp Filter
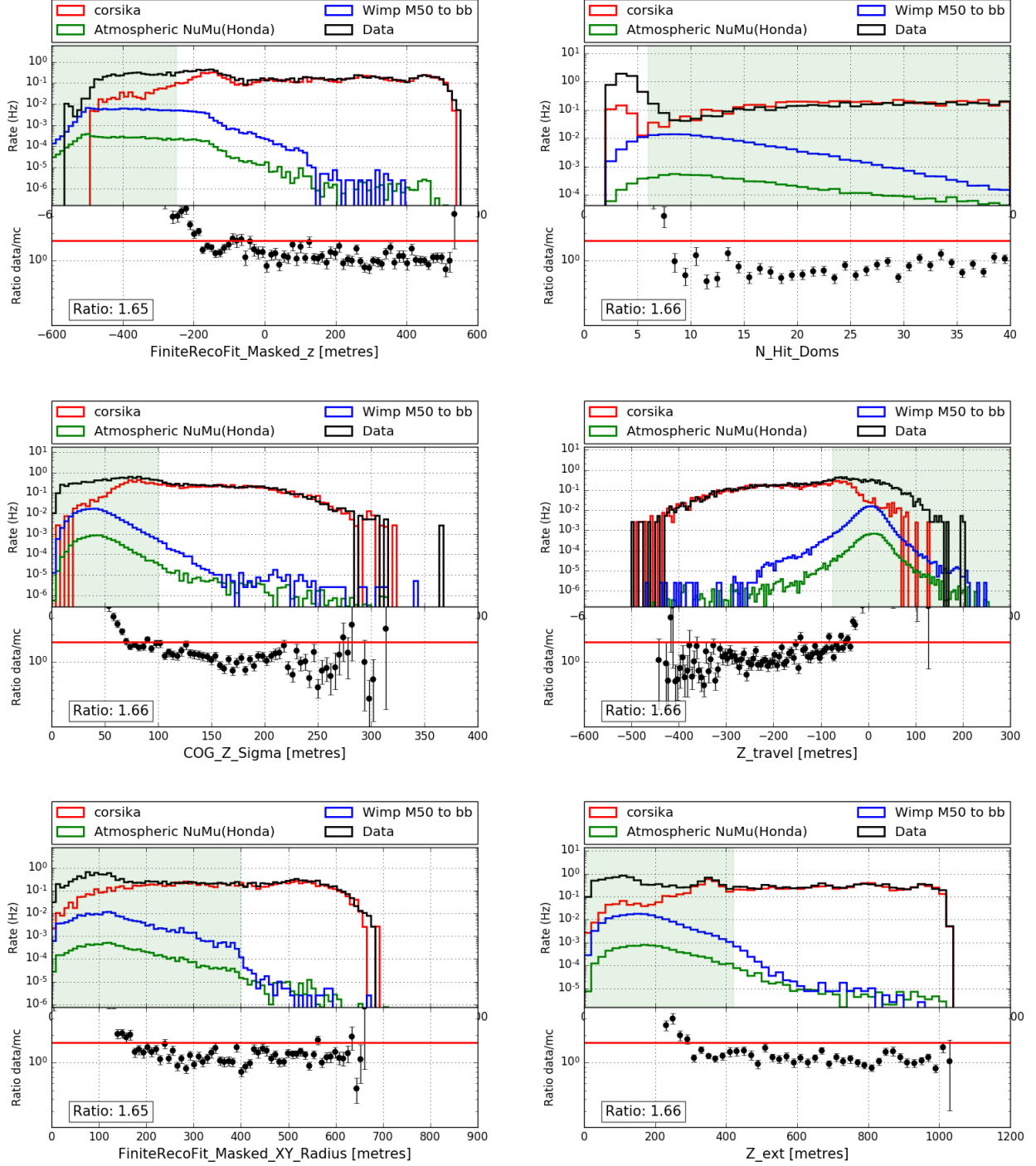
FIGURE 5.18: Level 3 cuts for the Summer stream: These distributions are after the first level 3 cut ($N\text{-}Hit\text{-}DOMs_{DCFid} > N\text{-}Hit\text{-}DOMs_{IC}$) has already been applied.
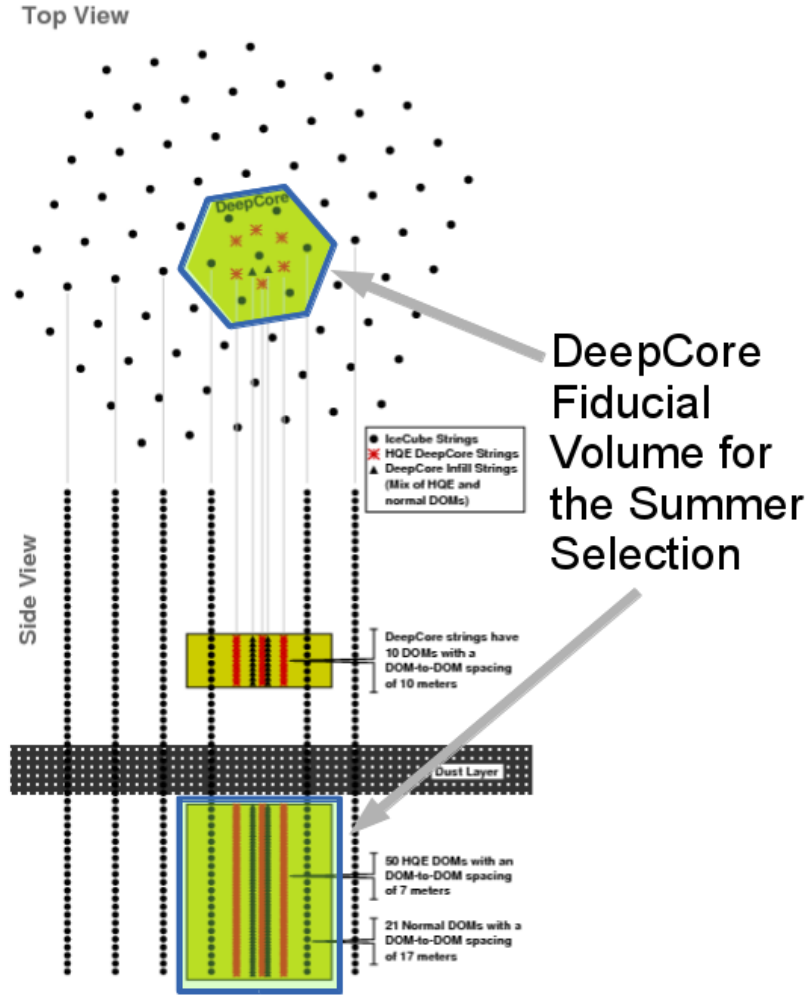
FIGURE 5.19: The austral summer DeepCore fiducial volume: The region above the dust layer is excluded.

The cut on *N-Hit-DOMs* imposes a basic quality criterion on the events while the cut on *N-Hit-Strings* rejects single string events, which are mostly vertical and cannot come from the Sun. Single string events that are horizontal are usually of very low energy and the direction of these events cannot be reconstructed with a good level of precision. The next two cuts insist that the reconstructed vertex of the event must be near the DeepCore region. Collectively, these cuts reduce the data to ~ 0.14 Hz. The DeepCore fiducial volume for the Austral Summer is illustrated in figure 5.19 and does not include the DeepCore region above the dust layer in order to obtain an additional level of background rejection.
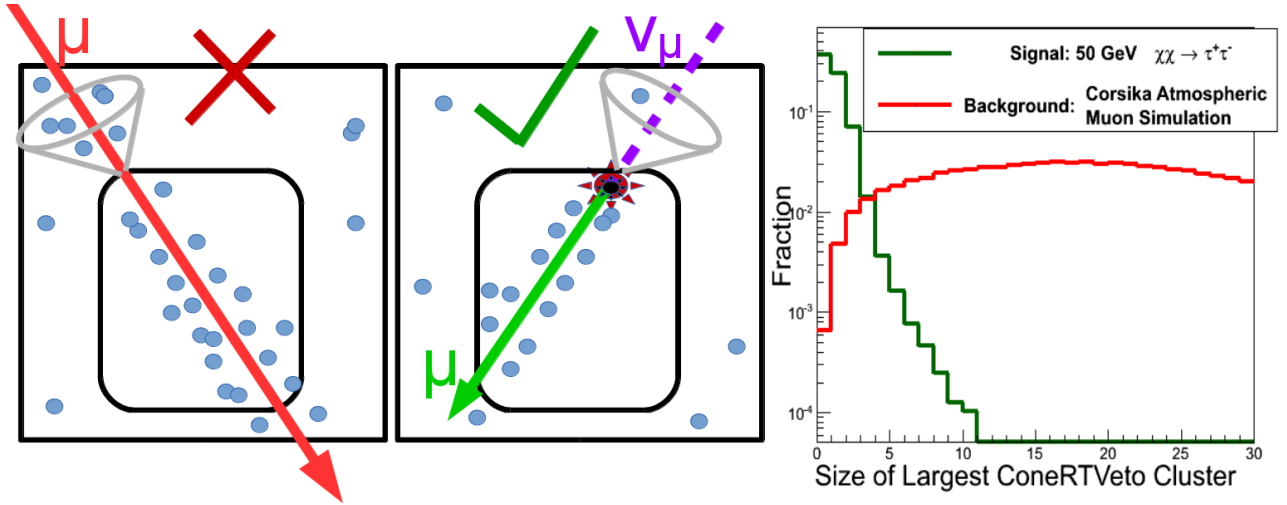
FIGURE 5.20: On the left and centre: An illustration of the ConeRT Veto concept. Only events with their reconstructed vertex near DeepCore are selected. Subsequently, the photon detections within a cone of 40° half-angle at the vertex and aligned along the muon track are sorted into clusters based on whether they are within a specific distance and time with respect to each other. The distribution of the size of the largest of these clusters of hits is shown on the right for signal (green) and background (red). Selecting events with cluster sizes ≤ 3 will keep more than 90% of signal while rejecting more than 90% of background of atmospheric muons.

5.4.2.2 Level 3 Processing

Paraboloid Fit on SPE4 : At this stage a Paraboloid fit is performed on the SPE4 track reconstruction to estimate the error on this reconstruction.

5.4.2.3 Level 4 Cuts - Votes

At this stage, the remaining data are still dominated by downgoing muons. While FiniteReco has correctly identified the vertices of many muons to be outside the fiducial volume, allowing them to be rejected by the cuts of previous section, some of these have managed to sneak in to the sample by producing too few correlated hits in the sparsely instrumented region outside DeepCore. These events can still be identified and rejected by the method described below.

ConeRT Veto A cone of half angle 40° is constructed at the FiniteReco Vertex, aligned along the reconstructed SPE4 track. Photons detected within this cone are sorted into clusters based on whether they are within 250 metres and 1000 ns of each other, in a process called 'RT clustering'[145]. The veto decision for an event is based on the size of the largest of these clusters. Fig 5.20 contains a schematic illustration of the method and the distribution of the size of the largest cluster for atmospheric muon simulation as well as a sample signal simulation. Keeping only events for which this value is < 3 lowers the data rate by an order of magnitude while keeping more than 90% of the signal. The Level 4 Cuts then are:
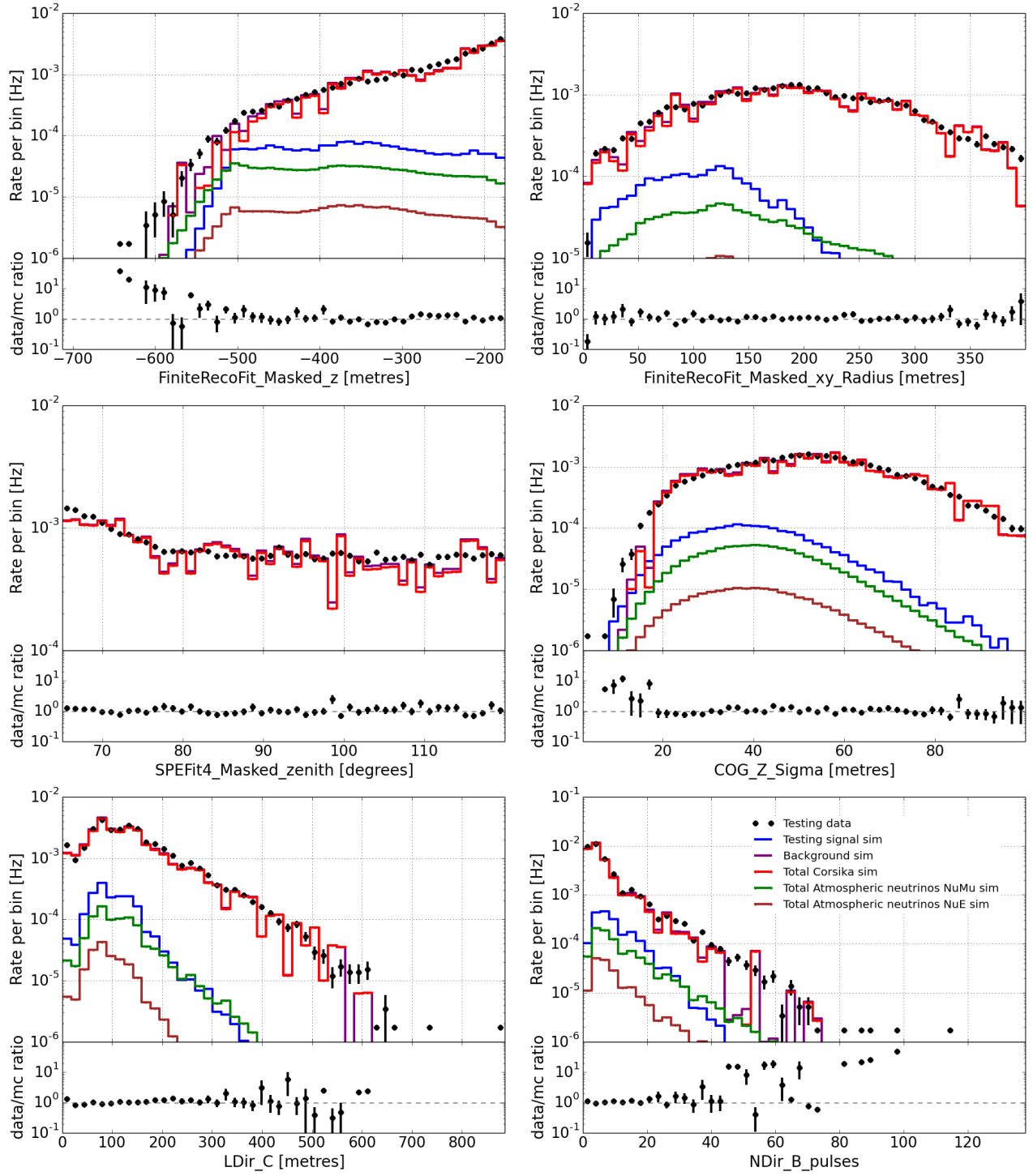
FIGURE 5.21: Summer stream BDT variable distributions

1. ConeRTVeto Cluster Size < 3

2. $\sigma_{paraboloid} < 30°$
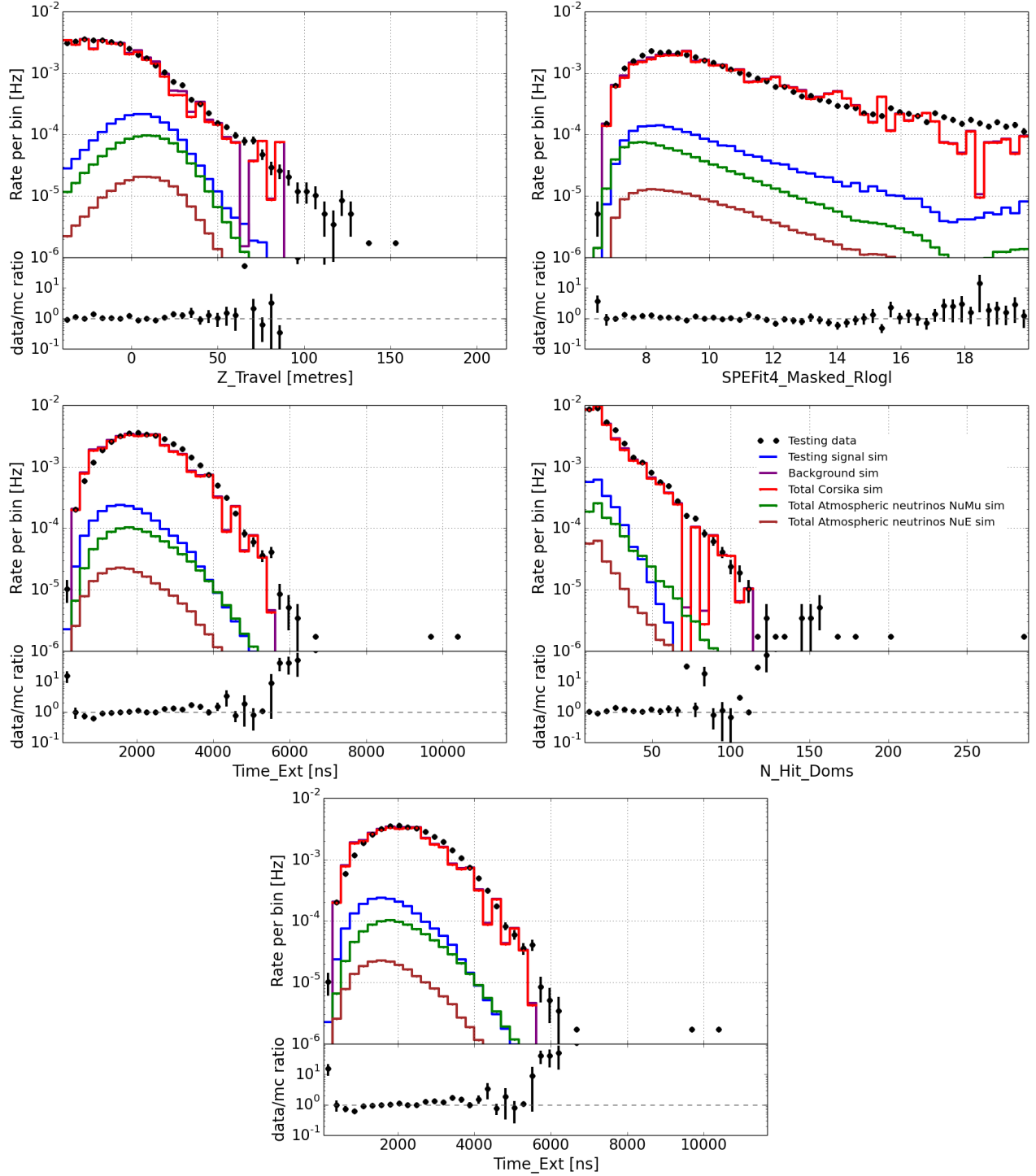
FIGURE 5.22: Summer stream BDT variable distributions.
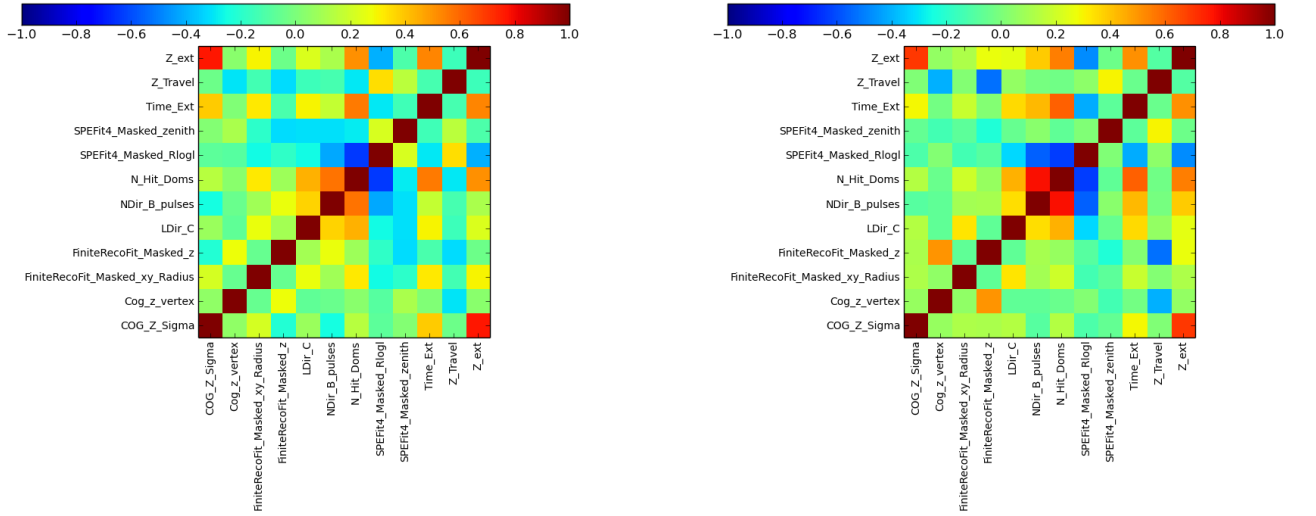
FIGURE 5.23: Summer stream BDT variable correlation matrices. Data Burn Sample (left) and Signal simulation (Right).
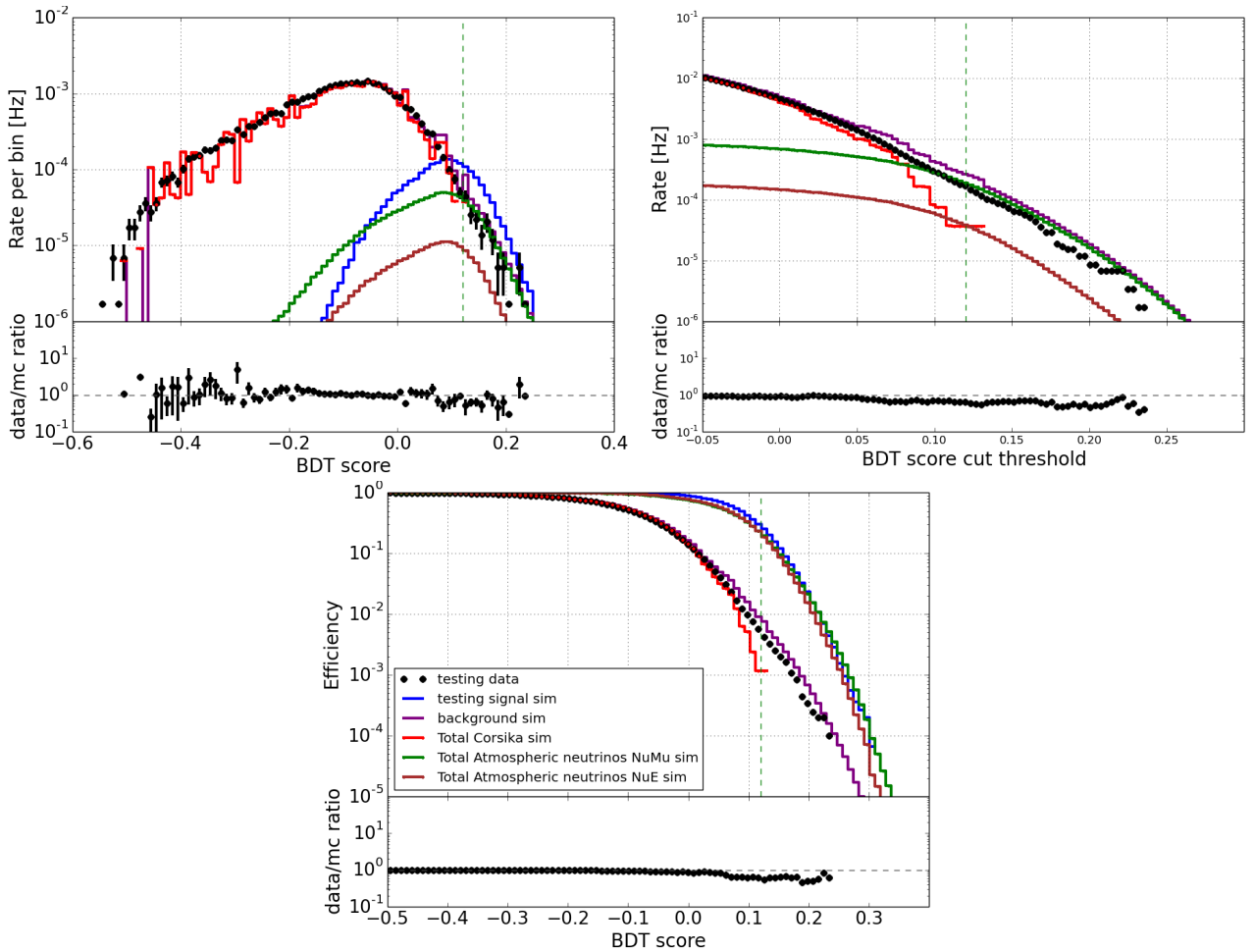
FIGURE 5.24: BDT score distributions for the Summer stream. Top Left : Distribution of the BDT score for the Data Burn Sample, as well as the signal and background Monte Carlos. Top Right: The rate of events that pass the cut for various BDT cut thresholds. Bottom: Efficiencies as a function of BDT cut threshold.
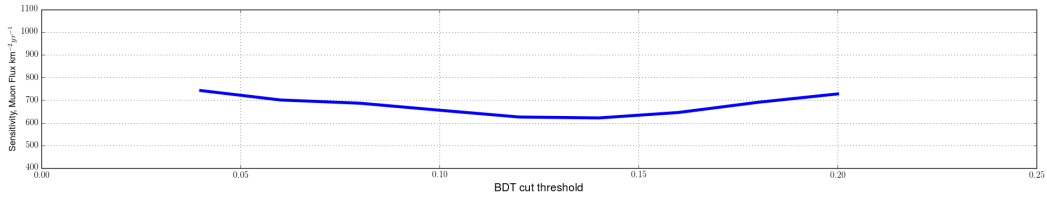
FIGURE 5.25: BDT cut optimization for the Winter DCLowEn Sample. The optimal BDT score to cut at is decided by trying various cuts and evaluating the sensitivity

5.4.2.4 Level 5: Boosted Decision Trees

At this point the AS sample is also optimized further using a BDT. The Burn Sample is used as background to train the BDT while a sum of $\chi\chi(50GeV) \rightarrow \tau^+\tau^-$, $\chi\chi(100GeV) \rightarrow W^+W^-$ and $\chi\chi(100GeV) \rightarrow b\bar{b}$ Monte Carlo events are used as the signal sample, just as in the case of the DCLowEn sample. The following variables were chosen.

1. σ_{COG_Z}

2. $\theta_{COG-z_{vertex}}$

3. $Z_{FiniteReco}$

4. $X\text{-}Y\text{-}Radius_{FiniteReco}$

5. $L\text{-}Dir_C$

6. $N_{Dir-B}\text{-}pulses$

7. $N_{Hit_D}oms$

8. $SPE4\text{-}RlogL$

9. θ_{SPE4}

10. $time\text{-}extension$

11. $N_{Dir-A+B+C}\text{-}strings$

12. $Z\text{-}travel$

The final cut threshold on the BDT score for all three samples is chosen such that the best sensitivity is obtained, by calculating the sensitivities across a range of cut thresholds, as illustrated in Figure 5.25

The performance of the three event selections can be specified in terms of their effective areas and angular resolutions, and are summarized in Figure 5.26. Tables 5.4, 5.5 and 5.6 summarize the rates, signal efficiencies and neutrino purities at various levels of selection for the three samples.

TABLE 5.4: DCLowEn rate summary at various cut levels: Atmospheric neutrino rates, both $\nu_\mu(+\bar{\nu}_\mu$ and $\nu_e(+\bar{\nu}_e)$, are estimated from `NuGen` and Genie simulations weighted to the predictions of Honda et. al [65]

Cut Level	Data(Hz)	Total Bkg MC (Hz)	CORSIKA (Hz)	Atmos $\nu_\mu(+\bar{\nu}_\mu)$(Hz)	Atmos $\nu_e(+\bar{\nu}_e)$(Hz)
L2	98.4	72.8	72.8	18.6×10^{-3}	
L3	2.81				
L4	0.09				
L5	3.4×10^{-4}	3.6×10^{-4}	2.0×10^{-5}	2.63×10^{-4}	8.0×10^{-5}

TABLE 5.5: Similar to Table 5.4 but for the Winter High Energy ('ICHighEn') stream

Cut Level	Data(Hz)	Total Bkg MC (Hz)	CORSIKA (Hz)	Atmos $\nu_\mu(+\bar{\nu}_\mu)$(Hz)	Atmos $\nu_e(+\bar{\nu}_e)$(Hz)
L2	98.4	72.8	72.8	18.6×10^{-3}	
L3	2.81				
L4	0.14				
L5	2.9×10^{-3}	3.0×10^{-3}	0.8×10^{-3}	2.1×10^{-3}	1.0×10^{-4}

TABLE 5.6: Similar to Table 5.4 but for the Summer stream

Cut Level	Data(Hz)	Total Bkg MC (Hz)	CORSIKA (Hz)	Atmos $\nu_\mu(+\bar{\nu}_\mu)$(Hz)	Atmos $\nu_e(+\bar{\nu}_e)$(Hz)
L2	30				
L3	0.14				
L4	0.028				
L5	2.5×10^{-4}	2.8×10^{-4}	3.3×10^{-5}	2.1×10^{-4}	5.0×10^{-5}

Effective Volume The effective volume V_{eff} for a signal hypothesis corresponds to the equivalent volume for 100% detection efficiency and is given by:

$$V_{eff} = \frac{\sum_N w_i V_i \delta_i}{\sum_N w_i} \tag{5.1}$$

where δ_i is 1 if the generated event has passed all the levels of selection and made it to the final sample and 0 otherwise. w_i is an energy dependent simulation weight provided in `WimpSim` [51] and V_i is the energy dependent cylindrical volume inside which `WimpSim` randomly places the event. N stands for the number of generated events.

Effective Area Similarly, the effective area for each bin in energy can be defined as:

$$A_{eff} = n.\frac{\sum_N w_i V_i \delta_i}{\sum_N w_i/\sigma(E_\nu^i)} \tag{5.2}$$

and is different for ν and $\bar{\nu}$ since the cross sections are different for the two.

Figures 5.27 to 5.29 show IceCube event displays for the typical data events in each of the 3 samples.
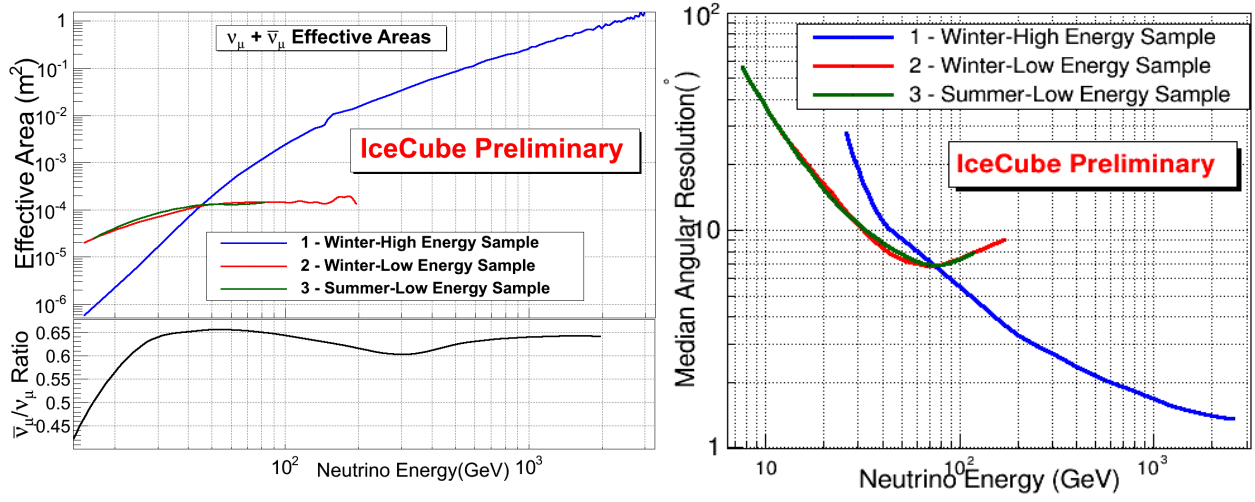
FIGURE 5.26: Left upper panel: $\nu_\mu + \bar{\nu}_\mu$ effective areas for the three different event selections. Left lower panel : Ratio of the $\bar{\nu}_\mu$ and ν_μ effective areas, determined by the relative cross sections and inelasticities of $\bar{\nu}_\mu$ and ν_μ. Right: The angular resolutions of the three samples at different energies, defined as the median of the angular separation between the incoming neutrino and the reconstructed muon.
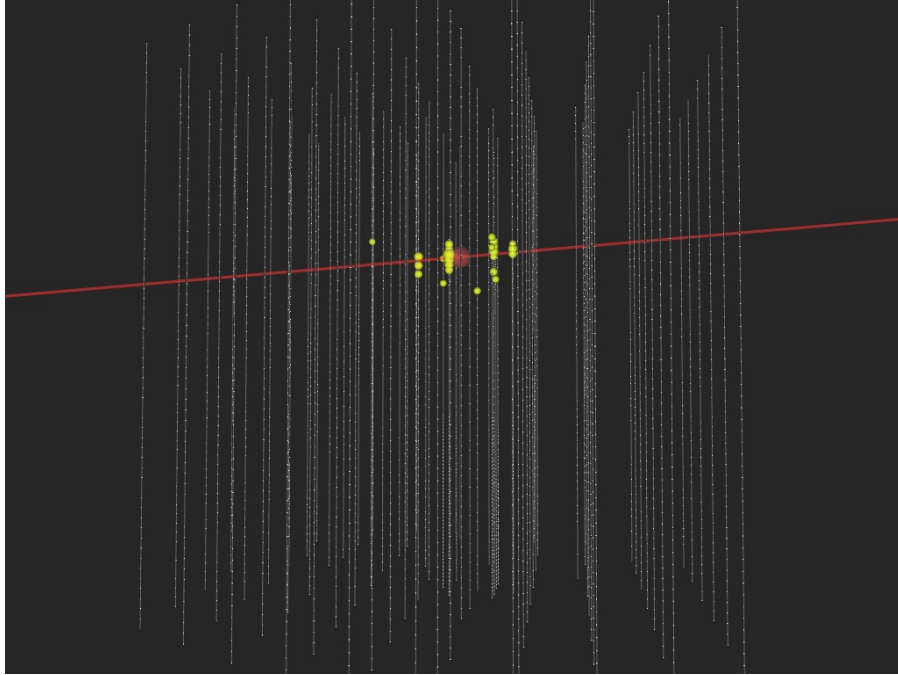
FIGURE 5.27: IceCube event display of a typical event that makes it to the Winter Low Energy ('DCLowEn') selection.
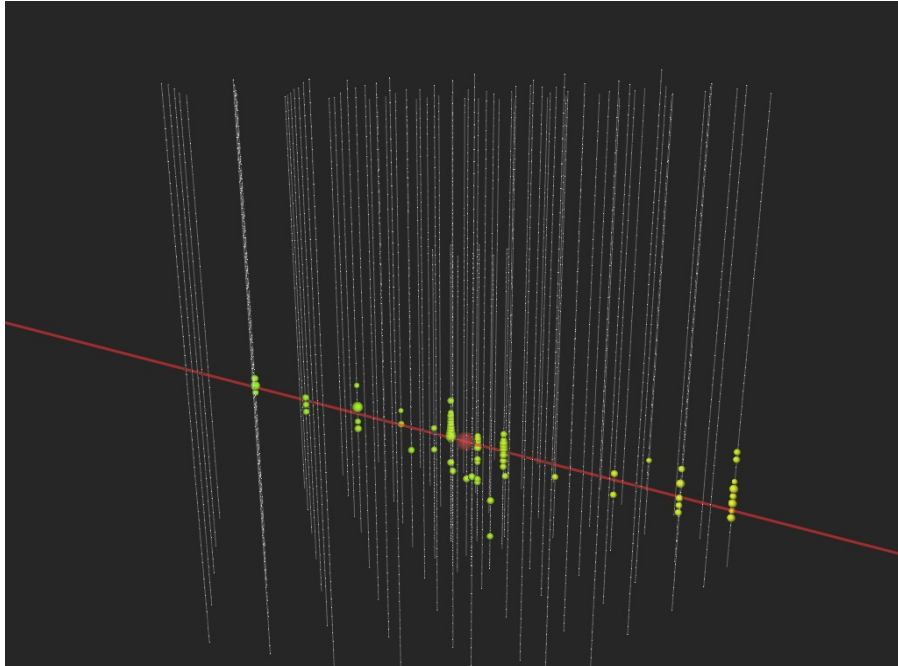
FIGURE 5.28: IceCube event display of a typical event that makes it to the Winter High Energy ('ICHighEn') selection.
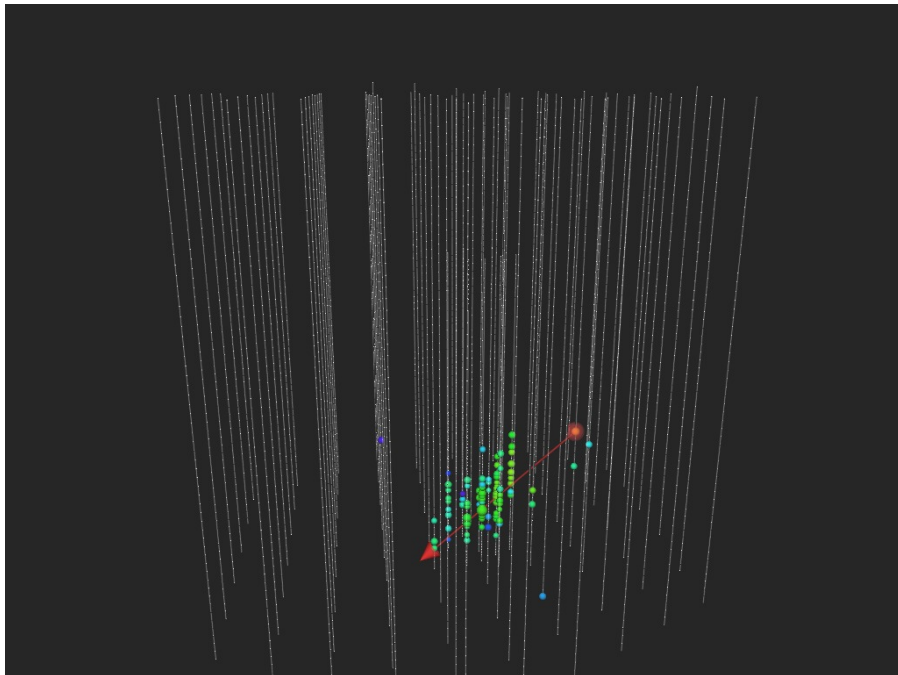
FIGURE 5.29: IceCube event display of a typical event that makes it to the Summer selection.

Data - Monte Carlo disagreements   Discrepancies can be observed between the distributions of some IceCube variables for data and Monte Carlo. They arise due to the following reasons:

Deficiencies in event generation: Discrepancies between data and atmospheric muons as predicted by `CORSIKA` at low energies and high inclinations, as seen in variables such as '`SPEFit4_Masked_zenith`' and '`Cog_z_vertex`' in Figures 5.9 and 5.10 can be attributed to deficiencies in shower simulation by `CORSIKA`, as reported in [146]. These discrepancies vanish at higher cut levels, where the muon background has been significantly reduced.

Deficiencies in detector simulation: Shortcomings in the simulation of the detector, such as a lack of simulation of correlated noise, can be observed in events triggered by the densely instrumented DeepCore detector region. This effect is visible in variables such as '`FiniteRecoFitMasked_z`' and '`N_Hit_Doms`' in Figure 5.18. The most significant discrepancy can be seen for values of '`FiniteRecoFitMasked_z`' below -200 metres, which corresponds to the position of DeepCore. These events have '`N_Hit_Doms`' less than 10, are not produced by an actual muon track traversing the detector. Similar discrepancies can also be observed in figs. 5.5 and 5.4 and the events responsible can be observed to populate the tails of variables quantifying reconstruction quality, such as 'SPEFit4_Masked_Rlogl'. Consequently, the cuts on these variables eliminate these events and they are not observed at Level 3 onwards.

In general, cuts that select events in domains where there are significant deficiencies in detector simulation have been avoided. Muon backgrounds have been reduced as much as possible. Consequently at final analysis level, the data are well described by the atmospheric neutrino hypothesis.

5.5   Analysis Method

The significance of a cluster of events in the direction of the Sun can be estimated using a modified version of the unbinned maximum likelihood ratio method described in Chapter. 4. Due to the very large point spread function of IceCube at these low neutrino energies, we model the spatial signal p.d.f of Eq. 4.3 as a Fisher-Bingham distribution as described in Section.4.3.

For the fully contained events of the DeepCore dominated samples ((2) and (3) of Figure 5.2), the energy of the neutrino can be estimated by summing the energy of the muon (obtained by reconstructing the starting and stopping vertex of the muon) and the hadronic cascade from the charged current interaction using the LEERA DeepCore energy reconstruction described in Section.1.5.2.6. Signal and background p.d.f.s are constructed from the signal simulation and datasets randomized in azimuth respectively. Energy weighting is added to the likelihood to enhance sensitivity. Thus the signal p.d.f. is given by:

$$S_i(|\vec{x}_i - \vec{x}_{sun}(t_i)|, E_i, m_\chi, c_{ann}) = \mathcal{K}(|\vec{x}_i - \vec{x}_{sun}(t_i)|, \kappa_i) \times \mathcal{E}_{m_\chi, c_{ann}}(E_i), \tag{5.3}$$

where $\mathcal{K}$ stands for the spatial and $\mathcal{E}$ for the spectral parts of the p.d.f. and m_χ and c_{ann} stand for the mass and annihilation channel of the WIMP respectively.

$$\mathcal{K}(|\vec{x}_i - \vec{x}_{sun}(t_i)|, \kappa_i) = \frac{\kappa_i e^{\kappa_i cos(\theta_{|\vec{x}_i - \vec{x}_{sun}(t_i)|})}}{2\pi(e^{\kappa_i} - e^{-\kappa_i})} \qquad (5.4)$$

where the concentration factor κ_i of the monovariate Fisher-Bingham distribution is obtained from the likelihood based estimate of the angular resolution of the track reconstruction [45].

Calibrating the paraboloid angular error estimator   The paraboloid angular error estimator has been found to systematically overestimate the accuracy of track reconstructions in other IceCube analyses[147, 148]. Studies have concluded that this energy dependent overestimation is due to deviations from the ideal track hypothesis at both high and low energies, where stochastic energy losses and the associated cascade of the CC interaction respectively dominate the light yield. This effect is corrected for each sample of events by rescaling the paraboloid sigma using a polynomial function of the number of hit doms, which serves as a crude estimator of the energy of an event. The polynomial function is derived from a fit obtained from examining simulation events.

The background p.d.f. is:

$$\mathcal{B}_i(\vec{x}_i, E_i) = B(\delta_i) \times P(E_i|\phi_{atm}) \qquad (5.5)$$

where $B(\delta_i)$ is the declination dependence and $P(E|\phi_{atm})$ indicates the distribution of the energy estimator E of the data sample at analysis level which is consistent with expectations from atmospheric muon and neutrino fluxes and is denoted by ϕ_{atm}.

The spatial p.d.f of the signal and the energy p.d.f of a specific signal and background are illustrated in Fig. 5.31.

For a sample of N events consisting of n_s signal events from the Sun and $N - n_s$ background events, the likelihood can then be written as:

$$\mathcal{L}(n_s) = \prod_N \left(\frac{n_s}{N} S_i + (1 - \frac{n_s}{N})\mathcal{B}_i \right) \qquad (5.6)$$

The best estimate for the number of signal events in the sample is obtained by maximizing the likelihood ratio as defined in Eq. 4.5. The significance of the observation can be estimated without depending on Monte Carlo simulations by repeating the process on datasets scrambled in right ascension. As the three separate event selections have no events in common, they can be combined statistically using the method described in 4.7. Confidence intervals on the number of signal events present within the sample are constructed using the method of Feldman and Cousins[136].
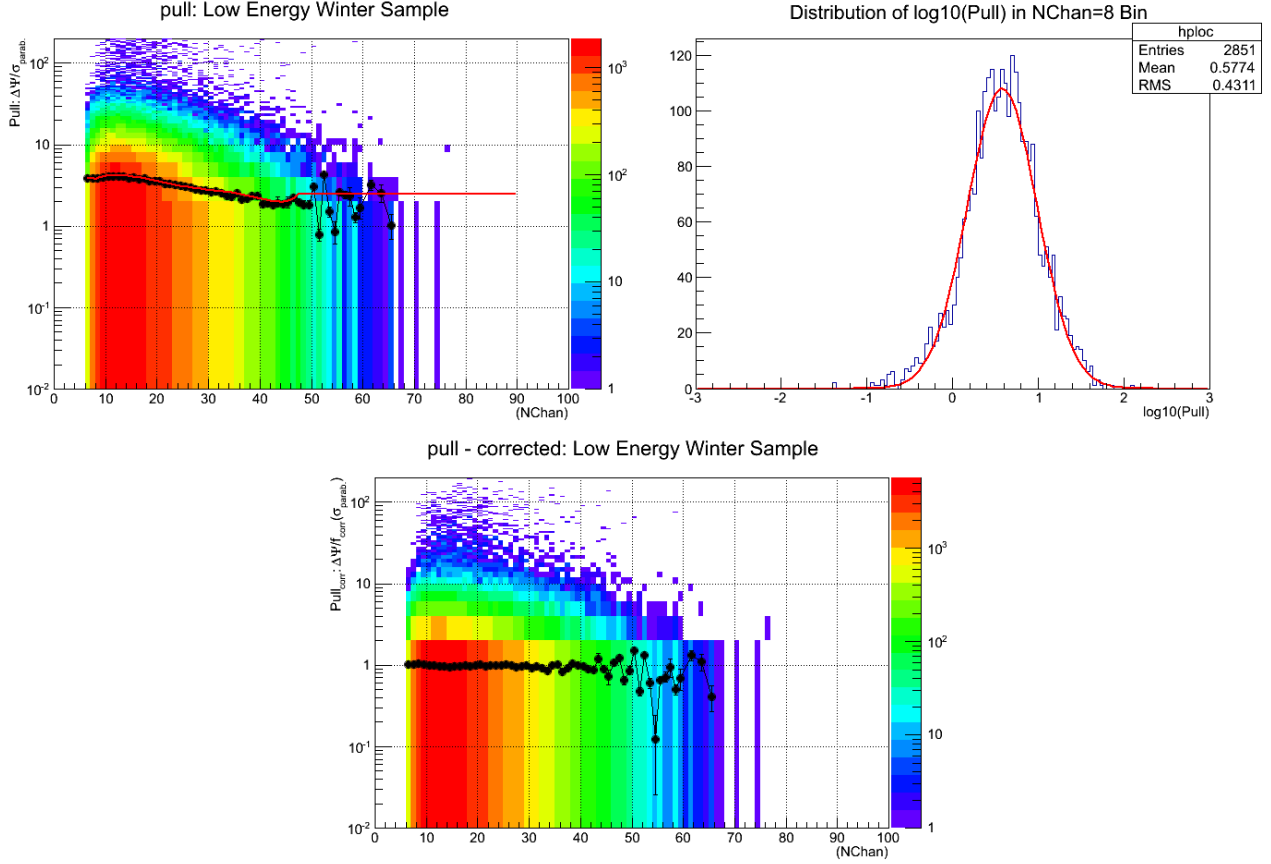
FIGURE 5.30: Top Left: Distribution of 'Pull', defined as the ratio of the difference between the reconstructed angle and the true neutrino direction, and the estimate of the error on the direction reconstruction provided by the paraboloid algorithm. Top Right: The distribution of the common logarithm of the Pull within a specific bin in NChan. Since the common logarithm of the Pull can be observed to follow a normal distribution, a fit is performed based on which the median can be extracted. The black dots in the figure on the left indicate the fitted median in each bin, to which the polynomial described by the red line is fitted. The polynomial is then used to rescale the value of paraboloid error estimate. Bottom : The 'Pull' with respect to the rescaled error estimate as a function of NChan.

5.6 Results

No significant excesses of events were observed in the direction of the Sun in any of the searches. Figure 5.32 compares the distribution of the angular separation between events against background expectations.

In the absence of any evidence of a signal, 90%C.L upper limits can be placed on n_s, the number of signal events in the sample using the prescription of Feldman and Cousins for each signal hypothesis. This can be interpreted as an upper limit on the neutrino to muon conversion rate $\Gamma_{\nu \to \mu}$ using the expression:

$$\Gamma_{\nu \to \mu}^{90\%C.L} = \frac{n_s^{90\%C.L}}{\sum_j T_{live}^j V_{eff}^j} \tag{5.7}$$
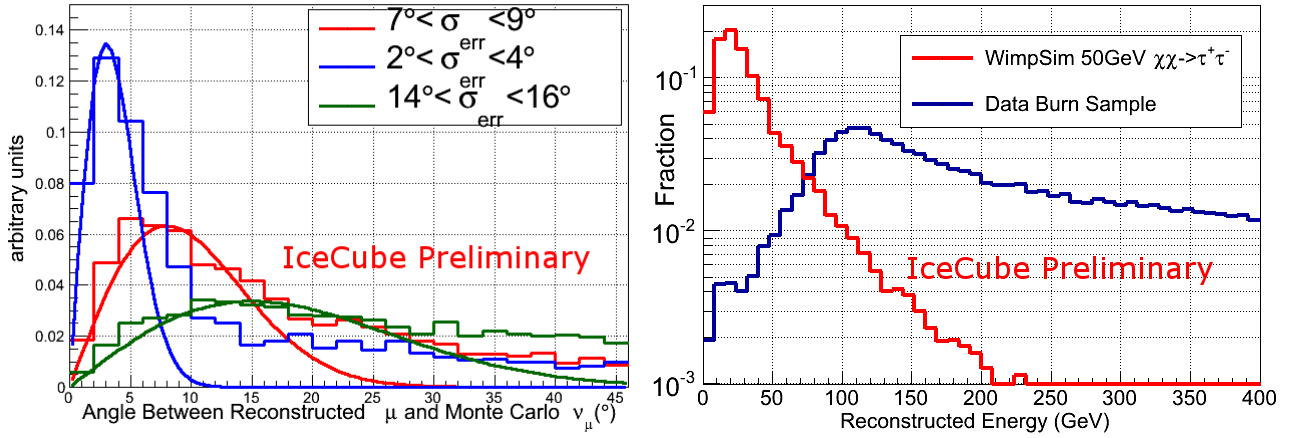
FIGURE 5.31: Left: Distribution of the angle between the Monte Carlo neutrino and the reconstructed muon for Monte Carlo events in three different ranges of values of the rescaled $\sigma_{paraboloid}$, a proxy for the error on track reconstruction. The histograms denote the observed distribution from Monte Carlo while the smooth curves are the analytical predictions from the Fisher Bingham distribution. The sensitivity can be further improved by using an analytical description of the point spread function that models the tails more correctly. Right: Normalized distributions of the reconstructed energy observed in real data as well as in signal Monte Carlo for 50 GeV WIMPs annihilating into the $\tau^+\tau^-$ channel. Both plots are for the Winter Low Energy selection.

where the index j runs over the different samples that are combined in likelihood for a specific signal.

Using routines provided with DarkSusy[149] and WimpSim [51], this can be interpreted as upper limits on the muon flux $\Phi_{\mu^++\mu^-}$, the neutrino flux $\Phi_{\nu+\bar{\nu}}$ and the annihilation rate in the Sun. Figure 5.33 summarizes the limits on $\Phi_{\mu^++\mu^-}$ for the annihilation channels considered.

Assuming that the annihilation and capture processes in the Sun have reached equilibrium, this can also be interpreted as limits on the WIMP-proton scattering cross section $\sigma_{\chi\text{-}p}$. Generally, any isospin conserving WIMP-proton interaction can be broken down into a spin dependent and a spin independent component. The limits can be interpreted as limits on either $\sigma_{\chi\text{-}p}^{SI}$ or $\sigma_{\chi\text{-}p}^{SD}$ under the assumption that the other is zero (Figures 5.34 and 5.35).

Table 5.7 summarizes the results obtained in this analysis for each signal hypothesis as well as the corresponding limits on $\Phi_{\mu^++\mu^-}$, $\Phi_{\nu+\bar{\nu}}$, the annihilation rate and scattering cross sections.

Figures 5.34 and 5.35 compare the constraints from this search on SD and SI cross sections with constraints from direct detection experiments, other neutrino detectors looking at the Sun, as well as the favoured parameter space of an MSSM[153]. The SD constraints are the most stringent above 80 GeV. Due to improved analysis methods, additional livetime as well as certain bugfixes in the simulation, the constraints have improved by almost an order of magnitude at high energies[142, 156], as shown in fig. 5.36.

While equilibrium is usually assumed, due to the fact that the time taken for equilibrium to be reached, $\tau = (C_C C_A)^{-1/2}$ there exists a lower limit on $\sigma_{\chi\text{-}p}$ below which the capture rate C_C (which is proportional to σ_χ-p) is so low that τ exceeds the age of the Sun [91]. This is given by:
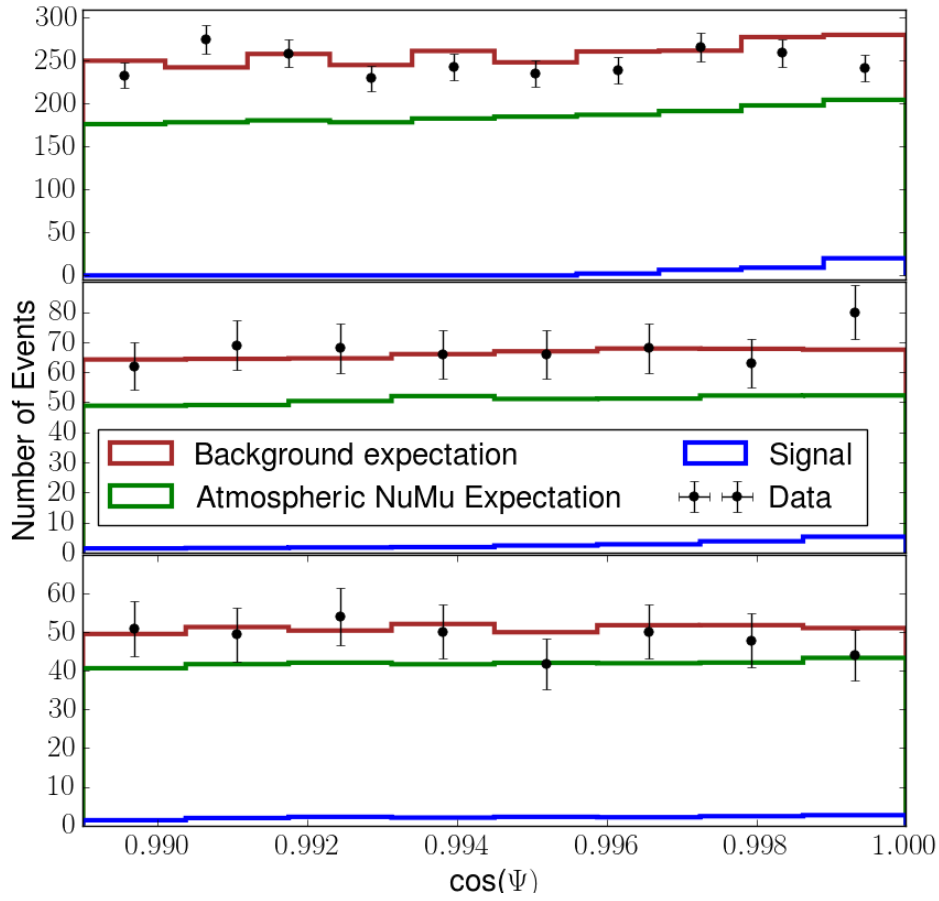
FIGURE 5.32: Distribution of cosinus of the angles between events observed and the Sun, for the three different samples. Top: Winter High Energy (ICHighEn) Sample, Middle: Winter Low Energy (DCLowEn) Sample and Bottom: Summer Sample. The black dots represent the real data events, the green line is the average $\nu_\mu + \bar{\nu}_\mu$ expectation from Monte Carlo weighted according to the predictions of Honda et al. The brown lines correspond to the background expectation, from the average of many scrambled real data sets. The blue lines correspond to the signals relevant to the samples, which are 1TeV$\rightarrow W^+W^-$ for ICHighEn, 50GeV$\rightarrow \tau^+\tau^-$ for DCLowen, and 20GeV$\rightarrow \tau^+\tau^-$ for Summer respectively.
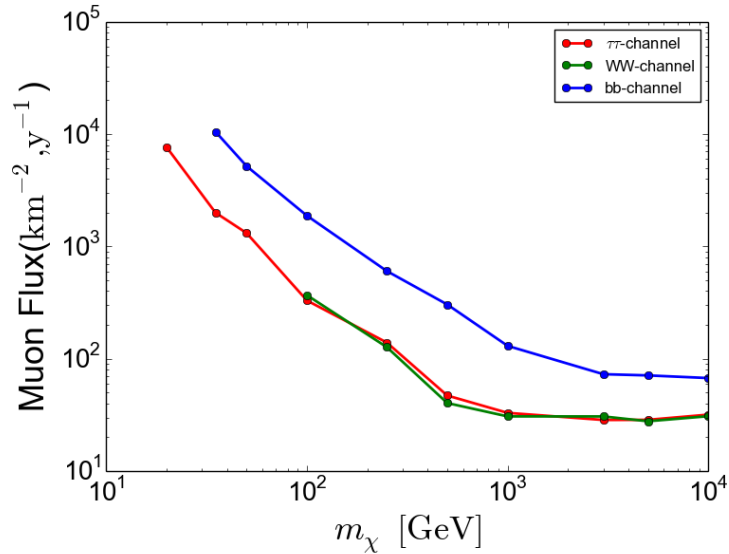
FIGURE 5.33: Limits on the muon flux $\Phi_{\mu^++\mu^-}$, integrated above 1 GeV.

TABLE 5.7: Best fit and 90%C.L upper limits on the number of signal events within the three samples in ∼1019 days of livetime. The average effective volumes over the three years of operation are also provided, as well as upper limits on the muon flux, annihilation rate, as well as the spin dependent and spin independent WIMP-proton scattering cross sections.

m_χ (GeV)	annihilation channel	$\hat{n}_s$	$n_s^{90\%C.L.}$	V_{eff} (km³)	$\Phi_{\mu+\bar\mu}^{90\%C.L.}$ km⁻²yr⁻¹	$\Gamma_{Ann}^{90\%C.L.}$ (s⁻¹)	$\sigma_{SD}^{90\%C.L.}$ (pb)	$\sigma_{SI}^{90\%C.L.}$ (pb)
20	$\tau^+\tau^-$	0	86.6	1.83e-04	7.48e+03	1.98e+24	1.05e-03	8.79e-06
35	$\tau^+\tau^-$	1.2	67.2	9.02e-04	2.06e+03	1.73e+23	2.17e-04	1.12e-06
35	$b\bar{b}$	0	77.8	8.89e-05	1.02e+04	1.88e+25	2.35e-02	1.21e-04
50	$\tau^+\tau^-$	8.3	48.9	1.33e-03	1.42e+03	6.02e+22	1.38e-04	5.15e-07
50	$b\bar{b}$	0	80.1	2.36e-04	5.35e+03	5.14e+24	1.18e-02	4.49e-05
100	$\tau^+\tau^-$		33.8	6.28e-03	3.99e+02	4.86e+21	3.93e-05	8.82e-08
100	W^+W^-	8.1	35.2	6.10e-03	4.49e+02	1.26e+22	1.02e-04	2.28e-07
100	$b\bar{b}$	6.4	55.6	7.45e-04	2.14e+03	6.53e+23	5.27e-03	1.18e-05
250	$\tau^+\tau^-$		89.9	7.08e-02	2.04e+02	6.09e+20	2.86e-05	3.58e-08
250	W^+W^-	17.4	65.6	6.81e-02	1.80e+02	1.25e+21	5.86e-05	6.92e-08
250	$b\bar{b}$	13.6	56.1	3.83e-03	8.21e+02	7.06e+22	3.32e-03	4.14e-06
500	$\tau^+\tau^-$		45.1	1.95e-01	5.93e+01	7.96e+19	1.46e-05	1.35e-08
500	W^+W^-	9.9	36.0	1.87e-01	5.53e+01	2.04e+20	3.76e-05	3.49e-08
500	$b\bar{b}$	24.4	74.5	1.35e-02	4.69e+02	1.88e+22	3.46e-03	3.19e-06
1000	$\tau^+\tau^-$		28.6	2.86e-01	3.46e+01	2.84e+19	2.07e-05	1.60e-08
1000	W^+W^-	2.6	24.6	2.67e-01	3.31e+01	9.34e+19	6.80e-05	5.28e-08
1000	$b\bar{b}$	8.4	43.1	3.24e-02	1.55e+02	3.56e+21	2.59e-03	2.00e-06
3000	$\tau^+\tau^-$		21.1	2.92e-01	2.90e+01	1.85e+19	1.20e-04	8.25e-08
3000	W^+W^-	2.5	23.1	2.86e-01	3.13e+01	8.33e+19	5.42e-04	3.70e-07
3000	$b\bar{b}$	2.5	32.1	6.62e-02	7.56e+01	1.04e+21	6.77e-03	4.65e-06
5000	$\tau^+\tau^-$		22.3	3.10e-01	2.93e+01	1.82e+19	3.28e-04	2.19e-07
5000	W^+W^-	2.5	22.4	3.09e-01	2.84e+01	7.59e+19	1.37e-03	9.14e-07
5000	$b\bar{b}$	2.5	33.7	7.72e-02	7.24e+01	8.74e+20	1.58e-02	1.06e-05
10000	$\tau^+\tau^-$		25.0	3.19e-01	3.21e+01	1.94e+19	1.40e-03	9.11e-07
10000	W^+W^-	2.5	25.2	3.18e-01	3.11e+01	8.26e+19	5.96e-03	3.88e-06
10000	$b\bar{b}$	2.5	32.5	8.26e-02	6.87e+01	7.31e+20	5.27e-02	3.46e-05
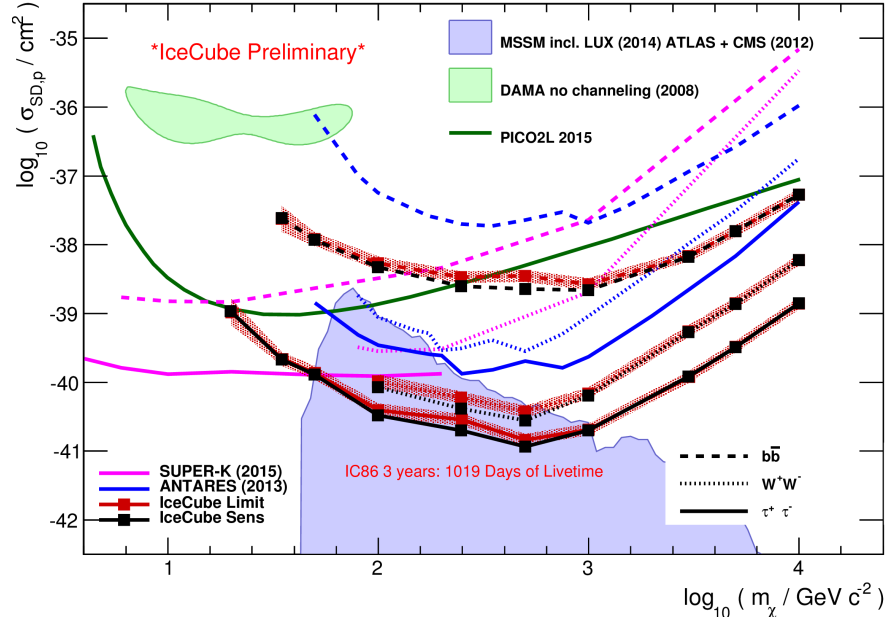
FIGURE 5.34: Limits on the $\sigma^{SD}_{\chi\text{-}p}$, compared to results from other neutrino detectors (ANTARES[150], Super-Kamiokande[151]) and direct detection experiments (DAMA[94], PICO2L[152]). The neutrino telescope limits are for the three benchmark channels. The shaded region corresponds to different CMSSM-25 models described in [153] that survive the LUX and LHC Run 1 constraints.
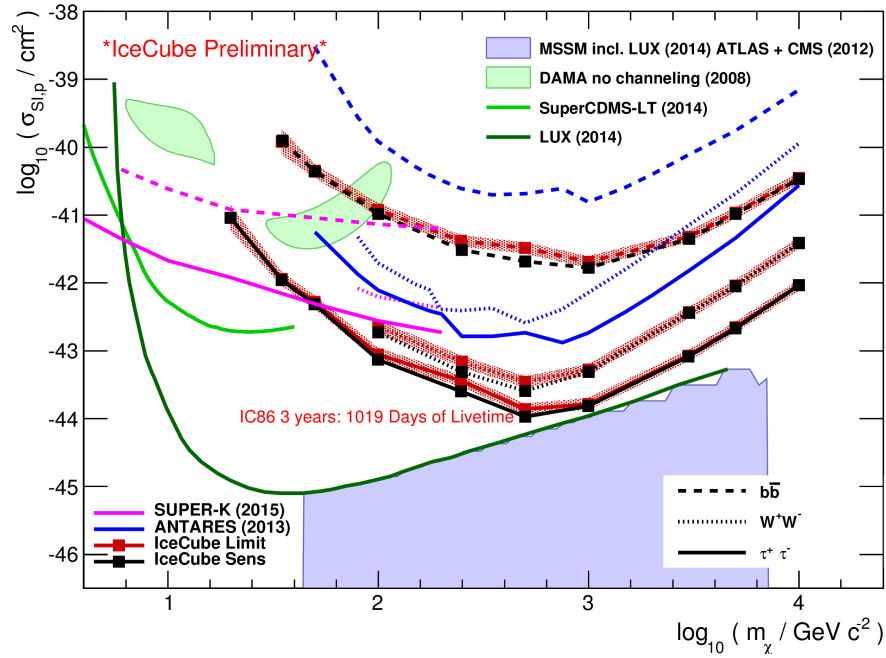
FIGURE 5.35: Limits on the $\sigma^{SI}_{\chi\text{-}p}$, compared to results from other neutrino detectors (ANTARES[150], Super-Kamiokande[151]) and direct detection experiments (DAMA[94], LUX[154], SuperCDMS[155]).
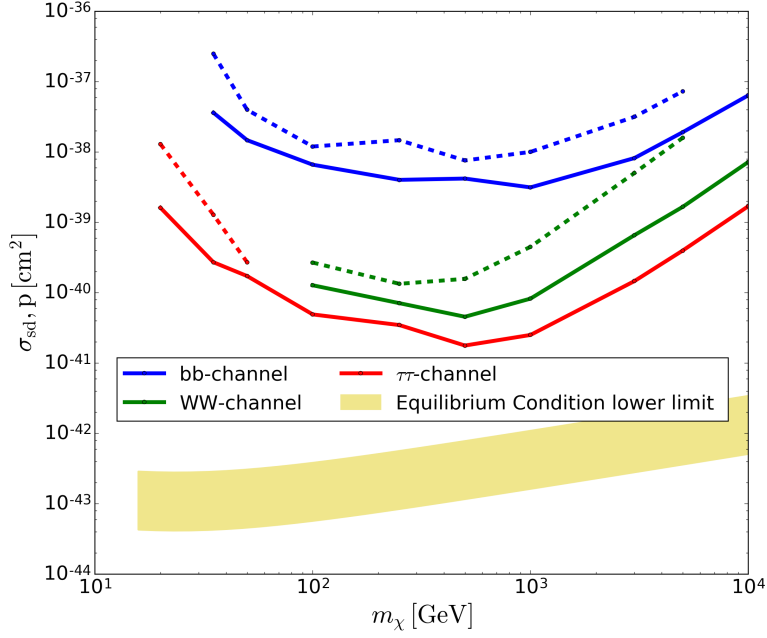
FIGURE 5.36: Limits on the $\sigma_{\chi\text{-}p}^{SD}$, for the three IceCube benchmark channels compared to the lower range below which the equilibrium condition becomes unlikely, indicated by the shaded area. The lower and upper edges of the shaded region corresponds to $\langle \sigma_A v \rangle = 2 \times 10^{-26} cm^3 s^{-1}$ and $3 \times 10^{-27} cm^3 s^{-1}$ respectively. The dashed lines indicate the limits from the previous IceCube analysis [142].

$$\frac{t_{sun}}{\tau} = 330 \times (\frac{C_C}{s^{-1}})^{1/2} (\frac{\langle \sigma_A v \rangle}{cm^3 s^{-1}})^{1/2} (\frac{m_\chi}{10 GeV})^{3/4} \tag{5.8}$$

where $\langle \sigma_A v \rangle$ is the velocity averaged annihilation cross section [91]. Figure 5.36 compares the present constraints with this lower limit for a range of values of $\langle \sigma_A v \rangle$ corresponding to the 'natural scale'. The lower limit $\sim$2 orders of magnitude beneath the constraints. However, in the near future, γ-ray telescopes such as Fermi and CTA will attain sensitivities far beneath the natural scale. Future Solar WIMP searches with IceCube will have to consider any potential constraints on $\langle \sigma_A v \rangle$ when assuming equilibrium.

Before the DM reaches equilibrium between capture and annihilation in the Sun, the annihilation rate can be obtained as function of the capture rate C_C using the expression

$$\Gamma_A = \frac{1}{2} C_C tanh^2(t/\tau). \tag{5.9}$$

5.6.1 Systematic Uncertainties

Background levels are estimated in the analysis method using scrambled data and are hence free of systematic effects. The leading sources of uncertainty in the signal simulation are the following:

1. Absolute DOM efficiency.

TABLE 5.8: Systematics summary.

M_χ (GeV)	Annihilation Channel	Uncertainty due to abs DOM eff (%)	Uncertainty due to Photon prop in Ice (%)
20	$\tau^+\tau^-$	-11/+29	-13/+18
50	$\tau^+\tau^-$	-8/+23	-9/+13
100	W^+W^-	-9/+19	-9/+11
500	$b\bar{b}$	-7/+11	-8/+7
1000	W^+W^-	-6/+9	-6/+4

2. Photon propagation in ice (absorption and scattering).

A previous study of the systematic uncertainties on data from the 79 string configuration of IceCube [142, 156] concluded that the following sources of uncertainty contribute sub-dominantly in comparison to the above ones.

1. Neutrino - nucleon cross sections.

2. Neutrino oscillations.

3. Muon propagation in ice.

To study the effect of uncertainties in absolute DOM efficiency and absorption and scattering properties of the ice, a set of signal simulations were generated for one year of data with DOM efficiencies differing from the baseline by $\pm 10\%$ for certain benchmark signals of interest. For these benchmark signals, signal simulation was also generated varying absorption and scattering parameters by $\pm 10\%$.

The % impact of these variations on $\Gamma^{Sens}_{\nu\to\mu}$ are summarized in table 5.8.

5.6.2 Astrophysical Uncertainties

The impact of astrophysical uncertainties on the $\sigma_{\chi\text{-}p}$ calculated from $\Gamma^{90\%C.L}_{\nu\to\mu}$ has been studied in literature [110]. The leading sources of uncertainty are:

1. **The local density of DM ρ_{DM}:** The results are interpreted using a conservative benchmark value of 0.3 GeV/cm^3. This also allows a comparison with other experiments that assume this value. Depending on the method by which it is estimated, uncertainties exist on this quantity. Fits of rotation curves of the inner milky way to different halo models suggest a value of 0.4 GeV/cm^3 [80], at the average radial distance of the Sun from the Galaxy, while non parametric methods using the z axis dispersion of the velocities of stars suggest a local value of ~ 0.7 GeV/cm^3 [79] at the specific location of the Sun, hinting at a slight non asphericity of the halo. All limits on $\sigma_{\chi\text{-}p}$, from this search as well as from direct detection experiments depend on ρ_{DM}.

2. **The DM velocity distribution:** A Standard Maxwellian Halo (SMH) velocity distribution is assumed [157]. However, N-body simulations of DM halos suggest variations from this benchmark due to local non uniformities[158, 159]. The spin dependent capture rate for velocity distributions obtained from two of these simulations[158, 159] have been evaluated in [110] and the impact has been found to be $\leq 20\%$.

3. **The escape velocity of the Galaxy:** The escape velocity of the Galaxy introduces a cutoff on the velocity distribution and thus affects the capture rate. However, the maximum effect of this has been found to be $\leq 3\%$[110].

4. **The velocity of the Sun:** The velocity of the Sun in the Galactic rest frame is assumed to be 230 km/s[160]. The impact of the maximum uncertainties in this value on the capture rate has been found to be $\sim 10\%(\sim 30\%)$ at low (high) WIMP masses.

5. **Solar mass and composition:** The Standard Solar Model [161] is assumed. For spin dependent scattering, the dominant contribution is from hydrogen, which makes up $\sim 74\%$ of the mass of the Sun. The impact of an alternative solar model on the SD capture rate has been found to be $< 4\%$, while for SI scattering it is $\sim 25\%$, due to the disproportionate contribution of heavier nuclei, the abundances of which in the Sun are known less precisely.

6. **Dark Disk:** Massive satellite accretions onto early Galactic disks can lead to a component of DM in addition to the halo in the configuration of a disk, corotating with the baryonic disk of the Galaxy. This can significantly increase Solar capture rates and thus dramatically improve the constraints on $\sigma_{\chi\text{-}p}$[110] from Solar WIMP searches, while the constraints from direct detection experiments are less affected due to the low relative velocity of this component of DM. The results presented above assume no dark disk fraction and are thus conservative. However, ref. [162] provides an interactive tool to estimate the impact of the dark disk fraction (as well as other astrophysical uncertainties) on $\sigma_{\chi\text{-}p}$.

In summary, except for the uncertainty in DM density, ρ_{DM} and with respect to the presence of a dark disk, astrophysical uncertainties on $\sigma_{\chi\text{-}p}$ are of the order of $\sim 20\%(\sim 50\%)$ at low (high) WIMP masses. The results presented above are conservative with respect to the uncertainties on ρ_{DM} and the possible presence of a dark disk.

5.7 Interpretations

5.7.1 Effective Field Theories

For any general theory with a WIMP candidate, with the interaction between the WIMP and SM particles mediated by a particle of mass M much larger than that of the WIMP, the WIMP-SM interaction can be described by an effective Lagrangian of the form:

$$\mathcal{L}_{effective} = \mathcal{L}_{SM} + \sum \frac{f^{(n)}}{\Lambda^{n-4}} \mathcal{O}^{(n)} \tag{5.10}$$

where $f^{(n)}$ are dimensionless constants, $\mathcal{O}^{(n)}$ are operators of mass dimension n and $\Lambda \sim M$ indicates the scale of new physics in the UV complete theory[163, 164].

Results from direct, indirect and collider searches for DM have been studied in the framework of these effective operators[165, 166]. Ref. [164] examines the various operators and concludes that for fermionic WIMPs, the following two operators of mass dimension 6

$$\mathcal{O}_{AA}^{(6)} = \bar{\chi}\gamma_\mu\gamma^5\chi\bar{q}\gamma^\mu\gamma^5 q \tag{5.11}$$

$$\mathcal{O}_{TT}^{(6)} = \bar{\chi}\sigma_{\mu\nu}\chi\bar{q}\sigma^{\mu\nu}q \tag{5.12}$$

with an axial-vector and tensor type interactions respectively lead to spin-dependent WIMP-proton scattering, with the latter vanishing for Majorana fermions. For these operators, the WIMP-proton scattering cross section in the non relativistic limit has been shown to be:

$$\sigma_{SD,AA} = \frac{4\mu^2}{\pi}\left[\sum_q d_q\lambda_q\right]^2 J_N(J_N+1) \tag{5.13}$$

and

$$\sigma_{SD,TT} = \frac{16\mu^2}{\pi}\left[\sum_q b_q\lambda_q\right]^2 J_N(J_N+1) \tag{5.14}$$

respectively for Dirac fermions. Here, μ is the WIMP-proton reduced mass, λ_q is the fraction of the spin of the nucleon carried by the quark q, and J_N is the spin of the nucleus N. d_q and b_q (with mass-dimension -2) are the coupling strengths of a quark q.

Similarly for real Vector Boson WIMPs, the relevant operator for spin-dependent scattering has been found to be:

$$\mathcal{O}_{VB}^{(6)} = \epsilon^{\mu\nu\rho\sigma}B_\mu^{(\dagger)}(\partial_\nu B_\rho)\bar{q}\gamma_\sigma\gamma^5 q \tag{5.15}$$

giving the non-relativistic scattering cross section:
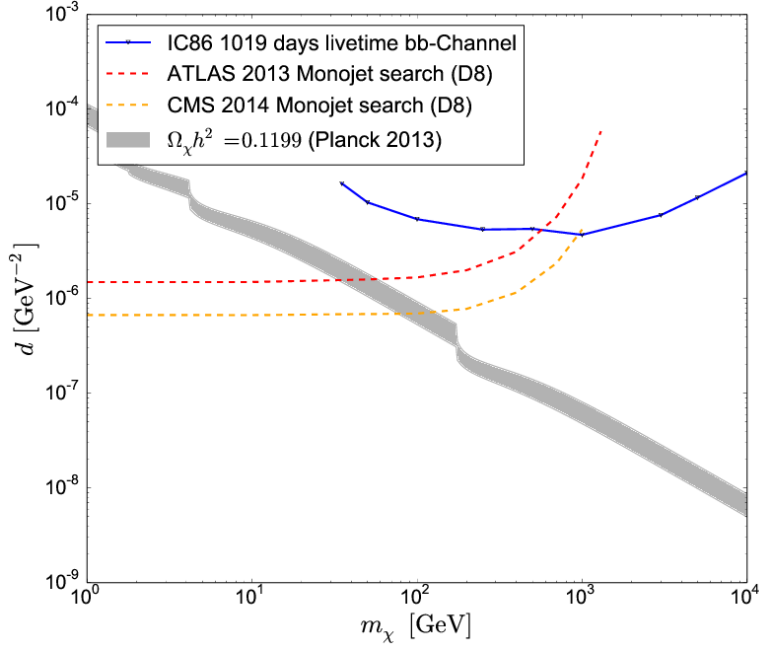
FIGURE 5.37: Constraints on the coupling to quarks for the axial vector interaction, for a Majorana Fermion WIMP that couples universally to all quarks. To be conservative, only constraints assuming the 100% annihilation to $b\bar{b}$ are shown, as it is not possible to construct a theory in which the WIMP can annihilate 100% into W^+W^- or $\tau^+\tau^-$ and still scatter off quarks.

$$\sigma_{SD,VB} = \frac{8\mu^2}{3\pi} \left[\sum_q c_q\lambda_q \right]^2 J_N(J_N+1). \tag{5.16}$$

Here, c_q is again a coupling strength with mass dimension -2. The limits set by IceCube on the WIMP-proton spin dependent scattering cross section can thus be used to set constraints on these couplings, under assumptions that they are either universal ($d_q = d$, $c_q = c$ and $b_q = b$) or Yukawa-like ($d_q = dm_q/m_e$ and so on).

Figure 5.37 shows such constraints for the axial vector case and are compared against constraints from missing transverse energy (E_T) searches carried out at colliders.

5.7.2 MSSM Scans

Supersymmetry remains well motivated despite the lack of detection at terrestrial colliders. In general, neutralino DM will scatter off nuclei through both SD and SI processes. Of particular interest to the solar WIMP search are the models with so-called 'well tempered' neutralinos, exhibiting a mixed gaugino-Higgsino character, and enhanced SD scattering cross sections due to which the solar capture rate is boosted[153].

Experimentally well motivated benchmark examples of the MSSM that predict the observed Higgs mass and dark matter relic density while avoiding the LHC constraints as of 2013 have been presented

TABLE 5.9: Snowmass benchmark MSSM models, their predicted SD and SI scattering cross sections, and capture rates in the Sun. The capture rates have been calculated by assuming that the neutralino of the model makes up 100% of the DM fraction. For the $\tilde{B} - \tilde{q}$ coannihilation model, this is not true[167] and hence the capture rate is optimistic. 90%C.L upper limits on the annihilation rates of WIMPs with the same mass and branching ratios are also shown.

M_χ (GeV)	Model description	Annihilation Channels	$\sigma_{\chi\text{-}p}^{SD}$ (cm^2)	$\sigma_{\chi\text{-}p}^{SI}$ (cm^2)	C_C (s)$^{-1}$	$\Gamma_{Ann}^{90\%C.L.}$ (s^{-1})
754.1	$\tilde{B} - \tilde{t}$ coannihilation	$\tau^+\tau^-$-79% $b\bar{b}$-15%	1.49×10^{-45}	1.45×10^{-47}	9.235×10^{16}	7.24×10^{19}
1047.5	Pure $\tilde{h}$	W^+W^--50% ZZ-6%	2.47×10^{-44}	1.75×10^{-46}	6.34×10^{17}	1.67×10^{20}
853.8	$\tilde{B} - \tilde{q}$ coannihilation	gg-69% $b\bar{b}$-29%	4.63×10^{-41}	1.64×10^{-47}	2.74×10^{20}	2.97×10^{12}
1013.4	A funnel	$\tau^+\tau^-$-10% $b\bar{b}$-72%	1.86×10^{-44}	3.10×10^{-47}	1.57×10^{17}	2.79×10^{20}
148.3	$\tilde{B} - \tilde{H}$ 'Well tempered'	W^+W^--53% ZZ-37%	3.05×10^{-40}	4.33×10^{-44}	3.87×10^{22}	1.52×10^{22}

in [167]. These points have been taken from scans of the phenomenological MSSM and are consistent with direct detection limits from XENON 100, in addition to other constraints from Big Bang Nucleosynthesis as well as diffuse photon and neutrino flux measurements. The compatibility of an MSSM model with the results of this analysis can be tested by the following process. a) From the theoretically predicted SD and SI neutralino-nucleon cross sections, the total expected capture rate in the Sun can be calculated using DarkSuSy. b) From the theoretically predicted branching ratios of the various annihilation channels of the neutralino, using `WimpSim` the total expected neutrino flux in IceCube can be calculated. c) Limits can be derived on the same flux based on which a decision can be made whether the model can be excluded or not. Table 5.9 lists the models from [167] as well as their capture rates in the Sun, leading annihilation channels and constraints from IceCube.

The upper limit on the annihilation rate of a 148.3 GeV WIMP with the branching ratios of the 'well tempered' $\tilde{B}-\tilde{H}$ neutralino is less than half the predicted capture rate and since the predicted capture rate is high enough to warrant assuming equilibrium, this model can be excluded at more than 90% C.L. The signal predictions from all other models in table 5.9 are far beneath IceCube sensitivity.

5.7.3 The 750 GeV $\gamma\gamma$ resonance as a portal to the dark sector.

Reference [168] considers the scenario wherein the emerging 750 GeV diphoton excess at ATLAS and CMS is a pseudoscalar (P) portal between the SM and a DM sector. The DM candidate itself can be either a Dirac fermion χ or a complex scalar ϕ, stable under a $\mathbb{Z}_2$ symmetry. A pseudoscalar was chosen because a scalar mediator would lead to the WIMP-proton scattering being spin-independent and consequently highly constrained by DM direct detection. Since the mass of P (750 GeV) is above the electroweak symmetry breaking scale of ~ 246GeV, its decay into $\gamma\gamma$ is made possible through a coupling to $B\widetilde{B}$ in an explicitly $SU(2)_L$-invariant way. This also guaranties decay to ZZ and $Z\gamma$ with
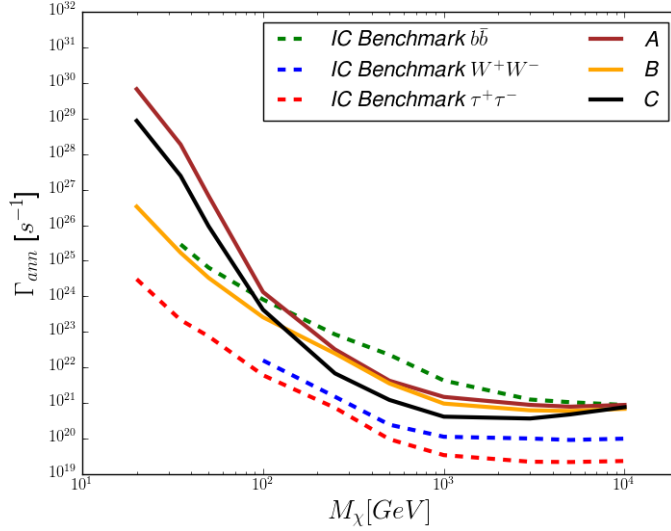
FIGURE 5.38: Limits on Γ_{Ann} for the three IceCube benchmark channels, as well as for DM mediated by a 750 GeV pseudoscalar particle with SM couplings according to the three scenarios described in this section.

partial decay widths proportional to $cos^4\theta_W$, $4sin^2\theta_W cos^2\theta_W$, and $cos^4\theta_W$ respectively, where θ_W is the weak mixing angle.

The choice of other SM couplings for P are dictated by various requirements. The non observance of the resonance in the LHC Run-1 (at a centre of mass energy of 8 TeV) strongly constrains the couplings of P to SM particles with significant parton distribution functions (PDF) in the proton at 8 TeV, such as light quarks. However, since the resonance does appear in Run 2 at 14 TeV centre of mass energy, P has to couple to something more than just photons as the photon PDF of a proton does not change much between 8 and 14 TeV. This leaves gluons, b quarks and t quarks. Three scenarios A,B and C were considered by the authors as explained in ref. [168], with a P coupling to gluons alone, gluons and b quarks, and gluons and t quarks respectively, in addition to B, u and χ. The specific values of the partial decay widths of P into these channels for the three scenarios are given in ref. [168]. This also determines the branching ratios of the $\chi\bar{\chi}$ annihilation. While these branching ratios can be used to predict precise ν fluxes at IceCube and set precise constraints on Γ_{Ann} as described in sec. 5.7.2, due to the fact that the data from this search has not been publicly released by the IceCube collaboration at the time of this work, an analytical approximation described in ref.[168] was used to rescale benchmark limits on Γ_{Ann}. Figure 5.38 shows the limits on Γ_{Ann} for the three IceCube benchmark channels as well as the three scenarios considered.

In the non relativistic limit, this can be interpreted as a constraint on WIMP-proton scattering. However, for ϕ and χ, WIMP-proton scattering in the nonrelativistic limit is described by neither of the simple spin-dependent or spin independent scenarios considered within this chapter, but by the nonrelativistic Galilean invariant operators $i(\vec{S}_N \cdot \vec{q})$ and $(\vec{S}_\chi \cdot \vec{q})(\vec{S}_N \cdot \vec{q})$ respectively, corresponding to $\mathcal{O}_{11}$ and $\mathcal{O}_6$ of ref. [112]. Using the capture rates evaluated in ref. [112], constraints were calculated on
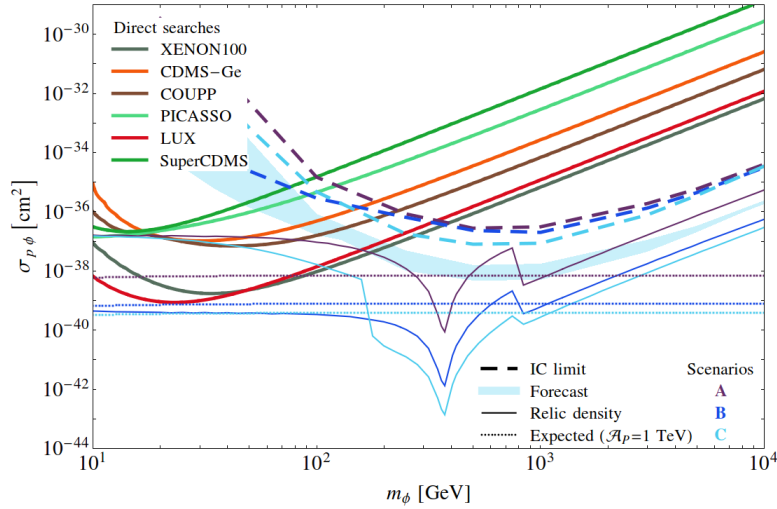
FIGURE 5.39: Limits from IceCube on $\sigma_{p\phi}$ for DM mediated by a 750 GeV pseudoscalar particle with SM couplings according to the three scenarios described in this section, as well as from direct detection experiments. Theoretically realistic values are also shown, as well as the values required to obtain the correct relic abundance of DM in the universe. The blue band corresponds to the predicted reach of a detector with 300 times the current exposure of IceCube. Figure taken from [168].

$\sigma_{p\phi}$ and $\sigma_{p\chi}$. In both scenarios IceCube gives the most stringent constraints for WIMP masses above $\sim$200 GeV. For the fermionic DM, the double velocity suppression in $\mathcal{O}_6$ renders the Solar capture rate too low and no neutrino telescope will ever achieve sensitivities required to see the signal.

However for the scalar DM, as shown in Figure 5.39, IceCube constraints are just ~ 1 order of magnitude above realistic theoretical predictions of $\sigma_{p\chi}$.

5.7.4 Isospin Violating Dark Matter

DM that has significantly different couplings to neutrons and protons has been proposed in order to alleviate the tension between CoGeNT and DAMA best fit cross sections as well as the null results from other experiments such as XENON and CDMS[169]. This scenario introduces an additional degree of freedom, the ratio between the couplings to neutrons and protons, indicated by f_n/f_p. For an isotope i with A_i nucleons out of which Z_i are protons, the ratio of the isospin-violating (IV) and isospin conserving (IC) cross sections is given by

$$\frac{\sigma_i^{IV}}{\sigma_i^{IC}} \sim \frac{[Z_i + (A_i - Z_i)f_n/f_p]^2}{A_i^2} \tag{5.17}$$

The constraints from a specific isotope i can be completely avoided for DM with $f_n/f_p = -Z_i/(A_i - Z_i)$, since the scattering amplitude will disappear entirely.

The suppression in the capture rate in the Sun due to isospin violation has been shown to be much weaker than in the case of signal rates in direct detection experiments [170]. Figure 5.40 illustrates
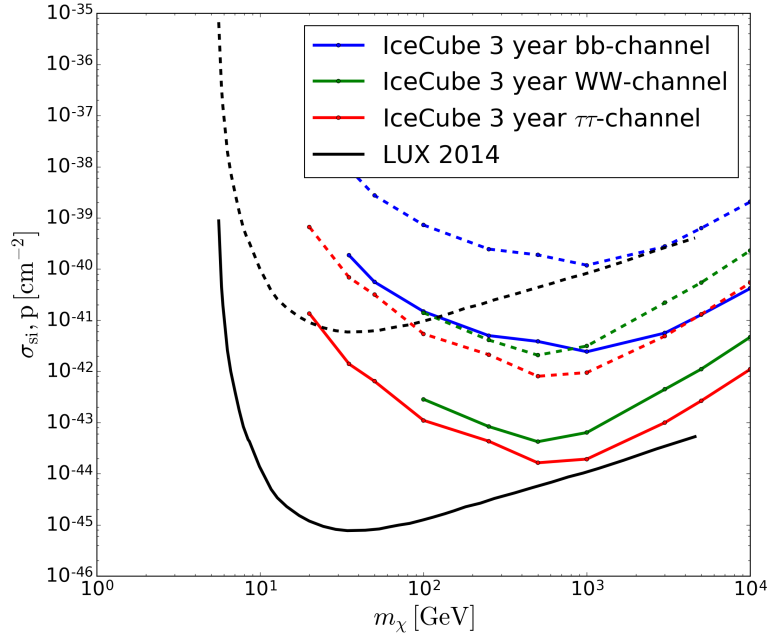
FIGURE 5.40: Constraints on $\sigma^{SI}_{\chi\text{-}p}$ for $f_n/f_p = 0$ (solid lines) and $f_n/f_p = -0.7$ (dashed lines).

the limits on $\sigma^{SI}_{\chi\text{-}p}$ from IceCube and LUX in both IC and IV scenarios for comparison. While LUX constraints are worse by ~ 4 orders of magnitude, IceCube constraints are worse only by an order of magnitude. Solar WIMP neutrino searches that are sensitive to WIMP masses below 10 GeV, such as those by Super-K and the future PINGU are the best ways of exploring the IVDM parameter near the DAMA/CoGeNT signal regions[170].

Chapter 6

Searches for Neutrino Emission from Galactic SNRs and Microquasars

6.1 Introduction

This chapter describes the searches carried out for neutrino emission from potential Galactic sources. Stacking searches were carried out for neutrino sources from Galactic SNRs, classified into subcatalogs based on morphology and source properties. A search was also carried out for periodic neutrino emission from microquasars.

6.2 Event Selection

The searches of this chapter and chapter 7 use the four year point source samples of throughgoing muons. These samples come from three years of operation of IceCube in the incomplete 40-, 59- and 79-string configurations [171, 172] as well as in one year of operation of the completed 86-string detector [140, 147]. The angular resolution of this sample has improved over the years, benefiting from the larger instrumented volumes achieved as the number of strings was increasing as well as from improvements in the reconstruction methods (see figure 6.1). These samples are dominated by muons from charged-current interactions of atmospheric ν_μ (and $\bar{\nu}_\mu$) in the northern hemisphere (up-going data) and muons produced by interactions of cosmic rays with the Earth's atmosphere in the southern hemisphere (down-going data). In the northern sky, the effective area of the detector, determined by the analysis cuts and the opacity of the Earth for neutrinos with energies above ~ 100 TeV, leads to a sample of events peaked in the $1\,\mathrm{TeV} - 1\,\mathrm{PeV}$ range. In the southern sky the sensitivity is in the $100\,\mathrm{TeV}$ - $100\,\mathrm{PeV}$ range (see Figure 6.2) due to the overwhelming background of atmospheric muons that needs to be reduced by imposing a higher threshold cut on the energy proxy.
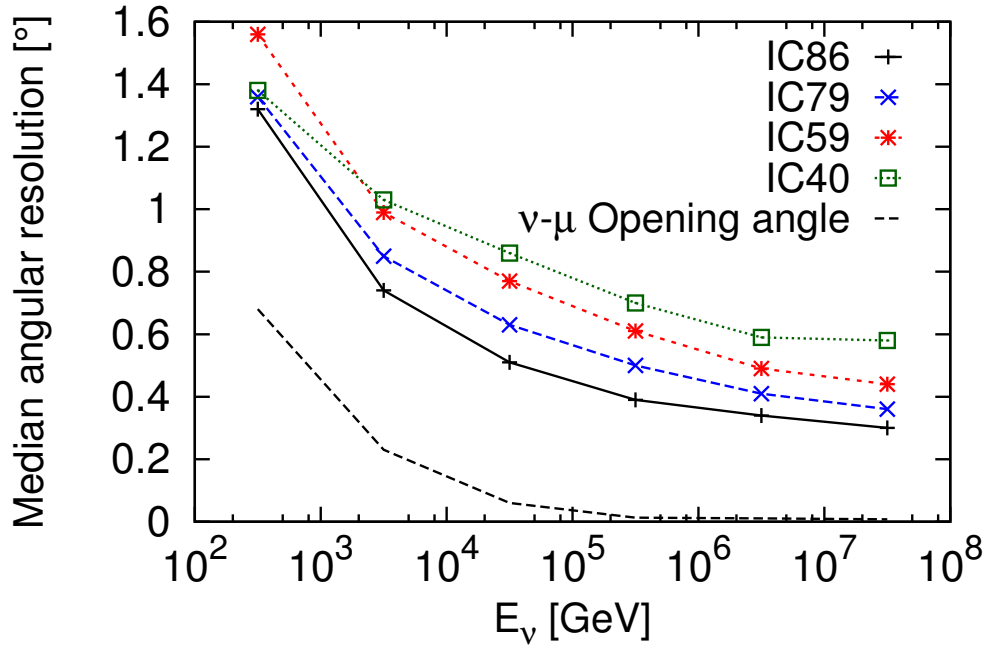
FIGURE 6.1: Muon neutrino angular resolution for the northern sky (up-going events), defined as the median of the angle between the true neutrino direction and the reconstructed muon direction. The resolution is given for different analysed samples as a function of the neutrino energy after all cuts used to select the final samples for the neutrino point-source searches. The kinematic angle between the muon and the neutrino is also shown with a dashed line. Image taken from [173].
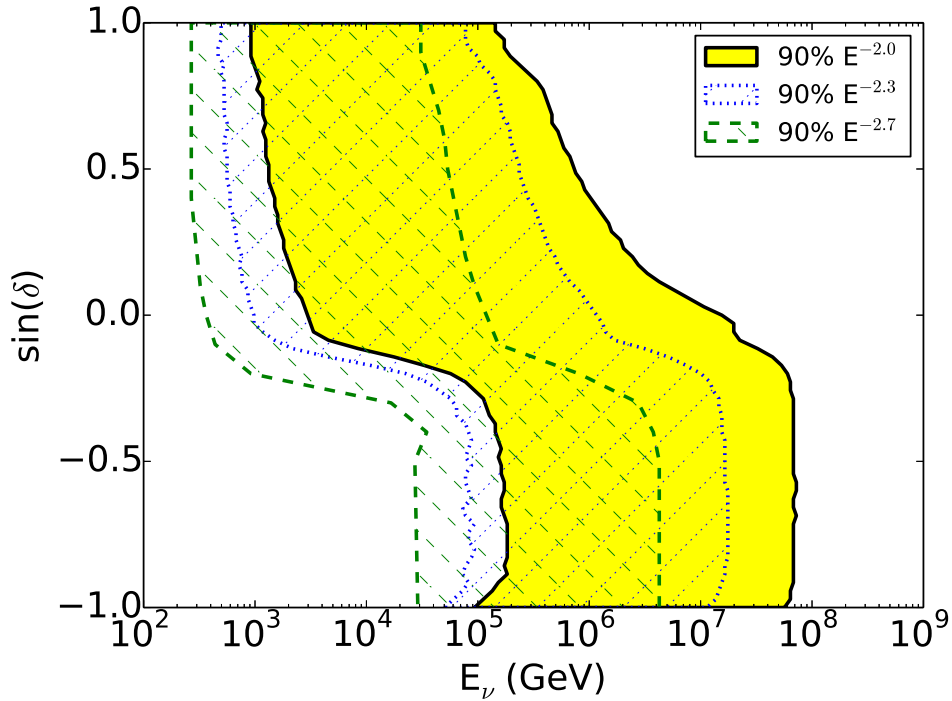
FIGURE 6.2: Neutrino energy interval containing 10% to 90% of the simulated signal events for different spectra and declinations for the four-year combined point-source samples after all analysis cuts are applied. Image taken from [173].

All-sky and catalog searches for point sources using these samples have produced results completely consistent with the background only hypothesis[140].

6.3 Stacking Searches

6.3.1 Search for neutrino emission from SNRs with Molecular Cloud Associations

A Giant Molecular Cloud (GMC) embedding, or in the vicinity of an SNR is a very interesting source from the point of view of neutrino astronomy. Since SNRs are the leading Galactic candidate source of CRs, a GMC near an SNR will serve as a target for these CRs, converting a significant fraction of the primary CR energy into γ-ray and neutrino emissions through p-p interactions[174]. The SNRs in the γ spectrum of which Fermi has found evidence of π^0 decay - IC443 and W44, both interact with nearby GMCs[124].

A selection was applied on the sources in SNRCat to reject the ones without certain molecular cloud interactions. Subsequently, sources that have neither been observed in the TeV nor are younger than 10000 years were also removed. This rejects sources that are too old to be in the Sedov-Taylor phase[123] (see section 3.5.1.1). The ten SNRs that survived these selection criteria are listed in Table 6.1. Due to the different properties of the selected IceCube events in the northern and southern skies, the selection is further split into two based on whether their declination is positive (northern sky) or negative (southern sky) and the two catalogs are stacked separately. Both W44 and IC443 have made it to the selection in the northern sky. Notable sources that make it to the six southern sky sources include Sagittarius A East, the SNR close to Sagittarius A*, the black hole near the centre of the Galaxy and RXJ1713-3946.

The measured flux of these sources integrated above 1 TeV can be expressed in Crab units (as a fraction of the Crab flux), and is used as the theoretical weight in the likelihood. For sources such as IC443 and W44 for which only the integrated flux above 0.3 TeV in Crab units have been published, the flux normalization and published best fit spectral index has been used to calculate the flux integrated above 1 TeV. The brightest source by far is RXJ1713.7-3946, which is 66% as bright as the Crab, integrated above 1 TeV.

SNRCat Name	Other Names	R.A (°)	DEC (°)	Flux (in Crab Units)	Age (yr)	Distance (kpc)	Observations and References
G000.0+00.0	Sgr A East	266.44	-29.0	5%	Shell: 1200 - 10000	Shell: 8	Chandra, XMM SUZAKU, ASCA
G029.7-00.3	Kes 75	281.60	-2.98%	Shell: 900 - 4300 Pulsar: 723	Shell: 6.3 - 10.6 Pulsar: 19	Chandra, ASCA	
G031.9+00.0	3C391, Kes 77	282.35	-0.917	0.8%	Shell: 3700 - 4400	Shell: 7.2 - 8.6	Chandra, XMM ROSAT, ASCA
G034.7-00.4	W44, 3C392	284.0	1.38	2%	Shell: 6000 - 29000 Pulsar: 20400	Shell: 2.5 - 2.6 Pulsar: 3	Chandra, XMM, SUZAKU, ROSAT ASCA, FERMI, AGILE
G043.3-00.2	W49B, 3C398	287.78	9.1	0.5%	Shell: 4000 - 6000	Shell: 8 - 11	Chandra, XMM, SUZAKU, ROSAT, ASCA
G189.1+03.0	IC443, 3C157, Sh2-248	94.25	22.57	1.6%	Shell: 3000 - 30000	Shell: 0.7 - 2	Chandra, XMM, SUZAKU, ROSAT, ASCA, FERMI, AGILE, VERITAS
G347.3-00.5	RX J1713.7-3946	258.46	-39.75	66%	Shell: 1000 - 10000	Shell: 1 - 6	Chandra, XMM, SUZAKU ROSAT, ASCA, FERMI, HESS
G348.5+00.1	CTB 37A	258.525	-38.53	3%	Shell: 2000 - 30000	Shell: 6.3 - 9.5	Chandra, SUZAKU, HESS
G349.7+00.2		259.50	-37.43	1.2%	Shell: 2800 - 3500	Shell: 11.2 - 22.4	Chandra, ASCA
G049.2-00.7	W51C	290.958	14.1	3%	Shell: 26000 - 30000	Shell: 4.3 - 6	Chandra, SUZAKU, ROSAT ASCA, FERMI, HESS, MAGIC

TABLE 6.1: The sources from SNRCat with confirmed Molecular Cloud interactions that are considered for the search. The Flux in Crab units is integrated above 1 TeV.

6.3.2 Search for neutrino emission from PWNs

Pulsar Wind Nebulae (PWN) are clouds of dust and ionized gasses in which particles are accelerated to relativistic velocities by the rapidly spinning magnetic field of a pulsar. These relativistic nuclei can interact with the nebula and produce γ-rays and neutrinos[175]. PWNs are often observed within the shell of an SNR. The pulsar soon loses energy through electromagnetic dipole radiation and also from transferring energy to relativistic wind and consequently spins down. As a result, only the youngest of PWNs are expected to produce a neutrino flux above the sensitivity of terrestrial neutrino detectors such as IceCube[176].

From SNRCat, sources younger than 10000 years with confirmed PWN associations were selected. These ten sources are listed in Table 6.2, and include SNRs such as W33 and the Crab. Out of these,three are in the northern sky while the remaining seven are in the southern sky, and the two skies are stacked separately. Due to the inverse linear relationship expected between the neutrino luminosity and age [176], the theoretical weight in the likelihood was chosen to be $1/(A*D^2)$ where A is the age of the SNR (in 10000 years) and D is the distance to the SNR (in kPc).

6.3.3 Search for neutrino emission from young SNRs

Sources from SNRCat that are younger than 10000 years but did not make it to either of the previous selections were included in this search. The resulting 29 sources include the remnants of historically relevant SNs such as Tycho and Cassiopeia A and are listed in 6.3. The pulsars at the center of such SNRs are expected to accelerate ions up to energies of ~ 1 PeV [177]. These ions can interact with X-rays and produce pions. In contrast to the scenario with PWNs and molecular clouds (where the pion production was mostly from p-p interactions), in this scenario the p-γ interactions dominate.

Of the 29 sources, 10 are in the northern sky while the remaining are in the southern sky. The two skies are stacked separately and the theoretical weight is chosen to be $1/(A*D^2)$ as before.

SNRCat Name	Other Names	R.A (°)	DEC (°)	Weight	Age (yr)	Distance (kpc)	Observations and References
G000.9+00.1		266.84	-28.15	0.15	Shell: 1900 Pulsar: 5000	Shell: 10 Pulsar: 13	Chandra, XMM
G011.2-00.3		272.86	-19.42	0.009	Shell: 960 - 3400 Pulsar: 23500	Shell: 5 - 10 Pulsar: 5	Chandra, XMM ROSAT, ASCA
G012.8-00.0	W33	273.40	-17.82	1.064	Shell: 1200 Pulsar: 5000	Shell: ≥ 4 Pulsar: 4.7	Chandra, XMM,
G021.5-00.9		278.39	-10.58	0.44	Shell: 720 - 1070 Pulsar: 4800	Shell: 4.3 - 5.1 Pulsar: 4.7	Chandra, XMM ROSAT, ASCA
G054.1+00.3		292.63	18.87	0.069	Shell: 2500 - 3300 Pulsar: 2900	Shell: 5.6 - 7.2 Pulsar: 5	Chandra, XMM SUZAKU, ROSAT, ASCA
G093.3+06.9	DA 530, 4C(T)55.38.1	313.10	55.35	0.034	Shell: 1000 - 5000	Shell: 1.7 - 2.7	Chandra, XMM,
G263.9-03.3	Vela, Pencil Nebula	128.5	-45.83	0.308	Shell: 9000 - 27000 Pulsar: 11200	Shell: 0.25 - 0.3 Pulsar: 0.29	Chandra, XMM, SUZAKU ROSAT, ASCA, FERMI, HESS
G292.0+01.8	MSH 11-54	171.15	-59.27	0.057	Shell: 2930 - 3050 Pulsar: 2900	Shell: 6 Pulsar: 6	Chandra, XMM ROSAT, ASCA
G292.2-00.5		169.83	-61.47	0.063	Shell: 4200 - 7100 Pulsar: 1900	Shell: 8 - 8.8 Pulsar: 8.4	Chandra, ROSAT ASCA, HESS
G184.6-05.8	Crab Nebula, 3C144 SN1054, NGC 1952, M1	83.629	22.017	0.56	Pulsar: 5000	Shell: 1.5 - 2.5 Pulsar: 2	Chandra, XMM, ROSAT ASCA, FERMI, HESS

TABLE 6.2: PWNs from SNRCat that are selected for the search. The weight corresponds to $1/(A * D^2)$.

6.3.4 Search for neutrino emission from 6 Milagro TeV gamma ray sources with SNR associations

The Milagro experiment, a water Cherenkov detector sensitive to TeV γ-rays, found 6 sources in its survey of the Galactic plane [178] with SNR associations. These sources were remarkable for being the sources of the highest energy γ-rays detected so far, with the spectrum extending into energies of tens of TeV. Directional air Cherenkov telescopes were subsequently pointed at three of these sources and they were found to have a spectrum consistent with E^{-2} with no evidence of a cutoff up to energies of a few tens of TeV, making them potential PeVatrons [179, 180], in sharp contrast to other well studied Galactic SNRs.

Of the six sources, four are in the Cygnus region, a well studied region known to show a diffuse excess of γ-ray production even after known point sources have been accounted for. Table 6.5 lists the sources, coordinates and observed extensions. Despite later being confirmed to be below the 5σ statistical significance level, MGRO J1852+01 is kept due to the relatively high level of flux.

Neutrino flux predictions for the sources were calculated based on the observed γ-ray spectra and published in [181] under the assumption that the sources cut off at 300 TeV. Ref. [182] calculates the IceCube event rates for various values of the spectral index and cutoff, and concludes that IceCube should be able to observe the neutrino flux from these sources at 5σ confidence level within 3 years.

The Milagro collaboration subsequently analysed the spectrum and morphology of MGRO J2031+41 and MGRO J2019+37 and concluded that the spectra are best described by an exponential cutoff at 24 TeV and 29 TeV with spectral indices of -2.7 and -2.0 respectively [183]. A similar analysis of MGRO J1908+06 by the ARGO-YBJ experiment concluded that the cutoff was much lower than previously reported [184], with a best fit value of 44 TeV.

Consequently a more realistic neutrino flux was derived from this spectral information using the method of [185]. Using a parametrization of the pion and secondary particle production in hadronic interactions, the authors have shown that both the γ and ν fluxes are of the form:

$$\frac{dN_{\gamma/\nu}}{dE_{\gamma/\nu}} \approx k_{\gamma/\nu}(\frac{E_{\gamma/\nu}}{1TeV})^{-\Gamma_{\gamma/\nu}}exp(-\sqrt{(\frac{E_{\gamma/\nu}}{\epsilon_{\gamma/\nu}})}) \tag{6.1}$$

where the parameters k, Γ, and ϵ are given by

$$k_\nu \approx (0.71 - 0.16\alpha)k_\gamma, \tag{6.2}$$

$$\Gamma_\nu \approx \Gamma_\gamma \approx \alpha - 0.1, \tag{6.3}$$

and

$$\epsilon_\nu \approx 0.59\epsilon_\gamma \approx \epsilon_p/40. \tag{6.4}$$

SNRCat Name	Other Names	R.A (°)	DEC (°)	Weight	Age (yr)	Distance (kpc)	Observations and References
G001.9+00.3		267.19	-27.17	0.635	Shell: 150 - 220	Shell: 8.5	Chandra,
G015.9+00.2		274.72	-15.03	0.059	Shell: 1000 - 3000	Shell: 8.5	Chandra,
G027.4+00.0	Kes 73, 4C-04.71	280.33	-4.93	0.121	Shell: 500 - 1500 Pulsar: 4300	Shell: 7.5 - 9.1	Chandra, ROSAT, ASCA,
G033.6+00.1	Kes 79, 4C00.70, HC13	283.2	0.68	0.016	Shell: 3000 - 15000	Shell: 7.1	Chandra, ROSAT, ASCA,
G035.6-00.4		284.43	2.197	0.121	Shell: 2300 Pulsar: 160000	Shell: 3.2 - 4 Pulsar: 8	HESS,
G078.2+02.1	W66, DR4, gamma Cygni	305.21	40.43	0.028	Shell: 8000 - 16000	Shell: 2 - 4	Chandra, ROSAT, ASCA, FERMI, VERITAS
G107.5-01.5		342.71	57.48	0.202	Shell: 3000 - 6000	Shell: 1.1	ROSAT
G111.7-02.1	Cassiopeia A, W81, 3C461	350.86	58.8	0.86	Shell: 316 - 352	Shell: 3.3 - 3.7	Chandra, XMM SUZAKU, ROSAT
G114.3+00.3		354.25	61.92	0.186	Shell: 7700	Shell: 0.7	ROSAT, FERMI
G116.9+00.2	CTB 1	359.79	62.43	0.031	Shell: 7500 - 15000	Shell: 1.6 - 3.5	Chandra, XMM ROSAT, ASCA
G120.1+01.4	Tycho, 3C10, SN1572	6.325	64.15	0.676	Shell:	Shell: 1.7 - 5	Chandra, XMM SUZAKU, ROSAT, ASCA
G160.9+02.6	HB9	75.25	46.67	0.076	Shell: 4000 - 7000	Shell: 0.8 - 4	Chandra, XMM SUZAKU, ROSAT
G260.4-03.4	Puppis A, MSH 08-44	125.542	-43.0	0.099	Shell: 3700 - 5500	Shell: 2.2	Chandra, XMM, SUZAKU ROSAT, ASCA, FERMI
G272.2-03.2		136.708	-52.117	0.048	Shell: 3600 - 8700	Shell: 1.8 - 5	Chandra, XMM, SUZAKU ROSAT, ASCA
G296.5+10.0	PKS 1209-51/52	182.42	-52.42	0.033	Shell: 3000 - 20000 Pulsar: 340	Shell: 1.3 - 3.9	Chandra, XMM ROSAT, ASCA, FERMI
G296.7-00.9		178.89	-63.11	0.015	Shell: 5800 - 7600	Shell: 9.1 - 10.9	XMM, ROSAT,
G299.2-02.9		183.8	-65.5	0.0303	Shell: 4500 - 8700	Shell: 5	Chandra, ROSAT, ASCA,
G306.3-00.9		200.46	-63.56	0.0424	Shell: 1300 - 4600	Shell: 8	Chandra,
G308.4-01.4	G308.3-0L.4	205.35	-63.71	0.016	Shell: 5000 - 7500	Shell: 9.1 - 10.7	Chandra, ROSAT,
G309.2-00.6		206.63	-62.9	0.106	Shell: 700 - 4000	Shell: 2 - 6	Chandra, XMM ROSAT, ASCA
G315.4-02.3	RCW 86, MSH 14-63	220.75	-62.5	0.061	Shell: 2000 - 10000	Shell: 2.3 - 3.2	Chandra, XMM, SUZAKU ROSAT, ASCA, HESS
G318.2+00.1		223.708	-59.07	0.020	Shell: 8000	Shell: 3.5 - 9.2	HESS
G327.4+00.4	Kes 27	237.08	-53.82	0.0144	Shell: 2400 - 23000	Shell: 4.3 - 6.5	Chandra, ROSAT, ASCA,
G330.2+01.0		240.275	-51.57	0.1	Shell: 1000 - 3000	Shell: $\geq$ 5	Chandra, XMM, ASCA,
G332.4+00.1	Kes 32, MSH 16-51	243.83	-50.7	0.067	Shell: 300 - 3000	Shell: 7 - 11	Chandra, ROSAT, ASCA,
G337.2-00.7		249.87	-47.85	0.0833	Shell: 750 - 3500	Shell: 2 - 9.3	Chandra, ROSAT, ASCA,
G348.7+00.3	CTB 37B	258.48	-38.18	0.046	Shell: 350 - 3150 Pulsar: 950	Shell: 13.2	Chandra, SUZAKU, HESS,
G350.1-00.3		259.42	-37.4	0.246	Shell: 900	Shell: 4.5	Chandra, XMM,
G352.7-00.1		261.92	-35.12	0.037	Shell: 2200 - 5000	Shell: 6.8 - 8.4	Chandra, XMM, ASCA,

TABLE 6.3: Young PSRs from SNRCat that are considered for the search. The weight corresponds to $1/(A * D^2)$.
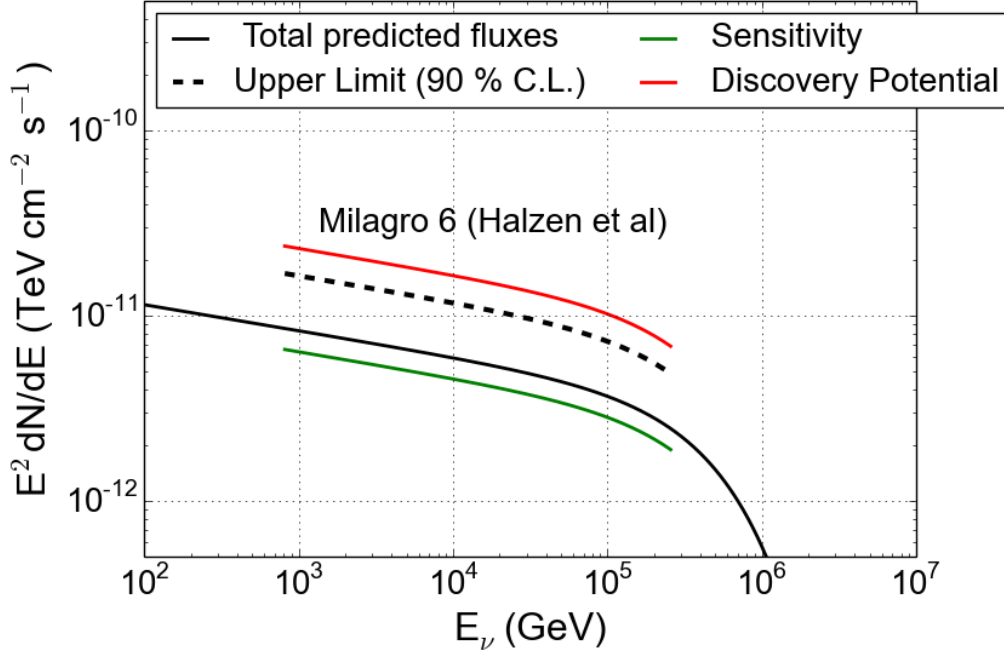
FIGURE 6.3: Upper Limits on the model of Halzen et al. [181] for the six Milagro sources with SNR associations. The flux required for sensitivity is beneath the model predictions. However, the excess observed at p-value of 0.02 makes the 90%C.L upper limits above the predictions.

where α is the primary proton spectral index. $\nu_\mu + \bar{\nu}_\mu$ fluxes were derived for the six sources based on their gamma ray spectral indices, normalizations and best fit cutoff values taken from [183] and [184]. For MGRO J2042+36, J2032+37 and J1852+01 for which these values are not available, an average cutoff of 31 TeV and a spectral index of 2 was used. The total flux predicted from this calculation is shown in figure 6.4 and referred to as M.F.2.in table 6.4.

These sources were included in a previous stacking search targeting 17 SNR candidates in the Fermi Bright Source List [186] using data from one year of the incomplete 40 string IceCube detector[172]. An *a-posteriori* examination of the data revealed an excess of neutrinos from these six sources that can be explained by random fluctuations of the background only 2% of the time. Consequently, in this analysis, data from the 40 string detector is not included in order to avoid bias. While the IC40 search utilized the relative normalization of the flux predictions from [181] as theoretical weights in likelihood, this search uses equal weights in the likelihood due to the unreliability of the assumptions in [181] as demonstrated.

6.3.5   Results

The results of all stacking searches are compatible with the background only hypothesis and are summarized in Table 6.4. The most significant deviation from the background only hypothesis was observed in the stacked search for neutrino emission from the six Milagro TeV γ-ray sources, with
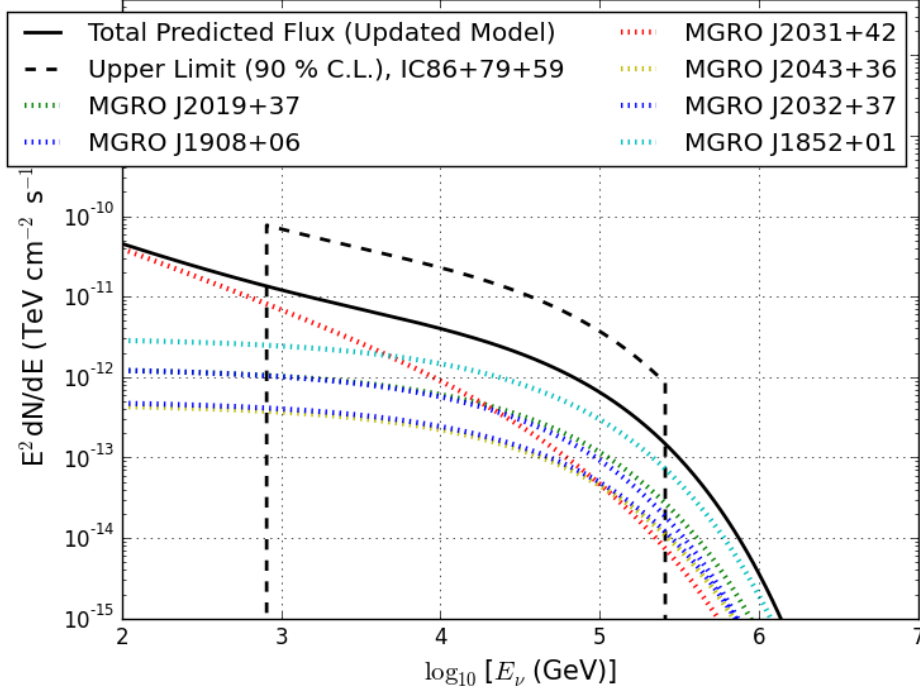
FIGURE 6.4: Upper Limits on the model M.F.2 described in section 6.3.4 based on updated γ-ray information, for the six Milagro sources with SNR associations. This flux prediction is significantly softer in spectrum compared to the prediction of Halzen et al. [181].

Catalog	$\hat{n}_S$	$\hat{\gamma}$	p-value	$\Phi^{90\%}_{\nu_\mu+\bar{\nu}_\mu}$
Milagro 6	51.4	3.95	0.02	$1.98\times$M.F. [181] $5.72\times$M.F.2
MC Associated SNRs	0.0	–	–	1.60×10^{-9} $\times\mathrm{E}^{2.7}$
Young SNRs	0.0	–	–	4.83×10^{-12} $\times\mathrm{E}^{2.0}$
Young PWNs	0.0	–	–	3.12×10^{-12} $\times\mathrm{E}^{2.0}$

TABLE 6.4: Results of the stacked searches for emission from source catalogs. M.F. stands for the model flux as described in the reference motivating the analysis, while M.F.2 is the model described in section 6.3.4. $\Phi^{90\%}_{\nu_\mu+\bar{\nu}_\mu}$ is the 90% confidence level upper limit on the combined flux of ν_μ and $\bar{\nu}_\mu$ from the catalogs. The $\mathrm{E}^{2.0}$ limits are in units of $\mathrm{TeV}^1\mathrm{cm}^{-2}\mathrm{s}^{-1}$.

a p-value of 0.02. The fitted spectral index of 3.95 however suggests that only low energy events contribute towards the observation and the observed significance is from spatial clustering only.

Figures 6.3 and 6.4 show the 90% C.L upper limits for the flux predictions of [181] as well as the model based on updated γ-ray information.

While the statistical significance of the excess is not high enough to allow a fit of the spectrum or to deconvolute individual source contributions a-posteriori point and extended source searches were carried out for the six sources separately. The resulting pre trial p values, fitted spectral indices and events are listed in table 6.5.

Source	R.A.($°$)	DEC ($°$)	Extension($°$)	$\hat{n}_s$	$\hat{\gamma}$	p-value
MGRO J2019+37	304.68	36.7	1.1	6.6	3.9	0.41
MGRO J1908+06	286.658	5.83	2.6	5.3	3.9	0.48
MGRO J2031+41	307.93	40.67	3.0	3.2	3.9	0.49
MGRO J2043+36	310.98	36.3	2.0	15.5	3.9	0.23
MGRO J2032+37	307.75	36.52	0	15.5	3.9	0.06
MGRO J1852+01	283.12	0.51	0	13.4	3.55	0.12

TABLE 6.5: A posteriori examination of the six Milagro sources.

6.4 Search for Periodic Neutrino emission from Microquasars

Microquasars that have also been observed to emit TeV γ-rays are potential candidates for neutrino emission. While evidence from multi wavelength observations mostly favours leptonic emission [187, 188], the possibility that protons or nuclei are being accelerated in the jets of these binary systems cannot be ruled out. The observation of neutrino emission from these sources would provide clear evidence for the presence of a hadronic component.

The neutrino flux from a binary system is expected to be periodically modulated, with a period equivalent to the orbital period of the binary system [126, 189, 190]. However, the duration, amplitude and phase of the recurring flares depend on parameters such as the angle between the line of sight and the axis of the binary system, as well as the velocity of the relativistic jet. Nevertheless, the knowledge of the period of the system from other observations can be used to boost IceCube's sensitivity towards such a periodic source.

6.4.1 The Method

The analysis method used here was previously applied to data from the IC-22 and IC-40 configurations of the IceCube detector, and is explained in detail in [191] and section 4.5 of this work.

The post-trial p-value of the most significant observation was estimated by calculating the fraction of time-scrambled datasets in which the most significant fluctuation observed among the ten sources was more significant than that which was observed in non-scrambled data. As can be seen in Figure 6.5, the search is more sensitive to flares of very short duration measured as a fraction of the period of the system.

As the considered periodic sources are not expected to change their long term behaviour the performance of this search improves as more data are included. For the source GRS1915+105, which has large relative uncertainty on the measured period, converting the event times into phases using the reported central value may lead to a smearing out of the actual flare if it happened with a different period within the error. The impact of this effect was evaluated and is illustrated in Fig. 6.6.
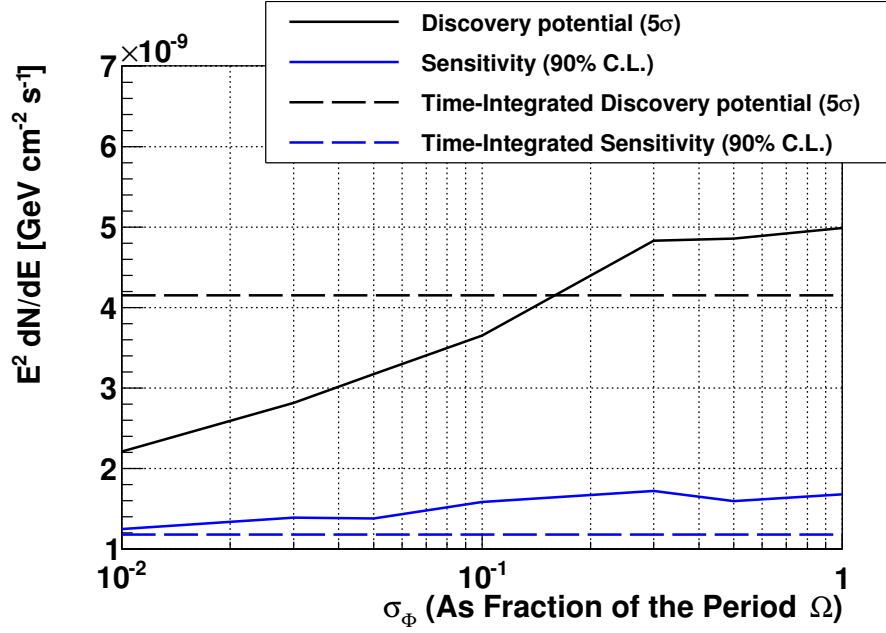
FIGURE 6.5: The power of the periodic search method. Discovery potential and sensitivity for four years of data (IC-40, IC-79, IC-59 and IC-86I) for periodic flares of varying width σ_Φ as a fraction of the total period (as defined in section 4.5), in terms of flux, for the source GRO J0422+32. The vertical axis denotes the mean flux over the period.
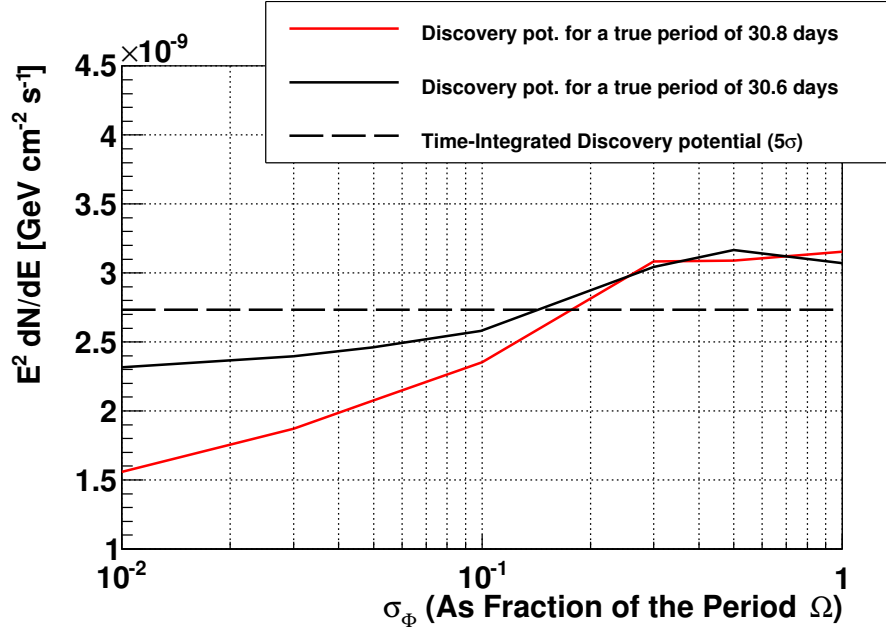
FIGURE 6.6: Impact of the uncertainty in the period. For the source GRS 1915+105, the reported period is 30.8 ± 0.2 days. While the median value of 30.8 days is used to convert event times to phase, if the true period happens to be 30.6, the 5σ discovery potential from this search for narrow flares is still better than that of the time integrated search.

Source [reference]	Period(days)	p-value	flare duration	phase	Time dependent 90% C.L. Upper Limit $(\mathrm{GeV^{-1}cm^{-2}s^{-1}})$	Time integrated 90% C.L. Upper Limit $(\mathrm{GeV^{-1}cm^{-2}s^{-1}})$
Cygnus X-1 [192]	5.599829 ± 0.000016	0.45	0.016	0.81	2.31×10^{-10}	2.33×10^{-9}
Cygnus X-3 [193]	0.199679 ± 0.000003	0.34	0.05	0.080	5.05×10^{-10}	1.70×10^{-9}
GRO J0422+32 [194]	0.212140 ± 0.000003	-	-	-	-	1.78×10^{-9}
GRS 1915+105 [195]	30.8 ± 0.2	0.31	0.17	0.28	3.33×10^{-10}	1.18×10^{-9}
LSI + 61 303 [187]	26.496 ± 0.0028	-	-	-	-	1.95×10^{-9}
SS 433 [189]	13.08227 ± 0.00008	-	-	-	-	6.5×10^{-10}
XTE J1118+480 [196]	0.1699339 ± 0.0000002	-	-	-	-	1.21×10^{-9}
HESS J0632+057 [188]	320 ± 5	0.087	0.0127	0.70	4.82×10^{-10}	1.37×10^{-9}
LS 5039 [197]	3.906 ± 0.002	-	-	-	-	5.24×10^{-9}
HESS J1018-589 [198]	16.58 ± 0.02	-	-	-	-	9.21×10^{-9}

TABLE 6.6: Candidate sources and results for the search for periodic neutrino emission. The p-values are pre-trial. The flare-durations given are the widths of the the fitted Gaussian flares, as fractions of the total periods. The time dependent upper limits are the normalization for an E^{-2} power law flux with with time dependence corresponding to the fitted signal in likelihood, and is hence provided only for sources that were positive fluctuations. Time integrated upper limits [140] are a factor of $3-8$ times lower than reported by analyses performed on data from the IC-22 and IC-40 configurations of the detector [191] and the time dependent upper limits have improved similarly, where comparable.

6.4.2 The Candidate Sources

The candidate sources selected for this search are summarized in Table 6.6. In addition to the sources considered previously in [191], three new sources were added to this list for a total of 10 sources (see Table 6.6). In the northern sky a recently reported binary HESS J0632+057 [188] was added, which is a variable point like source of VHE (> 100 GeV) γ-rays located in the Galactic plane and is positionally coincident with a Be star. It also emits variably in the radio and X-ray domains and has been found to have a hard X-ray spectrum [188]. The periodicity of the X-ray emission is $\Omega = 320 \pm 5$ days [199]. Bearing a close resemblance to the source LS I +61 303, this source has now been confirmed to be a γ-ray binary [199]. Background rejection techniques introduced recently [140] have increased IceCube's sensitivity to neutrino sources in the southern sky. As a result, two new sources are added in the Southern Sky. LS 5039 is a High Mass X-Ray Binary which was also the first micro-quasar to be established as a high-energy γ-ray source [197]. It has been confirmed to have a period of 3.906 ± 0.002 days [197]. The second new source in the southern sky is HESS J1018-589, a Gamma Ray Binary in the Carina arm region of the galaxy. This source position is coincident with 1FGL J1018.6 reported by the Fermi-LAT collaboration [200] and is a source of (> 100 GeV) γ-rays. Its periodicity has been reported to be 16.58 ± 0.02 days [198].

6.4.3 Results

The results of the periodic analysis for each of the selected sources are given in Table 6.6. The most significant observation was from the source HESS J0632+057 with a pre-trial probability of 8.67%. This Gaussian fitted flare was observed at a phase of 0.702 with a width of $\sigma_\Phi = 0.012$ in terms of the fraction of the period. Figure 6.7 shows the fitted Gaussian and the IceCube event weights from a point source analysis of the same source without time dependence. Cyg X-1, Cyg X-3 and and GRS 1915+105 were observed to have flares of probability 0.45, 0.34 and 0.32 respectively. All other sources produced under-fluctuations indicating that the number of events in the direction of the source was less than or equal to the number expected from background-only. The post-trial probability of the fluctuation from HESS J0632+057 was found to be 44.3%, making the observation compatible with the background-only hypothesis.
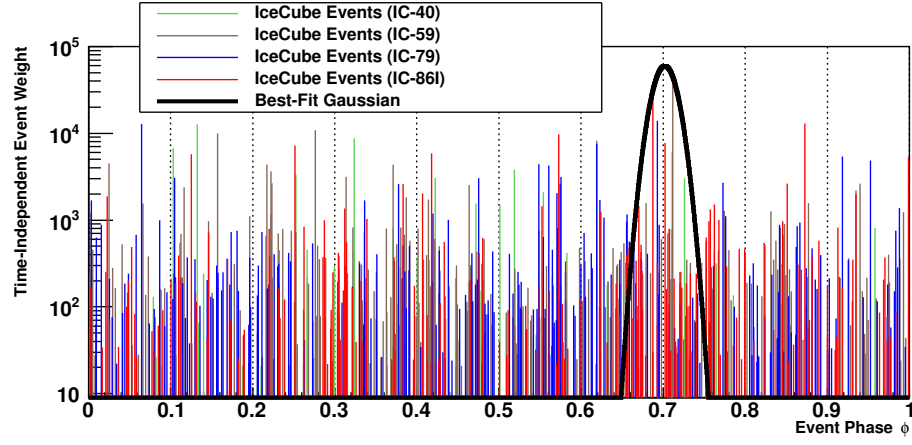
FIGURE 6.7: Events from the direction of HESS J0632+057. The most significant fluctuation from the background-only hypothesis was observed for this source. The fitted flare at a phase of 0.7 with a width 3.84 days is also shown.

Chapter 7

Searches for Neutrino Emission from Extragalactic Sources

7.1 Introduction

This chapter summarizes the stacking searches carried out for neutrino emission from extragalactic sources. Both galaxy clusters and starburst galaxies have been proposed as potential acceleration sites for CRs and are thus promising candidates for neutrino emission. A catalog of AGNs within the GZK radius - compiled for UHECR correlation studies is also considered. Finally, the arrival directions of the highest energy UHECRs reported by Pierre Auger Observatory and Telescope Array are considered.

7.2 Stacking Search for Neutrino emission from Galaxy Clusters

Galaxy clusters are promising sources of CRs above the knee but below the ankle. The CRs can interact with the intracluster gas and produce neutrinos through p-p interactions[130]. The neutrino flux is thus proportional to the product of the CR flux as well as the ambient matter distribution within the GC. The spatial distribution of the intracluster medium is well constrained from X-Ray observations [201], however the distribution of CRs is uncertain. The authors of [130] thus consider four different scenarios of the CR distribution. Model A assumes that the CRs are uniformly distributed out to the shock radius r_{sh}, determined so as to keep the dynamical time $t_{dyn} = 1Gyr$, where $t_{dyn} = r_{sh}/V_{sh}$, and the shock velocity V_{sh} is taken to be the velocity of the infalling gas. Model B assumes that the CRs are uniformly distributed within the r_{vir} and thus give a conservative estimate of the neutrino flux. The isobaric model (I) allows the CRs at each radii to have energy densities proportional to that of the thermal gas, while the central AGN model (C) ignores the merger and accretion shocks to consider only the CRs that are diffusing out from a central AGN.

TABLE 7.1: Galaxy clusters considered for the stacking analysis. C and I stand for the central AGN and isobaric models respectively.

Name	R.A(°)	DEC(°)	redshift(z)	Distance(Mpc)	A	B	C	I
Virgo	186.63	12.72	0.0036	15.4	4	8	0	6
Perseus	49.95	41.52	0.0179	76.7	0.5	0.5	0	0.5
Centaurus	192.2	-41.31	0.0114	48.4	0	1	0	0
Coma	194.95	27.94	0.0231	98.9	0	1	0	0
Ophiuchus	258.11	-23.36	0.0280	119.9	0.5	1	0	0.5

(header: Angular Extend(°) spans columns A, B, C, I)

Table 7.1 lists the five most massive galaxy clusters in the nearby universe, along with their coordinates, distances and extensions under the various models. The individual and combined flux predictions for the different model assumptions have been published in [130]. These sources were considered in a previous stacking analysis with data from the 40-string IceCube detector [172].

As the extensions of the sources are different under different assumptions, the four hypotheses are tested as four different stacking searches. Ref. [172] performed broken power law fits to the flux predictions by [172] for each source for different models and the normalizations from these fits are again used as theoretical weights of the sources in the likelihood.

7.3 Stacking Search for Neutrino emission from Starburst Galaxies

The case for starburst galaxies as candidate sources of neutrinos has been discussed in section 3.6. A catalog of 127 starburst galaxies within the nearby universe (z<0.03) has been compiled in ref. [131]. The authors also present a model that traces the significant correlation observed between FIR and radio emissions to the single underlying cause of high star formation rates, predicting also a correlation with the neutrino flux.

The 127 starburst galaxies as well as their coordinates and observed FIR flux at 60μm are compiled in [131]. A search that has been previously carried out on data from the 40-string configuration of IceCube [148, 172] has now been updated to include 4 years of data, including one year of the completed 86-string configuration of IceCube. As with the previous search, the FIR flux at 60μm is used as the theoretical weight in likelihood.

7.4 Stacking Search for Neutrino emission from AGNs within the GZK radius

Reference [202] systematically catalogs the possible black hole candidates within the GZK limit of around ~100 Mpc. The authors start with the 2 micron all sky survey (2MASS) [203], focus on early Hubble-type galaxies and constrain the catalog to redshifts < 0.025. The NIR flux at 2μm has been
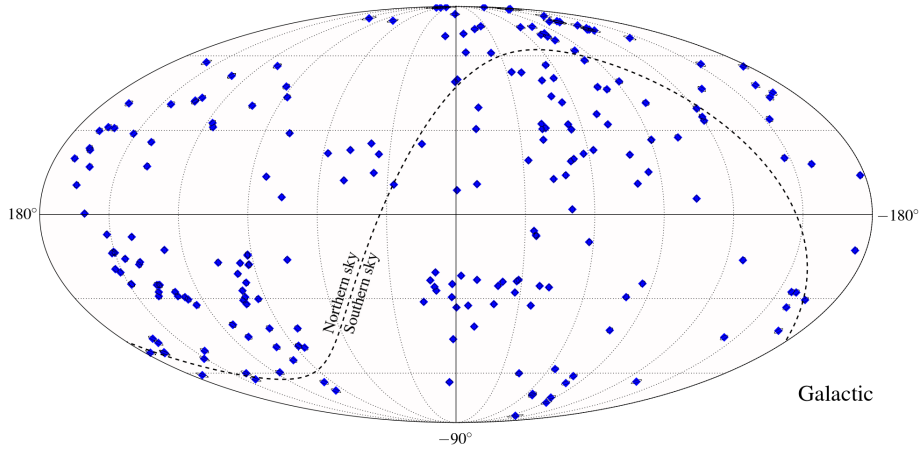
FIGURE 7.1: The remaining 233 AGNs from the 2MASS catalog used in this analysis, in Galactic coordinates.

used along with a spheroidal stellar component - black hole mass relationship to derive black hole masses, and these masses are tested against the black hole masses known from other methods. The remaining sample contains ~ 6000 AGNs with masses above 10^6 solar masses.

A further cut was applied on the derived masses to keep only sources more massive than 5×10^8 solar masses. This cut was chosen to reduce the sample to a size suitable for a stacking analysis and leaves behind 233 of the most massive and potentially powerful candidate sources from within the catalog.

Figure 7.1 illustrates the positions in the sky of the final 233 sources selected for this search.

A stacking analysis was carried out for neutrino emission from these 233 sources on data from 4 years of operation of IceCube in the 40, 59, 79 and 86 string configurations. The 2μm NIR flux is used as the theoretical weight in likelihood.

7.5 Stacking Search for Neutrino emission from the arrival directions of UHECRs

While CRs in general are deflected and isotropized by magnetic fields, the deflection is lower for higher energy CRs. Faraday rotation measurements of extragalactic magnetic fields indicate that they are smaller than $\sim 10^{-9}$ G[204]. The deflection of a 10^{20} eV proton over a 50 Mpc distance due to such a small magnetic field is expected to be smaller than $2°$.

The Galactic magnetic fields are much better understood. Further divided into regular and turbulent components, the regular part is expected to contribute dominantly towards the UHECR deflections. Various models of regular component of the Galactic magnetic field have been studied in literature, and the average magnitude of the deflection predicted across the sky by each model agree, even though individual deflections in a given direction vary substantially. Figure 7.2, presented in [173] illustrates
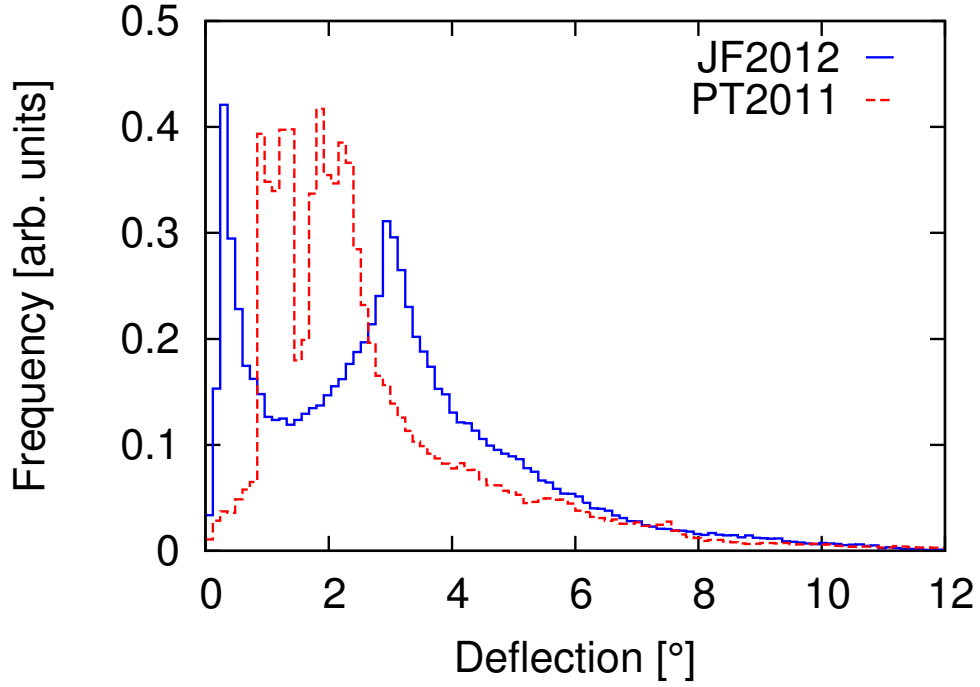
FIGURE 7.2: Distribution of UHECR deflections in two Galactic magnetic field models marked PT2011 [205] and JF2012 [206] for the regular component. The energies of actual UHECRs are renormalized to show the distributions for $E/Z = 100$ EeV. The double-peak structure is mostly due to the fact that UHECRs from different Galactic hemispheres undergo different deflections. Figure taken from [173].

the deflections observed by 10^5 protons at 100 EeV according to two different models of the Galactic magnetic field [205]. In both cases, the median deflection can be seen to be $\sim 3°$. All estimates of the turbulent component of the Galactic magnetic field predict the deflection due to the turbulent component to be sub-dominant to that of the regular component.

The Pierre Auger Observatory and Telescope Array experiments have observed 231 and 87 UHECRs above the energies of 57 and 52 EeV respectively. Searches for anisotropies in the arrival directions of these events have revealed evidence of statistically significant clustering [207].

An analysis was performed using the stacking method to look for excesses of neutrinos in the 4 year point source sample in the arrival directions of the UHECRs. The magnetic deflections were accommodated as extensions in the source hypothesis, with the deflection given by:

$$\sigma_{\mathrm{MD}}(E) = D \times 100\,\mathrm{EeV}/E. \tag{7.1}$$

where D is the median deflection across the sky for a 100 EeV proton and the extension is given by $\sigma_{ext} = \sqrt{\sigma_j^2 + \sigma_{\mathrm{MD}}^2(E_j)}$. Here σ_j is the angular resolution of the UHECR event j, which is taken to be $0.9°$ for Pierre Auger events and $1.5°$ for events reported by the Telescope Array respectively. E_j stands for the UHECR energy.
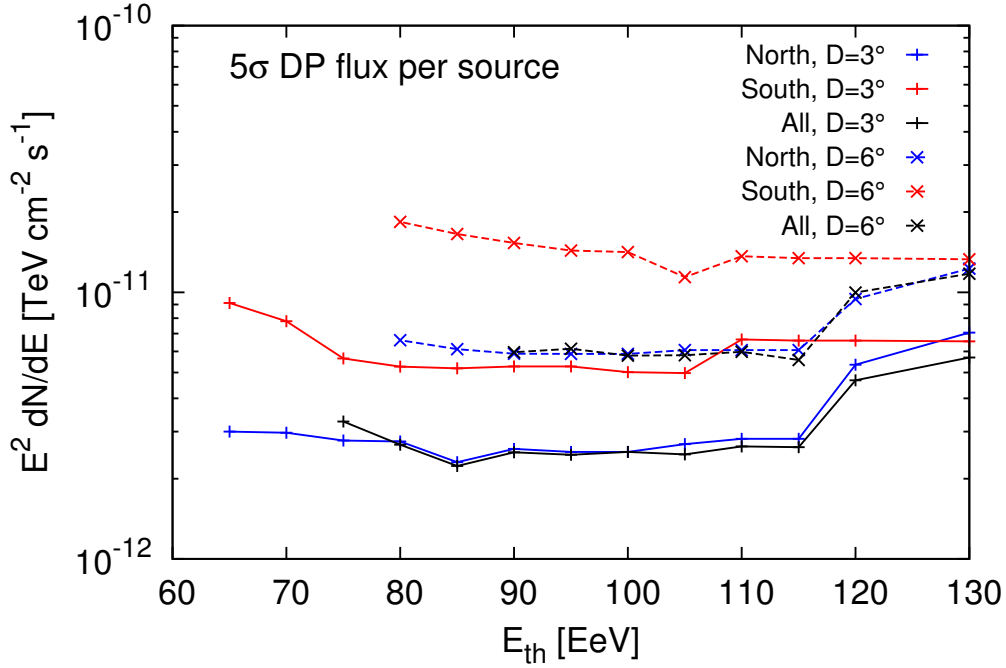
FIGURE 7.3: Pre-trial discovery potential for the UHECR stacking search the 5σ level. The normalization of the flux per source required is shown as a function of the UHECR threshold energy E_{th}. The results from Northern and Southern skies, as well as the whole sky, are shown for $D = 3°$ and $6°$.

Since stacking all of the 318 events as sources with their associated angular extensions would essentially cover the whole sky, the possible gain associated to the stacking of more sources is reduced. Restricting the UHECR sample to those with energies above a given threshold E_{th} could give the advantage of having smaller associated magnetic spreads, potentially enhancing the discovery potential. Thus, a potential optimum value of E_{th} exists for which the per-source flux required for discovery is minimum, as a consequence of these two competing effects.

A simulation was then performed to determine the discovery potential of the UHECR stacking analysis obtained for different values of E_{th} (see Figure 7.4) for both the southern and northern hemispheres separately as well as for the whole sky sample. To calculate the discovery potentials, events were injected from point sources in the direction of the UHECRs, adopting source spectra with $\gamma = 2$ and considering two deflection hypotheses, $D = 3°$ and $6°$. Each point source was positioned with a deflection Δ_j from the UHECR, where Δ_j is sampled randomly from a Gaussian distribution of width $\sqrt{\sigma_j^2 + \sigma_{\text{MD}}^2(E_j)}$. As seen in Figure 7.4, the discovery potentials are characterized by a broad flat region, based on which a value of $E_{\text{th}} = 85\,\text{EeV}$ was chosen. This keeps the 12 highest-energy UHECRs in the southern sky and 15 in the northern sky.

Due to the different energy ranges between the neutrino candidate events in the southern hemisphere ($\sim$100 TeV - 100 PeV) and in the northern hemisphere ($\sim$1 TeV - 1 PeV), the flux normalization required for northern sources turns out to be smaller than for southern ones. However, thanks to the gain provided by having more stacked sources, the whole sky sensitivity turns out to be similar to the
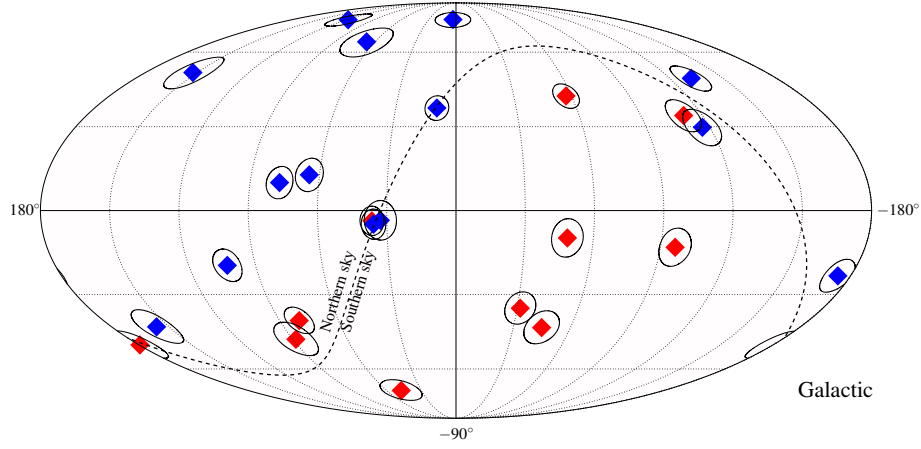
FIGURE 7.4: The 27 highest energy UHECR events that are stacked as sources, in Galactic coordinates. The red diamonds denote events seen by the Pierre Auger Observatory, while the blue ones are from Telescope Array. The black circles denote the 2σ diameter of the effective extension under a $D = 6°$ magnetic deflection hypothesis, including detector angular uncertainties. The triplet of events near the equator consists of a doublet noted in [208] which is now a triplet from an additional new TA event.

one in the northern sky alone (Figure 7.4). This analysis thus considers the entire sky with UHECRs above $E_{\text{th}} = 85\,\text{EeV}$.

7.6 Results and Conclusions

Catalog		$\hat{n}_S$	$\hat{\gamma}$	p-value	$\Phi^{90\%}_{\nu_\mu+\bar{\nu}_\mu}$
Galaxy Clusters	*Model A*	1.4	3.95	0.50	$3.89\times$M.F. [130]
	Model B	12.6	3.95	0.48	$6.17\times$M.F. [130]
	Central AGN	0.0	–	–	$1.54\times$M.F. [130]
	Isobaric	0.0	–	–	$4.65\times$M.F. [130]
Starburst Galaxies		0.0	–	–	$7.93 \times 10^{-12} \times\text{E}^{2.0}$ $3.47 \times 10^{-11} \times\text{E}^{2.5}$
Supermassive Black Holes		17.1	3.95	0.43	$6.88 \times 10^{-12} \times\text{E}^{2.0}$ $3.10 \times 10^{-11} \times\text{E}^{2.5}$

TABLE 7.2: Results of the stacked searches for emission from source catalogs. M.F. stands for the model flux as described in the references motivating the analyses. $\Phi^{90\%}_{\nu_\mu+\bar{\nu}_\mu}$ is the 90% Confidence Level upper limit on the combined flux of ν_μ and $\bar{\nu}_\mu$ from the catalogs. The $\text{E}^{2.0}$ limits are in units of $\text{TeV}^1\text{cm}^{-2}\text{s}^{-1}$, while the $\text{E}^{2.5}$ limits are in units of $\text{TeV}^{1.5}\text{cm}^{-2}\text{s}^{-1}$

Results are presented in table 7.2. No statistically significant excess was found in any of the searches. In the absence of a signal, upper limits are presented. In the case of galaxy clusters, IceCube sensitivity is not good enough to detect even the most optimistic predictions (the central AGN model), and consequently the upper limit is ~50% more than the predicted flux.

The upper limit for neutrino flux from starburst galaxies tells us that starburst galaxies contribute less than 1% of the astrophysical neutrino flux observed by IceCube. Similar conclusions can be drawn also for supermassive black holes within the GZK radius.

The upper limit on the neutrino flux from the arrival directions of UHECRs is a factor of $\sim$25 lower than previous limits reported by the ANTARES experiment [209].

The results of these searches suggest that there are no significantly luminous extragalactic sources of neutrinos within the nearby universe and that the IceCube astrophysical neutrino flux comes from a large population of weak sources much farther into the universe. Assuming that astrophysical neutrino sources extend out to z=6, the contribution of sources within the GZK horizon to the astrophysical neutrino flux is expected to be a few percentage only. The results of the searches presented within this chapter are compatible with this expectation.

Chapter 8

Conclusions

8.1 Summary

Point like sources of neutrinos can arise in the cosmos from the pair annihilation of gravitationally captured dark matter or the interactions of cosmic rays at their acceleration sites. This work presented results from searches performed for point-like sources of neutrinos using samples of ν_μ (and $\bar{\nu}_\mu$) CC events across the energy range in which IceCube-DeepCore has sensitivity. The first analysis employed innovative background rejection strategies, including vetos to isolate three samples of track like events from three years of operation of the completed IceCube detector. Two of these samples consist of events within the DeepCore region while one sample consists of events traversing the IceCube array. The two DeepCore contained samples offer sensitivity to neutrinos from the direction of the Sun in the 10-150 GeV energy range and have an energy dependent angular resolution between 30° and 4°. As all the energy of these events is deposited inside the detector, the energy resolution is significantly better. The sample of events traversing the IceCube array extends the sensitivity to neutrinos of 1 TeV and above and offers an angular resolution of $\sim 1°$. An unbinned maximum likelihood ratio analysis employing energy estimators for improved signal-background separation failed to find any evidence of an excess of muon neutrinos from the direction of the Sun. The resultant constraints on the flux of muon neutrinos from the direction of the Sun are the most stringent ever above $\sim 80 GeV$. These constraints can be interpreted as a limit on the number of DM particles annihilating within the Sun and subsequently, as a limit on the WIMP-Nucleon scattering cross section. In the case of spin-dependent scattering, these constraints are the most stringent ever and are an order of magnitude more constraining than previous limits at higher energies. These limits can be used to constrain particle physics models with DM candidates, such as supersymmetry. They can also be interpreted as constraints on free parameters in effective theories. In both scenarios, the limits can be shown to be complementary to the constraints obtained by other searches for DM, both direct searches as well as those looking for production at colliders.

The second set of analyses employed the stacking technique to look for neutrino emission from different catalogs of Galactic SNRs and PWNs using a sample of through-going events isolated from 3 years of operation of the partial detector as well as one year of the completed one. Although no statistically significant excess was found, an excess which has a 2% probability of being background fluctuation was observed from the directions of 6 Galactic TeV γ-ray sources with SNR associations reported by the Milagro experiment. Only more data can confirm if this is real or a statistical fluctuation. However, the energy distribution of the events that constitute the observed excess imply that the signal if any is significantly softer in spectrum than theoretical predictions. A search was also carried out employing observed periodicities of Galactic binary systems to enhance sensitivity towards periodic neutrino signals. No statistically significant excess was found.

The stacking technique was also employed to look for neutrinos from catalogs of starburst galaxies, galaxy clusters and supermassive blackholes within the GZK horizon. A similar method was also used to look for neutrino emission from the arrival directions of the highest energy UHECRs. No significant excess was found in any of the searches, pointing towards the conclusion that on their own, none of these source classes can contribute more than $\sim 15\%$ of the measured IceCube astrophysical neutrino flux. This indicates that no particularly bright sources of astrophysical neutrinos exist within the GZK horizon, and that the IceCube astrophysical neutrino flux comes from a larger population of weaker sources further out into the universe, in line with theoretical expectations.

Sensitivity to all the above searches is expected to improve as more data accumulate over the future years of operation of the detector. As of today, IceCube has operated for more than 4 years in its completed configuration and three more years of IceCube data are ready to be analysed for point source searches. The construction and commission of the Precision IceCube Next Generation Upgrade (PINGU) is expected to open up the sensitivity of IceCube to neutrinos from the annihilation of DM particles less massive than 10GeV, down to 1 GeV, in addition to its goals of determining the neutrino mass hierarchy. Neutrino detectors already under construction such as KM3NeT, a cubic kilometre detector in the Mediterranean sea are expected to offer additional sensitivity through its low energy array, ORCA.

The proposed high energy extension to IceCube, IceCube GenTwo, should accelerate the accumulation of the events that constitute the astrophysical neutrino flux, and thus aid in the identification of their sources. It will have unprecedented sensitivity towards point sources in the northern sky. The high energy array of KM3NeT, ARCA should similarly allow the observation of the southern sky. Together, the two detectors will measure the Galactic and extragalactic components of the astrophysical neutrino flux, estimated to be of the same order of magnitude[210].

During the course of this work, I have been able to gather a wealth of knowledge in the fields of astronomy, cosmology, statistics, data analysis and programming. It has been a pleasant and enlightening first experience in the field of academic research. Most importantly, it has made me further aware of how little I know, and how much remains to be found out.

Bibliography

[1] W. Pauli, "Dear radioactive ladies and gentlemen", *Phys. Today*, **vol. 31N9**:p. 27, 1978

[2] C. L. Cowan, F. Reines, F. B. Harrison, H. W. Kruse, A. D. McGuire, "Detection of the free neutrino: A Confirmation", *Science*, **vol. 124**:pp. 103–104, 1956

[3] S. L. Glashow, "Partial Symmetries of Weak Interactions", *Nucl. Phys.*, **vol. 22**:pp. 579–588, 1961

[4] S. Weinberg, "A Model of Leptons", *Phys. Rev. Lett.*, **vol. 19**:pp. 1264–1266, 1967

[5] A. Salam, "Weak and Electromagnetic Interactions", *Conf. Proc.*, **vol. C680519**:pp. 367–377, 1968

[6] G. 't Hooft, M. J. G. Veltman, "Regularization and Renormalization of Gauge Fields", *Nucl. Phys.*, **vol. B44**:pp. 189–213, 1972

[7] J. N. Bahcall, R. Davis, "Solar Neutrinos - a Scientific Puzzle", *Science*, **vol. 191**:pp. 264–267, 1976

[8] Y. Fukuda, *et al.* (Super-Kamiokande), "Evidence for oscillation of atmospheric neutrinos", *Phys. Rev. Lett.*, **vol. 81**:pp. 1562–1567, 1998. http://arxiv.org/abs/hep-ex/9807003

[9] F. P. An, *et al.* (Daya Bay), "Observation of electron-antineutrino disappearance at Daya Bay", *Phys. Rev. Lett.*, **vol. 108**:p. 171803, 2012. http://arxiv.org/abs/1203.1669

[10] J. K. Ahn, *et al.* (RENO), "Observation of Reactor Electron Antineutrino Disappearance in the RENO Experiment", *Phys. Rev. Lett.*, **vol. 108**:p. 191802, 2012. http://arxiv.org/abs/1204.0626

[11] K. Abe, *et al.* (Super-Kamiokande), "Evidence for the Appearance of Atmospheric Tau Neutrinos in Super-Kamiokande", *Phys. Rev. Lett.*, **vol. 110** (18):p. 181802, 2013. http://arxiv.org/abs/1206.0328

[12] D. G. Michael, *et al.* (MINOS), "Observation of muon neutrino disappearance with the MINOS detectors and the NuMI neutrino beam", *Phys. Rev. Lett.*, **vol. 97**:p. 191801, 2006. http://arxiv.org/abs/hep-ex/0607088

[13] K. Abe, *et al.* (T2K), "Precise Measurement of the Neutrino Mixing Parameter θ_{23} from Muon Neutrino Disappearance in an Off-Axis Beam", *Phys. Rev. Lett.*, **vol. 112** (18):p. 181801, 2014. http://arxiv.org/abs/1403.1532

[14] N. Agafonova, *et al.* (OPERA), "Discovery of τ Neutrino Appearance in the CNGS Neutrino Beam with the OPERA Experiment", *Phys. Rev. Lett.*, **vol. 115** (12):p. 121802, 2015. http://arxiv.org/abs/1507.01417

[15] Z. Maki, M. Nakagawa, S. a. Sakata, "Remarks on the unified model of elementary particles", in "High-energy physics. Proceedings, 11th International Conference, ICHEP'62, Geneva, Switzerland, Jul 4-11, 1962", pp. 663–666 (1962). URL http://inspirehep.net/record/1341897/files/C62-07-04-p663.pdf

[16] B. Pontecorvo, "Inverse beta processes and nonconservation of lepton charge", *Sov. Phys. JETP*, **vol. 7**:pp. 172–173, 1958. [Zh. Eksp. Teor. Fiz.34,247(1957)]

[17] K. Abazajian, *et al.*, "Cosmological and astrophysical neutrino mass measurements", *Astroparticle Physics*, **vol. 35** (4):pp. 177 – 184, 2011. URL http://www.sciencedirect.com/science/article/pii/S0927650511001344

[18] K. A. Olive, *et al.* (Particle Data Group), "Review of Particle Physics", *Chin. Phys.*, **vol. C38**:p. 090001, 2014

[19] P. B. Pal, "Dirac, Majorana and Weyl fermions", *Am. J. Phys.*, **vol. 79**:pp. 485–498, 2011. http://arxiv.org/abs/1006.1718

[20] C. Giunti, C. W. Kim, "Quantum mechanics of neutrino oscillations", *Found. Phys. Lett.*, **vol. 14**:pp. 213–229, 2001. http://arxiv.org/abs/hep-ph/0011074

[21] S. M. Bilenky, J. Hosek, S. T. Petcov, "On Oscillations of Neutrinos with Dirac and Majorana Masses", *Phys. Lett.*, **vol. B94**:p. 495, 1980

[22] M. G. Aartsen, *et al.* (IceCube PINGU), "Letter of Intent: The Precision IceCube Next Generation Upgrade (PINGU)", 2014. http://arxiv.org/abs/1401.2046

[23] S. P. Mikheev, A. Yu. Smirnov, "Resonance Amplification of Oscillations in Matter and Spectroscopy of Solar Neutrinos", *Sov. J. Nucl. Phys.*, **vol. 42**:pp. 913–917, 1985. [Yad. Fiz.42,1441(1985)]

[24] L. Wolfenstein, "Neutrino Oscillations and Stellar Collapse", *Phys. Rev.*, **vol. D20**:pp. 2634–2635, 1979

[25] A. Yu. Smirnov, "The MSW effect and matter effects in neutrino oscillations", *Phys. Scripta*, **vol. T121**:pp. 57–64, 2005. http://arxiv.org/abs/hep-ph/0412391

[26] F. W. Stecker, "Cosmic gamma-rays and cosmic ray neutrinos from galactic and solar dark matter annihilation", 1988

[27] J. S. Hagelin, G. L. Kane, "Cosmic Ray Antimatter From Supersymmetric Dark Matter", *Nucl. Phys.*, **vol. B263**:p. 399, 1986

[28] A. Cooper-Sarkar, S. Sarkar, "Predictions for high energy neutrino cross-sections from the ZEUS global PDF fits", *JHEP*, **vol. 01**:p. 075, 2008. http://arxiv.org/abs/0710.5303

[29] W. Hampel, "The Gallium Solar Neutrino Detector", *AIP Conf. Proc.*, **vol. 126**:pp. 162–174, 1985

[30] M. Muether (NOvA), "NOvA detector technology with initial performance from the surface prototype", 2011. [J. Phys. Conf. Ser.408,012076(2013)]

[31] R. Gandhi, C. Quigg, M. H. Reno, I. Sarcevic, "Ultrahigh-energy neutrino interactions and neutrino telescope event rates", in "Neutrino mass, dark matter, gravitational waves, monopole condensation, and light cone quantization. Proceedings, International Conference, Orbis Scientiae 1996, Miami Beach, USA, January 25-28, 1996", (1996). http://arxiv.org/abs/hep-ph/9604276, URL http://lss.fnal.gov/archive/preprint/fermilab-conf-96-477-t.shtml

[32] P. A. Cherenkov, "Visible emission of clean liquids by action of γ-radiation.", *Usp. Fiz. Nauk*, **vol. 93** (10):pp. 385–388, 1967. URL http://ufn.ru/ru/articles/1967/10/n/

[33] I. M. Frank, I. Tamm, "Coherent visible radiation of fast electrons passing through matter", *C. R. Acad. Sci. URSS*, **vol. 14**:pp. 109–114, 1937

[34] A. Achterberg, *et al.* (IceCube), "First Year Performance of The IceCube Neutrino Telescope", *Astropart. Phys.*, **vol. 26**:pp. 155–173, 2006. http://arxiv.org/abs/astro-ph/0604450

[35] D. Chirkin, "Study of South Pole ice transparency with IceCube flashers", in "Proceedings, 32nd International Cosmic Ray Conference (ICRC 2011)", vol. 4, p. 161. URL http://inspirehep.net/record/1352396/files/v4_0333.pdf

[36] M. Ackermann, *et al.*, "Optical properties of deep glacial ice at the South Pole", *J. Geophys. Res.*, **vol. 111** (D13):p. D13203, 2006

[37] R. Abbasi, *et al.* (IceCube), "Calibration and Characterization of the IceCube Photomultiplier Tube", *Nucl. Instrum. Meth.*, **vol. A618**:pp. 139–152, 2010. http://arxiv.org/abs/1002.2442

[38] R. Abbasi, *et al.* (IceCube), "The Design and Performance of IceCube DeepCore", *Astropart. Phys.*, **vol. 35**:pp. 615–624, 2012. http://arxiv.org/abs/1109.6096

[39] R. Abbasi, *et al.* (IceCube), "The IceCube Data Acquisition System: Signal Capture, Digitization, and Timestamping", *Nucl. Instrum. Meth.*, **vol. A601**:pp. 294–316, 2009. http://arxiv.org/abs/0810.4930

[40] H. Taavola, "Dark matter in the galactic halo: A search using neutrino induced cascades in the deepcore extension of icecube", 2015

[41] M. G. Aartsen, *et al.* (IceCube), "Search for Astrophysical Tau Neutrinos in Three Years of IceCube Data", *Phys. Rev.*, **vol. D93** (2):p. 022001, 2016. http://arxiv.org/abs/1509.06212

[42] P. J. Huber, "Robust estimation of a location parameter", *Ann. Math. Stat.*, **vol. 35** (1):pp. 73–101, 1964. URL http://www.jstor.org/stable/2238020

[43] D. Pandel, "Bestimmung von Wasser- und Detektorparametern und Rekonstruktion von Myonen bis 100 TeV mit dem Baikal-Neutrinoteleskop NT-72.", *Diploma Thesis, Humboldt-Universitat zu Berlin,*, 1996

[44] N. Whitehorn, J. van Santen, S. Lafebre, "Penalized Splines for Smooth Representation of High-dimensional Monte Carlo Datasets", *Comput. Phys. Commun.*, **vol. 184**:pp. 2214–2220, 2013. http://arxiv.org/abs/1301.2184

[45] T. Neunhoffer, "Estimating the angular resolution of tracks in neutrino telescopes based on a likelihood analysis", *Astropart. Phys.*, **vol. 25**:pp. 220–225, 2006. http://arxiv.org/abs/astro-ph/0403367

[46] V. Blobel, C. Kleinwort, F. Meier, "Fast alignment of a complex tracking detector using advanced track models", *Comput. Phys. Commun.*, **vol. 182**:pp. 1760–1763, 2011. http://arxiv.org/abs/1103.3909

[47] J. N. Capdevielle, *et al.*, "Extensive air shower simulations with the CORSIKA program", in "Proceedings, 7th International Symposium on Very High Energy Cosmic Ray Interactions (ISVHECRI 1992)", (1992)

[48] E.-J. Ahn, R. Engel, T. K. Gaisser, P. Lipari, T. Stanev, "Cosmic ray interaction event generator SIBYLL 2.1", *Phys. Rev.*, **vol. D80**:p. 094003, 2009. http://arxiv.org/abs/0906.4113

[49] A. Gazizov, M. P. Kowalski, "ANIS: High energy neutrino generator for neutrino telescopes", *Comput. Phys. Commun.*, **vol. 172**:pp. 203–213, 2005. http://arxiv.org/abs/astro-ph/0406439

[50] C. Andreopoulos, *et al.*, "The GENIE Neutrino Monte Carlo Generator: Physics and User Manual", 2015. http://arxiv.org/abs/1510.05494

[51] M. Blennow, J. Edsjö, T. Ohlsson, "Neutrinos from WIMP annihilations using a full three-flavor Monte Carlo", *JCAP*, **vol. 0801**:p. 021, 2008. http://arxiv.org/abs/0709.3898

[52] D. Chirkin, W. Rhode, "Muon Monte Carlo: A High-precision tool for muon propagation through matter", 2004. http://arxiv.org/abs/hep-ph/0407075

[53] J. Lundberg, *et al.*, "Light tracking for glaciers and oceans: Scattering and absorption in heterogeneous media with Photonics", *Nucl. Instrum. Meth.*, **vol. A581**:pp. 619–631, 2007. http://arxiv.org/abs/astro-ph/0702108

[54] D. Chirkin (IceCube), "Photon tracking with GPUs in IceCube", *Nucl. Instrum. Meth.*, **vol. A725**:pp. 141–143, 2013

[55] C. Kopper. URL https://github.com/claudiok/clsim

[56] J. Apostolakis, D. H. Wright (Geant4), "An overview of the GEANT4 toolkit", *AIP Conf. Proc.*, **vol. 896**:pp. 1–10, 2007. [,1(2007)]

[57] M. G. Aartsen, *et al.* (IceCube), "The IceCube Neutrino Observatory - Contributions to ICRC 2015 Part II: Atmospheric and Astrophysical Diffuse Neutrino Searches of All Flavors", in "Proceedings, 34th International Cosmic Ray Conference (ICRC 2015)", (2015). http://arxiv.org/abs/1510.05223, URL http://inspirehep.net/record/1398539/files/arXiv:1510.05223.pdf

[58] M. G. Aartsen, *et al.* (IceCube), "Evidence for Astrophysical Muon Neutrinos from the Northern Sky with IceCube", *Phys. Rev. Lett.*, **vol. 115** (8):p. 081102, 2015. http://arxiv.org/abs/1507.04005

[59] M. G. Aartsen, *et al.* (IceCube), "Determining neutrino oscillation parameters from atmospheric muon neutrino disappearance with three years of IceCube DeepCore data", *Phys. Rev.*, **vol. D91** (7):p. 072004, 2015. http://arxiv.org/abs/1410.7227

[60] R. Enberg, M. H. Reno, I. Sarcevic, "Prompt neutrino fluxes from atmospheric charm", *Phys. Rev.*, **vol. D78**:p. 043005, 2008. http://arxiv.org/abs/0806.0418

[61] M. G. Aartsen, *et al.* (IceCube), "Development of a General Analysis and Unfolding Scheme and its Application to Measure the Energy Spectrum of Atmospheric Neutrinos with IceCube", *Eur. Phys. J.*, **vol. C75** (3):p. 116, 2015. http://arxiv.org/abs/1409.4535

[62] R. Abbasi, *et al.* (IceCube), "A Search for a Diffuse Flux of Astrophysical Muon Neutrinos with the IceCube 40-String Detector", *Phys. Rev.*, **vol. D84**:p. 082001, 2011. http://arxiv.org/abs/1104.5187

[63] M. G. Aartsen, *et al.* (IceCube), "Measurement of the Atmospheric ν_e Spectrum with IceCube", *Phys. Rev.*, **vol. D91**:p. 122004, 2015. http://arxiv.org/abs/1504.03753

[64] M. G. Aartsen, *et al.* (IceCube), "Measurement of the Atmospheric ν_e flux in IceCube", *Phys. Rev. Lett.*, **vol. 110** (15):p. 151105, 2013. http://arxiv.org/abs/1212.4760

[65] M. Honda, "Atmospheric neutrino and muon fluxes", *Czech. J. Phys.*, **vol. 56**:pp. A281–A290, 2006

[66] M. G. Aartsen, *et al.* (IceCube), "Characterization of the Atmospheric Muon Flux in IceCube", *Astropart. Phys.*, **vol. 78**:pp. 1–27, 2016. http://arxiv.org/abs/1506.07981

[67] M. Honda, T. Kajita, K. Kasahara, S. Midorikawa, "Calculation of the flux of atmospheric neutrinos", *Phys. Rev.*, **vol. D52**:pp. 4985–5005, 1995. http://arxiv.org/abs/hep-ph/9503439

[68] A. Ferrari, P. R. Sala, A. Fasso, J. Ranft, "FLUKA: A multi-particle transport code (Program version 2005)", 2005

[69] V. Agrawal, T. K. Gaisser, P. Lipari, T. Stanev, "Atmospheric neutrino flux above 1-GeV", *Phys. Rev.*, **vol. D53**:pp. 1314–1323, 1996. http://arxiv.org/abs/hep-ph/9509423

[70] M. Sajjad Athar, M. Honda, T. Kajita, K. Kasahara, S. Midorikawa, "Atmospheric neutrino flux at INO, South Pole and Pyhasalmi", *Phys. Lett.*, **vol. B718**:pp. 1375–1380, 2013. http://arxiv.org/abs/1210.5154

[71] F. Zwicky, "Die Rotverschiebung von extragalaktischen Nebeln", *Helv. Phys. Acta*, **vol. 6**:pp. 110–127, 1933

[72] V. C. Rubin, N. Thonnard, W. K. Ford, Jr., "Rotational properties of 21 SC galaxies with a large range of luminosities and radii, from NGC 4605 /R = 4kpc/ to UGC 2885 /R = 122 kpc/", *Astrophys. J.*, **vol. 238**:p. 471, 1980

[73] T. S. van Albada, J. N. Bahcall, K. Begeman, R. Sancisi, "The Distribution of Dark Matter in the Spiral Galaxy NGC-3198", *Astrophys. J.*, **vol. 295**:pp. 305–313, 1985

[74] J. F. Navarro, C. S. Frenk, S. D. M. White, "The Structure of cold dark matter halos", *Astrophys. J.*, **vol. 462**:pp. 563–575, 1996. http://arxiv.org/abs/astro-ph/9508025

[75] A. W. Graham, D. Merritt, B. Moore, J. Diemand, B. Terzic, "Empirical models for Dark Matter Halos. I. Nonparametric Construction of Density Profiles and Comparison with Parametric Models", *Astron. J.*, **vol. 132**:pp. 2685–2700, 2006. http://arxiv.org/abs/astro-ph/0509417

[76] J. E. Gunn, D. H. Weinberg, "The Sloan digital sky survey", 1994. http://arxiv.org/abs/astro-ph/9412080

[77] J. Loveday (SDSS), "The Sloan Digital Sky Survey and dark matter", 1998. http://arxiv.org/abs/astro-ph/9810130

[78] H. Silverwood, S. Sivertsson, P. Steger, J. I. Read, G. Bertone, "A non-parametric method for measuring the local dark matter density", 2015. http://arxiv.org/abs/1507.08581

[79] T. Piffl, *et al.*, "Constraining the Galaxy's dark halo with RAVE stars", *Mon. Not. Roy. Astron. Soc.*, **vol. 445** (3):pp. 3133–3151, 2014. http://arxiv.org/abs/1406.4130

[80] F. Iocco, M. Pato, G. Bertone, "Evidence for dark matter in the inner Milky Way", *Nature Phys.*, **vol. 11**:p. 245–248, 2015. http://arxiv.org/abs/1502.03821

[81] E. L. Wright, "Theoretical overview of cosmic microwave background anisotropy", in "Measuring and modeling the universe. Proceedings, Symposium, Pasadena, USA, November 17-22, 2002", pp. 291–308 (2003). http://arxiv.org/abs/astro-ph/0305591

[82] P. A. R. Ade, *et al.* (Planck), "Planck 2015 results. XIII. Cosmological parameters", 2015. http://arxiv.org/abs/1502.01589

[83] W. Hu, M. J. White, "Acoustic signatures in the cosmic microwave background", *Astrophys. J.*, **vol. 471**:pp. 30–51, 1996. http://arxiv.org/abs/astro-ph/9602019

[84] E. Komatsu, D. N. Spergel, "Acoustic signatures in the primary microwave background bispectrum", *Phys. Rev.*, **vol. D63**:p. 063002, 2001. http://arxiv.org/abs/astro-ph/0005036

[85] W. J. Percival, *et al.*, "Measuring the Baryon Acoustic Oscillation scale using the SDSS and 2dFGRS", *Mon. Not. Roy. Astron. Soc.*, **vol. 381**:pp. 1053–1066, 2007. http://arxiv.org/abs/0705.3323

[86] P. Kroupa, *et al.*, "Local-Group tests of dark-matter Concordance Cosmology: Towards a new paradigm for structure formation?", *Astron. Astrophys.*, **vol. 523**:p. A32, 2010. http://arxiv.org/abs/1006.1647

[87] F. Zwicky, "Nebulae as gravitational lenses", *Phys. Rev.*, **vol. 51**:p. 290, 1937

[88] M. Markevitch, *et al.*, "Direct constraints on the dark matter self-interaction cross-section from the merging galaxy cluster 1E0657-56", *Astrophys. J.*, **vol. 606**:pp. 819–824, 2004. http://arxiv.org/abs/astro-ph/0309303

[89] D. J. E. Marsh, "Axion Cosmology", 2015. http://arxiv.org/abs/1510.07633

[90] Y. Zhang, Y. Zhao, "Unconventional dark matter models: a brief review", *Sci. Bull.*, **vol. 60** (11):pp. 986–994, 2015

[91] G. Jungman, M. Kamionkowski, K. Griest, "Supersymmetric dark matter", *Phys. Rept.*, **vol. 267**:pp. 195–373, 1996. http://arxiv.org/abs/hep-ph/9506380

[92] M. T. Frandsen, F. Kahlhoefer, C. McCabe, S. Sarkar, K. Schmidt-Hoberg, "Resolving astrophysical uncertainties in dark matter direct detection", *JCAP*, **vol. 1201**:p. 024, 2012. http://arxiv.org/abs/1111.0292

[93] J. Cooley, "Overview of Non-Liquid Noble Direct Detection Dark Matter Experiments", *Phys. Dark Univ.*, **vol. 4**:pp. 92–97, 2014. http://arxiv.org/abs/1410.4960

[94] R. Bernabei, *et al.*, "Final model independent result of DAMA/LIBRA-phase1", *Eur. Phys. J.*, **vol. C73**:p. 2648, 2013. http://arxiv.org/abs/1308.5109

[95] R. Agnese, *et al.* (CDMS), "Silicon Detector Dark Matter Results from the Final Exposure of CDMS II", *Phys. Rev. Lett.*, **vol. 111** (25):p. 251301, 2013. http://arxiv.org/abs/1304.4279

[96] E. Aprile, *et al.* (XENON100), "Dark Matter Results from 225 Live Days of XENON100 Data", *Phys. Rev. Lett.*, **vol. 109**:p. 181301, 2012. http://arxiv.org/abs/1207.5988

[97] E. Behnke, *et al.* (COUPP), "First Dark Matter Search Results from a 4-kg CF$_3$I Bubble Chamber Operated in a Deep Underground Site", *Phys. Rev.*, **vol. D86** (5):p. 052001, 2012. [Erratum: Phys. Rev.D90,no.7,079902(2014)], http://arxiv.org/abs/1204.3094

[98] V. Sanglard, *et al.* (EDELWEISS), "Final results of the EDELWEISS-I dark matter search with cryogenic heat-and-ionization Ge detectors", *Phys. Rev.*, **vol. D71**:p. 122002, 2005. http://arxiv.org/abs/astro-ph/0503265

[99] M. Farina, D. Pappadopulo, A. Strumia, T. Volansky, "Can CoGeNT and DAMA Modulations Be Due to Dark Matter?", *JCAP*, **vol. 1111**:p. 010, 2011. http://arxiv.org/abs/1107.0715

[100] J. Cherwinka, *et al.*, "A Search for the Dark Matter Annual Modulation in South Pole Ice", *Astropart. Phys.*, **vol. 35**:pp. 749–754, 2012. http://arxiv.org/abs/1106.1156

[101] J. Cherwinka, *et al.* (DM-Ice), "Measurement of Muon Annual Modulation and Muon-Induced Phosphorescence in NaI(Tl) Crystals with DM-Ice17", *Phys. Rev.*, **vol. D93** (4):p. 042001, 2016. http://arxiv.org/abs/1509.02486

[102] M. Ackermann, *et al.* (Fermi-LAT), "Dark matter constraints from observations of 25 Milky Way satellite galaxies with the Fermi Large Area Telescope", *Phys. Rev.*, **vol. D89**:p. 042001, 2014. http://arxiv.org/abs/1310.0828

[103] A. Abramowski, *et al.* (HESS), "Search for a Dark Matter annihilation signal from the Galactic Center halo with H.E.S.S", *Phys. Rev. Lett.*, **vol. 106**:p. 161301, 2011. http://arxiv.org/abs/1103.3266

[104] J. Aleksic, *et al.* (MAGIC), "MAGIC Gamma-Ray Telescope Observation of the Perseus Cluster of Galaxies: Implications for Cosmic Rays, Dark Matter and NGC 1275", *Astrophys. J.*, **vol. 710**:pp. 634–647, 2010. http://arxiv.org/abs/0909.3267

[105] V. A. Acciari, *et al.* (VERITAS), "VERITAS Search for VHE Gamma-ray Emission from Dwarf Spheroidal Galaxies", *Astrophys. J.*, **vol. 720**:pp. 1174–1180, 2010. http://arxiv.org/abs/1006.5955

[106] D. Hooper, L. Goodenough, "Dark Matter Annihilation in The Galactic Center As Seen by the Fermi Gamma Ray Space Telescope", *Phys. Lett.*, **vol. B697**:pp. 412–428, 2011. http://arxiv.org/abs/1010.2752

[107] S. K. Lee, M. Lisanti, B. R. Safdi, T. R. Slatyer, W. Xue, "Evidence for Unresolved Gamma-Ray Point Sources in the Inner Galaxy", *Phys. Rev. Lett.*, **vol. 116**:p. 051103, 2016. http://arxiv.org/abs/1506.05124

[108] T. E. Jeltema, S. Profumo, "Discovery of a 3.5 keV line in the Galactic Centre and a critical look at the origin of the line across astronomical targets", *Mon. Not. Roy. Astron. Soc.*, **vol. 450** (2):pp. 2143–2152, 2015. http://arxiv.org/abs/1408.1699

[109] A. Cakir (ATLAS, CMS), "Searches for Beyond the Standard Model Physics at the LHC: Run1 Summary and Run2 Prospects", *PoS*, **vol. FPCP2015**:p. 024, 2015. http://arxiv.org/abs/1507.08427

[110] K. Choi, C. Rott, Y. Itow, "Impact of the dark matter velocity distribution on capture rates in the Sun", *JCAP*, **vol. 1405**:p. 049, 2014. http://arxiv.org/abs/1312.0273

[111] K. Griest, D. Seckel, "Cosmic Asymmetry, Neutrinos and the Sun", *Nucl. Phys.*, **vol. B283**:p. 681, 1987. [Erratum: Nucl. Phys.B296,1034(1988)]

[112] R. Catena, B. Schwabe, "Form factors for dark matter capture by the Sun in effective theories", *JCAP*, **vol. 1504** (04):p. 042, 2015. http://arxiv.org/abs/1501.03729

[113] V. Hess. URL http://www.nobelprize.org/nobel_prizes/physics/laureates/1936/press.html

[114] S. P. Ahlen (AMS), "Alpha magnetic spectrometer on the international space station", in "International School of Cosmic Ray Astrophysics: 10th Course: Toward the Millennium in Astrophysics: Problems and Prospects Erice, Italy, June 16-26, 1996", (1996)

[115] A. M. Hillas, "Cosmic Rays: Recent Progress and some Current Questions", in "Conference on Cosmology, Galaxy Formation and Astro-Particle Physics on the Pathway to the SKA Oxford, England, April 10-12, 2006", (2006). http://arxiv.org/abs/astro-ph/0607109

[116] G. T. Zatsepin, V. A. Kuzmin, "Upper limit of the spectrum of cosmic rays", *JETP Lett.*, **vol. 4**:pp. 78–80, 1966. [Pisma Zh. Eksp. Teor. Fiz.4,114(1966)]

[117] E. Fermi, "On the Origin of the Cosmic Radiation", *Phys. Rev.*, **vol. 75**:pp. 1169–1174, 1949

[118] C. Grupen, *Astroparticle Physics*, SpringerLink: Springer e-Books (Springer, 2005). URL https://books.google.ch/books?id=wlVGJ4X1BKkC

[119] M. S. Longair, *High Energy Astrophysics* (Cambridge University Press, 1992)

[120] A. R. Bell, "The Acceleration of cosmic rays in shock fronts. I", *Mon. Not. Roy. Astron. Soc.*, **vol. 182**:pp. 147–156, 1978

[121] L. Anchordoqui, T. C. Paul, S. Reucroft, J. Swain, "Ultrahigh-energy cosmic rays: The State of the art before the Auger Observatory", *Int. J. Mod. Phys.*, **vol. A18**:pp. 2229–2366, 2003. http://arxiv.org/abs/hep-ph/0206072

[122] D. Perkins, *Particle Astrophysics*, Oxford Master Series in Condensed Matter Physics (Oxford University Press, 2003). URL https://books.google.ch/books?id=WJnARsI5uywC

[123] A. Burrows, E. Livne, L. Dessart, C. Ott, J. Murphy, "A new mechanism for core-collapse supernova explosions", *Astrophys. J.*, **vol. 640**:pp. 878–890, 2006. http://arxiv.org/abs/astro-ph/0510687

[124] M. Ackermann, *et al.* (Fermi-LAT), "Detection of the Characteristic Pion-Decay Signature in Supernova Remnants", *Science*, **vol. 339**:p. 807, 2013. http://arxiv.org/abs/1302.3307

[125] G. Ferrand, S. Safi-Harb, "A Census of High-Energy Observations of Galactic Supernova Remnants", *Adv. Space Res.*, **vol. 49**:pp. 1313–1319, 2012. http://arxiv.org/abs/1202.0245

[126] C. Distefano, D. Guetta, E. Waxman, A. Levinson, "Neutrino flux predictions for known galactic microquasars", *Astrophys. J.*, **vol. 575**:pp. 378–383, 2002. http://arxiv.org/abs/astro-ph/0202200

[127] J. Abraham, *et al.* (Pierre Auger), "Correlation of the highest-energy cosmic rays with the positions of nearby active galactic nuclei", *Astropart. Phys.*, **vol. 29**:pp. 188–204, 2008. [Erratum: Astropart. Phys.30,45(2008)], http://arxiv.org/abs/0712.2843

[128] R. Abbasi, *et al.* (IceCube), "An absence of neutrinos associated with cosmic-ray acceleration in γ-ray bursts", *Nature*, **vol. 484**:pp. 351–353, 2012. http://arxiv.org/abs/1204.4219

[129] M. G. Aartsen, *et al.* (IceCube), "An All-Sky Search for Three Flavors of Neutrinos from Gamma-Ray Bursts with the IceCube Neutrino Observatory", 2016. http://arxiv.org/abs/1601.06484

[130] K. Murase, S. Inoue, S. Nagataki, "Cosmic Rays Above the Second Knee from Clusters of Galaxies and Associated High-Energy Neutrino Emission", *Astrophys. J.*, **vol. 689**:p. L105, 2008. http://arxiv.org/abs/0805.0104

[131] J. K. Becker, P. L. Biermann, J. Dreyer, T. M. Kneiske, "Cosmic Rays VI - Starburst galaxies at multiwavelengths", 2009. http://arxiv.org/abs/0901.1775

[132] A. Loeb, E. Waxman, "The Cumulative background of high energy neutrinos from starburst galaxies", *JCAP*, **vol. 0605**:p. 003, 2006. http://arxiv.org/abs/astro-ph/0601695

[133] W. Rodejohann, "Neutrino Mixing and Neutrino Telescopes", *JCAP*, **vol. 0701**:p. 029, 2007. http://arxiv.org/abs/hep-ph/0612047

[134] S. Choubey, W. Rodejohann, "Flavor Composition of UHE Neutrinos at Source and at Neutrino Telescopes", *Phys. Rev.*, **vol. D80**:p. 113006, 2009. http://arxiv.org/abs/0909.1219

[135] J. Neyman, "Outline of a Theory of Statistical Estimation Based on the Classical Theory of Probability", *Phil. Trans. R. Soc. A*, **vol. 236**:pp. 333–380, 1937 Aug

[136] G. J. Feldman, R. D. Cousins, "A Unified approach to the classical statistical analysis of small signals", *Phys. Rev.*, **vol. D57**:pp. 3873–3889, 1998. http://arxiv.org/abs/physics/9711021

[137] J. Braun, *et al.*, "Methods for point source analysis in high energy neutrino telescopes", *Astropart. Phys.*, **vol. 29**:pp. 299–305, 2008. http://arxiv.org/abs/0801.1604

[138] F. James, M. Roos, "Minuit: A System for Function Minimization and Analysis of the Parameter Errors and Correlations", *Comput. Phys. Commun.*, **vol. 10**:pp. 343–367, 1975

[139] J. T. Kent, "The fisher-bingham distribution on the sphere", *Journal of the Royal Statistical Society. Series B (Methodological)*, **vol. 44** (1):pp. 71–80, 1982. URL http://www.jstor.org/stable/2984712

[140] M. G. Aartsen, *et al.* (IceCube), "Searches for Extended and Point-like Neutrino Sources with Four Years of IceCube Data", *Astrophys. J.*, **vol. 796** (2):p. 109, 2014. http://arxiv.org/abs/1406.6757

[141] J.-M. Levy, "Cross-section and polarization of neutrino-produced tau's made simple", *J. Phys.*, **vol. G36**:p. 055002, 2009. http://arxiv.org/abs/hep-ph/0407371

[142] M. G. Aartsen, *et al.* (IceCube), "Search for dark matter annihilations in the Sun with the 79-string IceCube detector", *Phys. Rev. Lett.*, **vol. 110** (13):p. 131302, 2013. http://arxiv.org/abs/1212.4097

[143] J. R. Klein, A. Roodman, "Blind analysis in nuclear and particle physics", *Ann. Rev. Nucl. Part. Sci.*, **vol. 55**:pp. 141–163, 2005

[144] B. P. Roe, *et al.*, "Boosted decision trees, an alternative to artificial neural networks", *Nucl. Instrum. Meth.*, **vol. A543** (2-3):pp. 577–584, 2005. http://arxiv.org/abs/physics/0408124

[145] M. G. Aartsen, *et al.* (IceCube), "Search for Dark Matter Annihilation in the Galactic Center with IceCube-79", *Eur. Phys. J.*, **vol. C75** (10):p. 492, 2015. http://arxiv.org/abs/1505.07259

[146] M. G. Aartsen, *et al.* (IceCube), "Characterization of the Atmospheric Muon Flux in IceCube", 2015. http://arxiv.org/abs/1506.07981

[147] J. Feintzeig, *Searches for Point-like Sources of Astrophysical Neutrinos with the IceCube Neutrino Observatory*, Ph.D. thesis, University of Wisconsin–Madison, 2014

[148] J. P. Dumm, *Searches for Point-like Sources of Neutrinos with the 40-String IceCube Detector*, Ph.D. thesis, University of Wisconsin–Madison, 2011

[149] P. Gondolo, *et al.*, "DarkSUSY: Computing supersymmetric dark matter properties numerically", *JCAP*, **vol. 0407**:p. 008, 2004. http://arxiv.org/abs/astro-ph/0406204

[150] S. Adrian-Martinez, *et al.* (ANTARES), "First results on dark matter annihilation in the Sun using the ANTARES neutrino telescope", *JCAP*, **vol. 1311**:p. 032, 2013. http://arxiv.org/abs/1302.6516

[151] K. Choi, *et al.* (Super-Kamiokande), "Search for neutrinos from annihilation of captured low-mass dark matter particles in the Sun by Super-Kamiokande", *Phys. Rev. Lett.*, **vol. 114** (14):p. 141301, 2015. http://arxiv.org/abs/1503.04858

[152] C. Amole, *et al.* (PICO), "Dark Matter Search Results from the PICO-2L C_3F_8 Bubble Chamber", *Phys. Rev. Lett.*, **vol. 114** (23):p. 231302, 2015. http://arxiv.org/abs/1503.00008

[153] H. Silverwood, *et al.*, "Sensitivity of IceCube-DeepCore to neutralino dark matter in the MSSM-25", *JCAP*, **vol. 1303**:p. 027, 2013. http://arxiv.org/abs/1210.0844

[154] D. S. Akerib, *et al.* (LUX), "Improved WIMP scattering limits from the LUX experiment", 2015. http://arxiv.org/abs/1512.03506

[155] R. Agnese, *et al.* (SuperCDMS), "Search for Low-Mass Weakly Interacting Massive Particles with SuperCDMS", *Phys. Rev. Lett.*, **vol. 112** (24):p. 241302, 2014. http://arxiv.org/abs/1402.7137

[156] M. Danninger, *Searches for Dark Matter with IceCube and DeepCore*, Ph.D. thesis, Stockholm U., 2013. URL http://www.diva-portal.org/smash/record.jsf?aq2=[[]]&c=1&af=[]&searchType=SIMPLE&query=621654&language=en&pid=diva2%3A621654&aq=[[]]&jfwid=-9380&sf=all&aqe=[]&sortOrder=author_sort_asc&onlyFullText=false&noOfRows=50&dswid=7188

[157] J. Binney, S. Tremaine, *Galactic Dynamics: Second Edition* (Princeton University Press, 2008)

[158] F. S. Ling, E. Nezri, E. Athanassoula, R. Teyssier, "Dark Matter Direct Detection Signals inferred from a Cosmological N-body Simulation with Baryons", *JCAP*, **vol. 1002**:p. 012, 2010. http://arxiv.org/abs/0909.2028

[159] M. Vogelsberger, S. D. M. White, "Streams and caustics: the fine-grained structure of LCDM haloes", *Mon. Not. Roy. Astron. Soc.*, **vol. 413**:p. 1419, 2011. http://arxiv.org/abs/1002.3162

[160] J. Bovy, *et al.*, "The Milky Way's circular velocity curve between 4 and 14 kpc from APOGEE data", *Astrophys. J.*, **vol. 759**:p. 131, 2012. http://arxiv.org/abs/1209.0759

[161] M. Asplund, N. Grevesse, A. J. Sauval, P. Scott, "The chemical composition of the Sun", *Ann. Rev. Astron. Astrophys.*, **vol. 47**:pp. 481–522, 2009. http://arxiv.org/abs/0909.0948

[162] M. Danninger, C. Rott, "Solar WIMPs unravelled: Experiments, astrophysical uncertainties, and interactive tools", *Phys. Dark Univ.*, **vol. 5-6**:pp. 35–44, 2014. http://arxiv.org/abs/1509.08230

[163] M. Beltran, D. Hooper, E. W. Kolb, Z. C. Krusberg, "Deducing the nature of dark matter from direct and indirect detection experiments in the absence of collider signatures of new physics", *Phys. Rev.*, **vol. D80**:p. 043509, 2009. http://arxiv.org/abs/0808.3384

[164] J. Blumenthal, P. Gretskov, M. Krämer, C. Wiebusch, "Effective field theory interpretation of searches for dark matter annihilation in the Sun with the IceCube Neutrino Observatory", *Phys. Rev.*, **vol. D91** (3):p. 035002, 2015. http://arxiv.org/abs/1411.5917

[165] A. Alves, S. Profumo, F. S. Queiroz, W. Shepherd, "Effective field theory approach to the Galactic Center gamma-ray excess", *Phys. Rev.*, **vol. D90** (11):p. 115003, 2014. http://arxiv.org/abs/1403.5027

[166] G. Aad, *et al.* (ATLAS), "Search for dark matter candidates and large extra dimensions in events with a jet and missing transverse momentum with the ATLAS detector", *JHEP*, **vol. 04**:p. 075, 2013. http://arxiv.org/abs/1210.4491

[167] M. W. Cahill-Rowley, J. L. Hewett, A. Ismail, M. E. Peskin, T. G. Rizzo, "pMSSM Benchmark Models for Snowmass 2013", in "Community Summer Study 2013: Snowmass on the Mississippi (CSS2013) Minneapolis, MN, USA, July 29-August 6, 2013", (2013). http://arxiv.org/abs/1305.2419, URL http://inspirehep.net/record/1233082/files/arXiv:1305.2419.pdf

[168] E. Morgante, D. Racco, M. Rameez, A. Riotto, "The 750 GeV Diphoton excess, Dark Matter and Constraints from the IceCube experiment", 2016. http://arxiv.org/abs/1603.05592

[169] S.-L. Chen, Y. Zhang, "Isospin-Violating Dark Matter and Neutrinos From the Sun", *Phys. Rev.*, **vol. D84**:p. 031301, 2011. http://arxiv.org/abs/1106.4044

[170] Y. Gao, J. Kumar, D. Marfatia, "Isospin-Violating Dark Matter in the Sun", *Phys. Lett.*, **vol. B704**:pp. 534–540, 2011. http://arxiv.org/abs/1108.0518

[171] M. G. Aartsen, *et al.* (IceCube), "Search for Time-independent Neutrino Emission from Astrophysical Sources with 3 yr of IceCube Data", *Astrophys. J.*, **vol. 779**:p. 132, 2013. http://arxiv.org/abs/1307.6669

[172] R. Abbasi, *et al.* (IceCube), "Time-Integrated Searches for Point-like Sources of Neutrinos with the 40-String IceCube Detector", *Astrophys. J.*, **vol. 732**:p. 18, 2011. http://arxiv.org/abs/1012.2137

[173] M. G. Aartsen, *et al.* (IceCube, Pierre Auger, Telescope Array), "Search for correlations between the arrival directions of IceCube neutrino events and ultrahigh-energy cosmic rays detected by the Pierre Auger Observatory and the Telescope Array", *Submitted title =*

[174] V. Cavasinni, D. Grasso, L. Maccione, "TeV Neutrinos from SuperNova Remnants embedded in Giant Molecular Clouds", *Astropart. Phys.*, **vol. 26**:pp. 41–49, 2006. http://arxiv.org/abs/astro-ph/0604004

[175] D. Guetta, E. Amato, "Neutrino flux predictions for galactic plerions", *Astropart. Phys.*, **vol. 19**:pp. 403–407, 2003. http://arxiv.org/abs/astro-ph/0209537

[176] W. Bednarek, "Neutrinos from the pulsar wind nebulae", *Astron. Astrophys.*, **vol. 407**:pp. 1–6, 2003. http://arxiv.org/abs/astro-ph/0305430

[177] G. F. Burgio, B. Link, "Production of high-energy mu neutrinos from young neutron stars", *Nucl. Phys. Proc. Suppl.*, **vol. 165**:pp. 231–236, 2007. [,231(2006)], http://arxiv.org/abs/astro-ph/0609561

[178] A. A. Abdo, *et al.*, "TeV Gamma-Ray Sources from a Survey of the Galactic Plane with Milagro", *Astrophys. J.*, **vol. 664**:pp. L91–L94, 2007. http://arxiv.org/abs/0705.0707

[179] A. Djannati-Atai, E. Ona-Wilhelmi, M. Renaud, S. Hoppe (HESS), "H.E.S.S. Galactic Plane Survey unveils a Milagro Hotspot", in "Proceedings, 30th International Cosmic Ray Conference (ICRC 2007)", vol. 2, pp. 863–868 (2007). http://arxiv.org/abs/0710.2418, URL http://inspirehep.net/record/764004/files/arXiv:0710.2418.pdf

[180] J. Albert, *et al.* (MAGIC), "MAGIC observations of the unidentified TeV gamma-ray source TeV J2032+4130", *Astrophys. J.*, **vol. 675**:pp. L25–L28, 2008. http://arxiv.org/abs/0801.2391

[181] A. Kappes, F. Halzen, A. O. Murchadha, "Prospects of identifying the sources of the galactic cosmic rays with IceCube", *Nucl. Instrum. Meth.*, **vol. A602**:pp. 117–119, 2009

[182] M. C. Gonzalez-Garcia, F. Halzen, S. Mohapatra, "Identifying Galactic PeVatrons with Neutrinos", *Astropart. Phys.*, **vol. 31**:pp. 437–444, 2009. http://arxiv.org/abs/0902.1176

[183] A. A. Abdo, *et al.*, "Spectrum and Morphology of the Two Brightest Milagro Sources in the Cygnus Region: MGRO J2019+37 and MGRO J2031+41", *Astrophys. J.*, **vol. 753**:p. 159, 2012. http://arxiv.org/abs/1202.0846

[184] "Observation of the TeV gamma-ray source MGRO J1908+06 with ARGO-YBJ", *Astrophys. J.*, **vol. 760**:p. 110, 2012. http://arxiv.org/abs/1207.6280

[185] C. Stegmann, A. Kappes, J. Hinton, F. Aharonian, "Potential neutrino signals in a northern hemisphere neutrino telescope from galactic gamma-ray sources", *Astrophys. Space Sci.*, **vol. 309**:pp. 429–433, 2007

[186] A. A. Abdo, *et al.*, "Milagro Observations of TeV Emission from Galactic Sources in the Fermi Bright Source List", *Astrophys. J.*, **vol. 700**:pp. L127–L131, 2009. [Erratum: Astrophys. J.703,L185(2009)], http://arxiv.org/abs/0904.1018

[187] A. A. Abdo, *et al.* (Fermi-LAT), "Fermi LAT Observations of LS I +61 303: First detection of an orbital modulation in GeV Gamma Rays", *Astrophys. J.*, **vol. 701**:pp. L123–L128, 2009. http://arxiv.org/abs/0907.4307

[188] P. Bordas, G. Maier (HESS, VERITAS), "VERITAS and H.E.S.S. observations of the gamma-ray binary HESS J0632+057", *AIP Conf. Proc.*, **vol. 1505**:pp. 366–369, 2012. http://arxiv.org/abs/1212.0350

[189] T. C. Hillwig, D. R. Gies, "Spectroscopic Observations of the Mass Donor Star in SS 433", *Astrophys. J.*, **vol. 676**:p. L37, 2008. http://arxiv.org/abs/0711.4348

[190] A. A. Abdo, *et al.*, "Modulated High-Energy Gamma-Ray Emission from the Microquasar Cygnus X-3", *Science*, **vol. 326** (5959):pp. 1512–1516, 2009

[191] R. Abbasi, *et al.* (IceCube), "Searches for periodic neutrino emission from binary systems with 22 and 40 strings of IceCube", *Astrophys. J.*, **vol. 748**:p. 118, 2012. http://arxiv.org/abs/1108.3023

[192] C. Brocksopp, A. E. Tarasov, V. M. Lyuty, P. Roche, "An improved orbital ephemeris for cygnus x-1", *Astron. Astrophys.*, **vol. 343**:p. 861, 1999. http://arxiv.org/abs/astro-ph/9812077

[193] A. A. Abdo, *et al.*, "Modulated High-Energy Gamma-Ray Emission from the Microquasar Cygnus X-3", *Science*, **vol. 326** (5959):pp. 1512–1516, 2009

[194] C. Chevalier, S. A. Ilovaisky, "The quiescent light curve and orbital period of gro j0422+32", *Astron. Astrophys.*, **vol. 312**:p. 105, 1996. http://arxiv.org/abs/astro-ph/9602114

[195] E. T. Neil, C. D. Bailyn, B. E. Cobb, "IR Monitoring of the Microquasar GRS 1915+105: Detection of Orbital and Superhump Signatures", *Astrophys. J.*, **vol. 657**:pp. 409–414, 2007. http://arxiv.org/abs/astro-ph/0610480

[196] M. A. P. Torres, *et al.*, "Mmt observations of the black hole candidate xte j1118+480 near and in quiescence", *Astrophys. J.*, **vol. 612**:pp. 1026–1033, 2004. http://arxiv.org/abs/astro-ph/0405509

[197] C. Mariaud, *et al.* (HESS), "VHE observations of the gamma-ray binary system LS 5039 with H.E.S.S", in "Proceedings, 34th International Cosmic Ray Conference (ICRC 2015)", (2015). http://arxiv.org/abs/1509.05791, URL http://inspirehep.net/record/1394109/files/arXiv:1509.05791.pdf

[198] A. Abramowski, *et al.* (HESS), "Discovery of VHE emission towards the Carina arm region with the H.E.S.S. telescope array: HESS J1018-589", *Astron. Astrophys.*, **vol. 541**:p. A5, 2012. http://arxiv.org/abs/1203.3215

[199] G. Maier (VERITAS), "Long-term TeV Observations of the Gamma-ray Binary HESS J0632+057 with VERITAS", in "Proceedings, 34th International Cosmic Ray Conference (ICRC 2015)", (2015). http://arxiv.org/abs/1508.05489, URL http://inspirehep.net/record/1389122/files/arXiv:1508.05489.pdf

[200] M. J. Coe, *et al.* (Fermi-LAT), "Periodic Emission from the Gamma-ray Binary 1FGL J1018.6-5856", *Science*, **vol. 335**:pp. 189–193, 2012. http://arxiv.org/abs/1202.3164

[201] C. Pfrommer, T. A. Ensslin, "Constraining the population of cosmic ray protons in cooling flow clusters with gamma-ray and radio observations: Are Radio mini-halos of hadronic origin?", *Astron. Astrophys.*, **vol. 426**:pp. 777–777, 2004. http://arxiv.org/abs/astro-ph/0306257

[202] L. I. Caramete, P. L. Biermann, "The catalog of nearby black hole candidates", 2011. http://arxiv.org/abs/1107.2244

[203] J. E. Gizis, M. F. Skrutskie, "The two micron all-sky survey: removing the infrared foreground", *IAU Symp.*, **vol. 204**:p. 197, 2001. http://arxiv.org/abs/astro-ph/0010461

[204] M. S. Pshirkov, P. G. Tinyakov, F. R. Urban, "New limits on extragalactic magnetic fields from rotation measures", 2015. http://arxiv.org/abs/1504.06546

[205] M. S. Pshirkov, P. G. Tinyakov, P. P. Kronberg, K. J. Newton-McGee, "Deriving global structure of the Galactic Magnetic Field from Faraday Rotation Measures of extragalactic sources", *Astrophys. J.*, **vol. 738**:p. 192, 2011. http://arxiv.org/abs/1103.0814

[206] R. Jansson, G. R. Farrar, "The Galactic Magnetic Field", *Astrophys. J.*, **vol. 761**:p. L11, 2012. http://arxiv.org/abs/1210.7820

[207] R. U. Abbasi, *et al.* (Telescope Array), "Indications of Intermediate-Scale Anisotropy of Cosmic Rays with Energy Greater Than 57 EeV in the Northern Sky Measured with the Surface Detector of the Telescope Array Experiment", *Astrophys. J.*, **vol. 790**:p. L21, 2014. http://arxiv.org/abs/1404.5890

[208] S. V. Troitsky, "A doublet of cosmic-ray events with primary energies $> 10^2 0$ eV", *JETP Lett.*, **vol. 96**:pp. 13–16, 2012. http://arxiv.org/abs/1205.6435

[209] S. Adrian-Martinez, *et al.* (ANTARES), "Search for a correlation between ANTARES neutrinos and Pierre Auger Observatory UHECRs arrival directions", *Astrophys. J.*, **vol. 774**:p. 19, 2013. http://arxiv.org/abs/1202.6661

[210] A. Neronov, D. V. Semikoz, "Evidence the Galactic contribution to the IceCube astrophysical neutrino flux", *Astropart. Phys.*, **vol. 75**:pp. 60–63, 2016. http://arxiv.org/abs/1509.03522

Abbreviations

PMNS	**P**ontecorvo **M**aki **N**akagawa **S**akata
CC	**C**harged **C**urrent
NC	**N**eutral **C**urrent
DOM	**D**igital **O**ptical Module
PMT	**P**hoto**m**ultiplier **T**ube
LED	**L**ight **E**mitting **D**iode
ATWD	**A**nalogue **T**ransient **W**aveform **D**igitizer
FADC	**F**ast **A**nalogue to **D**igital **C**onverter
PE	**P**hoto**e**lectron
HLC	**H**ard **L**ocal **C**oincidence
SLC	**S**oft **L**ocal **C**oincidence
CR	**C**osmic **R**ay
SPE	**S**ingle **P**hoto**e**lectron
MPE	**M**ulti **P**hoto**e**lectron
CORSIKA	**CO**smic **R**ay **SI**mulations for **KA**scade
MMC	**M**uon **M**onte **C**arlo
PPC	**P**hoto**P**ropagation **C**ode
GPU	**G**raphic **P**rocessing **U**nit
EM	**E**lectro**M**agnetic
SM	**S**tandard **M**odel
DM	**D**ark **M**atter
SDSS	**S**loan **D**igital **S**ky **S**urvey
CMB	**C**osmic **M**icrowave **B**ackground
BAO	**B**aryon **A**ccoustic **O**scillation
LRG	**L**uminous **R**ed **G**alaxy
MSSM	**M**inimally **S**upersymmetric **S**tandard **M**odel

NFW	**N**avarro **F**renk **W**hite
HESS	**H**igh **E**nergy **S**tereoscopic **S**ystem
SNR	**S**uper**N**ova **R**emnant
AGN	**A**ctive **G**alactic Nucleus
GRB	**G**amma **R**ay **B**urst
UHECR	**U**ltra **H**igh **E**nergy **C**osmic **R**ay
TS	**T**est **S**tatistic
CTEQ	**C**oordinated **T**heoretical **E**xperimental **P**roject on **Q**CD
DIS	**D**eep **I**nelastic **S**cattering
AW	**A**ustral **W**inter
AS	**A**ustral **S**ummer
MJD	**M**odified **J**ulian **D**ay
BDT	**B**oosted **D**ecision **T**ree
RT	**R**adius-**T**ime
MC	**M**onte **C**arlo
SD	**S**pin-**D**ependent
SI	**S**pin-**I**ndependent
CTA	**C**herenkov **T**elescope **A**rray
SMH	**S**tandard **M**axwellian **H**alo
GMC	**G**iant **M**olecular **C**loud
PWN	**P**ulsar **W**ind **N**ebula
VHE	**V**ery **H**igh **E**nergy
GZK	**G**reisen **Z**atsepin **K**uzmin
GC	**G**alaxy **C**luster
FIR	**F**ar Infra**Red**
NIR	**N**ear Infra**Red**